The good placement

Doctoral thesis

The Good Placement:

Information-driven choice of fNIRS optode location and its impact on brain-computer interface performance

Amaia Benitez-Andonegui

2021

Production: Ipskamp printing

Cover: Amaia Benitez-Andonegui

ISBN: 978-94-6423-145-8

The Good Placement:

Information-driven choice of fNIRS optode location and its impact on brain-computer interface performance

Dissertation

to obtain the degree of Doctor at Maastricht University,
on the authority of the Rector Magnificus Prof. dr. Rianne M. Letschert
in accordance with the decision of the Board of Deans,
to be defended in public on Monday 1st of March 2021, at 16.00 hours

by

Amaia Benitez-Andonegui

Supervisors

Prof. dr. Rainer Goebel

Dr. Bettina Sorger

Co-supervisor

Dr. Rico Möckel

Assessment Committee

Prof. dr. David Linden (Chair)

Prof. dr. Jody Culham (Western University, London, Ontario)

Dr. Christian E. Herff

Dr. Sabrina Brigadoi (Università di Padova, Italy)

The projects presented in this thesis were co-funded by Maastricht University through Luik 3 initiative (Funding for Strategic Innovation).

Amari, Aitari eta Anderri

Table of Contents

1

General Introduction

1 Prologue

Nearly a century ago, in the late 1920s, Hans Berger successfully demonstrated that brain activity can be recorded using electrodes placed on a participant's head (Berger, 1929). In the decades that followed, the idea emerged that recorded brain activity could be used as a communication channel or for controlling the environment without the need to engage the normal intermediaries of peripheral nerves and muscles. In his seminal paper, Vidal (1973) detailed a comprehensive theoretical and technical plan for direct brain-computer communication. In this work, he coined the term "brain-computer interface" (BCI) and described that "*to provide a direct link between the inductive mental processes used in solving problem and the symbol-manipulating, deductive capabilities of the computer, is, in a sense, the ultimate goal in man-machine communication"* and envisioned that BCIs *"would indeed elevate the computer to a genuine prosthetic extension of the brain*". He also predicted that "t*o achieve that goal with adequate generality is a formidable task that will require considerable advances in neurophysiology, in signal analysis, and in computer science."* While Vidal's vision influenced the development of BCIs, it would take several decades and technological advancements for that vision to materialize.

A BCI may be defined as a system that measures and converts brain activity into artificial output. This output replaces, restores or enhances outputs produced by the central nervous system, thereby enabling interactions with the external environment in the absence of motor output (Wolpaw et al., 2002; Wolpaw and Wolpaw, 2012). Since BCI technology augments human capabilities by providing a new motor-independent interactive link with the outside world, it constitutes a particularly relevant tool for patients suffering from neuronal damage such as brainstem stroke (Bauer et al., 1979), traumatic brain injury (Carrai et al., 2009), central pontine myelinolysis or end-stage amyotrophic lateral sclerosis (Birbaumer et al., 1999; León-Carrión et al., 2002; Bruno et al., 2008). These conditions can result in a so-called 'locked-in' state, which lacks voluntary muscle control abilities. For patients with such conditions, replacing (lost) motor functions through communication BCIs (Birbaumer et al., 1999; Nijboer et al., 2008; Sellers et al., 2010) and control systems such as wheelchairs, robotic body-parts or robotic agents (Galan et al., 2008; Muller-Putz and Pfurtscheller, 2008; Iturrate et al., 2009; Rebsamen et al., 2011; Tumanov et al., 2015; Murphy et al., 2017) are specially relevant.

BCIs have also been applied to a wide range of other applications: changing brain activation and associated behavior voluntarily through neurofeedback (Subramanian et al., 2011; Scharnowski et al., 2012; Shereena et al., 2018); mental state monitoring, namely alertness, workload and pain (Gagnon et al., 2012a; Shibata et al., 2014; Afergan et al., 2015; Khan and Hong, 2015; Myrden and Chau, 2015; Hu et al., 2019); entertainment purposes such as gaming (Tangermann et al., 2008; Congedo et al., 2011; Coyle et al., 2011; Maby et al., 2012; Vourvopoulos et al., 2016) and for artistic expression such as Multimodal Brain Orchestra (Le Groux et al., 2010) or Brain Painting (Kübler and Botrel, 2019).

With technological development, the number of BCI-related publications has increased almost exponentially. However, the number of real-life applications benefiting potential end-users has not grown as quickly (Shih et al., 2012). This could be due to substantial challenges associated with using BCIs in everyday situations, namely home-use or hospital settings. This ultimate goal of improving the lives of patients is a demanding endeavor since a BCI should be efficient, accurate and reliable but also easy to use, intuitive, and simple to set up. In this dissertation, we identify and address key factors hindering the translational potential of BCIs.

2 Components of brain-computer interfaces

BCIs aim to detect and extract meaningful information from brain signals that indicate what the user wants the BCI to do. BCIs then translate this information in real-time to an appropriate form for device control while providing feedback to the user about the intended act.

2.1 Measuring brain signals

Several functional neuroimaging modalities exist to measure brain activity for BCI applications. They can be divided into two categories: electrophysiological methods, which measure electrical potentials arising from neural activity directly, and hemodynamic (or metabolic) methods, which measure the vascular or metabolic response to neural activity and thus constitute an indirect measure of neural activity (see Figure 1.1).

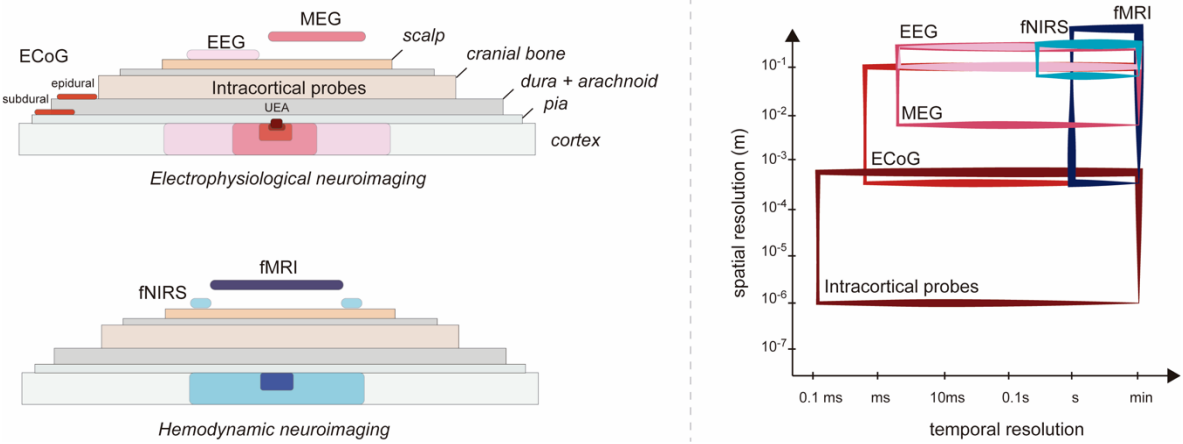

Figure 1.1. Summary of functional neuroimaging modalities used for BCI purposes. Electrophysiological methods (top, left) include electroencephalography (EEG), magnetoencephalography (MEG) and invasive electrocorticography (ECoG) and intracortical recordings (Utah electrode arrays, UAE). Hemodynamic imaging methods (bottom, left) include functional magnetic resonance imaging (fMRI) and functional near-infrared spectroscopy (fNIRS). The size of the rectangles in the cortex provide a qualitative reference for the relative spatial resolutions of the various imaging technologies. Figure adapted with permission from (Sitaram et al., 2017). **Right**. Temporal (x-axis) and spatial resolution (y-axis) of the different functional neuroimaging methods. Figure adapted with permission from Hong and Lieber (2019).

2.1.1 Electrophysiological methods

The billions of neurons in the brain communicate with each other by transmitting neural signal across their synapses (Herculano-Houzel, 2009; Rothwell, 2009). Electroencephalography (**EEG**) measures ensembles of neurons that generate measurable potentials at the scalp surface when transmitting such signals synchronously (Min et al., 2010; Jackson and Bolger, 2014). The generated electric potentials in the brain are conducted through the cerebrospinal fluid, skull and scalp. Conductance through these tissues smears the electrical potentials recorded in the scalp, making the localization of brain activity in EEG challenging (Jackson and Bolger, 2014; Herff, 2016). Additionally, EEG is very susceptible to motion artifacts, particularly from head movements since EEG is very sensitive electrical activity from muscle movement (Yilmaz et al., 2014). Modern EEG devices are very easy to set up and can be used out of the lab easily (Debener et al., 2015). The only cumbersome aspect of an EEG setup is the electrode gel which is required to lower impedance between scalp and electrodes (Herff, 2016). Nonetheless, EEG is the most widely used functional neuroimaging method for BCI purposes due to its excellent temporal

resolution (milliseconds or below), good portability and cost-effectiveness (Min et al., 2010).

Electrocorticography (**ECoG**) measures the same neural signals as EEG, but records them using grid electrodes placed above (epidural) or below (subdural) the dura mater (Schalk and Leuthardt, 2011; Buzsáki et al., 2012). ECoG enjoys higher spatial resolution than EEG because it does not suffer the same volume conduction effects (Chauveau et al., 2004). ECoG measures neural ensemble activity directly below each electrode, effectively combining the advantageous temporal resolution of EEG with improved spatial resolution. However, ECoG is an invasive technique that requires a craniotomy (or at least minimally invasive procedures, depending on the size of the grid) to implant electrodes, limiting its usage to clinical populations (Schalk and Leuthardt, 2011).

Intracortical measurements use penetrating electrode arrays to record action potentials from a small population of neurons in close proximity to the electrode tip (Brandman et al., 2017). While there are multiple intracortical recording devices available, the Utah electrode array (Maynard et al., 1997) is the only intracortical electrode array with FDA approval for long-term human (clinical) studies. It consists of 100 silicon micro-needles (1.5mm long) arranged on a square grid (Fernández et al., 2014). Despite its high temporal resolution and spatial specificity, the Utah electrode array is limited by its ability to target deep neural structures (Choi et al., 2018) and can lead to surgical complications due to the craniotomy required for microarray placement (Szostak et al., 2017; Herff et al., 2020).

The neuronal activity measured by the abovementioned methods also induces magnetic field changes that can be detected by magnetometers placed around the head. Magnetic fields are less affected by the conductance properties of the skull and scalp than electric fields (Min et al., 2010). This gives Magnetoencephalography (**MEG**) better spatial resolution than EEG while remaining non-invasive (Hari et al., 2010; Sitaram et al., 2017). However, magnetic-field changes induced by neuronal activity are very weak (Hari et al., 2010; Singh, 2014) and thus require very sensitive and costly magnetometers to measure such signal (Min et al., 2010). Further, magnetometers require dedicated shielding from electromagnetic interference (Kobayashi et al., 2017), making the method less portable and less affordable than EEG. Finally, similar to EEG, MEG is also sensitive to strong contamination by motion artifacts (Muthukumaraswamy, 2013).

2.1.2 Hemodynamic methods

Oxygen is transported in the blood via hemoglobin. Based on its saturation state, hemoglobin can be oxygenated (i.e., HbO) or deoxygenated (i.e., deoxyhemoglobin, HbR). Neuronal activity increases oxygen metabolism, resulting in decreases in oxygen concentration in local capillary beds (Uludağ et al., 2015). This process triggers an increase in local cerebral blood flow and blood volume, which in turn supplies more oxygen than consumed to the area. This temporary oversupply of oxygen in regional cerebral blood flow results in relative increases in HbO concentration and a concurrent relative decrease in HbR.

HbO and HbR have different magnetic properties and functional magnetic resonance imaging (**fMRI)** utilizes this local blood oxygenation level dependency (termed the BOLD effect) to non-invasively measure neuronal activation (Ogawa et al., 1990; Bandettini et al., 1992; Kwong et al., 1992; Ogawa et al., 1992). Using fMRI, neuronal signals across the entire brain can be measured with relatively high spatial resolution (see Figure 1.1). However, hemodynamic responses build up much slower than electrical or magnetic changes caused by neuronal activity, which results in lower effective temporal resolution than all electrophysiological methods. Additionally, there are several practical constraints that limit the ecological validity of fMRI as a method for BCI applications. These include an unnatural supine subject position, noise produced by the scanner, contraindications to being in a magnetic field and potential patient claustrophobia. fMRI can also be strongly affected by motion artifacts. Thus, participants' movements are highly restricted during measurements (Scarapicchia et al., 2017).

In addition to having different magnetic properties, HbO and HbR also differ in their optical properties in the near-infrared (NIR) range of the electromagnetic spectrum (~650–950 nm (Scholkmann et al., 2014)). Light in the NIR range can propagate relatively deep (a few centimeters) into most biological tissue but is absorbed predominantly by hemoglobin molecules. In functional near-infrared spectroscopy (**fNIRS**), optical sensors ('optodes') are placed on the scalp, which can be classified into sources (emitters) and detectors (receivers), depending on their function. Light emitted from a source is propagated through extracerebral and cerebral tissues up to a few centimeters, where some photons are scattered and absorbed before light reaches the detectors (Machado et al., 2014). Common fNIRS systems use at least two different wavelengths as to be sensitive to both HbO and HbR. The shorter

wavelength (650–700 nm) is predominantly absorbed by HbR, while the longer wavelength (800–850 nm) is predominantly absorbed by HbO (Nishiyori, 2016). By emitting NIR light at different wavelengths and measuring absorption at detector sites, fNIRS can detect changes in concentrations of both HbO and HbR (here on referred to as Δ[HbO] and Δ[HbR], respectively) caused by neuronal activation.

Modern fNIRS systems are compact, portable, cost-effective, safe, user friendly and more robust against motion artifacts than most of other functional neuroimaging modalities (Boas et al., 2004; Lloyd-Fox et al., 2010; Pinti et al., 2018). These features make fNIRS a powerful technique for use in BCIs aimed at communication and control. In many ways, fNIRS can be regarded as an effective compromise between the high temporal resolution of EEG (Irani et al., 2007) and the robustness of the hemodynamic response in fMRI. Its mobility and cost are comparable to EEG, which is currently the most widely used modality for BCIs. FNIRS, however, has higher spatial resolution than EEG (although lower than fMRI (Lloyd-Fox et al., 2010). Penetration depth is shallow, similar to EEG, but this does not impose a limiting factor for BCI applications since measurable brain signals can be acquired from superficial cortical areas (Naseer and Hong, 2015a).

The work presented in this dissertation focuses on fNIRS-based BCIs due to the abovementioned features of fNIRS, which offer distinct advantages for developing practical, portable and robust BCIs. The remainder of this section describes the components constituting a BCI with an emphasis on fNIRS.

2.2 Encoding user intentions

Brain signals used in fNIRS (and fMRI) BCIs can be generated by moving a body part to activate the motor cortex, i.e., by performing a motor-execution task, or by covertly performing a task (Naseer and Hong, 2015a). Examples of covert tasks include:

- Motor imagery - imagining one’s own body part moving without muscular activity
- Mental calculation/arithmetic - performing calculations in one’s head
- Mental singing - reproducing a song in one’s head without any external music input

- Mental talking or inner speech - reciting a text or having a monologue in one's head
- Object rotation - imagining a rotating object
- Spatial navigation –imagining walking through and visualizing a (changing) three-dimensional scene

Covert tasks hold potential in BCI applications since they act as a non-muscular communication channel for generating commands. Further, these covert tasks engage superficial cortical areas, such as the prefrontal or motor cortices (Naseer and Hong, 2015a), which are easily measured using fNIRS.

2.3 Detecting and extracting relevant information

Regardless of the employed functional neuroimaging modality, measured brain signals are often weak, containing physiological and instrumental noise, and motion artifacts (Krusienski et al., 2012; Naseer and Hong, 2015a). The aim of data preprocessing pipelines is to correct or remove these noise sources. Next, information present in the preprocessed time-series is summarized in trials, blocks or epochs using a summary measure or feature. For fNIRS-BCIs, examples include temporal averages, slope or peak value in a predefined window (Naseer and Hong, 2015a; Hong et al., 2018) or the resulting *beta* or *t*-value after fitting a General Linear Model on the time points associated with a given trial (Valente et al., 2019).

2.4 Translating information and providing feedback to the user

User's intentions are indirectly measured by recording brain activity and must be translated into appropriate device commands to convey user intent. A model known as classifier must be trained to translate features of brain activity to one of a pre-defined set of user intentions (McFarland and Krusienski, 2012). Importantly, as BCIs preferably operate in real-time, this translation must occur as new observations come in, thus requiring generalization to new, unseen data.

The translated output of BCI applications serves a dual purpose. First, it serves as a command for the control device or communication system. For example, if the goal of the BCI is to establish a communication channel for the user, then the model would map brain activity onto a word or an answer to a question (see Figure 1.2). Alternatively, if the goal is

to control a robotic arm so that the user can, e.g., grab a coffee mug, then the brain activity would be mapped to joint movements of the robotic arm to accomplish the user's intents. Second, the translated output serves as feedback to the user about the success or failure of the intended act (Leeb et al., 2007). fNIRS-based BCI systems that rely on computer screens/displays for proving the output, most commonly use 2D visual displays/interfaces, such as pictures (Luu and Chau, 2009), geometrical figures (Coyle et al., 2004; Weyand and Chau, 2015), cartoon-like stimuli (Power et al., 2012) or auditory stimuli such as questions in communication paradigms (Naito et al., 2007; Gallegos-Ayala et al., 2014; Abdalmalak et al., 2017; Nagels-Coune et al., 2017; Abdalmalak et al., 2020; Nagels-Coune et al., 2020). In recent years, Augmented and Virtual Reality (AR/VR) technology has matured to enable complex and immersive interfaces (Putze, 2019; Putze et al., 2020). Virtual reality is an immersive system that provides users with a sense of presence through potential interactions with a simulated virtual world, rendered in real-time (Lécuyer et al., 2008). Augmented reality enhances the user's perception by overlaying virtual objects onto the user's environment (Si-Mohammed et al., 2017). These technologies enable multisensory display integration and have the potential to increase engagement and motivation in users (Chin et al., 2010).

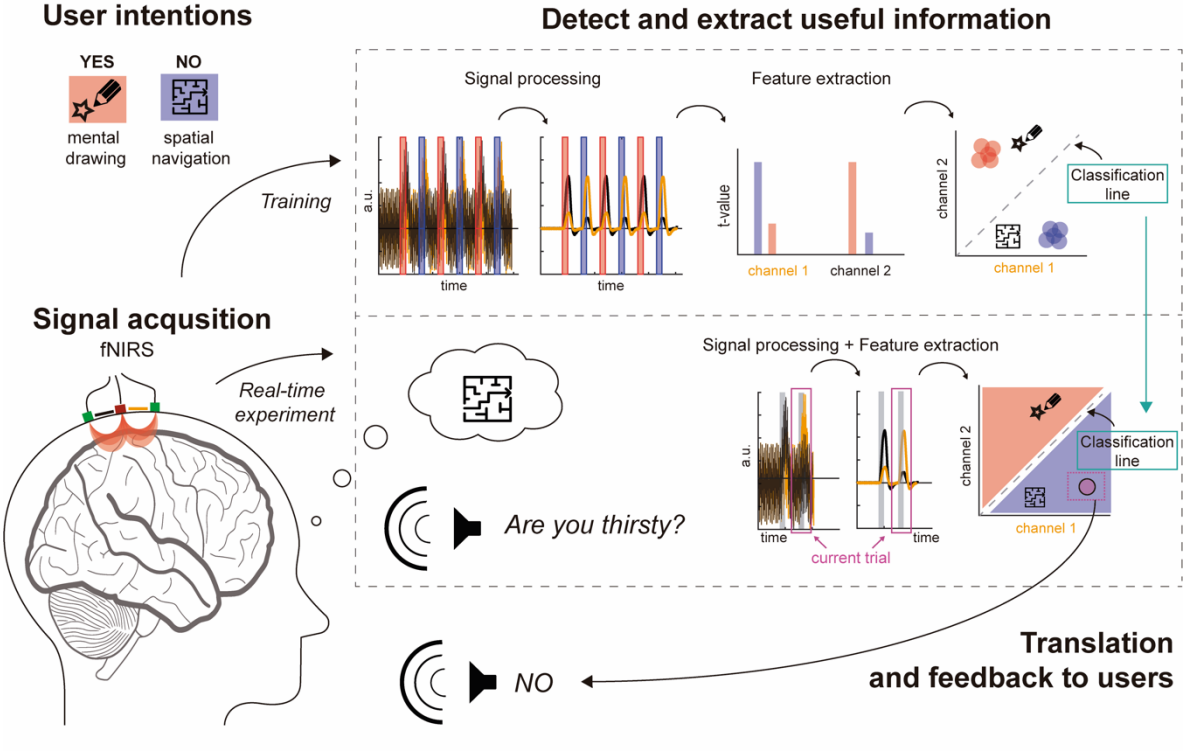

Figure 1.2. Schematic representation of an fNIRS-BCI system for communication. In this example, the participant is asked different sets of questions and encodes the answer YES via mental drawing (symbolized in red), where the participant imagines drawing simple geometric figures such as a star, while (s)he encodes the answer NO using spatial navigation (depicted in blue), which involves to imagine walking through and visualizing a (changing) three-dimensional scene. The neural activity is recorded through fNIRS channels (black and yellow lines) located on the motor and parietal cortex. The recorded noisy signal is processed before a general linear model is fitted onto the time points, after which t-values are estimated per channel. Here, channel 1 (yellow) is more sensitive to the spatial navigation task, while channel 2 (black) is more sensitive to mental drawing. A classification line that best distinguishes the two tasks is defined based on the training data across channels. During the real-time experiment, the participant's intention is decoded based on which side of the line in the feature space the current trial falls. For the current trial, the participant performed the spatial navigation task to indicate (s)he was not thirsty.

3 Challenges associated with fNIRS BCIs

The complex, interconnected processes that constitute a BCI pose numerous challenges to establishing communication and control interfaces using brain signals. While some obstacles are independent of the chosen functional brain-imaging modality, others are modality-specific. Here, we describe a number of challenges facing fNIRS-based BCIs.

3.1 Measuring brain signals: the problem of optode layout design

The spatial resolution of fNIRS depends on how source-detector pairs (or 'channels') are arranged on the scalp (Culver et al., 2001). The distance between a source and detector pair, along with the anatomical tissues between them, determines how deep light will travel and the sensitivity to underlying cortex physiology (Brigadoi et al., 2018). Therefore, fNIRS signal quality can differ dramatically between optode layouts.

Researchers often define a region of interest (ROI) in line with their research question and consequently design an optode layout in a grid-like fashion to target that ROI (Brigadoi et al., 2018). The simplest and most common optode layout design assigns source and detector locations on the scalp to cover a given cortical ROI according to the standardized 10-20 EEG system or its extended versions (Oostenveld and Praamstra, 2001). These locations can relate to underlying assumed cortical structure (Koessler et al., 2009; Giacometti et al., 2014) to standard Montreal Neurological Institute (MNI) stereotactic coordinates (Okamoto et al., 2004; Jurcak et al., 2007; Tsuzuki et al., 2007; Tsuzuki and Dan, 2014). Sometimes this approach results in a setup consisting of many optodes, resulting in increasing user discomfort over time. This approach may also lead to a suboptimal sampling of the active area. This is because fNIRS interrogates tissue located between a given source-detector pair and thus regions between a source-source and a detector-detector cannot be sampled or are not sampled optimally (see Figure 1.3).

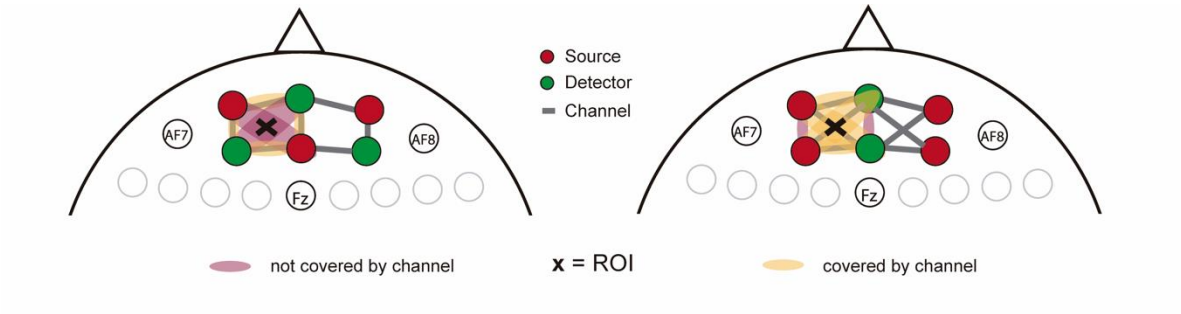

Figure 1.3. Schematic representation of the influence of optode placement on the coverage of the target ROI. This figure shows the top view of the international 10-5 EEG layout and an optode setup that covers the frontal cortex. The arrangement on the left does not properly cover the target ROI, but as indicated in the arrangement on the right, swapping optodes in the second row solves the issue.

To overcome this problem, one could design a given optode layout based on the approach described above, perform fNIRS measurements on a real subject and subsequently assess the quality of measured signals. This layout could then be iteratively modified until the researcher identifies the channels that best capture the signal of the target ROI. However, this is an unfeasible procedure that would require lengthy measurements.

Instead, models can describe the probability that a given photon transmitted from a source to a detector has traveled through a given tissue (Aasted et al., 2015). These models, also called light-sensitivity profiles, require the diffusion approximation of the radiative transport equation to be solved (Boas et al., 2002). However, finding an analytical solution is difficult because light propagation through scattering media with heterogeneous structure (such as the head) is inherently complex (Boas et al., 2002; Strangman et al., 2013). In the absence of analytical solutions, sensitivity-profile computations rely on numerical approaches, such as Monte Carlo Simulations (Strangman et al., 2013). Light-sensitivity profiles computed with Monte Carlo Simulations have been used by the fNIRS community as an objective measure to assess optode layout designs and a number of toolboxes, software and pipelines have been developed specifically for that purpose (Tadel et al., 2011; Machado et al., 2014; Aasted et al., 2015; Wijeakumar et al., 2015; Brigadoi et al., 2018; Zimeo Morais et al., 2018).

Monte Carlo simulations of photon migration use a set of rules to describe consecutive absorption and scattering events that the photons experience when traveling through the head. Simulations require three-dimensional tissue geometry (an anatomical MRI image), segmented into voxels of different tissue types. A common head model consists of five tissues – white matter, gray matter, cerebrospinal fluid, skull and scalp. Every voxel is assigned a set of optical properties (absorption and scattering coefficients, among others) depending on the tissue type they belong to. To begin, an initial position (source location) and direction of the photon is defined, together with an initial surviving weight set to 1. A scattering length L is probabilistically calculated from an exponential distribution, and the photon is moved through the voxels by this length. The photon's weight is incrementally decreased by an exponential factor that takes into account the length L and the absorption coefficient assigned to the voxel the photon had landed. A scattering angle is then calculated using a probability distribution and a new scattering length is determined from an

exponential distribution. The photon is moved the new distance in the updated direction defined by the scattering angle. This process continues until the photon exits the medium or has traveled longer than a predefined period of time, after which a new photon is launched. Millions of photons are typically launched in this process.

One of the outputs of the simulations is the accumulation of all photon weights within each voxel in the tissue, also known as the 2-point Green's function. The light sensitivity can be computed by multiplying the 2-point function obtained from the source location by the 2-point function from the detector location, voxel by voxel (Strangman et al., 2013)[1]. Although Monte Carlo simulations are computationally intensive, the resulting sensitivity profiles offer a way to design optode layouts that maximize sensitivity for an ROI prior to any experiment, thus promising increased signal quality and coverage. This becomes particularly relevant for fNIRS-based BCIs, where developing robust systems that use limited number of optodes is crucial to remain practical and comfortable for clinical applications.

Although Monte Carlo simulations follow a clearly predefined set of rules, approaches to optode layout design that use them allow for certain degree of individualization in their input parameters, such as the type of anatomical head model used (atlas based MRI vs. subject-specific models) or how the target ROIs are defined (anatomically or functionally). Importantly, the final choice will often depend on the temporal/monetary/material resources available to the researcher since collecting additional individualized data has always an associated cost. Therefore, it is important to elucidate the amount of individual MRI-derived information worth to include for designing optode layouts, more so when these resources are limited.

[1] This is true in continuous-wave fNIRS measurements. There are three types of fNIRS systems, namely continuous-wave, frequency-domain and time-domain instruments. The continuous-wave (cw) fNIRS systems emit light at a constant intensity and then only measure the changes in the intensity of the light that passed through the tissue at the detector site. Meanwhile, frequency- and time-domain systems, besides the change in light intensity, they measure the arrival times of the photons that emerge from the tissue (Scholkmann et al., 2014). In this dissertation, a cw-fNIRS system was used.

3.2 Detecting and extracting meaningful information: the presence of physiological noise

The fNIRS signal is susceptible to physiological fNIRS noise originating from global systemic and local regulatory processes of intra- and extra-cerebral origins (Kirilina et al., 2013). These noise sources can compromise sensitivity to brain activation measured by fNIRS BCIs, particularly when insufficiently preprocessed single-trial data feeds back noise instead of brain activity (Klein and Kranczioch, 2019).The main sources of physiological noise are heart rate (~1 Hz), respiration (~0.3 Hz) and blood pressure-related variations. These variations mainly come from so-called Mayer waves (~0.1 Hz) and very low frequency oscillations (<0.04 Hz), as outlined in Figure 1.4 (Boas et al., 2004; Scholkmann et al., 2014; Tachtsidis and Scholkmann, 2016; Tong et al., 2019). Mayer waves occur spontaneously in conscious subjects and are thought to be tightly coupled with synchronous oscillations of sympathetic nervous activity (Julien, 2006; Sassaroli et al., 2012). Very low-frequency oscillations are thought to be related to neurogenic activity of vessels and with vascular endothelial function (Stefanovska, 2007).

The most common approach to reduce the impact of these noise components is to remove specific frequency bands in fNIRS signals by means of digital filters (low-, high- or band-pass filters). The frequency of heart rate is relatively high with respect to the typical fNIRS responses and thus can be can be easily and effectively removed by low-pass filtering. However, the remaining noise sources are more difficult to remove due to their spectral proximity and potential for synchronization with BCI-task activity. If not correctly accounted for, these noise sources can be falsely interpreted as functional brain activity (Tachtsidis and Scholkmann, 2016) or can hinder the recovery of hemodynamic responses from the brain signal of interest (Yücel et al., 2016).

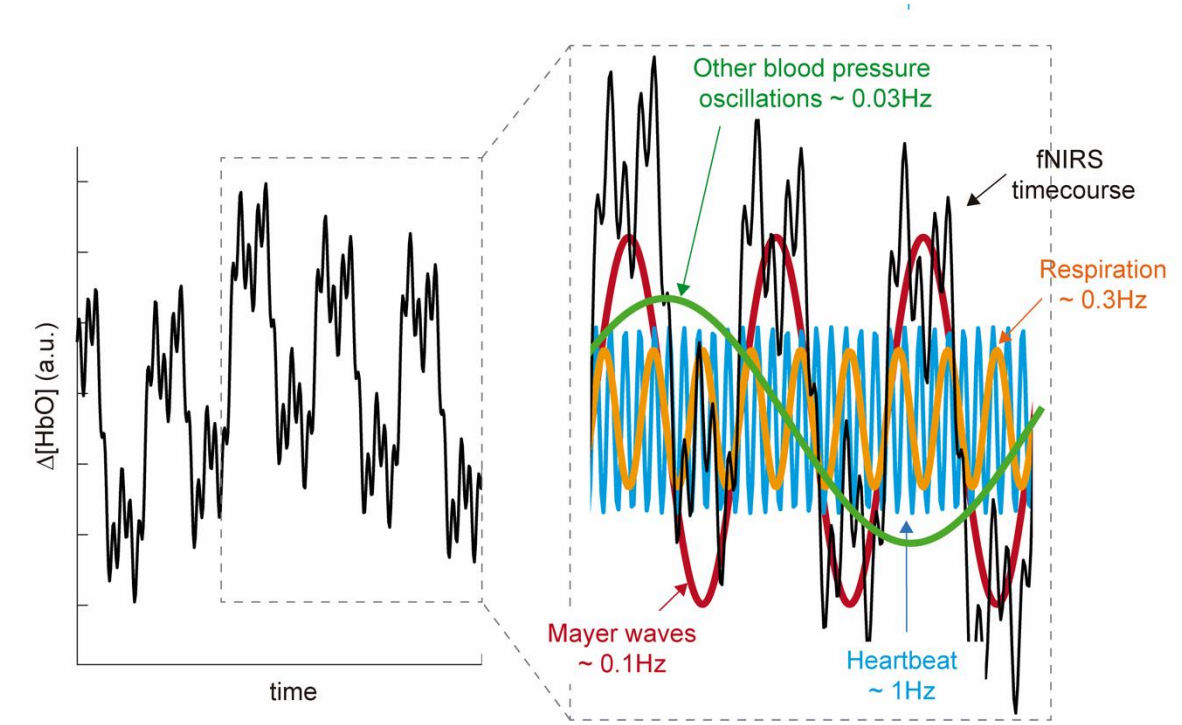

Figure 1.4. Schematic representation of physiological fluctuations present in the fNIRS signal (in black). Physiological processes, which contribute to the physiological noise in fNIRS, operate at different time scales: heartbeat (~1 Hz) in blue, respiration (~0.3 Hz) in orange, Mayer waves (~0.1 Hz) in red, and very low frequency oscillations (usually under 0.04 Hz and in this example depicted at ~0.003 Hz), in green.

A number of methods have been proposed for separating physiological noise from cerebral activation other than digital filtering. Some methods assume that systemic physiology is globally (spatially) uniform and thus aim to remove global covariance from the signal with multivariate techniques such as principal component analysis (Zhang et al., 2005), independent component analysis (Satoru et al., 2007) or global averaging (Batula et al., 2017). Others use auxiliary physiological measurements such as blood-pressure monitors, pulse oximeters, electrocardiograms, chest-band respirometers, spirometers or capnographs (Diamond et al., 2006; Kirilina et al., 2013; Scholkmann et al., 2013) to filter the fNIRS time course. State-space models based on Kalman filters have also been used (Kolehmainen et al., 2003; Prince et al., 2003; Diamond et al., 2006).

Another approach that is particularly powerful for real-time BCI applications relies on the idea that systemic physiological noise present in extracerebral regions can be locally measured using channels with short source-detector separations (<1 cm usually, here on

referred to as short-distance channels or SDCs). Since this approach assumes that the same systemic physiological noise present in the longer distance channels dominates the signal acquired with SDCs (Saager and Berger, 2005; Saager et al., 2011), they can be used to minimize/reduce unwanted physiological noise from the longer distance channels (usually >2.5 cm). SDCs constitute a versatile approach to account for the influence of physiological noise. Among others, they have been used as regressors using a general linear model (Saager et al., 2011; Goodwin et al., 2014; Sato et al., 2016) and in combination with state-space modeling (Gagnon et al., 2011; Gagnon et al., 2012b; Gagnon et al., 2014).

Although systemic interference is thought to be a global process, previous work reported a non-homogeneous distribution of physiological noise components present in fNIRS channels (Kirilina et al., 2012; Yücel et al., 2016). Further, it has been suggested that the contribution of certain components, such as Mayer's waves, may be different at measurements collected at different sites because of heterogeneity in blood vessel sizes, location, or geometry (Zhang et al., 2009; Gagnon et al., 2011). Therefore, understanding whether fNIRS channels capture physiological noise differently depending on their location is crucial to design physiological noise correction strategies.

3.3 Translating information: low information transfer rate

Information transfer rate (ITR) shows the amount of information transmitted per unit of time. ITR is measured in bits per second (or minute) and is a standard measure of BCIs systems that takes into account the number of possible selections, accuracy and the trial duration (McFarland et al., 2003; Allison et al., 2012):

$$ITR = \left(log_2 N + P * log_2 P + (1 - P) * log_2 \left(\frac{1 - P}{N - 1} \right) \right) * \frac{60}{\tau} \qquad (1.1)$$

where N is the number of classes, P is the classification accuracy and τ is the duration of the trial period, in seconds.

The performance of fMRI-BCIs using motor/mental imagery tasks ranges between 0.463 and 2.30 bits/min (Lee et al., 2009a; Sorger et al., 2009; Bardin et al., 2011; Sorger et al., 2012) in healthy participants, while reaching 0.07 bits/min in the patient with traumatic brain

injury (Patient 23, reported in Monti et al. (2010)). fNIRS-BCI applications that use motor/mental imagery tasks range between 0.02 and 1.5 bits/min in healthy participants (Sitaram et al., 2007; Batula et al., 2014; Naseer et al., 2014; Hong et al., 2015; Weyand and Chau, 2015; Naseer and Hong, 2015b; Nagels-Coune et al., 2017; Sereshkeh et al., 2018; Nagels-Coune et al., 2020) while reaching 0.47 bits/min in a case studies with an ALS patient (Gallegos-Ayala et al., 2014) and 0.18 bits/min in a patient with Guillain–Barré syndrome (Abdalmalak et al., 2017). Given the immobility of fMRI hardware, the studies mentioned above show great potential of mobile setups employing fNIRS, thereby enabling ecological BCI applications. To put this into perspective, normal speech rate ranges between 110 and 175 words per minute (Tikofsky, 2000) or 550 to 875 bits/min[2]. Keyboard typing rates range between 20.9 and 89.5 words per minute (Dhakal et al., 2018) or 104.5 to 447.8 bits/min[1]. Clearly, current hemodynamic-BCI systems convey considerably less information in healthy and clinical populations. However, it is important to note that even low ITR values have the potential to improve significantly the quality of life of someone who relies on these systems for communicating with the outer world.

A number of interconnected factors influence information rates for hemodynamic BCI systems. Shorter trials (τ) can increase performance of the BCI by allowing a greater number of selections per unit time. However, performance may decrease due to less information, thereby decreasing the information transfer of the system. The number of selections per unit time is dependent on the temporal resolution of the brain imaging method used. Unlike electrophysiological recordings, the lower temporal resolution of fNIRS constitutes a major limiting factor when used for BCI applications. The hemodynamic response to neuronal activation shows a small initial dip, followed by a tall peak around 5-10s after neuronal activation, subsequently followed by a variable post-stimulus undershoot. The total duration of a hemodynamic response is between 20 and 30s. For this reason, the biggest body of hemodynamic BCI applications has used a trial duration of 10s (Herff et al., 2013; Naseer and Hong, 2013; 2015b; Hong and Santosa, 2016; Nagels-Coune et al., 2017; Shin et al., 2017). Only a few studies have used trial durations under 10s. For example, Lee et al. (2009b) used a task duration of 5s and Shin and Jeong (2014) and Sorger et al. (2009) used

[2] Considering that the average English word is 5 characters long (Norvig, 2012) and that Shannon determined that the information content of typical written English was around 1.0 bit per letter (Shannon, 1951).

variable task durations of 6/8/10/15 s and 5/10/15 s, respectively. In addition, effort has been made reduce trial length and cope with the sluggishness of the hemodynamic response by focusing on the detection of the initial-dip (Zafar and Hong, 2016; Zafar et al., 2018).

The performance of a BCI (P) also depends on how well a classifier can discriminate the user's intentions. This in turn depends on the quantity and quality of data used for model training and the type of classification algorithm used to translate user's intention to output commands. The hemodynamic BCI community has adopted a number of multivariate classification techniques, including Linear Discriminant Analysis, Support Vector Machines and Artificial Neural Networks. All of these algorithms exploit the spatial features of fNIRS signals evoked by performing different mental-imagery tasks (Naseer and Hong, 2015a; Hong et al., 2018). In addition to training data, which may require several acquisition sessions to collect, multivariate approaches require multiple channels, which may increase optode setup time. Alternatively, BCI commands can be generated (encoded) and translated (decoded) by exploiting the temporal (onset, offset and/or duration) as well as spatial aspects of a set of mental tasks (Sorger et al., 2009; Bardin et al., 2011; Sorger et al., 2012; Nagels-Coune et al., 2017; Nagels-Coune et al., 2020). For example, up to four commands can be generated by assigning a unique encoding time for each command, e.g., commands would be generated in 0-10, 10-20, 20-30 and 30-40s time windows within a particular information-encoding trial. This temporal information approach is serial in nature, so it will have longer trial durations than multivariate approaches. Advantageously though, the temporal information approach can be implemented in a single measurement channel if only temporal encoding is pursued. It can also be combined with spatial encoding using two channels, each coding for a distinct mental imagery task, thus minimizing setup time and while increasing user comfort.

A greater number of possible selections or targets (N) could increase performance of a BCI system, since more targets convey more information. The majority of hemodynamic studies using motor/mental imagery tasks have focused on binary classification (Sitaram et al., 2007; Monti et al., 2010; Naseer and Hong, 2013; Stangl et al., 2013; Gallegos-Ayala et al., 2014; Naseer et al., 2016; Abdalmalak et al., 2017; Nagels-Coune et al., 2017; Abdalmalak et al., 2020; Nagels-Coune et al., 2020) and to a lower extent in multi-class problems. Studies on multi-class BCI applications have used three (Power et al., 2012; Hong et al.,

2015; Weyand and Chau, 2015; Sereshkeh et al., 2018; Shin et al., 2018), four (Sorger et al., 2009; Bardin et al., 2011; Batula et al., 2014; Weyand and Chau, 2015; Naseer and Hong, 2015b), five (Weyand and Chau, 2015), twenty-seven (Sorger et al., 2012) or thirty (Borgheai et al., 2019) targets. The primary reason why multi-class fNIRS-BCIs have not been elaborately studied relative to binary BCIs is that more targets will make trials longer when using (spatio)temporal encoding paradigms and may require longer training sessions or complex channel configurations for multivariate classification procedures. However, efficient stimulation paradigms design (as in Sorger et al. (2012) and Borgheai et al. (2019)) show the utility of using a high number of possible targets.

Improving ITR is important for hemodynamic BCIs, particularly for fNIRS-BCIs. Improvements have the potential to enable convenient BCI-based communication and control functionalities of patients in ecological settings. Thus, working towards lowering trial durations, increasing the number of targets while simultaneously maximizing classification accuracy is crucial to reach this goal.

3.4 Providing feedback to users: unnatural interfaces for communication and control

The interaction between the user and the BCI systems need to be simple and meaningful in clinical settings. In communication BCIs, letters or answer options to be encoded can be presented acoustically or visually. The output is usually a word or answer option recited out loud by the computer program or by the experimenter and no other sophisticated forms of output are necessary. In control BCIs, the interaction between the patient and the BCI system should result in a visible change in their environment. Thus, an ideal interface should be embedded in the environment itself. Interfaces such as robots and wheelchairs are a clear example of that. Importantly, other interfaces, such as the ones based on AR, allow for such scenarios too, since AR technology enables projecting virtual objects, such as control menus, as overlays into the real world.

4 Outline of this thesis

The principal rationale for BCI development has been that such systems could ultimately restore communication and control in the absence of words/gestures to people with severe neuromuscular disabilities (Shih et al., 2012). Although the number of BCI-related publications has increased almost exponentially, there have been fewer applications including end-users affected by disease, despite historically being the primary target population for BCI systems (Kübler, 2020). This dissertation addresses the limitations described above to ultimately reduce the translational challenges that fNIRS-BCIs face.

In **Chapter 2**, we aim to develop an fNIRS-BCI for communication and control purposes that is more integrated in the environment. To do so, 12 healthy participants used AR technology, a single mental task and fNIRS channel to communicate their intentions by navigating through an adaptive, six-choice menu. This work conveys fundamental steps toward developing fNIRS-based AR-BCI systems for bedside applications.

Designing optode layouts is an essential step when preparing an fNIRS-BCI setup as the quality of the measured signal and the sensitivity to cortical regions of interest depend on how sources and detectors are arranged on the scalp. Different amount of MRI-derived individualized data can be used for designing optode layouts and available resources often dictate the approach researchers will use. In **Chapter 3**, we investigate whether guiding layout design using different amounts of individual (f)MRI data affects the fNIRS signal quality and sensitivity to brain activation when healthy participants perform mental-imagery tasks typically used in fNIRS-BCI experiments. Based on insights gained as part of this work, we give preliminary advice to efficiently using resources for developing robust and convenient optode layouts for fNIRS-based communication/control and neurofeedback applications.

fNIRS is susceptible to extra-cerebral physiological noise, potentially compromising its sensitivity to detect task-related brain activation. Several studies have speculated that the presence of some physiological noise components in the fNIRS signal may be related to the position of optodes relative to the location, size and geometry of blood vessels. In **Chapter 4**, we first verify that physiological noise amplitude varies across channels in our optode layout. We then investigate whether fNIRS channels capture physiological noise differently

depending on their proximity to vessels in the scalp and brain and how this dependency affects physiological noise correction approaches. This chapter thus extends our understanding of the relationship between vasculature features, the fNIRS signal quality and methods designed to increase its applicability of fNIRS (and BCIs) for accurately detect brain activity.

5 References

Aasted, C.M., Yücel, M.A., Cooper, R.J., Dubb, J., Tsuzuki, D., Becerra, L., et al. (2015). Anatomical guidance for functional near-infrared spectroscopy: AtlasViewer tutorial. *Neurophotonics* 2(2)**,** 020801-020801. doi: 10.1117/1.NPh.2.2.020801.

Abdalmalak, A., Milej, D., Norton, L., Debicki, D., Gofton, T., Diop, M., et al. (2017). Single-session communication with a locked-in patient by functional near-infrared spectroscopy. *Neurophotonics* 4(4)**,** 1-4. doi: 10.1117/1.NPh.4.4.040501.

Abdalmalak, A., Milej, D., Yip, L.C.M., Khan, A.R., Diop, M., Owen, A.M., et al. (2020). Assessing Time-Resolved fNIRS for Brain-Computer Interface Applications of Mental Communication. *Frontiers in Neuroscience* 14**,** 105.

Afergan, D., Hincks, S.W., Shibata, T., and Jacob, R.J.K. (2015). Phylter: A System for Modulating Notifications in Wearables Using Physiological Sensing. *Foundations of Augmented Cognition: 9th International Conference, AC* doi: 10.1007/978-3-319-20816-9_17.

Allison, B., Dunne, S., Leeb, R., Millán, J.D.R., and Nijholt, A. (2012). *Towards Practical Brain-Computer Interfaces; Bridging the Gap from Research to Real-World Applications.* Springer.

Bandettini, P.A., Wong, E.C., Hinks, R.S., Tikofsky, R.S., and Hyde, J.S. (1992). Time course EPI of human brain function during task activation. *Magn Reson Med* 25(2)**,** 390-397. doi: 10.1002/mrm.1910250220.

Bardin, J.C., Fins, J.J., Katz, D.I., Hersh, J., Heier, L.A., Tabelow, K., et al. (2011). Dissociations between behavioural and functional magnetic resonance imaging-based evaluations of cognitive function after brain injury. *Brain : a journal of neurology* 134(Pt 3)**,** 769-782. doi: 10.1093/brain/awr005.

Batula, A.M., Ayaz, H., and Kim, Y.E. (2014). Evaluating a four-class motor-imagery-based optical brain-computer interface. *Conf Proc IEEE Eng Med Biol Soc* 2014**,** 2000-2003. doi: 10.1109/embc.2014.6944007.

Batula, A.M., Mark, J.A., Kim, Y.E., and Ayaz, H. (2017). Comparison of Brain Activation during Motor Imagery and Motor Movement Using fNIRS. *Computational intelligence and neuroscience* 2017**,** 5491296-5491296. doi: 10.1155/2017/5491296.

Bauer, G., Gerstenbrand, F., and Rumpl, E. (1979). Varieties of the locked-in syndrome. *J Neurol* 221(2)**,** 77-91. doi: 10.1007/bf00313105.

Berger, H. (1929). Über das Elektrenkephalogramm des Menschen. *Archiv für Psychiatrie und Nervenkrankheiten* 87(1)**,** 527-570. doi: 10.1007/BF01797193.

Birbaumer, N., Ghanayim, N., Hinterberger, T., Iversen, I., Kotchoubey, B., Kübler, A., et al. (1999). A spelling device for the paralysed. *Nature* 398(6725)**,** 297-298. doi: 10.1038/18581.

Boas, D.A., Culver, J.P., Stott, J.J., and Dunn, A.K. (2002). Three dimensional Monte Carlo code for photon migration through complex heterogeneous media including the adult human head. *Optics Express* 10(3)**,** 159-170. doi: 10.1364/OE.10.000159.

Boas, D.A., Dale, A.M., and Franceschini, M.A. (2004). Diffuse optical imaging of brain activation: approaches to optimizing image sensitivity, resolution, and accuracy. *NeuroImage* 23**,** S275-S288. doi: https://doi.org/10.1016/j.neuroimage.2004.07.011.

Borgheai, S.B., Abtahi, M., Mankodiya, K., McLinden, J., and Shahriari, Y. (2019). *Towards a Single Trial fNIRS-based Brain-Computer Interface for Communication.*

Brandman, D.M., Cash, S.S., and Hochberg, L.R. (2017). Review: Human Intracortical Recording and Neural Decoding for Brain-Computer Interfaces. *IEEE transactions on neural systems and rehabilitation engineering : a publication of the IEEE Engineering in Medicine and Biology Society* 25(10)**,** 1687-1696. doi: 10.1109/TNSRE.2017.2677443.

Brigadoi, S., Salvagnin, D., Fischetti, M., and Cooper, R.J. (2018). Array Designer: automated optimized array design for functional near-infrared spectroscopy. *Neurophotonics* 5(3)**,** 1-19, 19.

Bruno, M., Bernheim, J.L., Schnakers, C., and Laureys, S. (2008). Locked-in: don't judge a book by its cover. *J Neurol Neurosurg Psychiatry* 79(1)**,** 2. doi: 10.1136/jnnp.2007.125294.

Buzsáki, G., Anastassiou, C.A., and Koch, C. (2012). The origin of extracellular fields and currents — EEG, ECoG, LFP and spikes. *Nature Reviews Neuroscience* 13(6)**,** 407-420. doi: 10.1038/nrn3241.

Carrai, R., Grippo, A., Fossi, S., Campolo, M.C., Lanzo, G., Pinto, F., et al. (2009). Transient post-traumatic locked-in syndrome: A case report and a literature review. *Neurophysiologie clinique = Clinical neurophysiology* 39**,** 95-100. doi: 10.1016/j.neucli.2008.11.003.

Chauveau, N., Franceries, X., Doyon, B., Rigaud, B., Morucci, J.P., and Celsis, P. (2004). Effects of skull thickness, anisotropy, and inhomogeneity on forward EEG/ERP computations using a spherical three-dimensional resistor mesh model. *Human brain mapping* 21(2)**,** 86-97. doi: 10.1002/hbm.10152.

Chin, Z.Y., Ang, K.K., Wang, C., and Guan, C. (2010). Online performance evaluation of motor imagery BCI with augmented-reality virtual hand feedback. *Conf Proc IEEE Eng Med Biol Soc* 2010**,** 3341-3344. doi: 10.1109/iembs.2010.5627911.

Choi, J.-R., Kim, S.-M., Ryu, R.-H., Kim, S.-P., and Sohn, J.-W. (2018). Implantable Neural Probes for Brain-Machine Interfaces - Current Developments and Future Prospects. *Experimental neurobiology* 27(6)**,** 453-471. doi: 10.5607/en.2018.27.6.453.

Congedo, M., Goyat, M., Tarrin, N., Ionescu, G., Varnet, L., Rivet, B., et al. (2011). "Brain Invaders": a prototype of an open-source P300- based video game working with the OpenViBE platform. *Proceedings of the 5th International Brain-Computer Interface***,** 280-283.

Coyle, D., Garcia, J., Satti, A.R., and McGinnity, T.M. (2011). EEG-based continuous control of a game using a 3 channel motor imagery BCI: BCI game. *IEEE Symposium on Computational Intelligence, Cognitive Algorithms, Mind, and Brain (CCMB)* 2011**,** 1-7. doi: 10.1109/CCMB.2011.5952128.

Coyle, S., Ward, T., Markham, C., and McDarby, G. (2004). On the suitability of near-infrared (NIR) systems for next-generation brain–computer interfaces. *Physiological Measurement* 25(4)**,** 815-822. doi: 10.1088/0967-3334/25/4/003.

Culver, J.P., Ntziachristos, V., Holboke, M.J., and Yodh, A.G. (2001). Optimization of optode arrangements for diffuse optical tomography: A singular-value analysis. *Optics Letters* 26(10)**,** 701-703. doi: 10.1364/OL.26.000701.

Debener, S., Emkes, R., De Vos, M., and Bleichner, M. (2015). Unobtrusive ambulatory EEG using a smartphone and flexible printed electrodes around the ear. *Scientific Reports* 5(1)**,** 16743. doi: 10.1038/srep16743.

Dhakal, V., Feit, A., Kristensson, P., and Oulasvirta, A. (2018). Observations on Typing from 136 Million Keystrokes. *Proceedings of the CHI Conference on Human Factors in Computing Systems* 646**,** 1-12. doi: 10.1145/3173574.3174220.

Diamond, S.G., Huppert, T.J., Kolehmainen, V., Franceschini, M.A., Kaipio, J.P., Arridge, S.R., et al. (2006). Dynamic physiological modeling for functional diffuse optical tomography. *NeuroImage* 30(1)**,** 88-101. doi: 10.1016/j.neuroimage.2005.09.016.

Fernández, E., Greger, B., House, P.A., Aranda, I., Botella, C., Albisua, J., et al. (2014). Acute human brain responses to intracortical microelectrode arrays: challenges and future prospects. *Frontiers in neuroengineering* 7**,** 24-24. doi: 10.3389/fneng.2014.00024.

Gagnon, J.-F., Durantin, G., Vachon, F., Causse, M., Tremblay, S., and Dehais, F. (2012a). "Anticipating human error before it happens: Towards a psychophysiological model for online prediction of mental workload," in *Human Factors: A view from an integrative perspective*, ed. K.B. D. de Waard, F. Dehais, C. Weikert, S. Röttger, D. Manzey, S. Biede, F. Reuzeau, P. Terrier.).

Gagnon, L., Cooper, R.J., Yücel, M.A., Perdue, K.L., Greve, D.N., and Boas, D.A. (2012b). Short separation channel location impacts the performance of short channel regression in NIRS. *NeuroImage* 59(3)**,** 2518-2528. doi: 10.1016/j.neuroimage.2011.08.095.

Gagnon, L., Perdue, K., Greve, D.N., Goldenholz, D., Kaskhedikar, G., and Boas, D.A. (2011). Improved recovery of the hemodynamic response in diffuse optical imaging using short optode separations and state-space modeling. *NeuroImage* 56(3)**,** 1362-1371. doi: 10.1016/j.neuroimage.2011.03.001.

Gagnon, L., Yücel, M.A., Boas, D.A., and Cooper, R.J. (2014). Further improvement in reducing superficial contamination in NIRS using double short separation measurements. *NeuroImage* 85 Pt 1(0 1)**,** 127-135. doi: 10.1016/j.neuroimage.2013.01.073.

Galan, F., Nuttin, M., Lew, E., W. Ferrez, P., Vanacker, G., Philips, J., et al. (2008). A Brain-Actuated Wheelchair: Asynchronous and Non-Invasive Brain-Computer Interfaces for Continuous Control of Robots. *Clinical Neurophysiology* 119. doi: 10.1016/j.clinph.2008.06.001.

Gallegos-Ayala, G., Furdea, A., Takano, K., Ruf, C.A., Flor, H., and Birbaumer, N. (2014). Brain communication in a completely locked-in patient using bedside near-infrared spectroscopy. *Neurology* 82(21)**,** 1930-1932. doi: 10.1212/WNL.0000000000000449.

Giacometti, P., Perdue, K.L., and Diamond, S.G. (2014). Algorithm to find high density EEG scalp coordinates and analysis of their correspondence to structural and functional regions of the brain. *Journal of neuroscience methods* 229**,** 84-96. doi: 10.1016/j.jneumeth.2014.04.020.

Goodwin, J.R., Gaudet, C.R., and Berger, A.J. (2014). Short-channel functional near-infrared spectroscopy regressions improve when source-detector separation is reduced. *Neurophotonics* 1(1)**,** 015002-015002. doi: 10.1117/1.NPh.1.1.015002.

Hari, R., Parkkonen, L., and Nangini, C. (2010). The brain in time: insights from neuromagnetic recordings. *Ann N Y Acad Sci* 1191**,** 89-109. doi: 10.1111/j.1749-6632.2010.05438.x.

Herculano-Houzel, S. (2009). The human brain in numbers: a linearly scaled-up primate brain. *Frontiers in human neuroscience* 3**,** 31-31. doi: 10.3389/neuro.09.031.2009.

Herff, C. (2016). *Speech Processes for Brain-Computer Interfaces.* Doktors der Ingenieurwissenschafte, University of Bremen.

Herff, C., Heger, D., Putze, F., Hennrich, J., Fortmann, O., and Schultz, T. (2013). Classification of mental tasks in the prefrontal cortex using fNIRS. *Conference proceedings : IEEE Engineering in Medicine and Biology Society* 2013**,** 2160-2163. doi: 10.1109/EMBC.2013.6609962.

Herff, C., Krusienski, D.J., and Kubben, P. (2020). The Potential of Stereotactic-EEG for Brain-Computer Interfaces: Current Progress and Future Directions. *Frontiers in Neuroscience* 14(123). doi: 10.3389/fnins.2020.00123.

Hong, G., and Lieber, C.M. (2019). Novel electrode technologies for neural recordings. *Nature reviews. Neuroscience* 20(6)**,** 330-345. doi: 10.1038/s41583-019-0140-6.

Hong, K.-S., Khan, M.J., and Hong, M.J. (2018). Feature Extraction and Classification Methods for Hybrid fNIRS-EEG Brain-Computer Interfaces. *Frontiers in Human Neuroscience* 12**,** 246.

Hong, K.-S., and Santosa, H. (2016). Decoding four different sound-categories in the auditory cortex using functional near-infrared spectroscopy. *Hearing Research* 333. doi: 10.1016/j.heares.2016.01.009.

Hong, K.S., Naseer, N., and Kim, Y.H. (2015). Classification of prefrontal and motor cortex signals for three-class fNIRS-BCI. *Neurosci Lett* 587**,** 87-92. doi: 10.1016/j.neulet.2014.12.029.

Hu, X.-S., Nascimento, T.D., Bender, M.C., Hall, T., Petty, S., O'Malley, S., et al. (2019). Feasibility of a Real-Time Clinical Augmented Reality and Artificial Intelligence Framework for Pain Detection and Localization From the Brain. *J Med Internet Res* 21(6)**,** e13594. doi: 10.2196/13594.

Irani, F., Platek, S.M., Bunce, S., Ruocco, A.C., and Chute, D. (2007). Functional Near Infrared Spectroscopy (fNIRS): An Emerging Neuroimaging Technology with Important Applications for the Study of Brain Disorders. *The Clinical Neuropsychologist* 21(1)**,** 9-37. doi: 10.1080/13854040600910018.

Iturrate, I., Antelis, J., Kübler, A., and Minguez, J. (2009). A Noninvasive Brain-Actuated Wheelchair Based on a P300 Neurophysiological Protocol and Automated Navigation. *Robotics, IEEE Transactions on* 25**,** 614-627. doi: 10.1109/TRO.2009.2020347.

Jackson, A.F., and Bolger, D.J. (2014). The neurophysiological bases of EEG and EEG measurement: a review for the rest of us. *Psychophysiology* 51(11)**,** 1061-1071. doi: 10.1111/psyp.12283.

Julien, C. (2006). The enigma of Mayer waves: Facts and models. *Cardiovascular Research* 70(1)**,** 12-21. doi: 10.1016/j.cardiores.2005.11.008.

Jurcak, V., Tsuzuki, D., and Dan, I. (2007). 10/20, 10/10, and 10/5 systems revisited: Their validity as relative head-surface-based positioning systems. *NeuroImage* 34(4)**,** 1600-1611. doi: https://doi.org/10.1016/j.neuroimage.2006.09.024.

Khan, M.J., and Hong, K.-S. (2015). Passive BCI based on drowsiness detection: an fNIRS study. *Biomedical optics express* 6(10)**,** 4063-4078. doi: 10.1364/BOE.6.004063.

Kirilina, E., Jelzow, A., Heine, A., Niessing, M., Wabnitz, H., Brühl, R., et al. (2012). The physiological origin of task-evoked systemic artefacts in functional near infrared spectroscopy. *NeuroImage* 61(1)**,** 70-81. doi: 10.1016/j.neuroimage.2012.02.074.

Kirilina, E., Yu, N., Jelzow, A., Wabnitz, H., Jacobs, A., and Tachtsidis, I. (2013). Identifying and quantifying main components of physiological noise in functional near infrared spectroscopy on the prefrontal cortex. *Frontiers in Human Neuroscience* 7(864). doi: 10.3389/fnhum.2013.00864.

Klein, F., and Kranczioch, C. (2019). Signal Processing in fNIRS: A Case for the Removal of Systemic Activity for Single Trial Data. *Frontiers in Human Neuroscience* 13(331). doi: 10.3389/fnhum.2019.00331.

Kobayashi, K., Yoshizawa, M., and Oyama, D. (2017). Development of SQUID Magnetometer With Direct-Feedback Noise Cancellation for Magnetocardiogram Without Magnetically Shielded Room. *IEEE Transactions on Applied Superconductivity* 27(4)**,** 1-4. doi: 10.1109/TASC.2016.2646899.

Koessler, L., Maillard, L., Benhadid, A., Vignal, J.P., Felblinger, J., Vespignani, H., et al. (2009). Automated cortical projection of EEG sensors: Anatomical correlation via the international 10–10 system. *NeuroImage* 46(1)**,** 64-72. doi: https://doi.org/10.1016/j.neuroimage.2009.02.006.

Kolehmainen, V., Prince, S., Arridge, S.R., and Kaipio, J.P. (2003). State-estimation approach to the nonstationary optical tomography problem. *J Opt Soc Am A Opt Image Sci Vis* 20(5)**,** 876-889. doi: 10.1364/josaa.20.000876.

Krusienski, D., McFarland, D., and Principe, J. (2012). BCI Signal Processing: Feature Extraction. *Brain-Computer Interfaces: Principles and Practice*. doi: 10.1093/acprof:oso/9780195388855.003.0007.

Kübler, A. (2020). The history of BCI: From a vision for the future to real support for personhood in people with locked-in syndrome. *Neuroethics* 13(2)**,** 163-180. doi: 10.1007/s12152-019-09409-4.

Kübler, A., and Botrel, L. (2019). "The Making of Brain Painting—From the Idea to Daily Life Use by People in the Locked-in State," in *Brain Art: Brain-Computer Interfaces for Artistic Expression*, ed. A. Nijholt. Springer International Publishing), 409-431.

Kwong, K.K., Belliveau, J.W., Chesler, D.A., Goldberg, I.E., Weisskoff, R.M., Poncelet, B.P., et al. (1992). Dynamic magnetic resonance imaging of human brain activity during primary sensory stimulation. *Proc Natl Acad Sci U S A* 89(12)**,** 5675-5679. doi: 10.1073/pnas.89.12.5675.

Le Groux, S., Manzolli, J., Sanchez, M., Luvizotto, A., Mura, A., Väljamäe, A., et al. (2010). Disembodied and Collaborative Musical Interaction in the Multimodal Brain Orchestra. *Proceedings of the international conference on New Interfaces for Musical Expression*.

Lécuyer, A., Lotte, F., Reilly, R.B., Leeb, R., Hirose, M., and Slater, M. (2008). Brain-Computer Interfaces, Virtual Reality, and Videogames. *Computer* 41.

Lee, J.-H., Marzelli, M., Jolesz, F.A., and Yoo, S.-S. (2009a). Automated classification of fMRI data employing trial-based imagery tasks. *Medical image analysis* 13(3)**,** 392-404. doi: 10.1016/j.media.2009.01.001.

Lee, J.H., Marzelli, M., Jolesz, F.A., and Yoo, S.S. (2009b). Automated classification of fMRI data employing trial-based imagery tasks. *Med Image Anal* 13(3)**,** 392-404. doi: 10.1016/j.media.2009.01.001.

Leeb, R., Friedman, D., Müller-Putz, G.R., Scherer, R., Slater, M., and Pfurtscheller, G. (2007). Self-paced (asynchronous) BCI control of a wheelchair in virtual environments: a case study with a tetraplegic. *Computational intelligence and neuroscience* 2007**,** 79642-79642. doi: 10.1155/2007/79642.

León-Carrión, J., Eeckhout, P.v., and Domínguez-Morales, M.d.R. (2002). Review of subject: The locked-in syndrome: a syndrome looking for a therapy. *Brain Injury* 16(7)**,** 555-569. doi: 10.1080/02699050110119466.

Lloyd-Fox, S., Blasi, A., and Elwell, C.E. (2010). Illuminating the developing brain: The past, present and future of functional near infrared spectroscopy. *Neuroscience & Biobehavioral Reviews* 34(3)**,** 269-284. doi: https://doi.org/10.1016/j.neubiorev.2009.07.008.

Luu, S., and Chau, T. (2009). Decoding subjective preference from single-trial near-infrared spectroscopy signals. *J Neural Eng* 6(1)**,** 016003. doi: 10.1088/1741-2560/6/1/016003.

Maby, E., Perrin, M., Bertrand, O., Sanchez, G., and Mattout, J. (2012). BCI Could Make Old Two-Player Games Even More Fun: A Proof of Concept with "Connect Four". *Advances in Human-Computer Interaction* 2012**,** 124728. doi: 10.1155/2012/124728.

Machado, A., Marcotte, O., Lina, J.M., Kobayashi, E., and Grova, C. (2014). Optimal optode montage on electroencephalography/functional near-infrared spectroscopy caps dedicated to study epileptic discharges. *Journal of Biomedical Optics* 19(2)**,** 1-17, 17.

Maynard, E.M., Nordhausen, C.T., and Normann, R.A. (1997). The Utah Intracortical Electrode Array: A recording structure for potential brain-computer interfaces. *Electroencephalography and Clinical Neurophysiology* 102(3)**,** 228-239. doi: https://doi.org/10.1016/S0013-4694(96)95176-0.

McFarland, D., and Krusienski, D. (2012). BCI Signal Processing: Feature Translation. *Brain-Computer Interfaces: Principles and Practice*. doi: 10.1093/acprof:oso/9780195388855.003.0008.

McFarland, D.J., Sarnacki, W.A., and Wolpaw, J.R. (2003). Brain–computer interface (BCI) operation: optimizing information transfer rates. *Biological Psychology* 63(3)**,** 237-251. doi: https://doi.org/10.1016/S0301-0511(03)00073-5.

Min, B.K., Marzelli, M.J., and Yoo, S.S. (2010). Neuroimaging-based approaches in the brain-computer interface. *Trends Biotechnol* 28(11)**,** 552-560. doi: 10.1016/j.tibtech.2010.08.002.

Monti, M.M., Vanhaudenhuyse, A., Coleman, M.R., Boly, M., Pickard, J.D., Tshibanda, L., et al. (2010). Willful modulation of brain activity in disorders of consciousness. *N Engl J Med* 362(7)**,** 579-589. doi: 10.1056/NEJMoa0905370.

Muller-Putz, G.R., and Pfurtscheller, G. (2008). Control of an Electrical Prosthesis With an SSVEP-Based BCI. *IEEE Transactions on Biomedical Engineering* 55(1)**,** 361-364. doi: 10.1109/TBME.2007.897815.

Murphy, D.P., Bai, O., Gorgey, A.S., Fox, J., Lovegreen, W.T., Burkhardt, B.W., et al. (2017). Electroencephalogram-Based Brain-Computer Interface and Lower-Limb Prosthesis Control: A Case Study. *Frontiers in neurology* 8**,** 696-696. doi: 10.3389/fneur.2017.00696.

Muthukumaraswamy, S.D. (2013). High-frequency brain activity and muscle artifacts in MEG/EEG: a review and recommendations. *Frontiers in human neuroscience* 7**,** 138-138. doi: 10.3389/fnhum.2013.00138.

Myrden, A., and Chau, T. (2015). Effects of user mental state on EEG-BCI performance. *Frontiers in Human Neuroscience* 9(308). doi: 10.3389/fnhum.2015.00308.

Nagels-Coune, L., Benitez-Andonegui, A., Reuter, N., Lührs, M., Goebel, R., De Weerd, P., et al. (2020). Brain-Based Binary Communication Using Spatiotemporal Features of fNIRS Responses. *Frontiers in Human Neuroscience* 14(113). doi: 10.3389/fnhum.2020.00113.

Nagels-Coune, L., Kurban, D., Reuter, N., Benitez, A., Gossé, L., Riecke, L., et al. (2017). Yes or no? binary brain-based communication utilizing motor imagery and fNIRS. *Proceedings of the 7th Graz Brain-Computer Interface*. doi: 10.3217/978-3-85125-533-1-65.

Naito, M., Michioka, Y., Ozawa, K., Ito, Y., Kiguchi, M., and Kanazawa, T. (2007). A Communication Means for Totally Locked-in ALS Patients Based on Changes in Cerebral Blood Volume Measured with Near-Infrared Light. *IEICE Transactions on Information and Systems* E90D. doi: 10.1093/ietisy/e90-d.7.1028.

Naseer, N., and Hong, K.-S. (2013). Classification of functional near-infrared spectroscopy signals corresponding to the right- and left-wrist motor imagery for development of a brain–computer interface. *Neuroscience Letters* 553**,** 84-89. doi: https://doi.org/10.1016/j.neulet.2013.08.021.

Naseer, N., and Hong, K.-S. (2015a). fNIRS-based brain-computer interfaces: a review. *Frontiers in human neuroscience* 9**,** 3-3. doi: 10.3389/fnhum.2015.00003.

Naseer, N., and Hong, K.-S. (2015b). Decoding Answers to Four-Choice Questions Using Functional near Infrared Spectroscopy. *Journal of Near Infrared Spectroscopy* 23(1)**,** 23-31. doi: 10.1255/jnirs.1145.

Naseer, N., Hong, K.-S., Bhutta, R., and Khan, M. (2014). Improving classification accuracy of covert yes/no response decoding using support vector machines: An fNIRS study. *International Conference on Robotics and Emerging Allied Technologies in Engineering (iCREATE)*, 6-9. doi: 10.1109/iCREATE.2014.6828329.

Naseer, N., Qureshi, N.K., Noori, F.M., and Hong, K.-S. (2016). Analysis of Different Classification Techniques for Two-Class Functional Near-Infrared Spectroscopy-Based Brain-Computer Interface. *Computational Intelligence and Neuroscience* 2016, 5480760. doi: 10.1155/2016/5480760.

Nijboer, F., Sellers, E.W., Mellinger, J., Jordan, M.A., Matuz, T., Furdea, A., et al. (2008). A P300-based brain-computer interface for people with amyotrophic lateral sclerosis. *Clinical neurophysiology : official journal of the International Federation of Clinical Neurophysiology* 119(8), 1909-1916. doi: 10.1016/j.clinph.2008.03.034.

Nishiyori, R. (2016). fNIRS: An Emergent Method to Document Functional Cortical Activity during Infant Movements. *Frontiers in psychology* 7, 533-533. doi: 10.3389/fpsyg.2016.00533.

Norvig, P. (2012). *English Letter Frequency Counts: Mayzner Revisited or ETAOIN SRHLDCU* [Online]. Available: http://norvig.com/mayzner.html [Accessed 22-07 2020].

Ogawa, S., Lee, T.M., Kay, A.R., and Tank, D.W. (1990). Brain magnetic resonance imaging with contrast dependent on blood oxygenation. *Proc Natl Acad Sci U S A* 87(24), 9868-9872. doi: 10.1073/pnas.87.24.9868.

Ogawa, S., Tank, D.W., Menon, R., Ellermann, J.M., Kim, S.G., Merkle, H., et al. (1992). Intrinsic signal changes accompanying sensory stimulation: functional brain mapping with magnetic resonance imaging. *Proc Natl Acad Sci U S A* 89(13), 5951-5955. doi: 10.1073/pnas.89.13.5951.

Okamoto, M., Dan, H., Sakamoto, K., Takeo, K., Shimizu, K., Kohno, S., et al. (2004). Three-dimensional probabilistic anatomical cranio-cerebral correlation via the international 10–20 system oriented for transcranial functional brain mapping. *NeuroImage* 21(1), 99-111. doi: https://doi.org/10.1016/j.neuroimage.2003.08.026.

Oostenveld, R., and Praamstra, P. (2001). The five percent electrode system for high-resolution EEG and ERP measurements. *Clinical Neurophysiology* 112(4), 713-719. doi: https://doi.org/10.1016/S1388-2457(00)00527-7.

Pinti, P., Aichelburg, C., Gilbert, S., Hamilton, A., Hirsch, J., Burgess, P., et al. (2018). A Review on the Use of Wearable Functional Near-Infrared Spectroscopy in Naturalistic Environments(). *The Japanese psychological research* 60(4), 347-373. doi: 10.1111/jpr.12206.

Power, S.D., Kushki, A., and Chau, T. (2012). Automatic single-trial discrimination of mental arithmetic, mental singing and the no-control state from prefrontal activity: toward a three-state NIRS-BCI. *BMC research notes* 5, 141-141. doi: 10.1186/1756-0500-5-141.

Prince, S., Kolehmainen, V., Kaipio, J.P., Franceschini, M.A., Boas, D., and Arridge, S.R. (2003). Time-series estimation of biological factors in optical diffusion tomography. *Physics in Medicine and Biology* 48(11), 1491-1504. doi: 10.1088/0031-9155/48/11/301.

Putze, F. (2019). "Methods and Tools for Using BCI with Augmented and Virtual Reality," in *Brain Art*, ed. A. Nijholt.), 433-446.

Putze, F., Vourvopoulos, A., Lécuyer, A., Krusienski, D., Bermúdez i Badia, S., Mullen, T., et al. (2020). Editorial: Brain-Computer Interfaces and Augmented/Virtual Reality. *Frontiers in Human Neuroscience* 14**,** 144.

Rebsamen, B., Guan, C., Zhang, H., Wang, C., Teo, C., Jr, M., et al. (2011). A Brain Controlled Wheelchair to Navigate in Familiar Environments. *Neural Systems and Rehabilitation Engineering, IEEE Transactions on* 18**,** 590-598. doi: 10.1109/TNSRE.2010.2049862.

Rothwell, J. (2009). "Meet the Brain: Neurophysiology," in *International Review of Neurobiology*, eds. L. Rossini, D. Izzo & L. Summerer. Academic Press), 51-65.

Saager, R.B., and Berger, A.J. (2005). Direct characterization and removal of interfering absorption trends in two-layer turbid media. *Journal of the Optical Society of America A* 22(9)**,** 1874-1882. doi: 10.1364/JOSAA.22.001874.

Saager, R.B., Telleri, N.L., and Berger, A.J. (2011). Two-detector Corrected Near Infrared Spectroscopy (C-NIRS) detects hemodynamic activation responses more robustly than single-detector NIRS. *NeuroImage* 55(4)**,** 1679-1685. doi: https://doi.org/10.1016/j.neuroimage.2011.01.043.

Sassaroli, A., Pierro, M., Bergethon, P.R., and Fantini, S. (2012). Low-Frequency Spontaneous Oscillations of Cerebral Hemodynamics Investigated With Near-Infrared Spectroscopy: A Review. *IEEE Journal of Selected Topics in Quantum Electronics* 18(4)**,** 1478-1492. doi: 10.1109/JSTQE.2012.2183581.

Sato, T., Nambu, I., Takeda, K., Aihara, T., Yamashita, O., Isogaya, Y., et al. (2016). Reduction of global interference of scalp-hemodynamics in functional near-infrared spectroscopy using short distance probes. *NeuroImage* 141**,** 120-132. doi: https://doi.org/10.1016/j.neuroimage.2016.06.054.

Satoru, K., Ichiro, M., Akitoshi, S., Ichiro, O., Akihiro, I., Shoichi, T., et al. (2007). Removal of the skin blood flow artifact in functional near-infrared spectroscopic imaging data through independent component analysis. *Journal of Biomedical Optics* 12(6)**,** 1-9. doi: 10.1117/1.2814249.

Scarapicchia, V., Brown, C., Mayo, C., and Gawryluk, J.R. (2017). Functional Magnetic Resonance Imaging and Functional Near-Infrared Spectroscopy: Insights from Combined Recording Studies. *Frontiers in human neuroscience* 11**,** 419-419. doi: 10.3389/fnhum.2017.00419.

Schalk, G., and Leuthardt, E.C. (2011). Brain-computer interfaces using electrocorticographic signals. *IEEE Rev Biomed Eng* 4**,** 140-154. doi: 10.1109/rbme.2011.2172408.

Scharnowski, F., Hutton, C., Josephs, O., Weiskopf, N., and Rees, G. (2012). Improving visual perception through neurofeedback. *The Journal of neuroscience : the official journal of the Society for Neuroscience* 32(49)**,** 17830-17841. doi: 10.1523/JNEUROSCI.6334-11.2012.

Scholkmann, F., Kleiser, S., Metz, A.J., Zimmermann, R., Mata Pavia, J., Wolf, U., et al. (2014). A review on continuous wave functional near-infrared spectroscopy and imaging instrumentation and methodology. *NeuroImage* 85**,** 6-27. doi: https://doi.org/10.1016/j.neuroimage.2013.05.004.

Scholkmann, F., Wolf, M., and Wolf, U. (2013). The Effect of Inner Speech on Arterial CO2 and Cerebral Hemodynamics and Oxygenation: A Functional NIRS Study. *Advances in experimental medicine and biology* 789**,** 81-87.

Sellers, E.W., Vaughan, T.M., and Wolpaw, J.R. (2010). A brain-computer interface for long-term independent home use. *Amyotrophic Lateral Sclerosis* 11(5)**,** 449-455. doi: 10.3109/17482961003777470.

Sereshkeh, A.R., Yousefi, R., Wong, A.T., and Chau, T. (2018). Online classification of imagined speech using functional near-infrared spectroscopy signals. *Journal of Neural Engineering* 16(1)**,** 016005. doi: 10.1088/1741-2552/aae4b9.

Shannon, C.E. (1951). Prediction and entropy of printed English. *Bell System Technical Journal* 30**,** 50-64.

Shereena, E.A., Gupta, R.K., Bennett, C.N., Sagar, K.J.V., and Rajeswaran, J. (2018). EEG Neurofeedback Training in Children With Attention Deficit/Hyperactivity Disorder: A Cognitive and Behavioral Outcome Study. *Clinical EEG and Neuroscience* 50(4)**,** 242-255. doi: 10.1177/1550059418813034.

Shibata, T., Peck, E.M., Afergan, D., Hincks, S.W., Yuksel, B.F., and Jacob, R.J.K. (2014). Building implicit interfaces for wearable computers with physiological inputs: zero shutter camera and phylter. *Proceedings of the adjunct publication of the 27th annual ACM symposium on User interface software and technology***,** 89–90. doi: 10.1145/2658779.2658790.

Shih, J.J., Krusienski, D.J., and Wolpaw, J.R. (2012). Brain-Computer Interfaces in Medicine. *Mayo Clinic Proceedings* 87(3)**,** 268-279. doi: https://doi.org/10.1016/j.mayocp.2011.12.008.

Shin, J., and Jeong, J. (2014). Multiclass classification of hemodynamic responses for performance improvement of functional near-infrared spectroscopy-based brain–computer interface. *Journal of Biomedical Optics* 19(6)**,** 1-9, 9.

Shin, J., Kwon, J., Choi, J.-K., and Im, C.-H. (2018). Ternary Near-Infrared Spectroscopy Brain-Computer Interface with Increased Information Transfer Rate Using Prefrontal Hemodynamic Changes during Mental Arithmetic, Breath-Holding, and Idle State. *IEEE Access* 6**,** 19491-19498. doi: 10.1109/ACCESS.2018.2822238.

Shin, J., Kwon, J., Choi, J., and Im, C.-H. (2017). Performance enhancement of a brain-computer interface using high-density multi-distance NIRS. *Scientific Reports* 7(1)**,** 16545. doi: 10.1038/s41598-017-16639-0.

Si-Mohammed, H., Argelaguet, F., Casiez, G., Roussel, N., and Lécuyer, A. (2017). Brain-Computer Interfaces and Augmented Reality: a State of the Art. *Proceedings of the 7th Graz Brain-Computer Interface*.

Singh, S.P. (2014). Magnetoencephalography: Basic principles. *Annals of Indian Academy of Neurology* 17(Suppl 1)**,** S107-S112. doi: 10.4103/0972-2327.128676.

Sitaram, R., Ros, T., Stoeckel, L., Haller, S., Scharnowski, F., Lewis-Peacock, J., et al. (2017). Closed-loop brain training: the science of neurofeedback. *Nature Reviews Neuroscience* 18(2)**,** 86-100. doi: 10.1038/nrn.2016.164.

Sitaram, R., Zhang, H., Guan, C., Thulasidas, M., Hoshi, Y., Ishikawa, A., et al. (2007). Temporal classification of multichannel near-infrared spectroscopy signals of motor imagery for developing a brain–computer interface. *NeuroImage* 34(4)**,** 1416-1427. doi: https://doi.org/10.1016/j.neuroimage.2006.11.005.

Sorger, B., Dahmen, B., Reithler, J., Gosseries, O., Maudoux, A., Laureys, S., et al. (2009). Another kind of 'BOLD Response': answering multiple-choice questions via online decoded single-trial brain signals. *Progress in brain research* 177**,** 275-292. doi: 10.1016/S0079-6123(09)17719-1.

Sorger, B., Reithler, J., Dahmen, B., and Goebel, R. (2012). A Real-Time fMRI-Based Spelling Device Immediately Enabling Robust Motor-Independent Communication. *Current Biology* 22(14)**,** 1333-1338. doi: https://doi.org/10.1016/j.cub.2012.05.022.

Stangl, M., Bauernfeind, G., Kurzmann, J., Scherer, R., and Neuper, C. (2013). A hemodynamic brain-computer interface based on real-time classification of near infrared spectroscopy signals during motor imagery and mental arithmetic. *Journal of Near Infrared Spectroscopy* 21**,** 157-171. doi: 10.1255/jnirs.1048.

Stefanovska, A. (2007). Coupled Oscillatros: Complex But Not Complicated Cardiovascular and Brain Interactions. *Engineering in Medicine and Biology Magazine, IEEE* 26**,** 25-29. doi: 10.1109/EMB.2007.907088.

Strangman, G.E., Li, Z., and Zhang, Q. (2013). Depth Sensitivity and Source-Detector Separations for Near Infrared Spectroscopy Based on the Colin27 Brain Template. *PLOS ONE* 8(8)**,** e66319. doi: 10.1371/journal.pone.0066319.

Subramanian, L., Hindle, J.V., Johnston, S., Roberts, M.V., Husain, M., Goebel, R., et al. (2011). Real-time functional magnetic resonance imaging neurofeedback for treatment of Parkinson's disease. *The Journal of neuroscience : the official journal of the Society for Neuroscience* 31(45)**,** 16309-16317. doi: 10.1523/JNEUROSCI.3498-11.2011.

Szostak, K.M., Grand, L., and Constandinou, T.G. (2017). Neural Interfaces for Intracortical Recording: Requirements, Fabrication Methods, and Characteristics. *Frontiers in neuroscience* 11**,** 665-665. doi: 10.3389/fnins.2017.00665.

Tachtsidis, I., and Scholkmann, F. (2016). False positives and false negatives in functional near-infrared spectroscopy: issues, challenges, and the way forward. *Neurophotonics* 3(3)**,** 031405-031405. doi: 10.1117/1.NPh.3.3.031405.

Tadel, F., Baillet, S., Mosher, J.C., Pantazis, D., and Leahy, R.M. (2011). Brainstorm: a user-friendly application for MEG/EEG analysis. *Computational intelligence and neuroscience* 2011**,** 879716-879716. doi: 10.1155/2011/879716.

Tangermann, M., Krauledat, M., Grzeska, K., Sagebaum, M., Blankertz, B., Vidaurre, C., et al. (2008). Playing Pinball with non-invasive BCI. *Advances in Neural Information Processing Systems* 21**,** 1641-1648.

Tikofsky, R.S. (2000). *Aphasia and language : theory to practice.* The Guilford Press.

Tong, Y., Hocke, L.M., and Frederick, B.B. (2019). Low Frequency Systemic Hemodynamic "Noise" in Resting State BOLD fMRI: Characteristics, Causes, Implications, Mitigation Strategies, and Applications. *Frontiers in Neuroscience* 13**,** 787.

Tsuzuki, D., and Dan, I. (2014). Spatial registration for functional near-infrared spectroscopy: From channel position on the scalp to cortical location in individual and group analyses. *NeuroImage* 85**,** 92-103. doi: https://doi.org/10.1016/j.neuroimage.2013.07.025.

Tsuzuki, D., Jurcak, V., Singh, A.K., Okamoto, M., Watanabe, E., and Dan, I. (2007). Virtual spatial registration of stand-alone fNIRS data to MNI space. *NeuroImage* 34(4)**,** 1506-1518. doi: https://doi.org/10.1016/j.neuroimage.2006.10.043.

Tumanov, K., Goebel, R., Möckel, R., Sorger, B., and Weiss, G. (2015). fNIRS-based BCI for Robot Control. *International Conference on Autonomous Agents and Multiagent Systems (AAMAS)***,** 1953–1954.

Uludağ, K., Uğurbil, K., and Berliner, L. (2015). *fMRI: From Nuclear Spins to Brain Functions.*

Valente, G., Kaas, A.L., Formisano, E., and Goebel, R. (2019). Optimizing fMRI experimental design for MVPA-based BCI control: Combining the strengths of block and event-related designs. *NeuroImage* 186**,** 369-381. doi: https://doi.org/10.1016/j.neuroimage.2018.10.080.

Vidal, J.J. (1973). Toward Direct Brain-Computer Communication. *Annual Review of Biophysics and Bioengineering* 2(1)**,** 157-180. doi: 10.1146/annurev.bb.02.060173.001105.

Vourvopoulos, A., Ferreira, A., and Bermúdez i Badia, S. (2016). NeuRow: An Immersive VR Environment for Motor-Imagery Training with the Use of Brain-Computer Interfaces and Vibrotactile Feedback. *3rd International Conference on Physiological Computing Systems*. doi: 10.5220/0005939400430053.

Weyand, S., and Chau, T. (2015). Correlates of Near-Infrared Spectroscopy Brain–Computer Interface Accuracy in a Multi-Class Personalization Framework. *Frontiers in Human Neuroscience* 9(536). doi: 10.3389/fnhum.2015.00536.

Wijeakumar, S., Spencer, J.P., Bohache, K., Boas, D.A., and Magnotta, V.A. (2015). Validating a new methodology for optical probe design and image registration in fNIRS studies. *NeuroImage* 106**,** 86-100. doi: https://doi.org/10.1016/j.neuroimage.2014.11.022.

Wolpaw, J., and Wolpaw, E.W. (2012). *Brain-Computer Interfaces: Principles and Practice.* Oxford Scholarship Online.

Wolpaw, J.R., Birbaumer, N., McFarland, D.J., Pfurtscheller, G., and Vaughan, T.M. (2002). Brain–computer interfaces for communication and control. *Clinical Neurophysiology* 113(6)**,** 767-791. doi: https://doi.org/10.1016/S1388-2457(02)00057-3.

Yilmaz, G., Ungan, P., Sebik, O., Uginčius, P., and Türker, K.S. (2014). Interference of tonic muscle activity on the EEG: a single motor unit study. *Frontiers in human neuroscience* 8**,** 504-504. doi: 10.3389/fnhum.2014.00504.

Yücel, M.A., Selb, J., Aasted, C.M., Lin, P.-Y., Borsook, D., Becerra, L., et al. (2016). Mayer waves reduce the accuracy of estimated hemodynamic response functions in functional near-infrared spectroscopy. *Biomedical optics express* 7(8)**,** 3078-3088. doi: 10.1364/BOE.7.003078.

Zafar, A., and Hong, K.-S. (2016). Detection and classification of three-class initial dips from prefrontal cortex. *Biomedical optics express* 8(1)**,** 367-383. doi: 10.1364/BOE.8.000367.

Zafar, A., Khan, M.J., Park, J., and Hong, K.-S. (2018). Initial-dip Based Quadcopter Control: Application to fNIRS-BCI. *IFAC-PapersOnLine* 51(15)**,** 945-950. doi: https://doi.org/10.1016/j.ifacol.2018.09.072.

Zhang, Q., Strangman, G.E., and Ganis, G. (2009). Adaptive filtering to reduce global interference in non-invasive NIRS measures of brain activation: how well and when does it work? *NeuroImage* 45(3)**,** 788-794. doi: 10.1016/j.neuroimage.2008.12.048.

Zhang, Y., Brooks, D., Franceschini, M., and Boas, D. (2005). Eigenvector-based spatial filtering for reduction of physiological interference in diffuse optical imaging. *Journal of Biomedical Optics* 10(1)**,** 011014.

Zimeo Morais, G.A., Balardin, J.B., and Sato, J.R. (2018). fNIRS Optodes' Location Decider (fOLD): a toolbox for probe arrangement guided by brain regions-of-interest. *Scientific Reports* 8(1)**,** 3341. doi: 10.1038/s41598-018-21716-z.

In the above reference list, 79.75% of first authors were male (vs. 20.25% that were female), while 86.08% of last authors were male (vs. 13.92 % that were female).

2

An Augmented-Reality fNIRS-Based Brain-Computer Interface: A Proof-of-Concept Study

Abstract

Augmented reality (AR) enhances the user's environment by projecting virtual objects into the real world in real-time. Brain-computer interfaces (BCIs) are systems that enable users to control external devices with their brain signals. BCIs can exploit AR technology to interact with the physical and virtual world and to explore new ways of displaying feedback. This is important for users to perceive and regulate their brain activity or shape their communication intentions while operating in the physical world. In this study, twelve healthy participants were introduced to and asked to choose between two motor-imagery tasks: mental drawing and interacting with a virtual cube. Participants first performed a functional localizer run, which was used to select a single fNIRS channel for decoding their intentions in eight subsequent choice-encoding runs. In each run participants were asked to select one choice of a six-item list. A rotating AR cube was displayed on a computer screen as the main stimulus, where each face of the cube was presented for 6 s and represented one choice of the six-item list. For five consecutive trials, participants were instructed to perform the motor-imagery task when the face of the cube that represented their choice was facing them (therewith temporally encoding the selected choice). In the end of each run, participants were provided with the decoded choice based on a joint analysis of all five trials. If the decoded choice was incorrect, an active error-correction procedure was applied by the participant. The choice list provided in each run was based on the decoded choice of the previous run. The experimental design allowed participants to navigate twice through a virtual menu that consisted of four levels if all choices were correctly decoded. Here we demonstrate for the first time that by using AR feedback and flexible choice encoding in form of search trees, we can increase the degrees of freedom of a BCI system. We also show that participants can successfully navigate through a nested menu and achieve a mean accuracy of 74% using a single motor-imagery task and a single fNIRS channel.

Based on: A. Benitez-Andonegui, R. Burden, R. Benning, R. Möckel, M. Lührs, B. Sorger (2020). An Augmented-Reality fNIRS-Based Brain-Computer Interface: A Proof-of-Concept Study. *Frontiers in Neuroscience*

1 Introduction

A brain-computer interface (BCI) is a system that enables users to send commands to the external world through brain signals in the absence of motor output (Wolpaw et al., 2002). BCI research has mainly focused on developing applications for (1) changing brain activation and associated behavior voluntarily through neurofeedback (Subramanian et al., 2011; Scharnowski et al., 2012; Shereena et al., 2018) and for (2) replacing (lost) motor functions through communication BCIs (Birbaumer et al., 1999; Nijboer et al., 2008; Sellers et al., 2010) and (e.g., wheelchair/robotic body-part) control systems (Galan et al., 2008; Muller-Putz and Pfurtscheller, 2008; Iturrate et al., 2009; Rebsamen et al., 2011; Murphy et al., 2017). Independent of the application, information is fed back to users about the success or failure of the intended act (Leeb et al., 2007). In communication and control BCIs, feedback may allow the BCI user to adapt the communication content (of a next encoding trial) in a sense of "back-and-forth communication", which enables users to communicate with or control a specific component of the external world.

The most common approach to provide feedback to users is through simplified unimodal (visual or auditory) representations of brain activation, such as bars or single tones (Sulzer et al., 2013). Alternative ways have emerged in the past years due to new technological developments in the areas of multimedia and entertainment, such as virtual reality (VR). VR is an immersive system that provides users with a sense of presence through potential interactions with a simulated virtual world rendered in real-time (Lécuyer et al., 2008). It has been suggested that VR environments can improve the BCI experience as it offers a richer and potentially more motivating feedback (Chin et al., 2010; Allison et al., 2012). Recent advances in VR research enabled the development of augmented reality (AR) systems. Unlike VR systems, AR enhances the environment the user is in by projecting virtual objects as overlays into the real world. This projection is called registration and it can be carried out using a camera that detects a number of fiducial markers placed in the real environment (Si-Mohammed et al., 2017). AR can be displayed using systems worn on the head (also known as head mounted displays, HMD) or visualized through a dedicated screen that the participant is not wearing (phone, computer screen, etc.). Depending on the augmentation type, AR systems can be divided into visual see-through (VST) and optical see-through (OST) systems. In VST-AR, real images are recorded in real-time by the camera of a device (tablet, phone, etc.) before being visualized through a screen, augmented with

virtual information. In OST-AR, the virtual content is directly displayed in front of the user's eyes onto a semi-transparent screen.

The number of studies exploring the use of BCIs in AR applications remains relatively small (Si-Mohammed et al., 2017). Up until now, the majority of the AR-BCI literature has focused on electroencephalography (EEG)-based evoked potentials applied to a wide range of fields, namely robotics (Lenhardt and Ritter, 2010), medicine (Blum et al., 2012), home automation (Takano et al., 2011; Park et al., 2019), navigation (Faller et al., 2010), and neurofeedback (Chin et al., 2010; Mercier-Ganady et al., 2014). Importantly, some of these studies have assessed the impact of AR feedback in mental workload and engagement compared to traditional forms of feedback. For example, Chin et al. (2010) compared 3D-AR displays vs. traditional 2D feedback (both displayed on a computer screen) and found that despite the higher mental load experienced by the participants during the 3D-AR feedback, participants reported the 3D-AR feedback being more engaging and motivating.

AR-BCIs based on hemodynamic signals have also been explored, but to a smaller extent (Si-Mohammed et al., 2017). One way of measuring hemodynamic signals is using functional near-infrared spectroscopy (fNIRS), a portable, silent, and affordable counterpart to functional magnetic resonance imaging (fMRI) (Scarapicchia et al., 2017). Both EEG and fNIRS make use of sensors [electrodes and optode pairs (sources and detectors), respectively] placed on the scalp to measure signals which correlate with neural activity (Allison et al., 2012). While EEG measures the postsynaptic potentials of ensembles of neurons, fNIRS is based on the optical measurement of the hemodynamic response of both oxy- and deoxyhemoglobin (Δ[HbO] and Δ[HbR], respectively) to neural activity (Lloyd-Fox et al., 2010). Although EEG offers a higher temporal resolution than fNIRS, the latter represents an interesting option as it provides higher spatial resolution and is less vulnerable to motion artifacts (Lloyd-Fox et al., 2010).

To our knowledge, only three fNIRS-based AR-BCIs have been reported. Hu et al. (2019) used an fNIRS-based AR-BCI in a simulated real-time environment aimed at clinicians to measure and visualize in real-time the ongoing cortical activity to determine when and where the patients were suffering from pain. For that, they placed fNIRS optodes over the patients' bilateral prefrontal cortex and primary somatosensory area and monitored brain activity while volunteers with hypersensitive teeth underwent a thermal stimulation session.

The cortical activity was superimposed onto a participant's head in the real world in real-time through an OST-HMD (HoloLens) device the clinician was wearing. Afergan et al. (2015) developed an fNIRS-based BCI using OST-HMD called Phylter. They developed a control system connected to Google Glass that helped preventing the user from getting flooded by notifications. By monitoring users' mental workload in real-time with an fNIRS device, their system would only show notifications to the user if the mental workload was low enough. In the context of mental workload monitoring, McKendrick et al. (2016) assessed the cognitive differences between a wearable AR display (Google Glass) and a handheld display (smartphone) using a mobile fNIRS system covering the lateral PFC during an outdoor navigation task. They complimented it with two separate secondary tasks to assess differences in mental workload and situation awareness during navigation. They concluded that navigating with an AR wearable display produced the least workload during one of the working-memory task, and reported a trend for improved situational awareness in their measures of prefrontal hemodynamics. In this proof-of-concept study we tested whether healthy participants can use an AR fNIRS-based BCI paradigm motivated by the successful implementation in fNIRS-based BCIs, the increased engagement associated to the use of AR reported in previous studies (Chin et al., 2010) and its ability to preserve the real world while blending digital components to it.

Generally speaking, the hemodynamic response to a given task execution/stimulus shows a specific and reproducible temporal behavior (Menon and Kim, 1999). Previous fMRI-based BCI work exploited this property and demonstrated that up to four distinctive BCI commands could be encoded/decoded by varying the temporal aspects (onset, offset and/or duration) of a (set of) mental task(s) (Sorger et al., 2009; Bardin et al., 2011; Sorger et al., 2012). Despite its simplicity, so far no fNIRS-based BCI has implemented this temporal information encoding approach. This is probably because the temporal encoding approach is serial in its nature, which can make the encoding process lengthy depending on the experimental design. In addition, it has been used in combination with univariate information decoding approaches, while the hemodynamic BCI community has mostly adopted multivariate classification techniques such as Linear Discriminant Analysis, Support Vector Machines or Artificial Neural Networks that have been used to exploit the spatial features of fNIRS signals evoked by performing different mental-imagery tasks (Naseer and Hong, 2015a; Hong et al., 2018). However, with appropriate experimental

designs, the temporal encoding approach offers a way to increase the degrees of freedom of a BCI using a single mental task. With this in mind, the present study aimed at transferring the fMRI-based temporal encoding approach mentioned above to fNIRS. For that, we used a selection paradigm where participants had to sift through a multi-leveled menu using a motor-imagery task. This menu consisted of four levels, in such a way that the choice options provided in each level (always six) were based on the decoded choice of the previous level. Thus, here we expanded the traditional four-choice temporal information encoding approach to include six options for choice selection in each of the levels comprising the menu, where an AR object guided the temporal encoding approach. We then used a univariate procedure for decoding participants' intention and used the same AR object to back-communicate the decoded answer. Additionally, to account for potential mistakes during the decoding process, we implemented an active error-correction procedure to be applied by the participants. Importantly, this specific combination of temporal encoding and univariate decoding approaches allows participants' intentions to be decoded based on the information recorded from even a single fNIRS channel provided that this channel has enough signal quality. With this in mind, in the present study we used a single channel for decoding participants' choices.

Although the application of BCIs has been limited primarily to a laboratory setting, some of the studies mentioned above have examined the possibility of using BCIs in everyday-life settings in different contexts (Takano et al., 2011; Blum et al., 2012; Afergan et al., 2015; Hu et al., 2019; Park et al., 2019). However, ecologically valid approaches are challenging to develop as, among other reasons, they should be as efficient, accurate and reliable as possible, but also easy to use, intuitive, and simple to (dis)assemble. This is probably the reason why most BCI research has focused predominantly on improving the technology (Liberati et al., 2015). There is a relevant body of work addressing that BCI design and development should become more user-centered in order to achieve successful everyday-life applications (Kübler et al., 2014; Liberati et al., 2015; Nijboer, 2015). Effort has been made to incorporate this aspect into various applications (Weyand and Chau, 2015; Weyand et al., 2015; Nagels-Coune et al., 2017; Weyand and Chau, 2017; Si-Mohammed et al., 2018). While still in a laboratory setting, in the present study we worked toward a user-centered communication system by letting participants choose their preferred motor-imagery task and by selecting participant-specific (single) most-informative fNIRS channel

for decoding their choices. Using a single channel constitutes the simplest setup to (dis)assemble. In addition, it should make the setup comfortable and thus prevent participants from withdrawing from fNIRS recordings due to setup-related discomfort (Suzuki et al., 2010; Cui et al., 2011; Rezazadeh Sereshkeh et al., 2018).

It is important to note that fNIRS measurements are contaminated by systemic interference of especially (but not limited to) extracerebral regions, which is mainly caused by cardiac pulsations, respiration, and blood-pressure variations (Boas et al., 2004; Tachtsidis and Scholkmann, 2016). Several approaches have been reported in the literature to reduce these noises: conventional band-pass filtering (Hocke et al., 2018; Pinti et al., 2019); modeling physiological noises as a sum of sinusoidal functions with known frequencies where their amplitudes are estimated by using the extended Kalman filter and regressed out using a general linear model (Prince et al., 2003); global signal-covariance removal by either principal/independent component analysis (Zhang et al., 2005; Aarabi and Huppert, 2016) or global average procedures (Batula et al., 2017); adaptive filters that use recursive least-squares estimation methods (Nguyen et al., 2018) or short-distance channel (SDC) regression (Saager and Berger, 2005; Saager et al., 2011; Goodwin et al., 2014). In fNIRS measurements these SDCs are channels that have reduced inter-optode separations such that the interrogated volume is confined primarily to extracerebral regions (Goodwin et al., 2014). The main assumption underlying their usability is that the same systemic physiological noise present in the normal-distance channels (NDCs) dominates the signal acquired with SDCs (Gagnon et al., 2012). Intuitively, SDCs can then be used to minimize/reduce unwanted physiological noise from the normal-distance channels. So far, not many fNIRS-based BCIs have employed them (but see (Shin et al., 2017)). This is partially because fNIRS equipment that allows such measurements has only recently become widely available. Here, SDC correction was used for the selection of the most-informative fNIRS channel as well as during the decoding process.

In this preliminary study participants achieved mean accuracy level of 74% (with a chance-level of 37.5% for six answer options), which shows that the temporal features of the fNIRS signal can be exploited in a temporal encoding paradigm to increase the degrees of freedom of a BCI using a single mental task. These accuracies also indicate that the proposed fNIRS-based AR-BCI setup can be successfully controlled, on average, by participants.

Importantly, this work conveys the fundamental steps toward developing the first fNIRS-based AR-BCI system to be used as a communication device for bedside applications in a clinical setting.

2 Materials and Methods

2.1 Participants

Twelve healthy volunteers [five males; mean age (SD) = 27.1 years (3.2 years)] with varying previous BCI/fNIRS/task experience participated in this study (see Table 2.1). Participants did not have a history of neurological disease and had a normal or corrected-to-normal vision. The experiment conformed to the Declaration of Helsinki and was approved by the ethics committee of the Faculty of Psychology and Neuroscience, Maastricht University. Informed consent was obtained from each participant before starting the measurements. Participants received financial compensation after the session.

Table 2.1. Participant characteristics

	Age range	fNIRS Cap Size (cm)	Previous experience			
			BCI	fNIRS	Task	
					Mental drawing	Interacting with cube
P01	20-25	56	First time	< 5 times	< 5 times	First time
P02	20-25	56	< 5 times	5 to 10 times	5 to 10 times	First time
P03	20-25	56	< 5 times	< 5 times	< 5 times	First time
P04	25-30	56	> 10 times	> 10 times	> 10 times	First time
P05	35-40	58	First time	First time	First time	First time
P06	25-30	56	< 5 times	< 5 times	5 to 10 times	First time
P07	25-30	58	< 5 times	5 to 10 times	< 5 times	First time
P08	25-30	58	First time	First time	First time	First time
P09	25-30	56	< 5 times	< 5 times	< 5 times	First time
P10	25-30	56	5 to 10 times	5 to 10 times	5 to 10 times	First time
P11	25-30	56	> 10 times	> 10 times	> 10 times	First time
P12	25-30	58	First time	< 5 times	< 5 times	First time

2.2 Experimental Design and Stimulus Display

2.2.1 General Structure

The experiment consisted of a training session and an immediately following experimental fNIRS session. The training session was self-paced and ranged between 15 and 35 min across participants: we only switched to the experimental fNIRS session when participants felt comfortable with the stimuli and the motor-task performance.

In an attempt to follow a user-centered approach, participants were introduced to two motor imagery tasks during the training session and asked to choose between them: (option 1) mental drawing [of small geometrical figures (a square, circle, etc.) or contour drawings (a star, flower, boat, etc.) and (option 2) imagine to interact with the virtually presented AR cube (by, e.g., to imagine to hit/squeeze it)]. Participants were asked to choose the mental task (mental drawing or imagining interacting with the cube), the specific strategy (drawing a square or imagining hitting the cube) they expected would work best and would interfere the least with the stimuli and to perform the motor-imagery task with their right hands. They were instructed to keep their eyes open throughout the experiment and to look at the computer screen while staying as still as possible during the runs.

The experimental fNIRS session lasted around 1.5 h. Participants first performed a functional localizer run, during which the participants were presented with a gray AR cube that contained specific symbols (5/6 = crosses, 1/6 = checkmark). For twelve consecutive times, they performed the selected motor imagery task when the checkmark was facing them (for 6 s) and had to rest for the remaining faces (for 30 s, see Figure 2.1). There was an initial baseline period of 36 s indicated by a blue rotating cube, in which participants rested. We chose a baseline period of 36 s to guarantee a stable baseline measure for real-time conversion of raw data into hemoglobin (Hb) concentration changes. After the twelve trials, the cube stopped rotating and became blue again, indicating the end of the run. This run was used to select a user-specific most-informative (“best”) fNIRS channel to decode participants’ choices in the eight subsequent choice-encoding runs (here on referred to as choice runs).

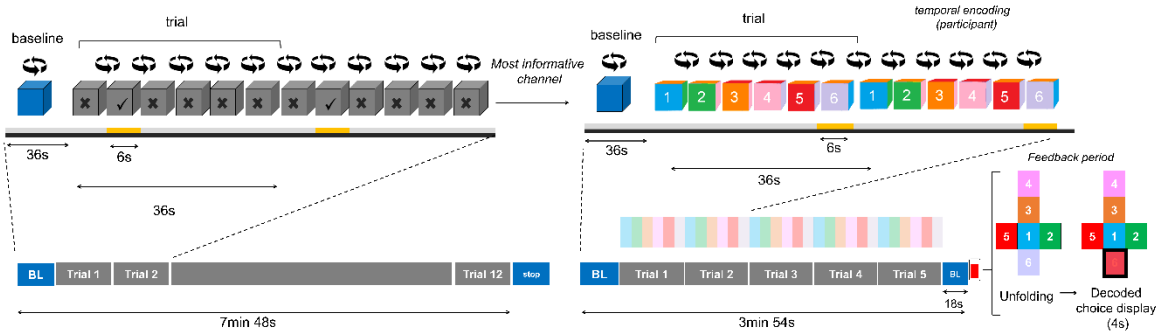

Figure 2.1. Experimental design. During the training session participants chose between two motor imagery tasks. Then, during the functional localizer run, participants performed the chosen task for twelve consecutive trials when the checkmark was facing them (indicated in yellow, below the face showing a checkmark) and had to rest for the remaining faces. There was an initial baseline (BL) period indicated by a blue rotating cube, in which participants rested. After the twelve trials the cube stopped rotating and became blue again, signaling the end of the run (indicated with the word stop in the figure). The user-specific most-informative channel from this run was used to decode participants' choices during the choice runs. Participants were asked to perform the mental task when the number corresponding to their choice was facing them (temporal information encoding), for five consecutive trials (in this example it corresponded to choice number 6, again underlined in yellow). After each run the feedback period started (indicated by the red square), during which the cube unfolded and the decoded choice was highlighted in red (for visualization purposes, we added a black thick square in this schematic representation). After the choice runs, participants were asked to fill in several questionnaires.

Each choice run aimed at selecting one option from a six-item list (menu). These runs differed from the functional localizer run in (1) the number of active motor imagery trials [five trials (choice runs) vs. twelve (functional localizer run)] and (2) the fact that the AR cube was color-coded and numbered (choice runs) vs. the AR cube was gray and contained geometrical shapes (functional localizer run). Importantly, the task duration remained at 6 s during the choice runs. During each choice run, participants selected one choice from a six-item list provided before the start of the run and performed the motor imagery task only when the number corresponding to their choice was facing them (temporal information encoding), for five consecutive times. There was an additional baseline period of 18 s after the last trial to ensure that the hemodynamic response goes back to baseline. After the run, the cube unfolded and the decoded choice (based on real-time analysis of the fNIRS data) was highlighted in red (see Figure 2.1).

2.2.2 AR Stimulus Display

In this experiment, we used a variation of a VST-AR system, where a rotating AR cube

displayed on a computer screen embodied the menu and each face of the cube represented one choice of the list (see Figure 2.2A for an example of a user's view). In the presented AR system, a white A4 cardboard was used to represent the real-world stimulus that also served as a spatial point of reference necessary for the visualization of the AR cube. The A4 cardboard was placed on the desk, between the computer screen and the participants. The left half of the board was wrapped in transparent wrapping paper and served as a whiteboard, where choice options were handwritten (and modified after each run). The right half of the board contained a marker (a 2D-image, see hand-icon in top-left image of Figure 2.2A) that, when detected by the HD webcam (Logitech C270 HD, which was fixated on the participant's forehead using an elastic band and recording the cardboard), triggered the visualization of the AR cube on a standard computer screen. The AR cube was placed relative to the marker as seen in the camera image (see top-left image in Figure 2.2A) with the help of Vuforia (v7.1.34), an AR software development kit (SDK) that was running in Unity3D. This SDK makes it possible to detect the marker and to place the virtual cube on it, creating the effect of augmented reality. The marker was motor imagery task-specific and reminded participants of the task to be performed (mental drawing or virtual interaction with the cube). After each run, an unfolded AR cube was displayed on the computer screen highlighting the decoded choice of the participant (see top-right image, Figure 2.2A).

Figure 2.2. AR display and example of a full cycle of the nested menu (next page). (A) A task-specific marker in the right-side of the A4 cardboard served as the spatial point of reference necessary for the visualization of the AR cube. This cube was used to navigate through a four-level nested menu with six options in each level. The choice options encoded by the participant are written in blue, while the decoded answers are written in black and highlighted in red with a black thick square in the schematic representation of the unfolded cube. The choice options provided in each level were based on the decoded choice of the previous run. (B) If the decoded choice was incorrect, they were asked to choose the "Error" option in the next run. If "Error" was decoded, they were provided with the same option list they saw before the error occurred. In this example, the participant chose to perform a mental drawing task, as indicated by the markers under "Navigating through the nested menu". In the first level, we provided participants with keywords that responded to the question "What would you like to do?" Since the decoded choice [Listen to] Music (highlighted in red only in the actual run; highlighted in red and with a black thick square in the schematic view) was correct, the next run summarized music-genre options (Level 2). Here, the participant chose "Rock" [music] but the decoded choice was "Jazz". Thus, the participant was provided with Jazz-band options in the next run (Level 3), where (s)he encoded the "Error" option. Since the "Error" option was correctly decoded (see displayed choice after Run 3), the participant was provided again with Level 2 choice options. The procedure went on until the participant reached the last level of the nested menu. At the end of the run, we played the decoded song ("Under pressure" in this example) to the participant and (s)he was directed back to the first level of the menu.

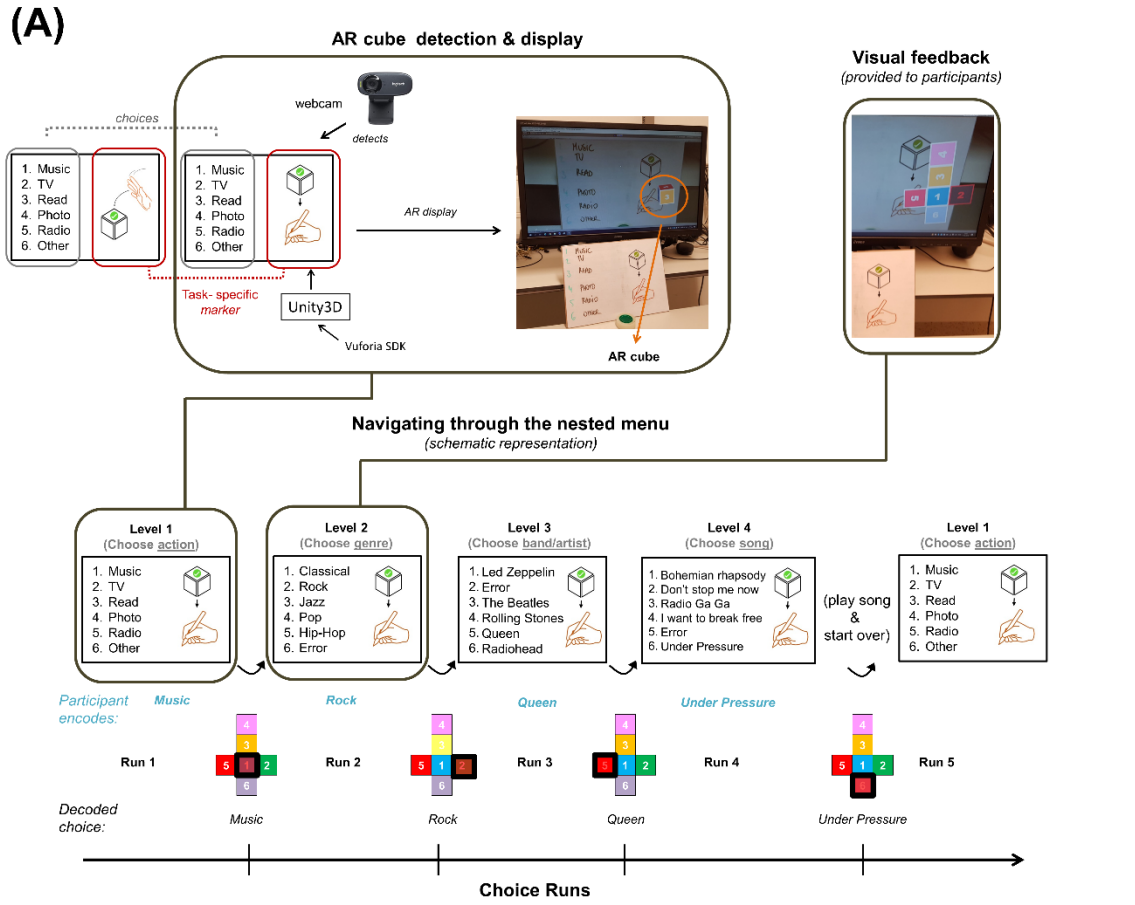
(A)
AR cube detection & display
webcam
detects
choices
1. Music
2. TV
3. Read
4. Photo
5. Radio
6. Other
AR display
Task- specific marker
Unity3D
Vuforia SDK
AR cube
Visual feedback
(provided to participants)
Navigating through the nested menu
(schematic representation)
Level 1
(Choose action)
Level 2
(Choose genre)
1. Classical
2. Rock
3. Jazz
4. Pop
5. Hip-Hop
6. Error
Level 3
(Choose band/artist)
1. Led Zeppelin
2. Error
3. The Beatles
4. Rolling Stones
5. Queen
6. Radiohead
Level 4
(Choose song)
1. Bohemian rhapsody
2. Don't stop me now
3. Radio Ga Ga
4. I want to break free
5. Error
6. Under Pressure
(play song & start over)
Participant encodes:
Music
Rock
Queen
Under Pressure
Run 1
Run 2
Run 3
Run 4
Run 5
Decoded choice:
Choice Runs

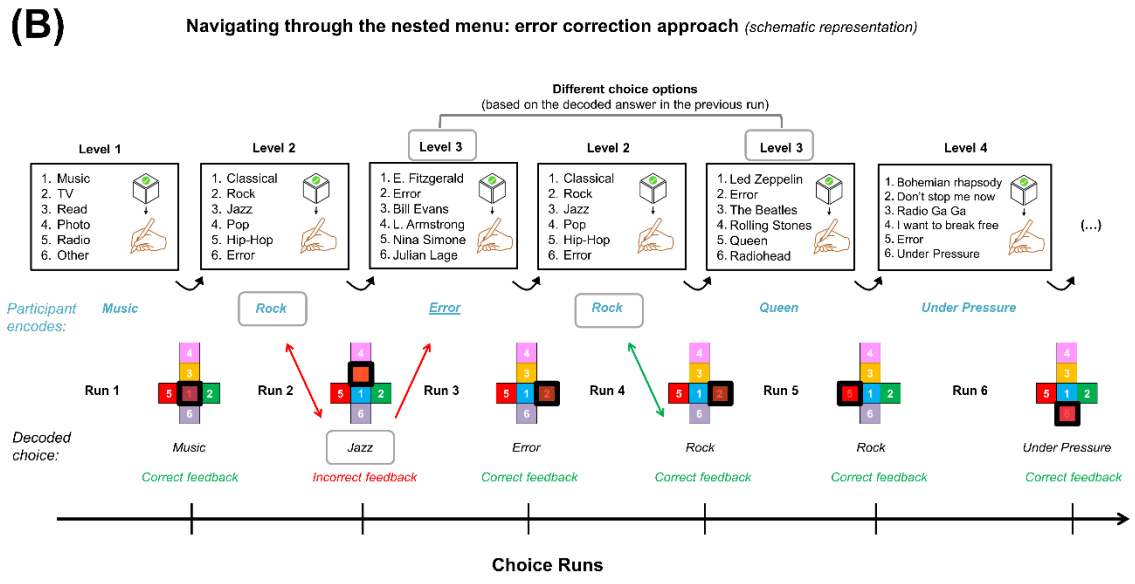
(B)
Navigating through the nested menu: error correction approach (schematic representation)
Different choice options
(based on the decoded answer in the previous run)
Level 1
Level 2
Level 3
Level 4
1. Music
2. TV
3. Read
4. Photo
5. Radio
6. Other
1. Classical
2. Rock
3. Jazz
4. Pop
5. Hip-Hop
6. Error
1. E. Fitzgerald
2. Error
3. Bill Evans
4. L. Armstrong
5. Nina Simone
6. Julian Lage
1. Led Zeppelin
2. Error
3. The Beatles
4. Rolling Stones
5. Queen
6. Radiohead
1. Bohemian rhapsody
2. Don't stop me now
3. Radio Ga Ga
4. I want to break free
5. Error
6. Under Pressure
(...)
Participant encodes:
Music
Rock
Error
Rock
Queen
Under Pressure
Run 1
Run 2
Run 3
Run 4
Run 5
Run 6
Decoded choice:
Music
Jazz
Error
Rock
Rock
Under Pressure
Correct feedback
Incorrect feedback
Correct feedback
Correct feedback
Correct feedback
Correct feedback
Choice Runs

2.2.3 Nested Menu and Error-Correction Approach

The menu presented during choice runs consisted of four levels that were interconnected in such a way that the choice options provided in each level were based on the decoded choice of the previous run. The provided answer options became more specific throughout the levels. An example transition of provided options from level one to level four would be: listen to music > choose a genre > choose a band/artist > choose a song. Displaying the selected choice of the fourth level (a song, a picture, a movie, etc., depending on the choice in the first level) indicated the end of the navigation round, and participants were directed back to the first level of the menu (see Figure 2.2A). This structure allowed participants to go through a four-level nested menu twice if all choices were correctly decoded.

Importantly, it could be that the decoded choice of any given level of the nested menu did not match the encoded option by the participant. To account for such decoding mistakes and in a first attempt to correct for it, participants were instructed to choose the "Error" option in the next run. This "Error" option was part of the choice list in levels > 1 and the position this option appeared on the menu list was balanced across the different levels. If "Error" was decoded, they were provided with the same option lists they saw before the decoding mistake was made (see first Level 2 trial in Figure 2.2B).

2.3 fNIRS Data Acquisition

fNIRS data was recorded using a continuous-wave system (NIRScout-816, NIRx, Medizintechnik GmbH, Berlin, Germany). The optode setup consisted of nine sources and eight detectors which were placed on the left hemisphere that cover areas commonly associated with motor imagery, i.e., premotor cortex and part of the supplementary motor area, primary motor cortex, somatosensory motor cortex and part of the parietal cortex following the extended 10/10 EEG system (see Figure 2.3; (Sorger et al., 2012; Abdalmalak et al., 2016; Batula et al., 2017; Erdogan et al., 2019; Klein and Kranczioch, 2019). An in-house SDC was created by placing source S9 as close as the optodes would allow (∼13 mm away) to detector D5 on the same sagittal plane that connects D5 and source S6 (see Figure 2.3). The signal measured by the SDC should be influenced by the mid-sagittal sinus and other large vascular structures commonly found in this region (Duvernoy et al., 1981), which have been shown to be affected by low frequency oscillations and cardiac signals (Tong and Frederick, 2012). We used this information as a proxy to account for physiological noise in

the region covered by the optode setup.

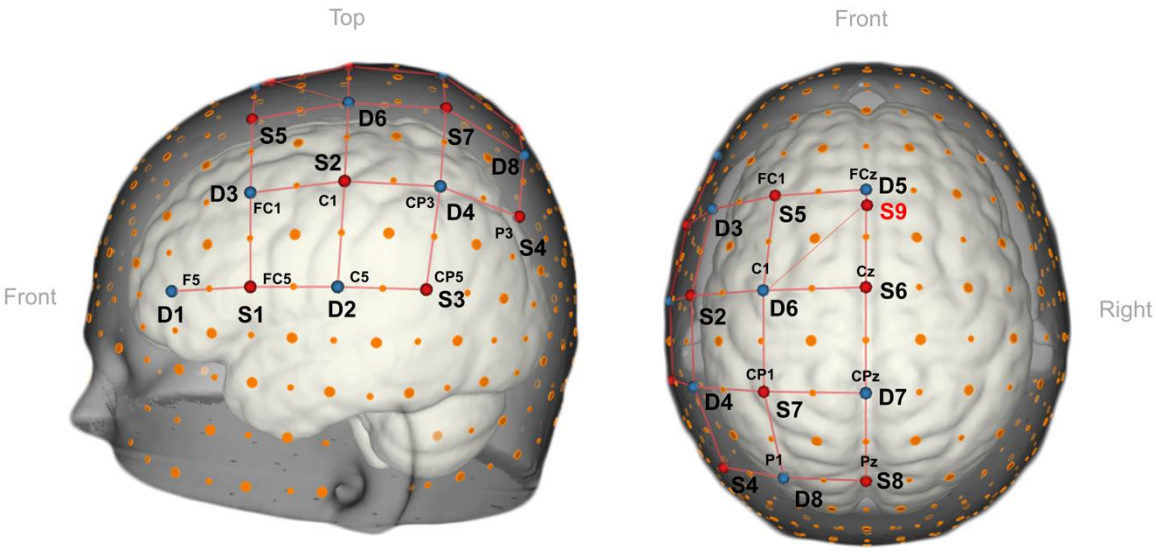

Figure 2.3. 3D view of the fNIRS-optode arrangement. The setup consisted of nine sources (in red), and eight detectors (in blue) placed over the left-hemipsheric motor and premotor regions. In total the setup contained one SDC (S9-D5) and 24 NDC. For the 3D representation we used NIRSite v1.0 software (NIRx Medizitechnik GmbH, Berlin, Germany; RRID: SCR_002491).

In total, the setup contained 24 NDCs and one SDC. The mean inter-optode distance of the standard channels spanned from 26.1 to 36.5 mm. Sources emitted light at wavelengths 760 and 850 nm, and the light intensity acquired at the detector side was sampled at 6.94 Hz. Besides the standard cap fixation (using the chin band), the fNIRS cap (EasyCap 128Ch ActiCap, EasyCap GmbH, Herrsching, Germany) was fixated onto the participants' head with three medical tape stripes (connecting the cap and the participant's forehead) to assure the cap would not shift during the measurements. In addition, a black, plastic overcap was placed on top of the fNIRS cap to additionally prevent the light in the room from reaching the optodes.

2.4 Apparatus

The session took place in a lab that consisted of two rooms, i.e., an inner and an outer room, where the hardware and materials comprising the setup were distributed (see Figure 2.4). We used NIRStar 15.2 (NIRx, Medizintechnik GmbH, Berlin, Germany) for recording the data and Turbo-Satori (TSI) 1.4.2 (BrainInnovation B.V., Maastricht, the

Netherlands;(Lührs and Goebel, 2017)) and Matlab 2017a (The MathWorks Inc., Natick, Massachusetts, United States) for real-time preprocessing and decoding the participants' choices, respectively (see Data Analysis section). The three programs ran on the data-recording and -analysis laptop (depicted with number 6 in Figure 2.4). NIRStar 15.2 was connected to the NIRScout system via USB and to TSI via Lab Streaming Layer (LSL). TSI and Matlab were connected via the TSI-Matlab interface, a self-designed network interface enabling real-time access to raw and preprocessed fNIRS data as well as protocol and statistical information (Lührs and Goebel (2017); BrainInnovationSupport, 2019). In addition, Matlab was used to log the different experimental conditions by sending triggers to the fNIRS system via LSL and to control the stimulus display that was running in Unity 3D software (v2018.3.2.f1, Unity Technologies, San Francisco, California, United States), which was running in the stimulus laptop (number 5 in Figure 2.4). During choice-encoding runs Matlab sent to Unity3D the following commands via TCP/IP: ("a") start of the run, which initiated the rotation of the inactive (blue) AR cube; ("b"), start of the encoding period, which turned the inactive cube into an active one by changing the blue-colored faces into color-coded faces; ("c") last rest period, which turned the face of the AR cube back to blue, indicating the last rest period of the run; ("1–6") decoded choice, which unfolded the cube and highlighted in red the decoded choice. All commands except for those pertaining to the decoded choice were used for the functional localizer run. The computer screen in the inner room was connected to the stimulus laptop through an HDMI cable. The HD webcam in the inner room (number 3 in Figure 2.4) was connected to the stimulus laptop via USB.

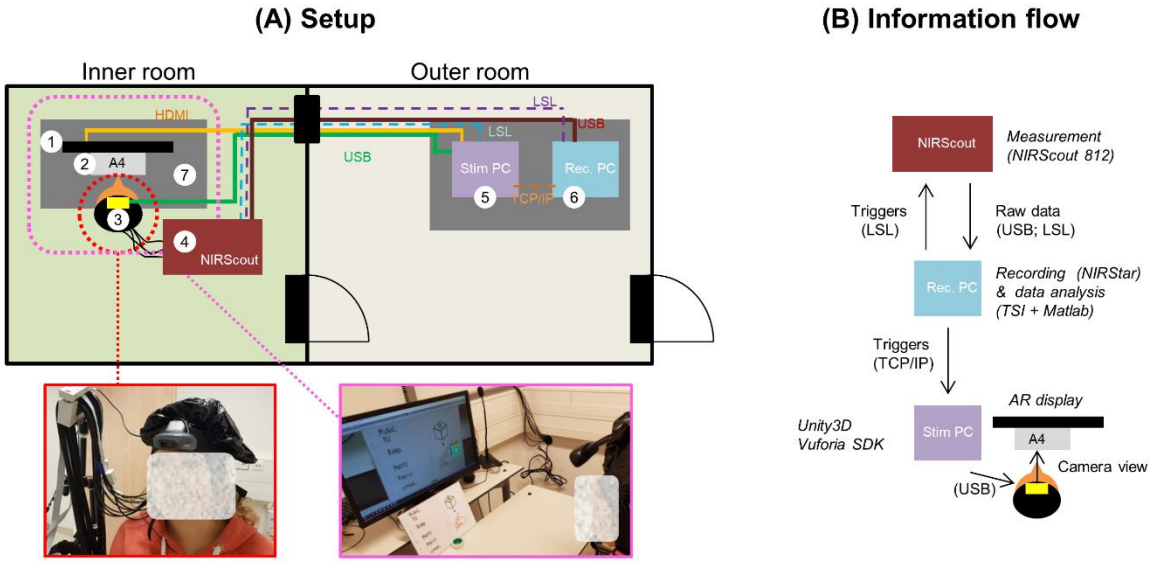

Figure 2.4. Summary of the technical setup and connections between its different components. (A) Setup. The inner room, where participants were measured while seated (see (3) and enlarged picture), contained the fNIRS system (4), a computer screen (1), an HD webcam (3), the A4 cardboard (2) and a desk (7). The outer room, where the experimenter was located, hosted the two laptops, i.e., the data-recording and -analysis laptop (6) and the stimulus laptop (5). Physical connections (wires) are depicted with continuous lines, while non-physical connections [Lab Stream Layer (LSL), TCP/IP] connections are depicted with dashed lines. (B) Information flow. NIRStar 15.2 was connected to the NIRScout system via USB and to Turbo-Satori (TSI) via LSL. TSI and Matlab were connected via the TSI-Matlab interface. Matlab was used to send triggers back to the fNIRS system via LSL and to control the stimulus display in Unity3D software (via TCP/IP).

2.5 Subjective Ratings and Previous Experience Report

After the completion of the experiment, participants first rated how comfortable the setup (optodes and webcam) felt throughout the session according to a Likert-scale ranging from 0 (extremely uncomfortable) to 10 (extremely comfortable). We predicted that comfortability ratings would decrease over time due to the presence of local pressure on the head surface caused by optodes (Nagels-Coune et al., 2017) and the webcam. Then participants rated the general easiness, pleasantness and vividness of the two motor imagery tasks they were trained on using another Likert-scale ranging from 0 (extremely difficult/unpleasant/not vivid at all) to 10 (extremely easy/pleasant/very vivid). In addition, participants were asked to report on their previous motor imagery task, fNIRS and BCI experience (first time, less than five, five to ten times or more than ten experiments).

2.6 Data Analysis

2.6.1 Real-Time Analysis

2.6.1.1 Data preprocessing

Raw fNIRS data were first converted into optical-density data and then into changes in Hb concentration through the modified Beer-Lambert law in real-time, using differential path-length factors of λ_{760} = 6.40 and λ_{850} = 5.85 (Essenpreis et al., 1993) and a baseline calculation period of 15 s (10–25 s after run onset). Data were filtered using a first-order moving-average high-pass filter with a cutoff of 0.01 Hz and a second-order moving-average low-pass filter with a cutoff of 0.25 Hz. No motion correction was applied.

2.6.1.2 Channel selection

The channel and Hb-type selection per participant was based on the result of the general linear model (GLM) analysis. Specifically, the selection was based on the chromophore and channel that led to the highest t-statistic of the task vs. rest contrast in the functional localizer run. The design matrix included one task predictor convolved with a standard hemodynamic response function (HRF). The default HRF from SPM12 was used (two Gamma HRF, the onset of response and undershoot 6 and 16 s, respectively, dispersion 1 s, response to undershot ratio 6) and the same amplitudes were used for the Δ[HbO] and Δ[HbR] task predictors. In addition, a constant term and the SDC time course were used as confound predictors should the latter satisfy the coefficient of variation criterion (CV < 7.5%, which was the case for all participants). The pre-whitening approach implemented in TSI was used to remove serial correlations (Lührs and Goebel, 2017).

2.6.1.3 Temporal decoding

During choice runs the time course of the selected channel was read in real-time in Matlab using the TSI-Matlab interface. Participants' choices were decoded by fitting a GLM in Matlab using glmfit to all five trials in each choice run (see Figure 2.5). The design matrix differed from the functional localizer run in that it included six task predictors (one for each choice option, i.e., choice period) instead of one convolved with the HRF. Importantly, the SDC time course was used as a confound predictor during choice runs only if it was used as a confound predictor during the channel selection process. No pre-whitening was applied. The condition that led to the highest t-estimate of the task vs. rest contrast was considered the selected choice (see Figure 2.5). It should be noted that this analysis was re-computed

offline using a simulated real-time approach for participants P01–P07 due to a technical mistake during these sessions.

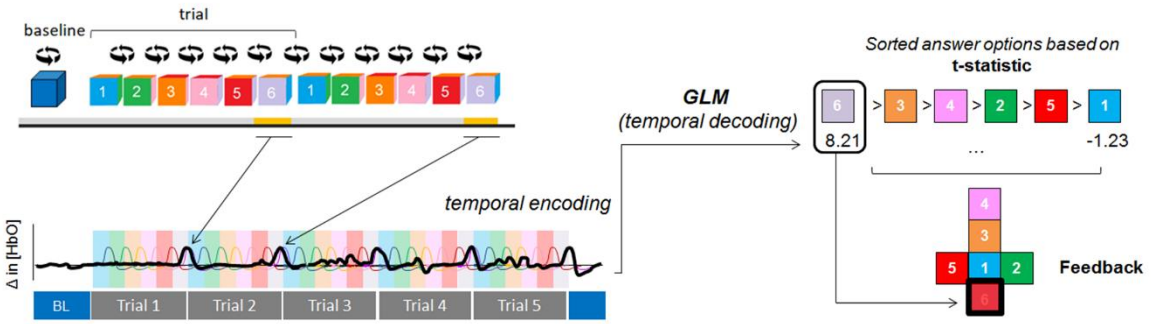

Figure 2.5. Temporal-decoding approach. A GLM was fitted to the Δ[HbX] data (from five repeated trials) to decode the participants' intentions. In this example, the participant encoded option #6 (represented by the black, thick line) and Δ[HbO] signal was used for decoding. Each colored area represents the encoding time (the period where participants were instructed to perform the mental task) for each of the cube faces. Each colored HRF represents the expected fNIRS response for each of the options. After the run the cube unfolded and feedback was provided by highlighting in red the decoded intention (which was the condition that led to the highest t-statistic [option 6, t-value = 8.21]). For visualization purposes, we added a black thick square in this schematic representation).

2.6.2 Offline Analysis

2.6.2.1 Channel-selection assessment

We evaluated the effect (on choice-decoding accuracies) of using a predefined Hb type for the channel selection vs. selecting the most informative Δ[HbX] channel (where Δ[HbX] ϵ{Δ[HbO], Δ[HbR]}). Importantly, and despite following a single-channel decoding approach, we kept all channels in place to carry out this assessment.

Besides, we evaluated the effect (on choice-decoding accuracies) of using the SDC as confound predictor in the channel-selection process. Differences across Hb-type and usage of SDC were tested for significance using a two-way ANOVA with factors SDC (with SDC, without SDC) × Hb-type (Δ[HbX], Δ[HbO], Δ[HbR]), followed by paired t-tests.

2.6.2.2 Effect of the number of trials in the decoding process

We used the same univariate choice-decoding approach as described in section *Temporal decoding* to evaluate the effect of the number of trials in a given run on decoding accuracies

(based on the most informative Δ[HbX] channel). For that, we computed the accuracies of all consecutive trial combinations for every trial number (1:n trials, where n={1,2,3,4,5}). For example, to compute the decoding accuracy of three trials, trial combinations 1-2-3, 2-3-4, and 3-4-5 were used. We then quantified the effect of the number of repetitions in the decoding accuracy at the group level using Spearman's rho correlation coefficient. The effect of number of trials was additionally evaluated using information transfer rate (ITR), defined as in (Allison et al., 2012):

$$ITR = \left(log_2 N + P * log_2 P + (1-P) * log_2 \left(\frac{1-P}{N-1} \right) \right) * \frac{60}{\tau} \qquad (2.1)$$

where N is the number of classes, P is the classification accuracy and τ is the duration of task and rest period, in seconds.

2.6.2.3 Decoding accuracy of error-correction trials

We incorporated an error-correction mechanism in our decoding process by including an "Error" option in levels > 1 of the menu. We assessed the accuracy of the error-correction approach with a confusion matrix. For that, we pooled all encoded answers across participants and divided them into "Error" and "Non-Error" instances, depending on whether the participant intended to encode "Error" or not, respectively. The encoded choices were then compared to the decoded ones. Four measures were extracted from the confusion matrix, namely accuracy, recall, precision and specificity, which were calculated as follows:

- Accuracy = (TP + TN)/(TP + TN + FP + FN)
- Recall = TP/(TP + FN)
- Precision = TP/(TP + FP)
- Specificity = TN/(TN + FP)

where TP = True positive or correctly detected "Error" trials; TN = True negative or correctly detected "Non-Error" trials; FP = False Positive or incorrectly detected "Error" trials; FN = False negative or incorrectly undetected "Error" trial.

2.6.2.4 Chance-level definition

A quantile function of a multinomial distribution was used to define the upper bound of the

chance-level (37.5% for N = eight runs, c = six classes and a $p < 0.05$).

2.6.2.5 Subjective ratings

Mean and SE of normalized subjective comfortability ratings was computed by calculating the mean (of eight runs) for each subject and subtracting the subject's mean to each item. The effect of the duration of the experiment (number of runs) on the comfortability score was quantified using Pearson's correlation. In addition, the relation between previous BCI/fNIRS/task experience on task accuracies reached by each participant was assessed using Spearman's correlation coefficient. Finally, to evaluate the perceptual differences the mental tasks elicit on each participant, normalized absolute mean differences between the preferred and non-preferred mental task ratings were assessed. First, each item was normalized following the same approach as for the comfortability ratings. Next, the three scores (easiness, pleasantness and vividness) were averaged for each mental task and participant. Then, absolute differences between mental tasks were computed and a right-tailed t-test was used in Matlab.

3 Results

3.1 Choice-Decoding Results Obtained in (Simulated) Real-Time

Figure 2.6 shows the individual and group accuracies achieved in the experiment. In addition, it shows that half of the participants chose to perform the mental-drawing task and that Δ[HbR] was selected for seven out of twelve participants. All participants but P04 exceeded the upper bound of the chance-level (37.50%, orange dashed line). It should be noted that accuracies from participants P01-P07 were computed offline using a simulated real-time approach due to a technical mistake during these sessions, while accuracies from participants P08-P12 were calculated online based on real-time results. On average, participants reached an accuracy of 73.96% (SD = 20.96), as depicted by the left-most gray bar of the group plots. Mean decoding accuracies with different grouping factors were also computed and descriptively did not differ substantially within each group (see Figure 2.6).

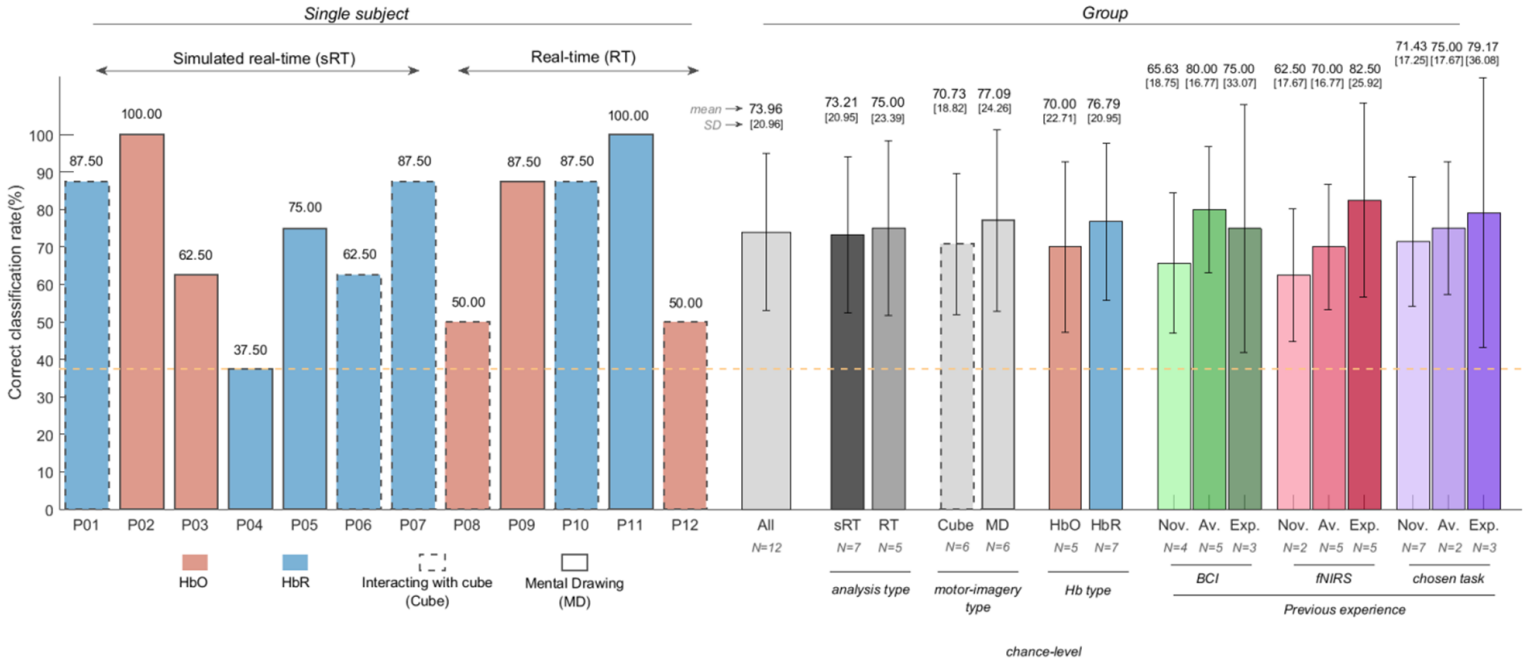

Figure 2.6. Choice-decoding accuracies obtained in (simulated) real-time (individual and group results) using Δ[HbX] channel selection and SDC correction. All participants but P04 reached accuracies higher than chance-level (orange, dashed line). The face colors and line pattern of the bar plots of each subject (left-half of the figure) represent the selected Hb-type and strategy participants chose to perform, respectively. Mean decoding accuracies and standard deviation of all participants and with different grouping factors can be found on the right-half of the figure. Groupings were based on the analysis type (simulated real-time vs. real-time), the motor imagery participants chose [interacting with the cube (cube) vs. mental drawing (MD)], the selected chromophore (Δ[HbO] vs. Δ[HbR]) and previous BCI experience (novices, average and experts). Participants with no previous BCI/fNIRS/task experience were considered novices; expert participants were those who had participated in more than five BCI experiments; the remaining participants were considered average (see Table 2.2). The integer after "N = " indicates the number of participants employed in each computation.

3.2 Evaluation of Error-Correction Procedure

In total, participants had to encode the "Error" option 22 times (see Figures 2.7A,B). Out of the 22 instances, the error option was correctly detected 14 times, missed eight times, and incorrectly labeled once, as indicated in the confusion matrix (Figure 2.7A). Overall, the accuracy of the error-correction trials was 90.6% (upper bound of the chance level was 58.88%, assessed by the quantile function of a multinomial distribution with n = 96 trials, c = 2 classes and alpha = 0.05).

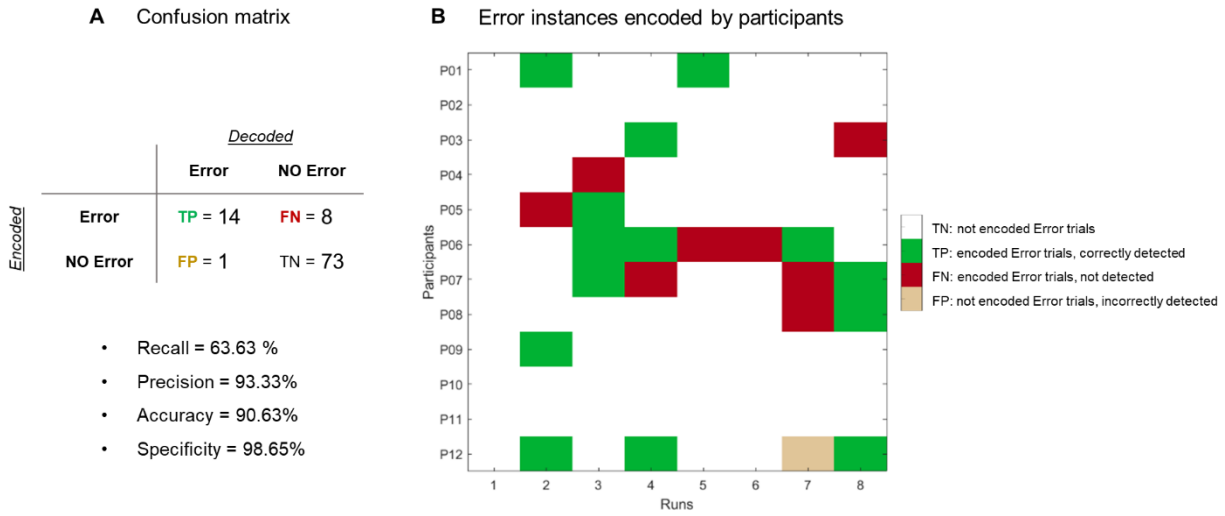

Figure 2.7. Evaluation of error-correction procedure. (A) Confusion matrix. Participants reached an accuracy of 90.62% (72/96 trials were correctly labeled as "Error" or "NoError") and a recall level of 65.22% (out of 22 error trials, 8 trials were missed). (B) Summary matrix of when participants encoded the "Error" option (marked in dark gray). Green (red) cells represent trials where the "Error" option was correctly (incorrectly) detected. The beige cell indicate a false positive trial.

3.3 Assessment of the Effect of Number of Trial Repetitions

To assess how the number of trial repetitions affects the decoding process, we sequentially reduced the number of trial repetitions we used for decoding. Table 2.2 summarizes the individual and group decoding accuracies for a decreasing number of repetitions and Figure 2.8A shows that the number of repetitions used to decode each run influences the decoding process. Specifically, we observed a significant negative correlation between the accuracies and the number of repetitions, as assessed by Spearman's rho correlation coefficient

($\rho = -0.639$, $p < 0.0001$). Importantly, mean- and several single-subject accuracies (7 out of 12 participants) remained above chance level even when using a single trial. As for the ITR computation, Figure 2.8B indicates that slightly higher ITR values can be reached, on average, when using four trials (0.34 bits/min) instead of five (0.29 bits/min).

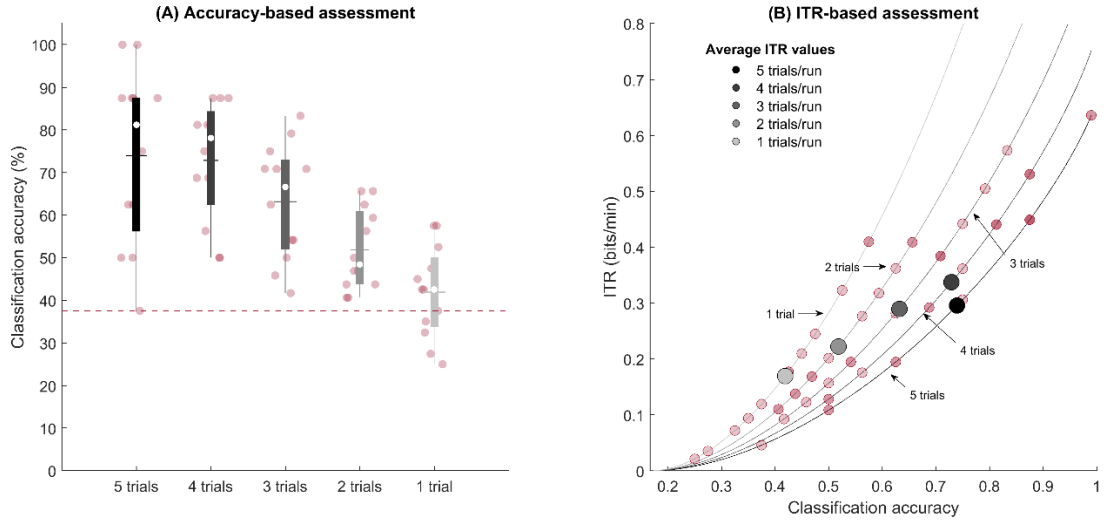

Figure 2.8. Effect of the number of trial repetitions on obtained decoding accuracy (individual and group results). (A) The box-plot shading depicts the number of repetitions used for decoding: from five trials (black) to a single trial (light gray). Median values are represented by the white circles, while the mean values are indicated with the horizontal lines. The y-axis represents the accuracy (%) achieved by the participant. The red, dashed line shows the chance-level defined by the cumulative multinomial distribution. The number of trials used to decode each run influences the decoding process, but mean- and several single-subject accuracies remain above chance level even with a single trial. (B) Average (gray-scale markers) and single-subject (red markers) ITR values (bits/min) for different number of trials as a function of achieved classification accuracies. Lines represent the theoretical values the ITR can take as a function of the number of classes, trial duration and accuracy.

Table 2.2. Individual and group decoding accuracies over decreasing number of repetitions

	Accuracies (%)				
	5 trials	**4 trials**	**3 trials**	**2 trials**	**1 trials**
P01	87.50	81.25	70.83	65.63	47.50
P02	100.00	81.25	70.83	59.38	57.50
P03	62.50	75.00	54.17	56.25	45.00
P04	37.50	50.00	54.17	43.75	37.50
P05	75.00	50.00	50.00	50.00	42.50
P06	62.50	68.75	41.67	46.88	27.50
P07	87.50	87.50	79.17	65.63	57.50
P08	50.00	56.25	45.83	40.63	32.50
P09	87.50	81.25	75.00	43.75	35.00
P10	87.50	87.50	83.33	62.50	52.50
P11	100.00	87.50	62.50	46.88	42.50
P12	50.00	68.75	70.83	40.63	25.00
Group [SD]	**73.96 [20.96]**	**72.92 [14.19]**	**63.19 [13.74]**	**51.82 [9.56]**	**41.88 [11.83]**

3.4 Assessment of Channel Selection

Although our channel selection approach was based on selecting the most informative Δ[HbX] channel for each participant, it is not uncommon to have a predefined Hb-type before the data acquisition (Naseer and Hong, 2015a). In this context, we looked at whether the selected channel would change had we decided to focus on only one chromophore. In addition, since we used the SDC time course as a confound predictor, we assessed whether applying SDC correction (or not) influences the channel selection. Table 2.3 shows that for some participants, the channel selection approach does not affect the selected channel (see P01, P02, P07 and P11 across all columns), while for other participants it does. Descriptively speaking, SDC correction slightly reduced the mean accuracy for the most-informative Δ[HbX]-channel approach. The reason behind this observation is that the increased accuracy for some participants (P03, P06, P09, P11, and P12) was smaller than the decrease in accuracies for other participants (P04, P05, P08, and P10). The mean decoding accuracy increased for the most-informative Δ[HbO] and Δ[HbR] channel approaches (although to a considerably lesser extent for the latter).

Table 2.3. Most informative channel for different channel selection approaches and (individual and mean) accuracies reached with each approach

	Accuracies (%)											
	Best Δ[HbX]				Best Δ[HbO]				Best Δ[HbR]			
	SDC		no SDC		SDC		no SDC		SDC		no SDC	
P01	S3-D2	87.5 (=)	S3-D2	87.5	S3-D2	75.0 (↑)	S3-D2	25.0	S3-D2	87.5 (=)	S3-D2	87.5
P02	S9-D6	100 (=)	S9-D6	100	S9-D6	100 (=)	S9-D6	100	S9-D6	87.5 (=)	S9-D6	87.5
P03	S6-D5	62.5 (↑)	S2-D6	37.5	S6-D5	62.5 (↑)	S9-D6	25.0	S2-D6	62.5 (↑)	S2-D6	37.5
P04	S1-D3	37.5 (↓)	S9-D6	100	S1-D3	25.0 (↓)	S9-D6	100	S1-D3	37.5 (↓)	S5-D6	75.0
P05	S2-D4	75.0 (↓)	S2-D4	87.5	S7-D8	25.0 (↑)	S6-D7	12.5	S2-D4	75.0 (↓)	S2-D4	87.5
P06	S2-D6	62.5 (↑)	S3-D2	25.0	S2-D6	62.5 (↑)	S2-D6	12.5	S2-D6	62.5 (↑)	S3-D2	25.0
P07	S2-D4	87.5 (=)	S2-D4	87.5	S2-D4	75.0 (↑)	S2-D4	37.5	S2-D4	87.5 (=)	S2-D4	87.5
P08	S1-D2	50.0 (↓)	S2-D2	100	S1-D2	50.0 (↓)	S1-D2	62.5	S2-D2	100 (=)	S2-D2	100
P09	S2-D3	87.5 (↑)	S2-D3	75.0	S2-D3	87.5 (↑)	S2-D3	75.0	S1-D3	75.0 (=)	S5-D6	75.0
P10	S1-D2	87.5 (↓)	S1-D2	100	S1-D2	87.5 (↑)	S3-D2	75.0	S1-D2	87.5 (↓)	S1-D2	100
P11	S1-D3	100 (↑)	S1-D3	62.5	S1-D3	50.0 (↑)	S1-D3	37.5	S1-D3	100 (↑)	S1-D3	62.5
P12	S5-D5	50.0 (↑)	S2-D4	37.5	S5-D5	50.0 (↑)	S2-D4	37.5	S2-D3	12.5 (↓)	S2-D4	37.5
Group (SD)		**73.96 (20.96) (↓)**		**75.00 (27.70)**		**62.50 (23.84) (↑)**		**50.00 (31.53)**		**72.92 (26.02) (↑)**		**71.88 (25.63)**

Note 1: Red (blue) cells indicate that the selected chromophore was Δ[HbO] (Δ[HbR])

Note 2: The different symbols summarize the effect in decoding accuracy (↑ [increased], ↓ [decreased], = [maintained]) when SDC was used as a confound predictor *vs. w*hen it was not

A repeated measures 2-way ANOVA with factors SDC (with SDC, without SDC) × Hb-type (Δ[HbX], Δ[HbO], Δ[HbR]) showed that the mean accuracies were different across Hb-types [main effect of Hb-types; $F(2,66) = 3.494$, $p = 0.036$; no significant interaction], but not across SDC. Subsequent paired t-tests showed that Δ[HbX] and Δ[HbR] performed better than Δ[HbO] [$t(23) = 3.83$; p(FDR [$q = 0.05$]) = 0.001, and $t(23) = 2.736$; p(FDR [$q = 0.05$]) = 0.008].

3.5 Previous Experience and Subjective Reports

Due to the (novel) AR component, the participants were enthusiastic about the research study. Independent of the achieved accuracies participants rated the setup positively and considered the experiment as "fun," "engaging," and "motivating." The setup became uncomfortable over the runs as indicated by a significant negative correlation ($r = -0.991$, p

< 0.0001). Participants reported the main source of discomfort to be the pressure caused by the webcam on their foreheads and to a lesser extent the optodes on the head surface. We observed that the preferred motor imagery task was rated significantly higher than the non-preferred task [$t(11) = 5.240$, $p < 0.001$]. In addition, we observed that previous BCI/fNIRS/task experience correlated positively with individual accuracies, but none of them reached significance ($\rho task = 0.429$, $\rho BCI = 0.360$, $\rho fNIRS = 0.566$, $p > 0.05$).

4 Discussion

The present proof-of-concept study combined AR technology and an fNIRS-based BCI to apply it in a communication context, where twelve healthy participants were asked to navigate in real-time through a nested six-choice menu while following a temporal information encoding approach. The decoded choice was defined for each participant based on the time course of the most-informative channel in the setup. In case the decoded choice was incorrect, an active error correction procedure was used. We achieved mean accuracy levels of 73.96% (with a chance-level of 37.5% for six answer options) and error detection accuracies of 90.6%. The following sections discuss the general implications of this study, together with its limitations and prospects for the future.

The Temporal Information Encoding Approach – A Powerful Paradigm for fNIRS-Based BCIs

In this experiment, we applied for the first time a temporal information encoding approach and a GLM-based decoding scheme previously reported in fMRI-based BCIs (Sorger et al., 2009; Bardin et al., 2011; Sorger et al., 2012) to an fNIRS-based BCI system to distinguish between six options using a single channel and mental task. An advantage of using this procedure is that a single channel may be sufficient for decoding participants' intentions without hampering our decoding ability. Intuitively, using a single channel should also make the setup more comfortable. It should be mentioned that although we assessed the feasibility of the single-channel approach and recorded participants' comfortability scores over time, we kept all channels in place for post hoc analyses. Another advantage is that, theoretically, this approach could allow including a considerably high number of conditions. In the present work we have further advanced previous applications by going from four (Sorger et al., 2009; Bardin et al., 2011) to now six temporally different but still differentiable encoding

phases. Importantly, future work should explore the upper limit of the included number of conditions that would yield a sufficiently high decoding accuracy. In any case, increasing the number of conditions would inevitably rise the duration of the run, but this could be solved by reducing the task duration to a certain extent. Until now the biggest body of hemodynamic BCI applications has used a task duration of 10 s (Herff et al., 2013; Naseer and Hong, 2013; Hong and Santosa, 2016; Nagels-Coune et al., 2017; Shin et al., 2017) or longer (Bardin et al., 2011; Bauernfeind et al., 2011; Batula et al., 2017), and very few studies have used task durations under 10 s: for example, (Sorger et al., 2009)and (Shin and Jeong, 2014) used variable task durations of 5/10/15 s and 6/8/10/15 s, respectively. To maintain the single-trial duration as low as possible without hindering the ability to distinguish between conditions, we opted to use 6 s task duration per condition for our experiment. However, the considerable inter-subject variability in accuracies suggests that user-tailored task durations should be considered in future studies.

Using a Single fNIRS Channel – A Promising Approach in the Context of Temporal Information Encoding

Selected Feature

Feature selection varies across studies, but in general, previous work has focused on either using only Δ[HbO] signal (Stangl et al., 2013; Erdoğan et al., 2014; Hong et al., 2015; Koo et al., 2015; Hong and Santosa, 2016; Lapborisuth et al., 2017; Noori et al., 2017; Liu et al., 2018) or the combination of different chromophores (computing the mean or the difference of Δ[HbO] and Δ[HbR], Naseer and Hong, 2015b). A few fNIRS-BCI applications have used/explored Δ[HbR] on its own (Cui et al., 2010; Naseer and Hong, 2015b; Hwang et al., 2016). The main reason is that Δ[HbO] is considered to exhibit larger and more pronounced concentration changes than Δ[HbR] in response to mental tasks (Stangl et al., 2013; Sato et al., 2016). Besides, it has been reported that Δ[HbO] signals are more discriminative and perform more robustly than Δ[HbR] signals (Mihara et al., 2012; Naseer and Hong, 2015b). However, Cui et al. (2010) and Hwang et al. (2016) found that Δ[HbO] and Δ[HbR] performed similarly in terms of accuracy. In the present work the channel selection approach led to selecting Δ[HbR] for 7/12 participants. In addition, our post hoc analysis revealed that at the group level channel selection using either Δ[HbX] approach or Δ[HbR] performed better than only Δ[HbO] channel selection. Despite having lower SNR, these results point at the usefulness of the Δ[HbR] signal for the classification of motor imagery (at least) in a

GLM-based decoding approach.

SDC Correction

SDCs are used to minimize/reduce unwanted physiological noise contained in NDCs (Goodwin et al., 2014). In the current work, a custom-built SDC was used as a GLM confound predictor during both, the selection of the most informative channel and the decoding process. Offline, we evaluated the effect of using SDC for channel selection and choice decoding. As derivable from Table 2.3, when using the Δ[HbX] approach, SDC correction did not affect the channel selection in seven out of twelve participants (P01, P02, P05, P07, P09, P10, and P11). The selected channels for the remaining participants differed either in location only (P06) or in location and Hb-type (P03, P04, P08, and P12). This suggests that the former group of participants had a relatively stable signal compared to the latter ones. Interestingly, the mean accuracies were higher for the former group, too [89.29% (SD = 8.63) vs. 58.33% (17.08)]. Although the accuracy did not significantly change on average when SDC correction was used vs. when it was not, a clear divergence between both approaches was observed in some participants. For example, the accuracy reached by P04 and P08 was considerably reduced after SDC correction (100–37.5% and 100–50%, respectively), while it improved for P06 and P11 (25–62.5% and 62.5–100%, respectively). It is not straightforward to attribute this opposing and seemingly irregular effect across participants to an isolated cause. Instead, it may be the result of an interaction between the spatial relation of the SDC and the selected channel, which suggests that the location of the SDC matters even in a relatively small setup. In addition, the selected chromophore (whether it is Δ[HbO] or Δ[HbR]) may influence the effect of SDC correction. Indeed, unlike for the Δ[HbX] (and the Δ[HbR]) approach, we observed a clear improvement before/after SDC correction when selecting channels based on Δ[HbO] (see Table 2.3, "Best Δ[HbO]"). Specifically, the mean decoded accuracy increased from 50 to 62.5% after SDC correction. This is expected, as Δ[HbO] signal is more affected by global systemic artifacts in both extracerebral and intracerebral compartments than Δ[HbR] (Kirilina et al., 2012).

t-Statistic for Channel Selection and Decoding

Different approaches for channel selection have been reported in the literature. Hu et al., (2013) compared the difference between the maximum value during the task and rest periods, and considered the channel to be active if the difference was positive. Hong and

Naseer (2016) and Khan and Hong (2017) suggested selecting channels where the initial dip could be reliably detected. For that, a vector-based phase analysis with a threshold circle as a decision criterion was employed. Previous fNIRS studies have also followed a t-value (Hong and Santosa, 2016; Nagels-Coune et al., 2017) or beta-value criterion (Klein and Kranczioch, 2019) between the measured and expected hemodynamic response by the given stimulation for channel selection.

In the present study we selected the most informative channel and Hb-type combination based on the highest t-statistic of the task vs. rest contrast of the functional localizer data. We ensured correct t-value estimation during channel selection by removing serial correlations generally present in the fNIRS data (Huppert, 2016). The decoded answer option was based on the choice that led to the highest t-statistic of the choice i vs. rest contrasts, where i = {1,2,3,4,5,6}. No pre-whitening was used during decoding since the ranking of the t-estimate should not change across choices. The reason for this is that, as a single channel was used for decoding, each t-estimate was affected by the same amount of serial correlations (Lührs et al., 2019).

Necessity of Trial Repetition

Sorger et al. (2009) and Bardin et al. (2011) used an fMRI-based temporal-encoding and decoding approach to carry out five and two communication runs (respectively) with four answer options; while Sorger et al. (2012) used it in a letter speller context with 27 letter options to encode words between 7 and 13 characters. They reached single-trial mean accuracies of 94.9% (Sorger et al., 2009), 100% (Bardin et al., 2011), and 82% (Sorger et al., 2012) in healthy participants. As for fNIRS-based BCIs, previous work has addressed classification problems using multivariate approaches that maximally distinguished between five mental tasks with an average single-trial accuracy of 37.2% (Weyand and Chau, 2015), or four commands involving motor-execution (Shin and Jeong, 2014) and motor imagery tasks(Batula et al., 2014; Weyand and Chau, 2015; Naseer and Hong, 2015b) that reached mean single-trial accuracies of 82.46, 45.6, 73.3, and 46.7%, respectively. In the present work, participants encoded the same choice five consecutive times in each of the eight choice runs, and we achieved mean (multi-trial/repetition) accuracy levels of 74%.

To assess whether five consecutive trials were actually necessary to successfully decode

their choice, the effect of reducing the repetitions on the decoding accuracy was evaluated post hoc. We observed a significant negative correlation between the accuracies and decreasing the number of repetitions ($\rho = -0.639$, $p < 0.0001$). Interestingly, encoding the same choice only once maintained the mean group accuracies above chance level although with considerably lower values than with five trials (73.96% vs. 41.88%). In line with the observed accuracies, the mean ITR value was considerably reduced when a single trial is used ($ITR_1 = 0.17$ bits/min) compared to when five trials were used ($ITR_5 = 0.30$ bits/min). In addition, we observed that reducing the number of repetitions to four slightly improves the mean ITR, with 0.34 bits/min. To put these values in a broader context, the average ITR of the studies mentioned above were calculated and can be compared to the present study in Figure 2.9. This figure shows that the ITR_1 is closely related to the ITR values from Batula et al. (2014) and Weyand and Chau (2015) and that with the approach employed in this study (ITR_5) considerably higher accuracies are reached, while maintaining the ITR value. This figure also depicts that ITR_5 is considerably lower than in Shin and Jeong (2014) and Naseer and Hong (2015b).

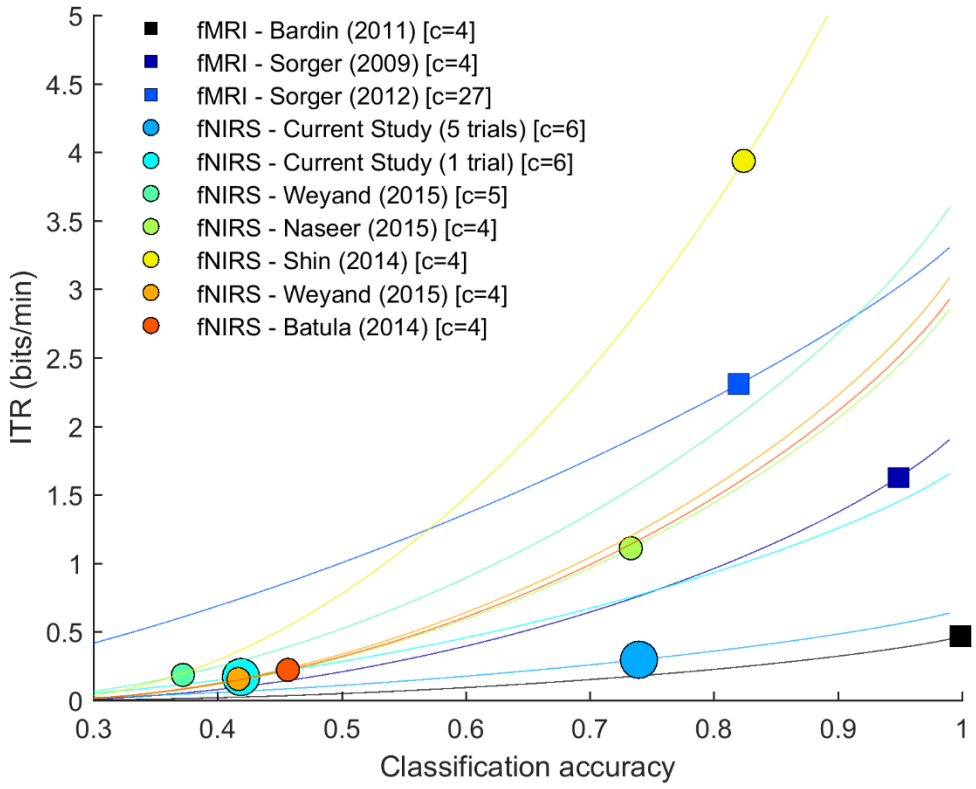

Figure 2.9. Average ITR values from relevant hemodynamic-BCI literature. Square markers represent fMRI-based BCIs, while circular markers represent fNIRS-based BCIs. Lines depict the theoretical values the ITR (bits/min) can take as a function of the number of classes (c), trial duration and accuracy.

Lower decoding accuracies compared to fMRI studies are expected since fMRI has a higher spatial resolution (Valente et al., 2019), fMRI signals have stronger signal-to-noise ratio (Cui et al., 2011) and because unlike fMRI, the brain signal measured with fNIRS also contains (unwanted) superficial scalp information (Erdoğan et al., 2014). This is because light traveling from a source to a detector to reach the brain must pass through scalp and skull tissues twice (Brigadoi and Cooper, 2015). Lower decoding accuracies compared to fNIRS-BCI studies employing multivariate approaches may require further explanation. Multivariate approaches are pattern-classification algorithms used to decode the information that is represented in a given pattern of activity (Norman et al., 2006). They integrate information of multiple voxels/electrodes/channels by optimizing their weights and theoretically should provide higher sensitivity to disentangle overlapping distributed activation patterns than univariate approaches (Valente et al., 2019). The fundamental steps

comprising multivariate approaches are, generally speaking, feature extraction, feature selection, model learning and validation (Norman et al., 2006). The available number of trials/examples for model learning and feature extraction influences the performance of multivariate approaches, as estimating a model based on few examples may not be sufficiently reliable or may not capture the differences between classes in a relatively high-dimensional space (Valente et al., 2019). Thus, it is expected that a model trained on a sufficient number of examples should be able to accurately classify examples never seen by the model. Naseer and Hong (2015b) and Shin and Jeong (2014) employed multivariate approaches and both used > 100 trials to train their models, collected over four separate sessions and a single session, respectively. In addition, their classification problem aimed at distinguishing between different task patterns, which we suspect may elicit more discernible patterns than classification problems aimed at detecting the presence or absence of a task-related information (i.e., task vs. rest scenario). It should be noted that Batula et al. (2014) and Weyand and Chau (2015) also applied multivariate approaches that aimed at distinguishing between different motor imagery tasks, but employed less total number of trials to address the classification problem, which can partially explain the lower accuracies reported in these studies. The temporal approach employed in this study did not require any model learning, but relied on a time course extracted from a single channel with certain degree of trial-to-trial variability that was not constant across participants. Indeed, in some participants (see P03, P04, P06, P08, or P12), we did not observe a linear decrease in the decoding performance with reducing the number of repetitions as in the group results, which suggests that for some participants the inter-trial variability is higher than for others. Altogether, we believe these are the main reasons that could explain the divergence in the mean single-trial accuracies observed in the present study and in the literature.

In the future, a multivariate temporal approach could be tested that would also only require a single localizer run. Specifically, instead of selecting and using a single (most-informative) channel for decoding participants' intentions, a task-specific activation pattern would be defined after the localizer session (based on a univariate approach over each channel comprising the setup), here called as "base-pattern." For each of the communication runs a new activation pattern for each condition would be calculated and compared to the base-pattern as in Monti et al. (2010). The answer option leading to the highest correlation or the smallest distance between the patterns would be the selected option. Importantly, the

number of optodes comprising the setup should be optimized to guarantee participants' comfort and a good accuracy level. In addition, due to the existing trial-to-trial variability within and across participants, a subject-specific number of trials could be considered instead of seeking a group-based criterion. This could be achieved, for example, by implementing an evidence accumulation process with a stopping criterion that trades speed and accuracy for each participant (Mattout et al., 2015).

Feasibility of Error-Correction Approach

Automatic recognition of error potentials has been successfully used in EEG-based BCIs that focus on sensorimotor rhythms and event-related potentials, since evoked responses by the feedback differ depending on whether the feedback is correct or not (Chavarriaga et al., 2014; Mattout et al., 2015). Hemodynamic signals do not show such distinct patterns, which makes direct forms of error-correction mechanisms more challenging to implement. Here we developed an active error-correction approach where participants were asked to indicate a decoding error by encoding the "Error" option in the next choice run if the decoded choice they received did not correspond to what they intended to encode. This approach assumes that we can correctly detect the "Error" option when participants encode it. We built a confusion matrix by pooling all encoded answers across participants to evaluate the performance of our proposed error detection approach. In an ideal scenario, the number of "Error" trials comprising this matrix should be zero or close to zero, which would indicate that no decoding mistakes were made. The fact that participants reached an average of ~74% accuracy indicates that participants had to encode "Error" several times, but importantly, this number differed across participants. Figure 2.7B shows that for example, P06 had to encode "Error" 5/8 times, while P02 did not have to encode any. The figure also indicates that the number of "Error" trials was lower than "not Error" trials (thus making the confusion matrix unbalanced). The confusion matrix shows that we reached an accuracy of 90.62% (72/96 trials were correctly labeled as "Error" or "not Error"). However, we only reached a recall level of 63.63% (out of 22 error trials, 8 trials were missed), which indicates that this approach did not always work.

It is also important to note that the number of encoded errors does not directly represent the accuracy of the BCI setup. This is due to three reasons: first of all, owing to a technical mistake, data from P01-P07 were reanalyzed offline. In turn, some trials that were

incorrectly decoded in real-time were correctly decoded offline (and vice versa), which misplaced the presence of "Error" encoding runs (and disrupted the semantic link between the encoded and decoded choices). This means that in the former case (after offline analysis the choice was correctly decoded), a subsequent error-encoding run became unnecessary, while for the latter case (after offline analysis the choice run was incorrectly decoded) a following "Error" encoding run should have occurred (see Supplementary Material). Second, our experimental design did not include an error option in the first level of the nested menu. This implies that if choices were wrongly decoded in the fourth level of the menu, participants were no longer able to encode the "Error" option in the next run. Third, and similarly, if a decoding error occurred in the last run of the experiment (run number eight), participants were no longer able to encode the "Error" option. These two scenarios could be addressed in the future by using additional short runs (under a minute) where the participant would verify if the decoded answer was correct or not. The run would consist of an initial and final baseline periods of 20 and 10 s, respectively, with a single full rotation of the AR cube presented in between. Specifically, the AR cube would show faces corresponding to yes/no answers, alternated with rest periods, i.e., YES-NO-REST-YES-NO-REST (6 s per face, 36 s in total). This would allow participants to encode twice whether the decoding option was correct or not in 66 s, while leaving enough time for the hemodynamic response to get back to baseline.

In this experiment participants navigated through a four-level, nested menu. After completing one full round (i.e., reaching level four), participants were directed back to the first level of the menu. Since participants performed eight choice runs, this structure allowed them to maximally go through the menu twice. Due to the technical mistake mentioned above, the following lines will only discuss results pertaining P08–P12: P11 completed two full rounds (100% accuracy), while P09 and P10 completed one full round (both participants reached a 87.5% accuracy); P08 and P12 did not manage to complete a single round (the decoding accuracy for both participants was 50%). These results clearly show that statistically significant accuracy is a necessary but not sufficient prerequisite to achieve a functionally significant accuracy. Indeed, the accuracy that would be necessary to use the system in a convenient way requires the accuracy to be much higher. Future work should include the "Error" option in each level of the nested menu. It should also consider an additional measure besides the magnitude of the t-statistic for decoding participants'

choices, such as a confidence measure based on the absolute differences in the t-estimate across conditions. We expect that a more informed decision helps improving the decoding and the error-detection processes.

Task Selection Based on Participants' Preference and Previous Experience

In the present study, we first trained participants to perform two different motor imagery tasks and subsequently let them choose their preferred option. However, unlike previous work, we did not test whether user preference leads to better performance compared to an experimenter-based task selection approach (Weyand and Chau, 2017).

Intuitively, experienced BCI users may have a more realistic idea of which mental strategy works best for them and thus choose the task that has worked well in the past. Although we asked participants to choose the task they felt most comfortable with in the given setup independent of their previous experience, P02, P04, P05, and P11 chose to use mental drawing for this very reason. In contrast, participants P07 and P10, who also reported being familiar with the mental drawing task (and unfamiliar to the interacting with the cube task), chose to use interacting with the cube as it felt more natural for them given the AR stimuli.

Previous experience with the mental task, BCI setups and fNIRS systems did not show significant correlation with obtained accuracies. However, differences in decoding accuracies between (1) novices and (2) average and more experienced BCI/fNIRS users were considerably high [65.63% vs. 80% (average) and 75% (more experienced) for BCI and 62.5% vs. 70% (average) and 82.5% (more experienced) for fNIRS]. Similarly, we observed differences between the same groups but to a lower extent regarding previous task experience. Specifically, novices reached a mean accuracy of 71.73%, while average and more experienced users reached 75 and 79.17%, respectively. These observations suggest that participants with a certain level of experience with a BCI/fNIRS system or a given mental task may have enough introspective information to make an adequate and informed decision on their preferred task after a single training session.

Using AR in BCIs Offers a Great Flexibility

Recent work has shown that EEG-based BCIs can successfully be used in combination with new technological developments such as AR to improve real-world practicality by offering

a richer, more direct, and intuitive interface (Kansaku et al., 2010; Takano et al., 2011; Borges et al., 2016; Faller et al., 2017). However, very few fNIRS applications have explored this option (Afergan et al., 2015; McKendrick et al., 2016; Si-Mohammed et al., 2018; Hu et al., 2019). In the present study, we employed an AR cube to guide the temporal-encoding approach and to display the decoded answer of participants' intentions. For that, we used a relatively simple and flexible setup from the hardware point of view: we made use of two laptops, one additional computer screen, an HD webcam, and home-made A4 cardboards. The home-made A4 cardboards served as whiteboards and triggered the display of the AR cube in Unity3D on an additional computer screen. Importantly, a whiteboard offers a high degree of flexibility and individuality as anyone (a caretaker, family member, experimenter, etc.) could write potential choice options based on previous knowledge of the user and/or the social context (although we used the same choice options for all participants in this experiment, see Supplementary Material). Also, a whiteboard provides a degree of proximity to the setup and interaction between the user and the experimenter as new choice options need to be written down after each run. Besides, handwriting may offer a sense of familiarity to the user. It is important to note that participants were instructed to look at the computer screen at all times throughout the runs, which makes the chosen location of the cardboard (on the desk, between the computer screen and the participant) not intuitive from a pure AR setup perspective. Indeed, the cardboard could have been placed in a different location (behind the screen, for example) as long as the webcam's placement would change accordingly. However, we chose consciously to place the cardboard between the screen and the participants exclusively to exploit the cardboards' interactive and proximity features mentioned above.

Altogether, this relatively simple setup has the potential to be successfully implemented in a more ecologically valid environment such as a hospital room or a rehab center. From the setup point of view, we picture a situation where the user would be placed comfortably in a Fowler's position (head is placed at a 45-degree angle), while wearing the optodes, fNIRS cap and overcap. The fNIRS system would be located next to the bed. A removable desk would be attached to the structure of the bed, above the user's thighs, slightly tilted toward the user's head. A tablet fixated almost perpendicular to the desk could be used instead of the additional computer screen to display the AR cube. To maximize comfort, the rotation of the desk would be adjusted to ensure the tablet was placed at the same height as the user's

eye gaze. The webcam would be integrated into the tablet or a separate camera would be placed on a stable structure such as a tripod located right next to the participant and it would be recording the contents of the whiteboard. Alternatively, smart glasses with an integrated camera could be used. These glasses would then also replace the tablet and could display the cube directly on the glasses.

From the data analysis point of view, the current decoding process could be improved to increase the performance of the BCI (as discussed in previous sections). Importantly, as the majority of the analysis steps have been streamlined (through scripts written in Matlab and Unity3D), a single BCI operator would be sufficient to perform the measurements. However, to assure that the channel selection procedure is properly done (i.e., the selected channel is sufficiently informative and not corrupted extensively by noise), an experienced researcher or a trained medical professional in understanding the fNIRS signal would be necessary. Of course, caretakers and family members should be encouraged at all times to assist the experimenter in selecting the most appropriate options to be presented to the user through the whiteboard.

5 Conclusions

In the present study, we showed that fNIRS-based BCIs can be successfully combined with AR technology to address a six-class problem using a single mental task and fNIRS channel. AR technology allows for a seamless real-world interaction that future studies should explore in more detail. The high inter-subject variability observed in this study not only in achieved accuracies but also in task preference and channel selection, points at the need of shifting the BCI field toward a true user-centered approach. Future studies should consider pursuing individualized approaches to bridge the gap from research to real-world applications.

6 Supplementary Material

6.1 Encoded and decoded answers

This section compiles all encoded (by participants) and decoded choices (based on the temporal decoding approach) for each participant. It is important to note that, the data from P01 to P07 were reanalyzed offline due to a technical mistake. Thus, some trials that were incorrectly decoded in real time were correctly decoded offline (and vice versa), which misplaced the presence of "Error" encoding runs (and disrupted the semantic link between the encoded and decoded choices). This is clearly observed in participants P03 (Table S2.3) to P07 (Table S2.7). Choices in **green** indicate a *successful* completion of the (four-level) navigation round, while choices in **red** indicate an *unsuccessful* completion of the navigation round.

Table S2.1. Encoded and decoded choices for P01

	Encoded *(based on real-time experiment)*		**Decoded** *(based on offline analysis)*	
	Name	*choice #*	*Name*	*choice #*
Run 1	Music	1	Photo	4
Run 2	Error	1	Error	1
Run 3	Music	1	Music	1
Run 4	Jazz	3	Classical	1
Run 5	Error	2	Error	2
Run 6	Jazz	3	Jazz	3
Run 7	Nina Simone	4	Nina Simone	4
Run 8	I put a spell on you	1	**I put a spell on you**	1

Note: due to a technical mistake, the choice order of Jazz artists presented to P01 was different than for the rest of the participants

Table S2.2. Encoded and decoded choices for P02

	Encoded *(based on real-time experiment)*		**Decoded** *(based on offline analysis)*	
	Name	*choice #*	*Name*	*choice #*
Run 1	Photo	4	Photo	4
Run 2	Pets	6	Pets	6
Run 3	Album 1	3	Album 1	3
Run 4	Picture 5	1	**Picture 5**	1
Run 5	Other	6	Other	6
Run 6	Room Control	1	Room Control	1
Run 7	Bed	6	Bed	6
Run 8	Move Up	2	**Move Up**	2

Table S2.3. Encoded and decoded choices for P03

	Encoded *(based on real-time experiment)*		**Decoded** *(based on offline analysis)*	
	Name	*choice #*	*Name*	*choice #*
Run 1	TV	2	TV	2
Run 2	Movie	1	Movie	1
Run 3	Action	4	Error	1
Run 4	Error	4	Series/News	4
Run 5	Action	4	Game Show	4
Run 6	Terminator	5	**First Date**	5
Run 7	Read	3	Other	6
Run 8	Error	2	Internet	5

Table S2.4. Encoded and decoded choices for P04

	Encoded *(based on real-time experiment)*		**Decoded** *(based on offline analysis)*	
	Name	*choice #*	*Name*	*choice #*
Run 1	TV	2	TV	2
Run 2	Series/News	4	Movies	1
Run 3	Error	1	Sci-Fi	2
Run 4	Series/News	4	**The martian**	5
Run 5	Comedy	3	Read	3
Run 6	The good place	6	Comic	1
Run 7	Music	1	Superhero	1
Run 8	Rock	2	**Capt. America**	5

Table S2.5. Encoded and decoded choices for P05

	Encoded *(based on real-time experiment)*		**Decoded** *(based on offline analysis)*	
	Name	*choice #*	*Name*	*choice #*
Run 1	Photo	4	Photo	4
Run 2	Error	6	Error	1
Run 3	Error	2	Music	1
Run 4	Albeniz	1	Classical	1
Run 5	Cordoba	3	Mozart	3
Run 6	TV	2	**Magic Flute**	2
Run 7	Series	4	Photo	4
Run 8	Children	6	Pets	6

Table S2.6. Encoded and decoded choices for P06

	Encoded *(based on real-time experiment)*		**Decoded** *(based on offline analysis)*	
	Name	*choice #*	*Name*	*choice #*
Run 1	Music	1	Music	1
Run 2	Hip-Hop	5	Hip-hop	5
Run 3	Error	2	Error	2
Run 4	Error	5	Hip-hop	5
Run 5	Error	2	Jay-Z	3
Run 6	Error	5	**King´s Dead**	6
Run 7	Error	2	TV	2
Run 8	Hip-Hop	5	Documentaries	2

Table S2.7. Encoded and decoded choices for P07

	Encoded *(based on real-time experiment)*		**Decoded** *(based on offline analysis)*	
	Name	*choice #*	*Name*	*choice #*
Run 1	Radio	5	Radio	5
Run 2	Spain	2	Spain	2
Run 3	Error	4	Error	4
Run 4	Error	6	Germany	6
Run 5	Music	1	**FM1**	1
Run 6	Rock	2	Program 5	5
Run 7	Error	2	TV	2
Run 8	Error	5	Shows/News	5

Table S2.8. Encoded and decoded choices for P08

	Encoded		Decoded	
	Name	*choice #*	*Name*	*choice #*
Run 1	Music	1	Music	1
Run 2	Jazz	3	Jazz	3
Run 3	Louis Armstrong	4	Louis Armstrong	4
Run 4	Let´s do it	3	**Blue Skies**	1
Run 5	Read	3	Read	3
Run 6	Magazine	5	Poetry	3
Run 7	Error	5	Emily Dickinson	3
Run 8	Error	3	Error	1

Table S2.9. Encoded and decoded choices for P09

	Encoded		Decoded	
	Name	*choice #*	*Name*	*choice #*
Run 1	TV	2	Radio	5
Run 2	Error	5	Error	5
Run 3	TV	2	TV	2
Run 4	Movies	1	Movies	1
Run 5	Sci-Fi	2	Sci-Fi	2
Run 6	Star Wars	3	**Star Wars**	3
Run 7	Photo	4	Photo	4
Run 8	Pets	6	Pets	6

Table S2.10. Encoded and decoded choices for P10

	Encoded		Decoded	
	Name	*choice #*	*Name*	*choice #*
Run 1	Music	1	Music	1
Run 2	Classical	1	Classical	1
Run 3	Chopin	6	Chopin	6
Run 4	Requiem	1	**Requiem**	1
Run 5	TV	2	TV	2
Run 6	Movies	1	Movies	1
Run 7	Sci-Fi	2	Sci-Fi	2
Run 8	The martian	5	Interstellar	1

Table S2.11. Encoded and decoded choices for P11

	Encoded		Decoded	
	Name	*choice #*	*Name*	*choice #*
Run 1	Photo	4	Photo	4
Run 2	Pets	6	Pets	6
Run 3	Album 2	2	Album 2	2
Run 4	Picture 1	1	**Picture 1**	1
Run 5	Read	3	Read	3
Run 6	Poetry	3	Poetry	3
Run 7	Pablo Neruda	1	Pablo Neruda	1
Run 8	Die Slowly	5	**Die Slowly**	5

Table S2.12. Encoded and decoded choices for P12

	Encoded		Decoded	
	Name	*choice #*	*Name*	*choice #*
Run 1	Photo	4	Other	6
Run 2	Error	2	Error	2
Run 3	Photo	4	Music	1
Run 4	Error	6	Error	6
Run 5	Photo	4	Photo	4
Run 6	Pets	6	Pets	6
Run 7	Album 3	3	Error	6
Run 8	Error	1	Trips I	2

6.2 Choices presented to participants

Participants were presented with the same set of choices, which can be viewed here (select Data Sheet 2).

7 References

Aarabi, A., and Huppert, T.J. (2016). Characterization of the relative contributions from systemic physiological noise to whole-brain resting-state functional near-infrared spectroscopy data using single-channel independent component analysis. *Neurophotonics* 3(2)**,** 025004-025004. doi: 10.1117/1.NPh.3.2.025004.

Abdalmalak, A., Milej, D., Diop, M., Naci, L., Owen, A., and St. Lawrence, K. (2016). Assessing the feasibility of time-resolved fNIRS to detect brain activity during motor imagery. *Conference: SPIE Photonics West: BiOS* 9690. doi: 10.1117/12.2209587.

Afergan, D., Hincks, S.W., Shibata, T., and Jacob, R.J.K. (2015). Phylter: A System for Modulating Notifications in Wearables Using Physiological Sensing. *Foundations of Augmented Cognition: 9th International Conference, AC* doi: 10.1007/978-3-319-20816-9_17.

Allison, B., Dunne, S., Leeb, R., Millán, J.D.R., and Nijholt, A. (2012). *Towards Practical Brain-Computer Interfaces; Bridging the Gap from Research to Real-World Applications.* Springer.

Bardin, J.C., Fins, J.J., Katz, D.I., Hersh, J., Heier, L.A., Tabelow, K., et al. (2011). Dissociations between behavioural and functional magnetic resonance imaging-based evaluations of cognitive function after brain injury. *Brain : a journal of neurology* 134(Pt 3)**,** 769-782. doi: 10.1093/brain/awr005.

Batula, A.M., Ayaz, H., and Kim, Y.E. (2014). Evaluating a four-class motor-imagery-based optical brain-computer interface. *Conf Proc IEEE Eng Med Biol Soc* 2014**,** 2000-2003. doi: 10.1109/embc.2014.6944007.

Batula, A.M., Mark, J.A., Kim, Y.E., and Ayaz, H. (2017). Comparison of Brain Activation during Motor Imagery and Motor Movement Using fNIRS. *Computational intelligence and neuroscience* 2017**,** 5491296-5491296. doi: 10.1155/2017/5491296.

Bauernfeind, G., Scherer, R., Pfurtscheller, G., and Neuper, C. (2011). Single-trial classification of antagonistic oxyhemoglobin responses during mental arithmetic. *Medical & Biological Engineering & Computing* 49(9)**,** 979. doi: 10.1007/s11517-011-0792-5.

Birbaumer, N., Ghanayim, N., Hinterberger, T., Iversen, I., Kotchoubey, B., Kübler, A., et al. (1999). A spelling device for the paralysed. *Nature* 398(6725)**,** 297-298. doi: 10.1038/18581.

Blum, T., Stauder, R., Euler, E., and Navab, N. (2012). Superman-like X-ray vision: Towards brain-computer interfaces for medical augmented reality. *IEEE International Symposium on Mixed and Augmented Reality (ISMAR)***,** 271-272. doi: 10.1109/ISMAR.2012.6402569.

Boas, D.A., Dale, A.M., and Franceschini, M.A. (2004). Diffuse optical imaging of brain activation: approaches to optimizing image sensitivity, resolution, and accuracy. *NeuroImage* 23**,** S275-S288. doi: https://doi.org/10.1016/j.neuroimage.2004.07.011.

Borges, L., Martins, F., Naves, E., Freire, T., and Lucena Jr, V. (2016). Multimodal System for Training at Distance in a Virtual or Augmented Reality Environment for Users of Electric-Powered Wheelchairs. *IFAC-PapersOnLine* 49**,** 156-160. doi: 10.1016/j.ifacol.2016.11.146.

Brigadoi, S., and Cooper, R.J. (2015). How short is short? Optimum source-detector distance for short-separation channels in functional near-infrared spectroscopy. *Neurophotonics* 2(2)**,** 025005-025005. doi: 10.1117/1.NPh.2.2.025005.

Chavarriaga, R., Sobolewski, A., and Millán, J.D.R. (2014). Errare machinale est: the use of error-related potentials in brain-machine interfaces. *Frontiers in neuroscience* 8**,** 208-208. doi: 10.3389/fnins.2014.00208.

Chin, Z.Y., Ang, K.K., Wang, C., and Guan, C. (Year). "Online performance evaluation of motor imagery BCI with augmented-reality virtual hand feedback", in: *2010 Annual International Conference of the IEEE Engineering in Medicine and Biology*), 3341-3344.

Cui, X., Bray, S., Bryant, D.M., Glover, G.H., and Reiss, A.L. (2011). A quantitative comparison of NIRS and fMRI across multiple cognitive tasks. *NeuroImage* 54(4)**,** 2808-2821. doi: 10.1016/j.neuroimage.2010.10.069.

Cui, X., Bray, S., and Reiss, A.L. (2010). Speeded Near Infrared Spectroscopy (NIRS) Response Detection. *PLOS ONE* 5(11)**,** e15474. doi: 10.1371/journal.pone.0015474.

Duvernoy, H.M., Delon, S., and Vannson, J.L. (1981). Cortical blood vessels of the human brain. *Brain Research Bulletin* 7(5)**,** 519-579. doi: https://doi.org/10.1016/0361-9230(81)90007-1.

Erdogan, S.B., Özsarfati, E., Dilek, B., Soğukkanlı Kadak, K., Hanoğlu, L., and Akin, A. (2019). Classification of motor imagery and execution signals with population-level feature sets: Implications for probe design in fNIRS based BCI. *Journal of Neural Engineering* 16. doi: 10.1088/1741-2552/aafdca.

Erdoğan, S.B., Yücel, M.A., and Akın, A. (2014). Analysis of task-evoked systemic interference in fNIRS measurements: Insights from fMRI. *NeuroImage* 87**,** 490-504. doi: https://doi.org/10.1016/j.neuroimage.2013.10.024.

Essenpreis, M., Cope, M., Elwell, C.E., Arridge, S.R., van der Zee, P., and Delpy, D.T. (1993). "Wavelength Dependence of the Differential Pathlength Factor and the Log Slope in Time-Resolved Tissue Spectroscopy," in *Optical Imaging of Brain Function and Metabolism*, eds. U. Dirnagl, A. Villringer & K.M. Einhäupl. (Boston, MA: Springer US), 9-20.

Faller, J., Allison, B., Brunner, C., Scherer, R., Schmalstieg, D., Pfurtscheller, G., et al. (2017). A feasibility study on SSVEP-based interaction with motivating and immersive virtual and augmented reality.

Faller, J., Leeb, R., Pfurtscheller, G., and Scherer, R. (2010). Avatar navigation in virtual and augmented reality environments using an SSVEP BCI. *Proceedings of the 1st International Conference on Apllied Bionics and Biomechanics (ICABB)***,** 1-4.

Gagnon, L., Cooper, R.J., Yücel, M.A., Perdue, K.L., Greve, D.N., and Boas, D.A. (2012). Short separation channel location impacts the performance of short channel regression in NIRS. *NeuroImage* 59(3)**,** 2518-2528. doi: 10.1016/j.neuroimage.2011.08.095.

Galan, F., Nuttin, M., Lew, E., W. Ferrez, P., Vanacker, G., Philips, J., et al. (2008). A Brain-Actuated Wheelchair: Asynchronous and Non-Invasive Brain-Computer Interfaces for Continuous Control of Robots. *Clinical Neurophysiology* 119. doi: 10.1016/j.clinph.2008.06.001.

Goodwin, J.R., Gaudet, C.R., and Berger, A.J. (2014). Short-channel functional near-infrared spectroscopy regressions improve when source-detector separation is reduced. *Neurophotonics* 1(1)**,** 015002-015002. doi: 10.1117/1.NPh.1.1.015002.

Herff, C., Heger, D., Putze, F., Hennrich, J., Fortmann, O., and Schultz, T. (2013). Classification of

mental tasks in the prefrontal cortex using fNIRS. *Conference proceedings : IEEE Engineering in Medicine and Biology Society* 2013**,** 2160-2163. doi: 10.1109/EMBC.2013.6609962.

Hocke, M.L., Oni, K.I., Duszynski, C.C., Corrigan, V.A., Frederick, D.B., and Dunn, F.J. (2018). Automated Processing of fNIRS Data—A Visual Guide to the Pitfalls and Consequences. *Algorithms* 11(5). doi: 10.3390/a11050067.

Hong, K.-S., Khan, M.J., and Hong, M.J. (2018). Feature Extraction and Classification Methods for Hybrid fNIRS-EEG Brain-Computer Interfaces. *Frontiers in Human Neuroscience* 12**,** 246.

Hong, K.-S., and Naseer, N. (2016). Reduction of Delay in Detecting Initial Dips from Functional Near-Infrared Spectroscopy Signals Using Vector-Based Phase Analysis. *International Journal of Neural Systems* 26(03)**,** 1650012. doi: 10.1142/S012906571650012X.

Hong, K.-S., Naseer, N., and Kim, Y.-H. (2015). Classification of prefrontal and motor cortex signals for three-class fNIRS–BCI. *Neuroscience Letters* 587**,** 87-92. doi: https://doi.org/10.1016/j.neulet.2014.12.029.

Hong, K.-S., and Santosa, H. (2016). Decoding four different sound-categories in the auditory cortex using functional near-infrared spectroscopy. *Hearing Research* 333. doi: 10.1016/j.heares.2016.01.009.

Hu, X.-S., Hong, K.-S., and Ge, S.S. (2013). Reduction of trial-to-trial variability in functional near-infrared spectroscopy signals by accounting for resting-state functional connectivity. *Journal of Biomedical Optics* 18(1)**,** 1-10, 10.

Hu, X.-S., Nascimento, T.D., Bender, M.C., Hall, T., Petty, S., O'Malley, S., et al. (2019). Feasibility of a Real-Time Clinical Augmented Reality and Artificial Intelligence Framework for Pain Detection and Localization From the Brain. *J Med Internet Res* 21(6)**,** e13594. doi: 10.2196/13594.

Huppert, T.J. (2016). Commentary on the statistical properties of noise and its implication on general linear models in functional near-infrared spectroscopy. *Neurophotonics* 3(1)**,** 010401-010401. doi: 10.1117/1.NPh.3.1.010401.

Hwang, H.-J., Choi, H., Kim, J.-Y., Chang, W.-D., Kim, D.-W., Kim, K., et al. (2016). Toward more intuitive brain–computer interfacing: classification of binary covert intentions using functional near-infrared spectroscopy. *Journal of Biomedical Optics* 21(9)**,** 091303.

Iturrate, I., Antelis, J., Kübler, A., and Minguez, J. (2009). A Noninvasive Brain-Actuated Wheelchair Based on a P300 Neurophysiological Protocol and Automated Navigation. *Robotics, IEEE Transactions on* 25**,** 614-627. doi: 10.1109/TRO.2009.2020347.

Kansaku, K., Hata, N., and Takano, K. (2010). My thoughts through a robot's eyes: an augmented reality-brain-machine interface. *Neurosci Res* 66(2)**,** 219-222. doi: 10.1016/j.neures.2009.10.006.

Khan, M.J., and Hong, K.-S. (2017). Hybrid EEG–fNIRS-Based Eight-Command Decoding for BCI: Application to Quadcopter Control. *Frontiers in Neurorobotics* 11**,** 6.

Kirilina, E., Jelzow, A., Heine, A., Niessing, M., Wabnitz, H., Brühl, R., et al. (2012). The physiological origin of task-evoked systemic artefacts in functional near infrared spectroscopy. *NeuroImage* 61(1)**,** 70-81. doi: 10.1016/j.neuroimage.2012.02.074.

Klein, F., and Kranczioch, C. (2019). Signal Processing in fNIRS: A Case for the Removal of Systemic Activity for Single Trial Data. *Frontiers in Human Neuroscience* 13(331). doi: 10.3389/fnhum.2019.00331.

Koo, B., Lee, H.-G., Nam, Y., Kang, H., Koh, C.S., Shin, H.-C., et al. (2015). A hybrid NIRS-EEG system for self-paced brain computer interface with online motor imagery. *Journal of Neuroscience Methods* 244**,** 26-32. doi: https://doi.org/10.1016/j.jneumeth.2014.04.016.

Kübler, A., Holz, E.M., Riccio, A., Zickler, C., Kaufmann, T., Kleih, S.C., et al. (2014). The User-Centered Design as Novel Perspective for Evaluating the Usability of BCI-Controlled Applications. *PLOS ONE* 9(12)**,** e112392. doi: 10.1371/journal.pone.0112392.

Lapborisuth, P., Zhang, X., Noah, A., and Hirsch, J. (2017). Neurofeedback-based functional near-infrared spectroscopy upregulates motor cortex activity in imagined motor tasks. *Neurophotonics* 4(2)**,** 021107-021107. doi: 10.1117/1.NPh.4.2.021107.

Lécuyer, A., Lotte, F., Reilly, R.B., Leeb, R., Hirose, M., and Slater, M. (2008). Brain-Computer Interfaces, Virtual Reality, and Videogames. *Computer* 41.

Leeb, R., Friedman, D., Müller-Putz, G.R., Scherer, R., Slater, M., and Pfurtscheller, G. (2007). Self-paced (asynchronous) BCI control of a wheelchair in virtual environments: a case study with a tetraplegic. *Computational intelligence and neuroscience* 2007**,** 79642-79642. doi: 10.1155/2007/79642.

Lenhardt, A., and Ritter, H. (Year). "An Augmented-Reality Based Brain-Computer Interface for Robot Control", in: *Neural Information Processing. Models and Applications*, eds. K.W. Wong, B.S.U. Mendis & A. Bouzerdoum: Springer Berlin Heidelberg), 58-65.

Liberati, G., Pizzimenti, A., Simione, L., Riccio, A., Schettini, F., Inghilleri, M., et al. (2015). Developing brain-computer interfaces from a user-centered perspective: Assessing the needs of persons with amyotrophic lateral sclerosis, caregivers, and professionals. *Applied Ergonomics* 50**,** 139-146. doi: https://doi.org/10.1016/j.apergo.2015.03.012.

Liu, X., Kim, C.-S., and Hong, K.-S. (2018). An fNIRS-based investigation of visual merchandising displays for fashion stores. *PLOS ONE* 13(12)**,** e0208843. doi: 10.1371/journal.pone.0208843.

Lloyd-Fox, S., Blasi, A., and Elwell, C.E. (2010). Illuminating the developing brain: The past, present and future of functional near infrared spectroscopy. *Neuroscience & Biobehavioral Reviews* 34(3)**,** 269-284. doi: https://doi.org/10.1016/j.neubiorev.2009.07.008.

Lührs, M., and Goebel, R. (2017). Turbo-Satori: a neurofeedback and brain-computer interface toolbox for real-time functional near-infrared spectroscopy. *Neurophotonics* 4(4)**,** 041504-041504. doi: 10.1117/1.NPh.4.4.041504.

Lührs, M., Riemenschneider, B., Eck, J., Andonegui, A.B., Poser, B.A., Heinecke, A., et al. (2019). The potential of MR-Encephalography for BCI/Neurofeedback applications with high temporal resolution. *NeuroImage* 194**,** 228-243. doi: https://doi.org/10.1016/j.neuroimage.2019.03.046.

Mattout, J., Perrin, M., Bertrand, O., and Maby, E. (2015). Improving BCI performance through co-adaptation: Applications to the P300-speller. *Annals of Physical and Rehabilitation Medicine* 58. doi: 10.1016/j.rehab.2014.10.006.

McKendrick, R., Parasuraman, R., Murtza, R., Formwalt, A., Baccus, W., Paczynski, M., et al. (2016).

Into the Wild: Neuroergonomic Differentiation of Hand-Held and Augmented Reality Wearable Displays during Outdoor Navigation with Functional Near Infrared Spectroscopy. *Frontiers in Human Neuroscience* 10(216). doi: 10.3389/fnhum.2016.00216.

Menon, R.S., and Kim, S.-G. (1999). Spatial and temporal limits in cognitive neuroimaging with fMRI. *Trends in Cognitive Sciences* 3(6)**,** 207-216. doi: https://doi.org/10.1016/S1364-6613(99)01329-7.

Mercier-Ganady, J., Lotte, F., Loup-Escande, E., Marchal, M., and Lécuyer, A. (2014). The Mind-Mirror: See your brain in action in your head using EEG and augmented reality. *IEEE Virtual Reality (VR)***,** 33-38. doi: 10.1109/VR.2014.6802047.

Mihara, M., Miyai, I., Hattori, N., Hatakenaka, M., Yagura, H., Kawano, T., et al. (2012). Neurofeedback Using Real-Time Near-Infrared Spectroscopy Enhances Motor Imagery Related Cortical Activation. *PLOS ONE* 7(3)**,** e32234. doi: 10.1371/journal.pone.0032234.

Monti, M.M., Vanhaudenhuyse, A., Coleman, M.R., Boly, M., Pickard, J.D., Tshibanda, L., et al. (2010). Willful Modulation of Brain Activity in Disorders of Consciousness. *New England Journal of Medicine* 362(7)**,** 579-589. doi: 10.1056/NEJMoa0905370.

Muller-Putz, G.R., and Pfurtscheller, G. (2008). Control of an Electrical Prosthesis With an SSVEP-Based BCI. *IEEE Transactions on Biomedical Engineering* 55(1)**,** 361-364. doi: 10.1109/TBME.2007.897815.

Murphy, D.P., Bai, O., Gorgey, A.S., Fox, J., Lovegreen, W.T., Burkhardt, B.W., et al. (2017). Electroencephalogram-Based Brain-Computer Interface and Lower-Limb Prosthesis Control: A Case Study. *Frontiers in neurology* 8**,** 696-696. doi: 10.3389/fneur.2017.00696.

Nagels-Coune, L., Kurban, D., Reuter, N., Benitez, A., Gossé, L., Riecke, L., et al. (2017). Yes or no? binary brain-based communication utilizing motor imagery and fNIRS. *Proceedings of the 7th Graz Brain-Computer Interface*. doi: 10.3217/978-3-85125-533-1-65.

Naseer, N., and Hong, K.-S. (2013). Classification of functional near-infrared spectroscopy signals corresponding to the right- and left-wrist motor imagery for development of a brain–computer interface. *Neuroscience Letters* 553**,** 84-89. doi: https://doi.org/10.1016/j.neulet.2013.08.021.

Naseer, N., and Hong, K.-S. (2015a). fNIRS-based brain-computer interfaces: a review. *Frontiers in human neuroscience* 9**,** 3-3. doi: 10.3389/fnhum.2015.00003.

Naseer, N., and Hong, K.-S. (2015b). Decoding Answers to Four-Choice Questions Using Functional near Infrared Spectroscopy. *Journal of Near Infrared Spectroscopy* 23(1)**,** 23-31. doi: 10.1255/jnirs.1145.

Nguyen, H.-D., Yoo, S.-H., Bhutta, M.R., and Hong, K.-S. (2018). Adaptive filtering of physiological noises in fNIRS data. *BioMedical Engineering OnLine* 17(1)**,** 180. doi: 10.1186/s12938-018-0613-2.

Nijboer, F. (2015). Technology transfer of brain-computer interfaces as assistive technology: Barriers and opportunities. *Annals of Physical and Rehabilitation Medicine* 58(1)**,** 35-38. doi: https://doi.org/10.1016/j.rehab.2014.11.001.

Nijboer, F., Sellers, E.W., Mellinger, J., Jordan, M.A., Matuz, T., Furdea, A., et al. (2008). A P300-based brain-computer interface for people with amyotrophic lateral sclerosis. *Clinical neurophysiology*

: official journal of the International Federation of Clinical Neurophysiology 119(8)**,** 1909-1916. doi: 10.1016/j.clinph.2008.03.034.

Noori, F.M., Naseer, N., Qureshi, N.K., Nazeer, H., and Khan, R.A. (2017). Optimal feature selection from fNIRS signals using genetic algorithms for BCI. *Neuroscience Letters* 647**,** 61-66. doi: https://doi.org/10.1016/j.neulet.2017.03.013.

Norman, K.A., Polyn, S.M., Detre, G.J., and Haxby, J.V. (2006). Beyond mind-reading: multi-voxel pattern analysis of fMRI data. *Trends in Cognitive Sciences* 10(9)**,** 424-430. doi: https://doi.org/10.1016/j.tics.2006.07.005.

Park, S., Cha, H., and Im, C. (2019). Development of an Online Home Appliance Control System Using Augmented Reality and an SSVEP-Based Brain–Computer Interface. *IEEE Access* 7**,** 163604-163614. doi: 10.1109/ACCESS.2019.2952613.

Pinti, P., Scholkmann, F., Hamilton, A., Burgess, P., and Tachtsidis, I. (2019). Current Status and Issues Regarding Pre-processing of fNIRS Neuroimaging Data: An Investigation of Diverse Signal Filtering Methods Within a General Linear Model Framework. *Frontiers in Human Neuroscience* 12(505). doi: 10.3389/fnhum.2018.00505.

Prince, S., Kolehmainen, V., Kaipio, J.P., Franceschini, M.A., Boas, D., and Arridge, S.R. (2003). Time-series estimation of biological factors in optical diffusion tomography. *Physics in Medicine and Biology* 48(11)**,** 1491-1504. doi: 10.1088/0031-9155/48/11/301.

Rebsamen, B., Guan, C., Zhang, H., Wang, C., Teo, C., Jr, M., et al. (2011). A Brain Controlled Wheelchair to Navigate in Familiar Environments. *Neural Systems and Rehabilitation Engineering, IEEE Transactions on* 18**,** 590-598. doi: 10.1109/TNSRE.2010.2049862.

Rezazadeh Sereshkeh, A., Yousefi, R., Wong, A.T., and Chau, T. (2018). Online classification of imagined speech using functional near-infrared spectroscopy signals. *Journal of Neural Engineering* 16(1)**,** 016005. doi: 10.1088/1741-2552/aae4b9.

Saager, R.B., and Berger, A.J. (2005). Direct characterization and removal of interfering absorption trends in two-layer turbid media. *Journal of the Optical Society of America A* 22(9)**,** 1874-1882. doi: 10.1364/JOSAA.22.001874.

Saager, R.B., Telleri, N.L., and Berger, A.J. (2011). Two-detector Corrected Near Infrared Spectroscopy (C-NIRS) detects hemodynamic activation responses more robustly than single-detector NIRS. *NeuroImage* 55(4)**,** 1679-1685. doi: https://doi.org/10.1016/j.neuroimage.2011.01.043.

Sato, T., Nambu, I., Takeda, K., Aihara, T., Yamashita, O., Isogaya, Y., et al. (2016). Reduction of global interference of scalp-hemodynamics in functional near-infrared spectroscopy using short distance probes. *NeuroImage* 141**,** 120-132. doi: https://doi.org/10.1016/j.neuroimage.2016.06.054.

Scarapicchia, V., Brown, C., Mayo, C., and Gawryluk, J.R. (2017). Functional Magnetic Resonance Imaging and Functional Near-Infrared Spectroscopy: Insights from Combined Recording Studies. *Frontiers in human neuroscience* 11**,** 419-419. doi: 10.3389/fnhum.2017.00419.

Scharnowski, F., Hutton, C., Josephs, O., Weiskopf, N., and Rees, G. (2012). Improving visual perception through neurofeedback. *The Journal of neuroscience : the official journal of the Society for Neuroscience* 32(49)**,** 17830-17841. doi: 10.1523/JNEUROSCI.6334-11.2012.

Sellers, E.W., Vaughan, T.M., and Wolpaw, J.R. (2010). A brain-computer interface for long-term independent home use. *Amyotrophic Lateral Sclerosis* 11(5)**,** 449-455. doi: 10.3109/17482961003777470.

Shereena, E.A., Gupta, R.K., Bennett, C.N., Sagar, K.J.V., and Rajeswaran, J. (2018). EEG Neurofeedback Training in Children With Attention Deficit/Hyperactivity Disorder: A Cognitive and Behavioral Outcome Study. *Clinical EEG and Neuroscience* 50(4)**,** 242-255. doi: 10.1177/1550059418813034.

Shin, J., and Jeong, J. (2014). Multiclass classification of hemodynamic responses for performance improvement of functional near-infrared spectroscopy-based brain–computer interface. *Journal of Biomedical Optics* 19(6)**,** 1-9, 9.

Shin, J., Kwon, J., Choi, J., and Im, C.-H. (2017). Performance enhancement of a brain-computer interface using high-density multi-distance NIRS. *Scientific Reports* 7(1)**,** 16545. doi: 10.1038/s41598-017-16639-0.

Si-Mohammed, H., Argelaguet, F., Casiez, G., Roussel, N., and Lécuyer, A. (2017). Brain-Computer Interfaces and Augmented Reality: a State of the Art. *Proceedings of the 7th Graz Brain-Computer Interface*.

Si-Mohammed, H., Petit, J., Jeunet, C., Argelaguet, F., Spindler, F., Évain, A., et al. (2018). Towards BCI-based Interfaces for Augmented Reality: Feasibility, Design and Evaluation. *IEEE Transactions on Visualization and Computer Graphics***,** 1-1. doi: 10.1109/TVCG.2018.2873737.

Sorger, B., Dahmen, B., Reithler, J., Gosseries, O., Maudoux, A., Laureys, S., et al. (2009). Another kind of 'BOLD Response': answering multiple-choice questions via online decoded single-trial brain signals. *Progress in brain research* 177**,** 275-292. doi: 10.1016/S0079-6123(09)17719-1.

Sorger, B., Reithler, J., Dahmen, B., and Goebel, R. (2012). A Real-Time fMRI-Based Spelling Device Immediately Enabling Robust Motor-Independent Communication. *Current Biology* 22(14)**,** 1333-1338. doi: https://doi.org/10.1016/j.cub.2012.05.022.

Stangl, M., Bauernfeind, G., Kurzmann, J., Scherer, R., and Neuper, C. (2013). A Haemodynamic Brain–Computer Interface Based on Real-Time Classification of near Infrared Spectroscopy Signals during Motor Imagery and Mental Arithmetic. *Journal of Near Infrared Spectroscopy* 21(3)**,** 157-171. doi: 10.1255/jnirs.1048.

Subramanian, L., Hindle, J.V., Johnston, S., Roberts, M.V., Husain, M., Goebel, R., et al. (2011). Real-time functional magnetic resonance imaging neurofeedback for treatment of Parkinson's disease. *The Journal of neuroscience : the official journal of the Society for Neuroscience* 31(45)**,** 16309-16317. doi: 10.1523/JNEUROSCI.3498-11.2011.

Sulzer, J., Haller, S., Scharnowski, F., Weiskopf, N., Birbaumer, N., Blefari, M.L., et al. (2013). Real-time fMRI neurofeedback: progress and challenges. *NeuroImage* 76**,** 386-399. doi: 10.1016/j.neuroimage.2013.03.033.

Suzuki, S., Harashima, F., and Katsuhisa, F. (2010). Human Control Law and Brain Activity of Voluntary Motion by Utilizing a Balancing Task with an Inverted Pendulum. *Advances in Human-Computer Interaction* 2010. doi: 10.1155/2010/215825.

Tachtsidis, I., and Scholkmann, F. (2016). False positives and false negatives in functional near-infrared

spectroscopy: issues, challenges, and the way forward. *Neurophotonics* 3(3)**,** 031405-031405. doi: 10.1117/1.NPh.3.3.031405.

Takano, K., Hata, N., and Kansaku, K. (2011). Towards intelligent environments: an augmented reality-brain-machine interface operated with a see-through head-mount display. *Frontiers in neuroscience* 5**,** 60-60. doi: 10.3389/fnins.2011.00060.

Tong, Y., and Frederick, B.d. (2012). Concurrent fNIRS and fMRI processing allows independent visualization of the propagation of pressure waves and bulk blood flow in the cerebral vasculature. *NeuroImage* 61(4)**,** 1419-1427. doi: 10.1016/j.neuroimage.2012.03.009.

Valente, G., Kaas, A.L., Formisano, E., and Goebel, R. (2019). Optimizing fMRI experimental design for MVPA-based BCI control: Combining the strengths of block and event-related designs. *NeuroImage* 186**,** 369-381. doi: https://doi.org/10.1016/j.neuroimage.2018.10.080.

Weyand, S., and Chau, T. (2015). Correlates of Near-Infrared Spectroscopy Brain–Computer Interface Accuracy in a Multi-Class Personalization Framework. *Frontiers in Human Neuroscience* 9(536). doi: 10.3389/fnhum.2015.00536.

Weyand, S., and Chau, T. (2017). Challenges of implementing a personalized mental task near-infrared spectroscopy brain–computer interface for a non-verbal young adult with motor impairments. *Developmental Neurorehabilitation* 20(2)**,** 99-107. doi: 10.3109/17518423.2015.1087436.

Weyand, S., Schudlo, L., Takehara-Nishiuchi, K., and Chau, T. (2015). Usability and performance-informed selection of personalized mental tasks for an online near-infrared spectroscopy brain-computer interface. *Neurophotonics* 2(2)**,** 1-14, 14.

Wolpaw, J.R., Birbaumer, N., McFarland, D.J., Pfurtscheller, G., and Vaughan, T.M. (2002). Brain–computer interfaces for communication and control. *Clinical Neurophysiology* 113(6)**,** 767-791. doi: https://doi.org/10.1016/S1388-2457(02)00057-3.

Zhang, Y., Brooks, D., Franceschini, M., and Boas, D. (2005). Eigenvector-based spatial filtering for reduction of physiological interference in diffuse optical imaging. *Journal of Biomedical Optics* 10(1)**,** 011014. [5]

In the above reference list, 76.00% of first authors were male (vs. 24.00% that were female), while 81.00% of last authors were male (vs. 19.00% that were female).

8 Data Availability Statement

The raw data supporting the conclusions of this article is readily available on https://dataverse.nl/dataset.xhtml?persistentId=doi:10.34894/DF83FF and the code will be made available by the authors, without undue reservation, to any qualified researcher.

9 Author Contributions

RBu, AB-A, and BS conceived the idea and designed the experiment. RBe and RBu prepared the Unity3D environment. RBe developed the dynamic object control functions. RBu, ML, and AB-A optimized the hardware setup. RBu and AB-A measured pilot participants. BS and AB-A adapted the design based on pilot measurements. AB-A carried out the fNIRS measurements, analyzed the data, and wrote the manuscript. BS, ML, and RM assisted on the interpretation of results and data analysis. AB-A, BS, and ML structured the manuscript. RBu, BS, RM, ML, RM, and RBe revised the manuscript critically.

10 Funding

This research was supported by The Luik 3 grant for joint research between Cognitive Neuroscience and Knowledge Engineering Departments, Maastricht University, on advanced brain-robot interfaces, 2015-2019 (to RM and BS).

11 Conflict of Interest

The authors declare that the research was conducted in the absence of any commercial or financial relationships that could be construed as a potential conflict of interest.

12 Acknowledgments

We would like to thank Giancarlo Valente and Andrew Morgan for their advice on data analysis; to Anita Tursic and Laurien Nagels-Coune for their advice on the experimental setup; the Instrumentation department for their timely assistance; and to all the participants for their time and effort.

3

Guiding functional near-infrared spectroscopy optode-layout design using individual (f)MRI data: Effects on signal quality and sensitivity

Abstract

Designing optode layouts is an essential step for functional near-infrared spectroscopy (fNIRS) experiments as the quality of the measured signal and the sensitivity to cortical regions-of-interest depend on how optodes are arranged on the scalp. This becomes particularly relevant for fNIRS-based brain-computer interfaces (BCIs), where developing robust systems with few optodes is crucial for clinical applications. Available resources often dictate the approach researchers use for optode-layout design. Here we compared four approaches that incrementally incorporated subject-specific magnetic resonance imaging (MRI) information while participants performed mental-calculation, mental-rotation and inner-speech tasks. The literature-based approach (LIT) used a literature review to guide the optode layout design. The probabilistic approach (PROB), employed individual anatomical data and probabilistic maps of functional MRI (fMRI)-activation from an independent dataset. The individual fMRI (iFMRI) approach used individual anatomical and fMRI data, and the fourth approach used individual anatomical, functional and vascular information of the same subject (fVASC). The four approaches resulted in different optode layouts and the more informed approaches outperformed the minimally informed approach (LIT) in terms of signal quality and sensitivity. Further, PROB, iFMRI and fVASC approaches resulted in a similar outcome. We conclude that additional individual MRI data leads to a better outcome, but that not all the modalities tested here are required to achieve a robust setup. Finally, we give preliminary advice to efficiently using resources for developing robust optode layouts for BCI and neurofeedback applications.

Based on: A. Benitez-Andonegui, M. Lührs, L. Nagels-Coune, D. Ivanov, R. Goebel, B. Sorger (2020). Guiding functional near-infrared spectroscopy optode-layout design using individual (f)MRI data: Effects on signal quality and sensitivity. *bioRxiv***,** 2020.2009.2027.315390

1 Introduction

Functional near-infrared spectroscopy (fNIRS) is a non-invasive, portable optical imaging method used to measure brain activity via hemodynamic responses involving increased oxygen consumption and cerebral blood flow (Scholkmann et al., 2014; Scarapicchia et al., 2017; Brigadoi et al., 2018). These physiological changes lead to local changes in the concentrations of oxy- (Δ[HbO]) and deoxy-hemoglobin (Δ[HbR]), which can be detected because near-infrared light is absorbed by hemoglobin located in blood vessels (Scholkmann et al., 2014; Quaresima and Ferrari, 2016).

When setting up an fNIRS experiment, optical sensors ('optodes') are placed on the scalp, which can be classified into sources (emitters) and detectors (receivers). Light emitted from a source is propagated through extracerebral and cerebral tissues up to a few centimeters, where some photons are scattered and absorbed before light reaches the detectors (Machado et al., 2014). The spatial resolution of fNIRS is therefore in the range of 5-10mm (Quaresima and Ferrari, 2016) depending on the way source-detector pairs (or 'channels') are arranged on the scalp (Culver et al., 2001). The distance between a source and detector pair, along with the anatomical tissues between them determines the depth of light penetration and the sensitivity to underlying cortex (Brigadoi et al., 2018). Therefore, the quality of the fNIRS signal can differ dramatically between optode layouts.

This effect of optode layout is particularly relevant for applications requiring sparse optode layouts, such as brain-computer interfaces (BCIs). BCIs provide an alternative means of motor-independent communication for clinical populations suffering from severe motor disabilities (Naseer and Hong, 2015a) by enabling users to send commands via brain activity in the absence of motor output (Wolpaw et al., 2002; Naseer and Hong, 2015a). FNIRS is a promising choice for implementing BCIs due to its portability, safety and relatively low cost (Sorger et al., 2009; Shin et al., 2017). However, it remains a challenging undertaking to develop efficient, accurate and robust systems using the limited number of optodes required for fNIRS-BCI systems to remain portable and comfortable for clinical applications. Indeed, a number of fNIRS-based BCI studies using small optode layouts (Naito et al., 2007; Power et al., 2012; Weyand et al., 2015; Nagels-Coune et al., 2017; Benitez-Andonegui et al., 2020; Nagels-Coune et al., 2020) have reported variability in the number of participants able to reach the minimum accuracy (70% in a two-class BCI) required for practical BCI use

(Kübler et al., 2001). This variability may originate from individual anatomical (Coyle et al., 2005; Allison and Neuper, 2010) or functional differences (Weyand et al., 2015) that affect fNIRS signal quality/sensitivity and therefore might be improved by designing optode layouts for individual users that account for such differences.

Researchers often define a region of interest (ROI) in line with their research question and design an optode layout in a grid-like fashion to target a specific brain area (Brigadoi et al., 2018). The simplest and most common optode-layout design is to assign source and detector locations on the head to cover a given cortical ROI according to the standardized 10-20 electroencephalography (EEG) system or its extended versions (Oostenveld and Praamstra, 2001). These locations can be related to the underlying assumed cortical structure (Koessler et al., 2009; Giacometti et al., 2014) or to the standard Montreal Neurological Institute (MNI) stereotactic coordinates (Okamoto et al., 2004; Jurcak et al., 2007; Tsuzuki et al., 2007; Tsuzuki and Dan, 2014). This procedure has proven effective for many applications but may be suboptimal for use in BCIs. In this study, we were interested in whether incorporating additional neuroimaging data such as anatomical or functional magnetic resonance imaging (MRI or fMRI) can improve optode-layout design for use in BCIs.

The selection of the ROIs in the procedure described above are commonly based on anatomically defined coordinates only. However, ROIs derived from functional neuroimaging techniques such as fMRI could increase the spatial specificity of ROI definition by accounting for individual local differences in elicited brain activity for a given task. Once an ROI is defined, the fNIRS community has developed several approaches to optimize optode-layout designs using light-sensitivity profiles (Brigadoi et al., 2018). Light-sensitivity profiles are probabilistic models of photon absorption based on the tissues found between source and detector optodes (Aasted et al., 2015). Software packages, toolboxes and pipelines compute these profiles using Monte Carlo simulations to optimize optode layouts (Tadel et al., 2011; Machado et al., 2014; Aasted et al., 2015; Wijeakumar et al., 2015; Brigadoi et al., 2018; Zimeo Morais et al., 2018), thus promising an increase on signal quality and sensitivity for BCI applications. However, light sensitivity profile models require anatomical head data, either from an MRI-derived atlas or from subject-specific MRI data. MRI atlases are an appealing option for computing profiles, as they do not require additional MRI measurements, which may be expensive, time-consuming or generally

unavailable. That said, subject-specific MRI data better capture specific anatomical and vascular features and therefore could improve the robustness of fNIRS setups across individuals. Considering subject-specific vascular information may be particularly relevant as vascular structures are highly scattering and absorbing media (Bosschaart et al., 2014) and can influence the estimates of light sensitivity profiles (Perdue et al., 2012).

Naturally, available resources for collecting additional data must dictate the approach researchers use to design optode layouts. We therefore asked the following question: What is the potential gain of incorporating (anatomical, functional, vascular) MRI data when optimizing optode-layout designs for fNIRS-based BCIs? With this question in mind, we selected four approaches that incrementally incorporated the amount of individual information from the same participant to design subject-specific optode layouts. The first layout was the literature-based approach (hereinafter referred to as LIT), where optodes were selected based on a literature review. LIT represents the scenario where no additional individual MRI information is available. The second setup was the probabilistic approach (referred to as PROB), which employed individual anatomical data together with a probabilistic functional map derived from an independent dataset to inform optode placement. PROB illustrates a situation where individual fMRI data is not available, but subject-specific anatomical information and functional data from other individuals is accessible. The third setup was the individual fMRI approach, which used anatomical data and functional activation maps of the same individual (referred to as iFMRI). Finally, the fourth setup was the vascular approach, which used individual anatomical, functional and vascular information of the same subject (referred to as fVASC).

We assessed whether different approaches resulted in distinct optode layouts and assessed whether the quality of the fNIRS signal and the detected task-related activation (fNIRS sensitivity) differed across optode layouts. Participants were asked to perform three mental-imagery tasks commonly used for hemodynamic BCIs: mental-calculation, mental-rotation and inner-speech (see Table S3.3). We designed approach-specific optode layouts using Monte Carlo simulations and an algorithmic procedure that used two main constraints: 1) the inter-optode distance did not exceed the 25-40mm range in order to provide a reasonable signal-to-noise ratio (Mansouri et al., 2010) and 2) the optode layout for each approach consisted of two channels that shared a common source. Importantly, the second constraint

allowed us to compare the four approaches within the same functional fNIRS run. We hypothesized that each approach would lead to different optode-layout designs and that the signal-to-noise ratio of resulting fNIRS signal would improve with more individualized approaches. Our results show that the four approaches indeed result in different optode layouts and that the more individualized approaches (PROB, iFMRI, and fVASC) outperform the minimally informed approach (LIT) in terms of fNIRS signal quality and sensitivity. Further, we find that PROB, iFMRI, and fVASC approaches produce similar signal quality and sensitivity. Finally, we give preliminary recommendations to help researchers efficiently use resources for developing robust and convenient optode layouts for fNIRS-BCIs.

2 Materials and Methods

This experiment consisted of three separate sessions that took place in the following order: one f/MRI session, a neuronavigation session and an fNIRS session. The first two sessions aimed at gathering necessary information for designing optode layouts, while the fNIRS session aimed at acquiring data to assess/compare the designed optode layouts (see Figure 3.1).

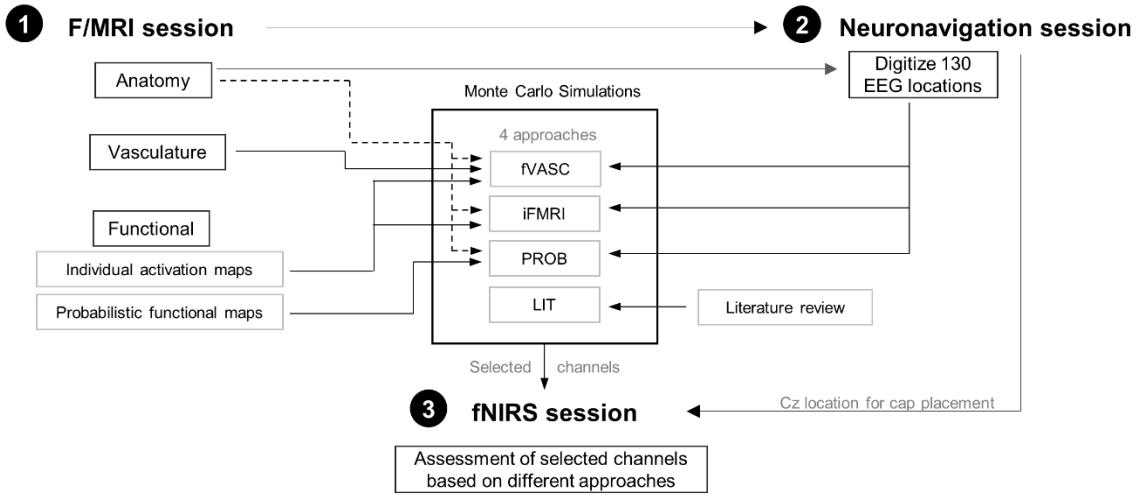

Figure 3.1. Overview of the present study. The study consisted of three separate sessions: one f/MRI, one neuronavigation and one fNIRS session. The first two sessions aimed at collecting necessary information to create the different optode layouts for each participant. Specifically, the LIT approach used a literature review to design the optode layout. The PROB approach used probabilistic functional MRI maps, individual anatomical data and head-anatomy information for channel selection. The iFMRI approach used individual anatomical data and individual functional activation maps, together with head-anatomy information for channel selection. Finally, the fVASC approach used individual anatomical, functional and vascular data, together with head-anatomy information for channel selection. Monte Carlo simulations were used to select the best channel pair for each approach, mental-imagery task and participant. The selected channels were used during the fNIRS session to obtain information on signal quality and to measure functional activity elicited by the mental-imagery tasks.

Twenty-one participants (eleven females) were recruited for the f/MRI session. From these participants, seventeen (eleven females) took part in the neuronavigation session and sixteen (ten females) participated in the fNIRS session (see Table 3.1 for a summary) as some participants became unavailable over the sessions. Participants did not have a history of neurological disease and had a normal or corrected-to-normal vision. The experiment conformed to the Declaration of Helsinki and was approved by the ethics committee of the Faculty of Psychology and Neuroscience, Maastricht University. Informed consent was obtained from each participant before starting the experiment. Participants received financial compensation after each session.

Table 3.1. Summary of participants' characteristics and involvement of different experimental sessions.

Participant ID	f/MRI (N=21)	Neuronavigation (N=17)	fNIRS (N=16)	Gender	Age range	Handedness
P01	YES	YES	YES	Female	25-30	Left
P02	YES	YES	YES	Female	25-30	Right
P03	YES	YES	YES	Male	25-30	Left
P04	YES	YES	YES	Female	25-30	Right
P05	YES	YES	YES	Female	25-30	Right
P06	YES	YES	YES	Female	40-45	Right
P07	YES	**NO**	**NO**	Male	25-30	Right
P08	YES	**NO**	**NO**	Male	30-35	Right
P09	YES	YES	YES	Male	25-30	Right
P10	YES	YES	YES	Female	25-30	Left
P11	YES	YES	YES	Female	25-30	Right
P12	YES	YES	**NO**	Female	25-30	Right
P13	YES	**NO**	**NO**	Male	20-25	Right
P14	YES	YES	YES	Male	30-35	Right
P15	YES	YES	YES	Male	30-35	Right
P16	YES	YES	YES	Male	25-30	Right
P17	YES	YES	YES	Female	20-25	Right
P18	YES	**NO**	**NO**	Male	25-30	Right
P19	YES	YES	YES	Female	20-25	Left
P20	YES	YES	YES	Female	20-25	Right
P21	YES	YES	YES	Female	25-30	Right

2.1 f/MRI session

2.1.1 Data acquisition

In this one-hour long session, anatomical, functional and (brain- and scalp) vascular data were acquired at a Siemens Magnetom Prisma Fit 3 Tesla (T) scanner at the *Maastricht Brain Imaging Center*, Maastricht, The Netherlands (see Figure 3.2).

We used a magnetization prepared-rapid gradient echo (MPRAGE) sequence to collect structural T1-weighted MRI data, with the following parameters: repetition time (TR)=2250ms, echo time (TE)=2.21ms, inversion time (TI)=900ms, flip angle (FA)=9°,

number of slices=192, 1-mm isotropic resolution, duration=5:05min. 2D Gradient Echo echo-planar imaging sequence with a TR=1s, number of slices=36, and 3-mm isotropic resolution was used to acquire functional data. Cerebral and pial vascular data was collected using 2D- and 3D- Time-of-Flight (TOF) sequences (FA=60º/18º, TR=21ms/20ms, TE=4.83/3.3ms, number of slabs=1/5, number of slices in slab=75/40, with distance factor=-33/-20%, 0.7-mm isotropic resolution, duration=9:11/4:56min). Finally, scalp-vascular data was obtained with a Multi-Echo Gradient Echo (GE) sequence with four different echoes (TR=34ms, $TE_1/TE_2/TE_3/TE_4$=3.02/8.56/15.11/23.91ms, number of slices=192, 0.7-mm isotropic resolution, duration= 8:06min).

2.1.2 Experimental design

Participants performed one ~13-min long functional run, where they were acoustically cued to rest ("Rest") or perform one of the three mental-imagery tasks, namely inner- (covert) speech ("Speech"), mental-calculation ("Calculate") or mental-rotation ("Rotate"). The order of the task trials (eight per mental task) was randomized. They were instructed to covertly recite a text they knew by heart (*e.g.*, a poem) when they heard "Speech". Participants were asked to calculate multiplication tables of multiples of 7, 8, or 9 up to the decuple when they heard "Calculate". When they heard "Rotate", participants had to imagine a diver jumping from a tower into the water while he spins around several times in the air. Participants were trained on the tasks for approximately 10min before entering the MRI scanner. During training, they had to recite overtly the chosen text and the multiplication tables for the inner-speech and mental-calculation tasks, respectively to ensure the speed was consistent, and to repeat the same procedure covertly until they felt comfortable with the tasks. As for the mental-rotation task, participants watched short clips of a jumping diver until they could comfortably imagine the movement. We instructed participants to perform the mental-imagery tasks, which lasted 10s, until they heard the instruction "Rest". During resting period, participants were requested not to do any specific mental activity and not to do/think about anything in particular for 20s (see Figure 3.2 for a visualization of the run). Participants were asked to keep their eyes closed throughout the functional run. After the session, participants' strategies were noted down and saved for the fNIRS session. BrainStim v1.1.0.1 stimuli presentation software (Gijsen, S., Maastricht University, The Netherlands) was used for both, the f/MRI and fNIRS sessions.

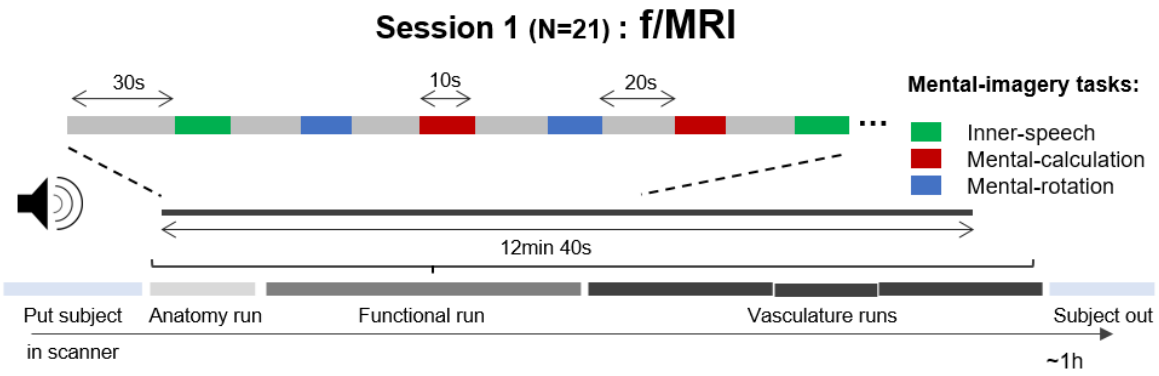

Figure 3.2. Schematic representation of session 1. Twenty-one participants underwent a one-hour long experiment in the MRI scanner, during which individual anatomical, functional and vascular data were collected. During the functional run, participants had to perform inner-speech, mental-calculation or mental-rotation for 10s each with interleaved resting periods of 20s. Task order was randomized.

2.1.3 Data analysis

Unless stated otherwise, all f/MRI data analyses were performed in BrainVoyager QX v2.8 (Brain Innovation B.V., Maastricht, Netherlands).

2.1.3.1 Structural data

Structural images were aligned to the plane containing the anterior and posterior commissures, corrected for spatial-intensity inhomogeneities and brain-masked. The white/grey matter (WM/GM) and grey matter/cerebrospinal (GM/CSF) boundaries were detected using automatic segmentation tools. These images were inspected, manually corrected when necessary and used to create WM and GM reconstructions of the cortical surface. In addition, the (head) skin surface was automatically segmented and reconstructed. These reconstructions were used for the neuronavigation session (see below).

Cortex-based alignment (CBA) is a whole-cortex alignment scheme (Fischl et al., 1999; Goebel et al., 2006; Fischl et al., 2007; Frost and Goebel, 2012) which uses curvature information of the cortical surface to iteratively reduce misalignment across participants and in turn increase functional overlap on the group level (Duecker et al., 2014). We used this approach to define our probabilistic functional maps. For that, individual WM reconstructions of each hemisphere were aligned to a dynamically generated group average (N=21).

2.1.3.1.1 Functional data

Data were pre-processed using inter-scan slice-time correction, 3D rigid-body motion correction (applying Trilinear interpolation for detection/sinc interpolation, for correction), and temporal high-pass filtering with a general linear model (GLM) Fourier basis set of 3 cycles/run. Functional data of 3-mm iso-voxel resolution were spatially co-registered to the structural image by using a gradient-based intensity-driven fine-tuning alignment.

2.1.3.1.2 Generation of individual functional maps

We first calculated a voxel-wise GLM. The model contained a separate boxcar predictor for each of the mental-imagery task conditions convolved with a standard double-gamma hemodynamic response function (onset time=0s, response undershoot ratio/time to response peak=6s/6s, time to undershoot peak=16s, response/undershoot dispersion=1s/1s), and six additional predictors estimated from the motion-estimation procedure in BrainVoyager QX (translation and rotation in x, y and z direction). Individual functional maps were created in volume space by contrasting the particular mental-imagery task predictor *vs.* the rest condition (for each of the three tasks separately) in the voxels that were part of the fNIRS-coverage mask. This mask was created to mask out active voxels from deeper regions, as we did not expect the fNIRS signal to be sensitive to these regions (Strangman et al., 2013), see supplementary materials Sec. A.1 and Figure S3.1 for details. Activation maps were corrected using a cluster threshold that allowed for a 5% loss of active voxels. These functional maps were then sampled to surface activation maps (from -1mm to +3mm from the GM/WM segmentation boundary).

2.1.3.1.3 Generation of probabilistic maps

While it is not uncommon for researchers to have previously acquired anatomical MRI data of the same participant (Duecker et al., 2014; Perdue and Diamond, 2014), having individual anatomical *and* functional data of the same participant represents a less likely scenario (Duecker et al., 2014). In the absence of individual functional data, probabilistic functional maps can be generated from other individuals whose functional data are available.

Probabilistic functional maps were created separately for each participant and mental-imagery task following a leave-one-subject-out procedure (Rosenke et al., 2018). For each participant, surface activation maps from the remaining participants were aligned using

individual transformation files derived from the CBA approach. It should be noted that MR *vs.* Rest map from P08 was excluded from subsequent analyses as the participant reported not being able to perform the mental-imagery task correctly and having used an alternative cognitive strategy instead. Thus, the probabilistic maps for each participant were created based on N=20 participants for the IS and MC tasks and based on N=19 participants for the MR task. We discarded mesh vertices that were active in less than 20% of the sample size for each task and hemisphere. The resulting probabilistic maps for each hemisphere were transformed back into individual volume space (by interpolating from -1mm to +3mm from the GM/WM segmentation boundary) and smoothed with a 2mm full-width-half-maximum kernel. The final maps (three per participant) were used as region of interests for Monte Carlo simulations (see Sec. 2.3.2). Examples of probabilistic maps are shown in Fig S2.

2.1.3.2 Vascular data

2.1.3.2.1 Cerebral and Pial vasculature

2D and 3D TOF data were aligned individually to an up-sampled version (0.7-mm isotropic resolution) of the anatomical data of the same session for each participant, following the same co-registration approach as for functional maps described above. Vascular data were segmented with automatic segmentation tools in BrainVoyager QX (intensity-based segmentation) and the software *Segmentator* (intensity gradient-based segmentation (Gulban et al., 2018)) and manually corrected when necessary. The latter was done using ITK-snap (Yushkevich et al., 2006) and BrainVoyager QX. The segmented vascular structures from 2D and 3D TOF data were then combined and were down-sampled to 1-mm isotropic resolution. The analyses procedures are summarized in a flow-chart diagram (Figure S3.3) and an example reconstruction is shown in Figure S3.4.

2.1.3.2.2 Scalp vasculature

All four echo images derived from the multi-echo GE protocol were first aligned to the 0.7-mm isotropic resolution anatomical images for each participant. We then isolated the extracerebral tissues by masking out the brain using *FSL BET* v5.0 (Jenkinson et al., 2012). Depending on which image(s) showed higher contrast for vascular structures, segmentation was performed manually in BrainVoyager QX using a combination of the four echoes or using the later echo images, *i.e.*, TE_3=15ms and TE_4=23ms, which showed higher contrast for vascular structures than earlier echoes. The segmented vascular structures were then

down-sampled to 1-mm isotropic resolution. The analyses procedures are also summarized in the flow-chart diagram provided in Figure S3.3.and an example reconstruction is shown in Figure S3.4.

2.2 Neuronavigation session

Seventeen of the originally included 21 participants underwent this session, as P07, P08, P13 and P18 dropped out of the study. A neuronavigation system (Zebris CMS20 ultrasound system, Zebris Medical GmbH, Isny, Germany) in combination with BrainVoyager QX 2.1 TMS Neuronavigator software (Brain Innovation, Maastricht, Netherlands) was used to acquire the coordinates of 130 EEG positions for each participant (see Figure 3.3). These 130 locations were determined based on the layout of EasyCap 128Ch ActiCap (EasyCap GmbH, Herrsching, Germany) whose size was selected based on individual head sizes. First, the head circumference for each participant was measured using a measuring tape. The cap was placed on and was secured using a chin band. Next, its position was adjusted so that the Cz location would be exactly half the nasion-inion distance. The inion was defined as the top part of the pronounced structure in the occipital region. In order to ensure that the cap was not tilted or shifted to one side, the distance between the left and right pre-auricular points was measured and the cap was gently moved in this virtual coronal plane until Cz was located half this distance. The preauricular points were defined as the location where the mandibular bone moves with the opening and closing of the mouth. Finally, the cap was secured with medical tape on the forehead to prevent any unwanted cap shift. The Cz location details (in terms of nasion-inion and pre-auricular distance) together with the cap size were noted down for the fNIRS session.

Single ultrasound markers (three in total) were attached to the participant's head using adhesive stickers. Next, three reference points (inion and left and right preauricular points) defined on the participant's head were used for the co-registration of the structural MRI image with the participant's head in the external (real) world. Once these steps were completed, the 130 EEG locations marked on the cap were digitized. The session lasted approximately 1h.

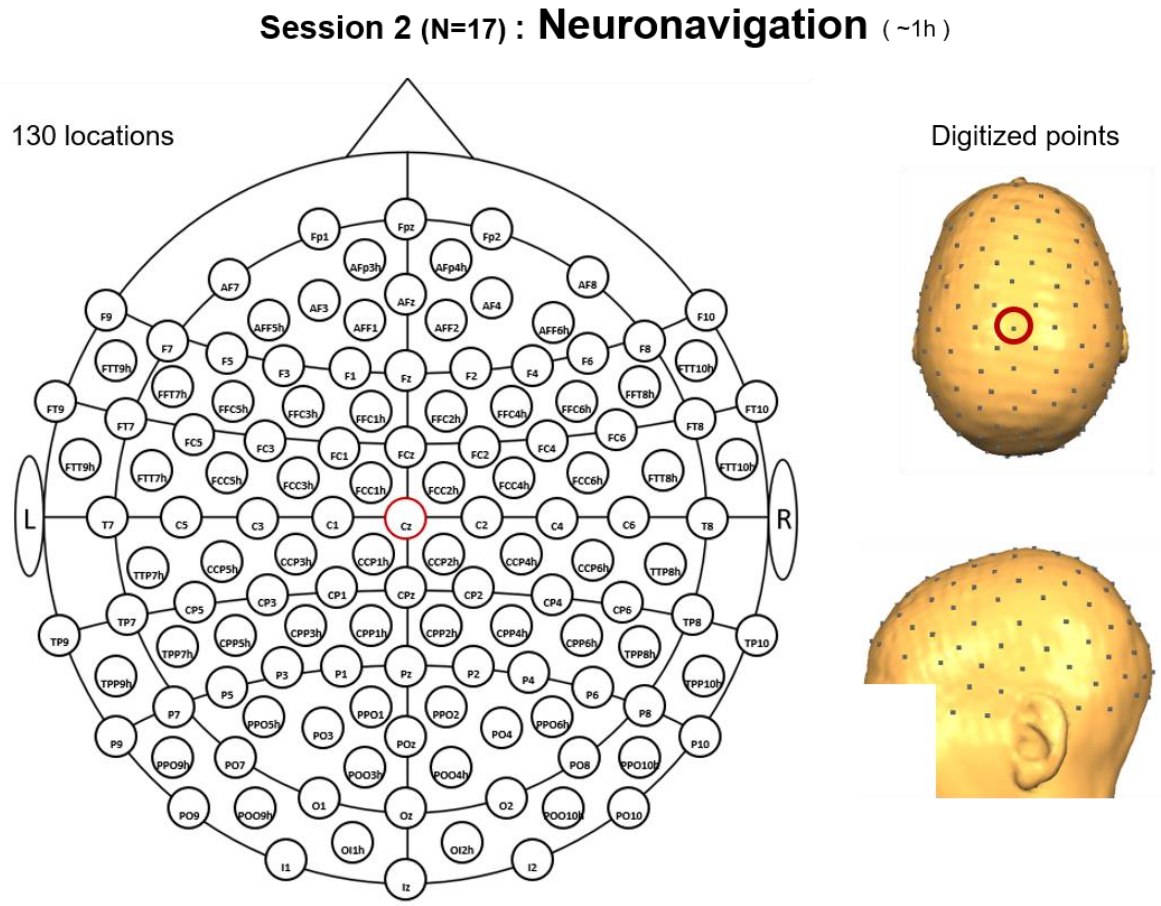

Figure 3.3. Schematic (left) and reconstructed (right) locations recorded during the Neuronavigation session. This layout is an extension of the international 10-20 system, it contains 130 locations and the nomenclature is based on (Oostenveld and Praamstra, 2001). The Cz location is indicated with a red circle. The schematic representation is based on the NIRx montage editor template, while the reconstructed locations belong to participant P04.

2.3 fNIRS session

2.3.1 Participants

P12 dropped out of the study. Thus, 16 of the 17 participants that participated in the fMRI and neuronavigation sessions took part in this session, out of which ten were female (mean age=29.81±5.22).

2.3.2 Designing approach-specific optode layouts

This process can be divided into three main stages: channel sensitivity computation, channel selection and building a participant-specific layout (see Figure 3.4 for a summary). The first

stage aimed at computing the channel-sensitivity profiles using Monte Carlo simulations. Each of the four approaches had a unique combination of ROI definition/type, software and brain model used to compute the simulations. During the second stage, the most-informative channels were selected for each of the four approaches, based on the solution to an optimization problem subject to a set of constraints. The first and second stages were repeated until approach- and task-specific optode layouts were created (twelve per participant, since there were three tasks and four approaches). The last stage aimed at combining all optode layouts into a single one individually for each participant.

2.3.2.1 Channel sensitivity to ROI computation

All four approaches (LIT, PROB, iFMRI, fVASC) were based on the light sensitivity profiles to a given ROI, but they differed in the following aspects (see Table 3.2 for a summary):

1. Software for Monte Carlo simulations

   The LIT approach represents a scenario where no individual MRI anatomical data is available and the target ROI is selected based on a literature review. Given such scenario, FOLD toolbox (Zimeo Morais et al., 2018) provides an easy way to compute the sensitivity profiles to the selected ROIs. This is because FOLD uses atlas head models as inputs to the Monte Carlo simulation and offers different brain parcellation atlases for ROI definition in the target head-model space. In addition, it is freely available, easy to install and has a user-friendly graphical interface. FOLD uses MCX package (Fang and Boas, 2009) to compute the light sensitivity profiles of optodes placed in pre-defined locations on the scalp, namely points corresponding to the extended 10-10 and 10-5 systems (130 points in total). It then provides a list of channels with the highest sensitivity to the ROI that can be exported for subsequent computations. PROB, iFMRI and fVASC approaches represent scenarios where individual MRI anatomical data are accessible. Since FOLD does not offer the option of using individual head models to compute Monte Carlo simulations, these were computed using the MCX package directly through its MATLAB interface (v2015b, The MathWorks, Inc., Natick, Massachusetts, United States).

2. Head models and tissue segmentations

Monte Carlo simulations require the anatomical head models to be segmented into different tissues. This is necessary for photon-transport simulations as different tissues of the human head present different optical properties (absorption, scattering, anisotropy and refraction). For the LIT approach, we used the MNI Colin27 head atlas (the default atlas available in FOLD). FOLD uses a five-layer segmentation of the MNI Colin27, which consists of scalp, skull, CSF, GM and WM tissues. For the remaining approaches, a five-layered model was created from the individual anatomical images using a hybrid segmentation algorithm (Perdue and Diamond, 2014). This algorithm, developed in MATLAB and available upon request from the authors, takes as input the standard GM and WM segmentations of a T1-weighted image from FreeSurfer and applies sequential morphological operations implemented in iso2mesh tools to accurately reconstruct skull, scalp, and CSF layer thickness. The GM and WM segmentation images were created in FreeSurfer v06 (Fischl, 2012) using the standard processing stream (*recon –all*, which took ~10 h per participant). The resulting tissues from the hybrid segmentation algorithm were converted into compatible BrainVoyager QX files to visually inspect and manually correct them if necessary. Although GM and WM segmentation files had been created in BrainVoyager QX in a previous step (see Sec. 2.1.3.1), the automatic segmentation in BrainVoyager usually disregards the cerebellum. We thus used the segmentations from FreeSurfer to create a head model for Monte Carlo simulations. From the corrected segmentation files, a single image file was created by assigning integer values ranging from 1 to 5 to the different tissues (as in FOLD). Specifically, voxels corresponding to scalp were assigned the value 1, voxels corresponding to skull were assigned value 2, CSF 3, GM 4 and WM 5. The remaining voxels were assigned value 0 (air). We ensured that voxels inside the head were not assigned the value 0 by first identifying them and subsequently assigning the value dictated by their direct neighbors.

The fVASC approach differed from the PROB-based and the iFMRI-based approaches in that vascular structures were included in the head model. For that, both pial/brain and scalp vasculature segmentations were combined and included as the sixth layer. To prevent voxels being assigned to two different tissues simultaneously,

all voxels considered as vascular tissue were removed from the remaining five tissues. Importantly, our segmentations could not distinguish veins from arteries and all voxels were treated as veins. Both, five- and six-layered models are shown in Figure S3.5.

3. Optical properties

For comparability purposes across approaches, we used the average optical properties across four NIRS wavelengths (690, 750, 780 and 830nm) as in FOLD. We defined the optical properties of vascular structures based on the scattering, absorption and anisotropy values provided by Bosschaart et al. (2014). We refer the reader to the Supplementary Tables S3.1 and S3.2 for computation details and Table 3.2 summary table of the optical properties used in the present study.

4. ROI selection and definition

The ROIs for the LIT approach were selected based on a literature review of the three mental-imagery tasks used in this study (we refer the reader to the Supplementary Material section 6.1.2 and Tables S3.3 and S3.4 for a summary of the reviewed studies and the selected ROIs, respectively). These ROIs were defined in the MNI Colin27 brain based on the Jülich histological atlas available in FOLD. The selected ROIs for the PROB-based approach were the active regions of the individual probabilistic mental-imagery maps. For iFMRI and the fVASC approaches, individual mental-imagery contrast maps were used as ROIs (as described in section. 2.1.3.2).

5. Inter-optode distance

FOLD performs the Monte Carlo simulations on neighboring optical positions of 10-10/10-5 systems only (that have a median inter-optode distance of 36mm) to avoid too long distances that cannot provide measurements with a proper signal-to-noise ratio (Zimeo Morais et al., 2018). For PROB, iFMRI and fVASC approaches, we only considered channels whose inter-optode distance was in the range of 25-40mm for Monte Carlo simulations. The number of channels differed across participants as the inter-optode distance could differ with varying head size/shapes across participants (see Table 3.3 for participant's cap size).

6. Computation of the sensitivity of a channel to a given ROI

Monte Carlo simulations are used to calculate the fluence distribution produced by a source transmitting light into a highly scattering medium (Strangman et al., 2013). By taking the product of the source and detector fluence distributions (also known as adjoint field), the photon measurement density function can be calculated (Boas et al., 2002). This is equivalent to the light sensitivity profiles mentioned earlier. FOLD calculates channel-wise normalized sensitivity profiles from the adjoint field by scaling the adjoint field with the sum of sensitivity of all voxels, so that each voxel represents percentage sensitivity to the whole volume. Then, the sensitivity of a channel to a given ROI is computed as a weighted mean of the voxels within the ROI to the sensitivity of voxels corresponding to the brain (GM and WM):

$$\mathrm{chanSens_{ch}} = 100 \cdot \sum_{k=1}^{nVoxROI} \frac{\mathrm{sens_{ch,k}} \cdot \mathrm{w_k}}{\mathrm{brainSens_{ch}} \cdot \mathrm{w'}} \tag{3.1}$$

where *nVoxROI* corresponds to the number of voxels comprising the target ROI, $\mathrm{sens_{ch,k}}$ is the normalized sensitivity value for channel *ch* and voxel *k*, $\mathrm{brainSens_{ch}}$ is the normalized sensitivity of channel *ch* of all GM and WM voxels, and *w* corresponds to the value (weight) of the voxel *k* in the target ROI (adapted from Zimeo Morais et al. (2018)).

The four approaches differed in the *nVoxROI* and the *w* parameters. The LIT approach assumed that all voxels belonging to a particular (anatomical) ROI contributed equally to the computation of the sensitivity of a channel to a given ROI and thus all weights were set to one. The PROB approach used probabilistic functional maps that represent the percent overlap of voxels across participants and thus weights ranged between 0 and 100%. As for iFMRI and fVASC, they relied on individual functional activation maps whose weights represent *t*-statistic values and ranged between 0 and 15.

For the LIT approach, channel sensitivity to a given ROI was computed separately for 10-10 and 10-5 systems as they cannot be computed simultaneously in FOLD. FOLD allows choosing the minimum value of the channel sensitivity to a given ROI to select/discard channels. We set this threshold to 0% in order to select all channels that were somewhat

sensitive to the target ROI and combined the list of output channels for every ROIs that was used for each mental-imagery task. If a channel appeared multiple times for a task, we selected the highest sensitivity value among all instances. As for the remaining three approaches, all channels that were considered for the Monte Carlo simulations together with their associated sensitivity values were selected as input to the next step.

Table 3.2. Comparison between Monte Carlo simulation approaches.

	FOLD				**DIRECT MCX**		
Approach where software is used	LIT				PROB, iFMRI, fVASC		
Number of simulated photons	10^8						
Source modelling	Pencil source						
Detector modelling	Pencil source						
Source/detector locations	130 points according to extended 10-20 EEG systems (defined using Mesh2EEG[1])				130 points according to extended 10-20 EEG system + subject-tailored (derived from Neuronavigation session)		
Channel definition criterion	Neighboring optical positions on 10-10 / 10-5 systems (median inter-optode distance of 36mm)				Inter optode distance range of 20-45mm		
Anatomical model	MNI Colin 27				Individual anatomy (Individual space)		
Number of tissues	5				5-6		
Wavelength (nm)	mean(690, 750, 780 830)						
Optical properties	**Used?**	**Tissue**	**μs (mm^{-1})**	**g**	**μa (mm^{-1})**	**n**	**Used?**
	Yes	*Scalp*	0.72	0.01	0.017275	1	Yes
	Yes	*Skull*	0.92	0.01	0.011925	1	Yes
	Yes	*CSF*	0.01	0.01	0.002500	1	Yes
	Yes	*Gray matter*	1.10	0.01	0.019500	1	Yes
	Yes	*White matter*	1.35	0.01	0.016900	1	Yes
	no	*Vasculature*	1.35	0.01	0.016900	1	Yes
Resolution	2x2x2 mm				1x1x1mm		
ROI type	Anatomical (Literature review + Juelich brain parcellation)				Functionally derived		
Output type	Anatomical sensitivity (in %) to a given ROI				Anatomical sensitivity (in %) to a given ROI		
Platform for MCX simulations	Ubuntu 16.04.02 LTS (Xenial Xeurs) with Intel Xeon E52650 v3 2.3 GHz, GeForce Gtx 770 and CUDA 8.0				Ubuntu 16.04.4 LTS, Intel(R) Xeon(R) CPU E5-2697 v2 @ 2.70GHz, 256 GB RAM, Tesla K20Xm and CUDA 9.1.85		

[1]*Multimodal Neuroimaging Laboratory;* μs/g/μa/n*: scattering/anisotropy/absorption/refraction parameters.*

2.3.2.2 Optimization of the optode layout

We determined the most informative set of channels (separately for each approach and mental-imagery tasks) by maximizing their total sensitivity to the target ROI. The maximization problem was subject to two constraints:

1. The inter-optode distance was limited to the 25-40mm range. We used individual inter-optode distance measures derived from the neuronavigation session for this step. It is important to note that this was applied to all four layouts layouts (thus including the layout based on the LIT approach). The FOLD toolbox (used for LIT approach) uses near-neighbor channels with a median inter-optode distance of all channels to be 36mm, in MNI space(Zimeo Morais et al., 2018). We used this additional information to ensure that (1) all channels were in the 25-40mm range in the subject-specific space, and that (2) the signal quality standards for all approaches were as similar as possible.
2. The optode layout for each approach consisted of two channels that shared a common detector (thus including three optodes per approach). Since we did not distinguish between sources and detectors in the Monte Carlo simulations, it is important to realize that the sensitivity of the channel will remain the same whether one considers optode X a source and optode Y a detector, or vice-versa. However, due to the second constraint, the algorithm may select a different channel pair that maximizes the total sensitivity to the ROI depending on which optode is considered a source or a detector. To ensure that as many candidate channels as possible were considered during the optimization approach, the optimization problem was solved twice: (1) using the original channel pool that consisted of all optode pairs that were considered for the Monte Carlo simulations (on average, there were 633.25 channels [SD=44.13] across participants); (2) considering their swapped versions (sources were considered detectors and vice-versa).

We followed an iterative approach to address the optimization problem. It begins with the construction of an empty solution, where no optode pair is selected. The algorithm then prunes the optode pairs that do not satisfy the inter-optode distance range constraint. Next, the algorithm ranks all possible optode pairs according to their contribution to the total sensitivity and selects one pair as the seed in each iteration. The algorithm then transfers the selected optode pair to the solution matrix and it removes from the list the channels that do

not share the same detector. Next, it selects the first channel from this list (*i.e.*, the one with the highest sensitivity). Since the target number of channels (=2) has been reached after this step, the accumulated total sensitivity of the selected two channels and the source-detector indices are stored in the solution matrix. These steps are repeated until all optode pairs are used as seeds. Finally, the two channels that lead to the highest total sensitivity for either constraint set constitute the selected channels for creating the setup.

2.3.2.3 Creating the setup

2.3.2.3.1 Mental-imagery task selection

Two out of the three mental-imagery tasks that participants performed during the f/MRI session were selected for the fNIRS session. This measure was necessary as pilot measurements performed with optode layouts designed to account for all three tasks elicited high discomfort in participants. This decision ensured that the optode setup would maximally consist of 24 optodes (3 optodes per layout × 4 approaches × 2 motor-imagery tasks), which should constitute a reasonably comfortable setup for participants and thus should prevent them from withdrawing from fNIRS recordings due to setup-related discomfort (Suzuki et al., 2010; Cui et al., 2011; Sereshkeh et al., 2018). This selection was carried out at the individual subject level. For that, we first calculated the number of overlapping channels across all four layouts for each mental-imagery task, and selected the two tasks with the least number of overlapping channels. An additional step was used in case this approach was not sufficient to select the two tasks, where we computed the center of gravity (COG) for all four layouts per mental-imagery task and calculated the distance between COGs. The tasks with the least number of overlapping channels and highest distance between them were the selected tasks. See Supplementary Table S3.5 for a summary of the mental-imagery task selection procedure and Table 3.3 for the resulting selected task pair per participant.

2.3.2.3.2 Combining all channels into a single layout

The eight layouts (four per task) were combined manually into a single one. This was first carried out digitally to simulate the final arrangement using schematic representations of source and detector positions. It consisted of two steps: an initial step combined all four layouts for each mental-imagery tasks and both layouts were combined into one in the second step. It could be that the source-detector arrangement was not compatible across

layouts (within or across mental tasks), since a source in a given channel cannot be a detector in another one (or *vice versa*). To account for such possibility, we first swapped sources for detectors in the problematic spots. This step solved the compatibility problem in all but four participants (P05, P16, P17 and P19). For these participants, using a different mental-imagery task combination solved the issue (see Supplementary Table S3.5). Since the fNIRS system used in this study uses lighter wires for sources than for detectors, we rearranged sources and detector positions in all participants (when possible) to maximize the number of sources while preserving the channels defined in the optimization step. It is important to note that each participant ended up with a unique optode layout, with a varying number of optodes (see Table 3.3 and Figure S3.6).

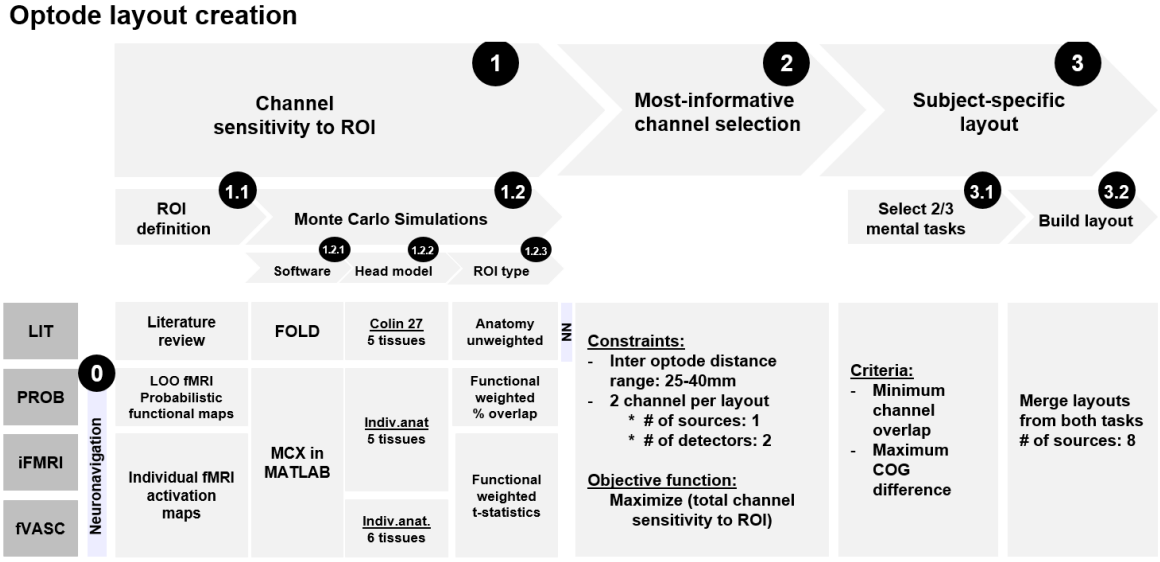

Figure 3.4. Summary of the key steps involved in optode-layout design for each of the four approaches evaluated in the present study. The process was divided into three main stages: (1) channel sensitivity to ROI computation, (2) channel selection and (3) building a subject-specific layout. For the first stage, each of the four approaches had a unique combination of ROI definition/type, software and brain model used to compute the Monte Carlo simulations. During the second stage, the most-informative channels were selected for each of the four approaches and two mental-imagery tasks. The last stage combined all the layouts into one. LOO = leave-one-out; COG = center of gravity; NN = neuronavigation.

2.3.3 Experimental design

The fNIRS experiment consisted of one session that lasted approximately 1.5h. During this time, participants performed six, around 8-min long functional runs. In each of the runs, participants were acoustically cued to perform one of the two mental-imagery tasks selected

for them or to rest. Six, 10-s long trials were presented for each mental-imagery task, interleaved with a jittered rest condition with mean duration of 22s (jittering was of ± 2s), see Figure 3.5. Thus, participants performed 60 trials for each mental-imagery task across the six runs. Trials were pseudo-randomized across runs. Participants were instructed to use the same strategy they used in the scanner (first session). For that, participants were given a document prior to the fNIRS experiment where their strategies had been noted down. Participants were asked to avoid any potential jaw movements during the functional runs and to keep their eyes closed throughout the run.

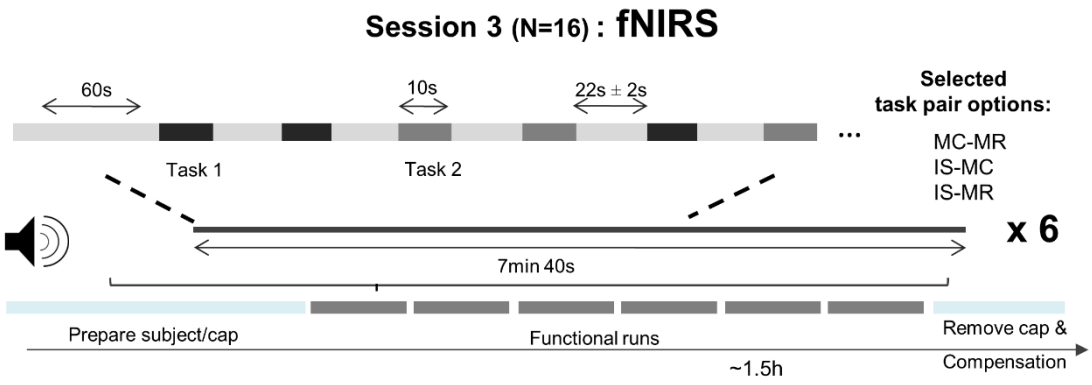

Figure 3.5. Schematic representation of a functional run during the fNIRS session. During each mental-task period, participants were acoustically cued to perform one of the two mental-imagery tasks for 10s while keeping their eyes closed. When participants heard "rest", they were asked to stop the task and await the next instruction. Abbreviations: IS= inner-speech; MC = mental-calculation; MR= mental-rotation.

2.3.4 fNIRS signal acquisition

fNIRS data were recorded using a continuous-wave system (NIRScout-816, NIRx, Medizintechnik GmbH, Berlin, Germany). The optode setup varied across participants, but they had some features in common: all setups contained eight sources and eight short-distance channels (SDC). The SDCs were formed by short-distance detectors placed at 8mm from a given source. The inter-optode distance of the standard channels (here on called normal-distance channels, NDC) ranged from 25-40mm. Sources emitted light at wavelengths 760nm and 850nm, and the light intensity acquired at the detector side was sampled at 7.8125Hz. The fNIRS cap was placed for each participant according to the measurements taken during the neuronavigation session. Besides the standard cap fixation (using the chin band), the fNIRS cap (EasyCap 128Ch ActiCap, EasyCap GmbH,

Herrsching, Germany) was fixated onto the participant's head with three medical tape stripes (connecting the cap and the participant's forehead) to assure the cap would not shift during the measurements. In addition, a black, plastic overcap was placed on top of the fNIRS cap to additionally prevent ambient light from reaching the spring-loaded optodes.

Table 3.3. Subject-specific fNIRS-session summary and optode-layout information.

Participant ID	Cap Size (cm)	Mental tasks		# Runs	# Optodes S | D		# NDC channels	IOD (mm) Mean (SD)
P01	56	MC	MR	6	8	7	13	29,92 (2,60)
P02	56	IS	MC	6	8	9	16	29,00 (3,48)
P03*	58	IS	MR	6	8	6	16	34,06 (6,84)
P04	56	MC	MR	6	8	10	15	31,60 (4,79)
P05	60	IS	MC	6	8	4	12	30,67 (4,52)
P06	56	MC	MR	6	8	9	14	31,07 (4,20)
P09	60	MC	MR	6	8	5	9	29,33 (4,42)
P10	56	MC	MR	6	8	7	10	30,40 (4,12)
P11	56	MC	MR	6	8	4	12	30,17 (3,19)
P14	58	MC	MR	5	8	6	11	31,09 (3,14)
P15	58	MC	MR	5	8	5	10	31,70 (4,64)
P16	58	MC	MR	6	8	8	12	31,58 (3,42)
P17	56	MC	MR	6	8	5	11	30,18 (4,33)
P19	56	MC	MR	6	8	7	12	29,83 (2,79)
P20	56	MC	MR	6	8	10	15	31,13 (4,50)
P21*	54	IS	MR	6	8	10	14	29,07 (3,25)

Note: P03 and P21 were excluded from data analysis (see participant exclusion criteria) Abbreviations: NDC= normal distance channels; IOD= inter-optode distance; MC = mental calculation; MR= mental rotation.

2.3.5 fNIRS data analysis

2.3.5.1 Participant exclusion criteria

Two of the sixteen participants, P03 and P21, were excluded from subsequent analysis for different reasons. The optode layout for P03 was created based on a different inter-optode distance range criterion than the rest of the participants (25-45mm vs. 25-40mm). This is because P03 was the first participant who participated in the fNIRS session and the original inter-optode distance range was expected to provide reasonable signal quality. However,

this range proved to be suboptimal as four NDC and three SDC did not survive the coefficient of variation threshold (CV < 7.5%), a metric used to estimate the signal-to-noise ratio for each channel (Piper et al., 2014). Given the restricted number of channels comprising each layout, we created the layouts for the rest of the participants using a more conservative inter-optode distance range criterion (25-40mm range, see first constraint in Sec. 2.3.3) to ensure that all (or as many as possible) channels survive the CV threshold. Thus, P03 was excluded for comparability reasons. As for P21, the data was corrupted and could not be retrieved.

2.3.5.2 Preprocessing

For every subject and run, the raw optical intensity data series were converted into changes in optical density (OD) values using Homer2 (Huppert et al., 2009). CV values were calculated for the entire run for each channel and those with a CV >=7.5% were discarded from the analysis (see Figure S3.7). Next, the motion detection algorithm *hmrMotionArtifactByChannel* was applied to the OD time-series to identify motion artifacts in each channel. We used the following parameters: AMPThresh=0.15, tMotion=0.5 and tMask=2. The SDThresh parameter ranged between 8 and 10 across participants. Motion artifact identification was visually assessed by experimenter AB and was manually corrected in case it was necessary. Motion artifacts were divided into spikes and baseline shifts. Baseline shifts were corrected using *hmrSplineInterp* algorithm in Homer2 (p=0.99), while *hmrMotionCorrectWavelet* algorithm in Homer2 (iqr=0.5) was used to correct for the spike artifacts only in the channels where motion artifacts had been detected (Figure S3.8 summarizes the detected number of motion events per participant). Then, motion-corrected OD data were transformed to change in concentration values through the modified Beer-Lambert law with an age-specific differential path length factor for each participant (Scholkmann and Wolf, 2013).

2.3.5.3 Assessment of degree of layout (dis)similarity across approaches

The first goal of this study was to assess whether the resulting optode layouts differed across approaches. To do so, for each pair of approach-specific layouts we calculated the number of overlapping channels and the Euclidian distance between their centers of gravity. These calculations were carried out for each mental-imagery task at the single-subject level and

were averaged across participants afterwards. In addition, frequency maps for each approach were computed.

2.3.5.4 Single-run estimates calculation

The Short Separation Regression approach (SSR (Goodwin et al., 2014)) was applied on the unfiltered Δ[HbO]- and Δ[HbR]-NDC data to remove signal from extra-cerebral layers of the head. This was done for each NDC and chromophore by using the SDC closest to the NDC as the regressor. The SDC-corrected time course was used as input for the *ar_irls* algorithm in NIRS Brain AnalyzIR Toolbox (Santosa et al., 2018). This algorithm uses an autoregressive (AR) model for correcting motion and serially correlated errors in fNIRS. The function was adapted to use the ordinary least squares method instead of the *robustfit* approach. The maximum AR model order to be considered was set to four times the sampling rate. The design matrix included the two task predictors convolved with a standard hemodynamic response function. The default hemodynamic response function from SPM12 was used (double gamma function, the onset of response and undershoot 6s and 16s, respectively, dispersion 1s, response to undershot ratio 6). The task predictor for Δ[HbR] was -1/3 of the Δ[HbO] amplitude. In addition, a set of low frequency discrete cosine terms were defined as confound predictors using the *dctmtx* function in NIRS Brain AnalyzIR Toolbox with a cut-off frequency of 0.009Hz.

2.3.5.5 Multi-run ROI analysis

We combined the information from both channels comprising each layout to run an ROI analysis as described in Santosa et al. (2018) and expanded their procedure to account for multiple runs:

$$\beta_{ROI} = c\beta_{channel} \tag{3.2}$$

$$Cov_{ROI} = cCov_{\beta}c^{T} \tag{3.3}$$

where in this study $\beta_{channel}$ is the multi-run beta estimate and the $Cov_{\beta roi}$ is the multi-run covariance matrix estimated from the concatenated residual time courses and the design matrix. Finally, c is the contrast vector whose coefficients are 0 if the channel does not belong to the ROI and is 0.5 in the two channels that belong to the ROI.

2.3.5.6 Multi-run block averages and contrast-to-noise ratio

The SDC-corrected and unfiltered Δ[HbO] and Δ[HbR] time courses were filtered using a zero-phase, band-pass finite impulse response filter of order 1000, with cutoff frequencies of [0.008, 0.25Hz]. Block averages were computed for each channel and mental-imagery task by taking the average of all trials and runs 4s before the onset of the task until 15s after the offset of the task.

The Contrast-to-Noise Ratio (CNR) as was calculated for each channel, ROI and chromophore using the formula described by Cui et al. (2011):

$$\frac{|mean(dur) - mean(pre)|}{\sqrt{var(dur) + var(pre)}} \tag{3.4}$$

where *pre* represents the rest period from 4s before onset of task to 0s; and *dur* represents the task period from 5-15s post task-onset, as in Hocke et al. (2018).

2.3.5.7 Statistical analysis

The second goal of this study was to compare the fNIRS-signal quality and sensitivity obtained from the optodes placed according to the four different approaches. Group differences across approaches in terms of CNR and ROI *t*-estimates were assessed using a non-parametric ANOVA (Friedman test) and follow-up Wilcoxon paired signed rank tests, one-sided and corrected for multiple comparison with the Benjamini-Hochberg method. Group differences were computed considering: (1) each mental-imagery task separately and (2) all mental-imagery tasks together. In addition, we quantified the number of participants that showed significant increase in the ROI activation.

2.3.5.8 fNIRS data projection onto cortical surface and comparison with fMRI data

We used the inverse distance weighting (IDW) method described in (Aihara et al., 2012) to interpolate fNIRS data on the cortical surface. In short, each fNIRS channel position was defined as the point in the scalp half way between the corresponding source and detector position. The cortical projection of each channel was determined by taking the point in the brain reconstruction closest to the channel position in the scalp. A sphere of radius *r* was centered in the projected cortical point and the voxels inside the sphere that were labeled as GM were assigned a weight depending on how far from the center they were located. The

weight (w) was calculated as $1/d^2$, where d is the Euclidian distance between the projected point (center of the sphere) and a given voxel inside the sphere. At each cortical vertex k inside the sphere, the interpolated fNIRS data was computed as:

$$s(k) = \frac{\sum_{i=1}^{n} w_i * f_i}{\sum_{i=1}^{n} w_i} \tag{3.5}$$

where n is the number of cortical projection points and f is the amplitude of the fNIRS channel value. Here we used two cortical projection points as two channels comprised a given layout. The channel-specific amplitude was calculated as the average value of the normalized fNIRS signal (computed as the channel time course divided by its peak value) in the range of 3s after task onset to 5s after task offset. In total, four spheres with varying radii (r = {10, 15, 20, 25} mm) were used.

We used channel-specific projection weights and projection spheres to compute spatially weighted fMRI block averages to assess the temporal correlation between fNIRS and fMRI signals. First, voxels inside the sphere of radius r that were labeled as GM were selected and mental imagery-specific events were extracted from each voxel's time courses. Task-specific ROI averages were computed by weighting the contribution of each voxel according to the projection weights. The standard error of the weighted average was estimated using bootstrapping (with 100 resamples and sample size equal to 60% of the initial number of voxels). These steps were repeated for every channel across all layouts in each participant. Finally, the temporal correlations of fNIRS and fMRI block averages were computed using Spearman's correlation. Next to channel-specific projection weights, layout-specific projection weights were also calculated. Their computation differed in that for the latter we used the center of gravity of each layout on the scalp to determine the cortical projection point. Layout projection weights were used to extract the peak and spatially weighted mean *t*-estimates of individual fMRI activation of the voxels labeled as GM to assess how well the fNIRS ROIs targeted individual activation maps.

3 Results

3.1 Using different information sources for optode placement results in different optode-layout designs

Figure 3.6 shows the mean percent overlap (top panel) and mean Euclidian distance between the COGs of each pair of optode layouts across participants (bottom panel). The color of each cell indicates the standard error of the mean. The LIT approach contained no channels that overlapped with the remaining approaches for neither mental-calculation (MC) nor mental-rotation (MR) tasks. Channels placed according to the PROB approach partially overlapped with those from iFMRI and fVASC approaches for MC task. Channels from iFMRI and fVASC approaches overlapped the most, with an average 85.71% [SE = 8.17] for MC and 41.67% [SE = 14.86] for MR. Regarding IS task, P05 showed an overlapping channel between PROB and fVASC layouts (P02 had none). The mean Euclidian distance between the COGs was considerably high (>55mm) for almost all pair of layouts, which indicates that layouts were located in spatially separated areas. IFMRI and fVASC layouts were located, on average, in close proximity for the MC task (6.45mm [SE = 5.64]) and to a lesser extent for MR (42.22 mm [SE = 13.32]). Similarly, the frequency maps shown in the Figure S3.9 indicate that (1) the selected channels vary considerably across participants for PROB, iFMRI and fVASC approaches; and (2) iFMRI and fVASC show the highest and most similar spatial extension for MC and MR tasks. As for inner-speech (IS) task, the Euclidean distance ranged between 9.08 mm (PROB- fVASC) and 100.19 mm (LIT-iFMRI) for P05 and between 26.83 mm (LIT-PROB) and 75.98 mm (LIT- iFMRI) for P02 (not shown in Figure 3.6).

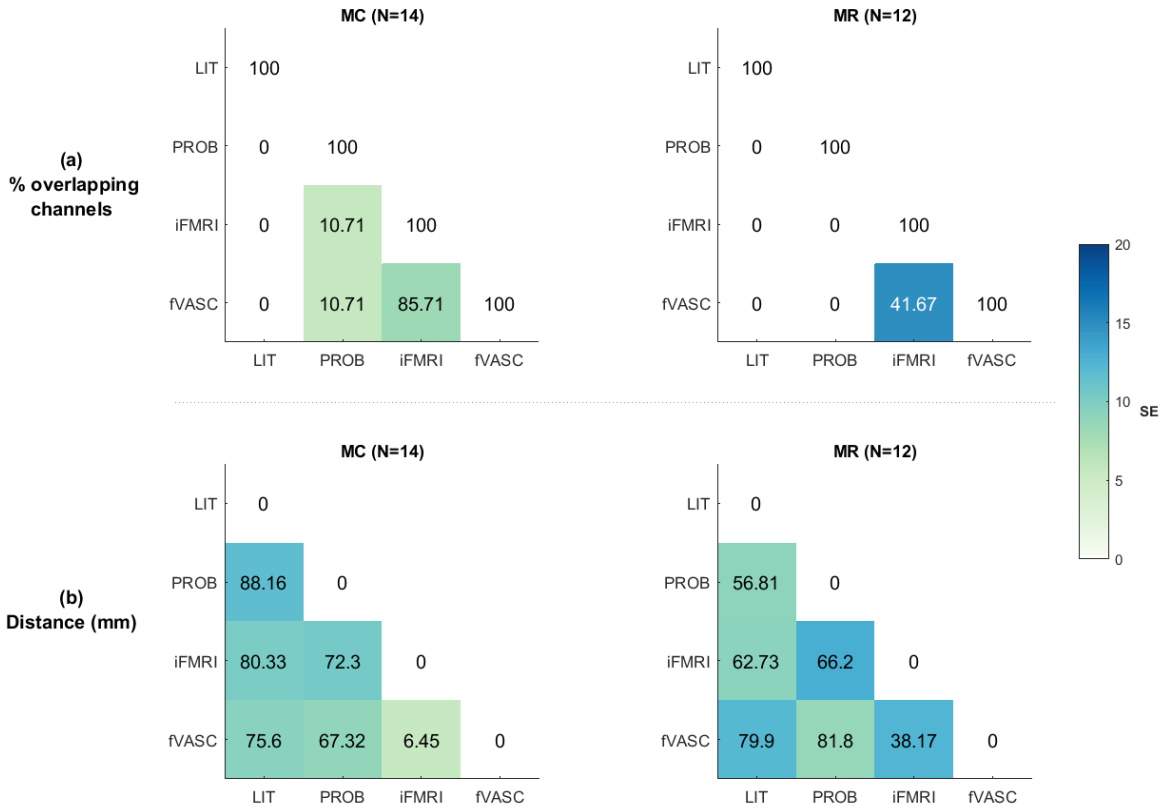

Figure 3.6. Assessment of degree of layout (dis)similarity across approaches. (a) Average number of overlapping channels for each pair of approach-specific layouts for MC (left) and MR (right) tasks. The numbers in each cell represent the average number of overlapping channels **(a)** or the average Euclidian distance between COG **(b)** for each pair of approach-specific layouts for MC (left) and MR (right) tasks. Colors represent the standard error of the mean. Abbreviations: MC = mental calculation; MR= mental rotation.

3.2 Significant differences in fNIRS-signal quality across the four optode-placement approaches

The Friedman test was computed separately for each chromophore (Δ[HbO] and Δ[HbR]) and considering (1) all mental-imagery tasks together and (2) each mental-imagery task separately. For Δ[HbO], CNR significantly differed across layouts ($Fr = 41.63$, df 4,14, $p < 0.0001$) when all mental imagery tasks were considered together. CNR also differed significantly across layouts for MC ($Fr = 24.67$, df 3,14 $p<0.0001$) and MR ($Fr = 25.72$, df 3,12 $p<0.0001$). Post-hoc pairwise comparison results with the Wilcoxon signed-rank test and the Benjamini-Hochberg correction method are summarized in Figure 3.7. These tests revealed significant differences when all mental-imagery tasks were considered together. Specifically, optodes placed using the LIT approach measured significantly lower CNR

values compared to the other three approaches (1) when all mental-imagery tasks were considered together (q[FDR]<0.001), (2) for MC only ($q[FDR]_{LIT\text{-}PROB}$ <0.01, $q[FDR]_{LIT\text{-}iFMRI}$ <0.001 and $q[FDR]_{LIT\text{-}fVASC}$ <0.05) and (3) for MR only (q[FDR] <0.001). In addition, channels placed according to the PROB-derived layout reached significantly lower CNR values than those from the fMRI ($q[FDR]_{PROB\text{-}iFMRI}$ <0.001) and fVASC ($q[FDR]_{PROB\text{-}fVASC}$ <0.05) approaches.

As for Δ[HbR], CNR significantly differed across layouts (Fr = 18.32, df 4,14, p < 0.001) when all mental imagery tasks were considered together. CNR also differed significantly across layouts for MC (Fr = 7.98, df 3,14, p<0.05) and MR (Fr = 8.23, df 3,12, p<0.05). *Post-hoc* pairwise comparisons revealed that the LIT approach reached significantly lower CNR values when all tasks were considered together for all other layouts ($q[FDR]_{LIT\text{-}PROB}$<0.05, $q[FDR]_{LIT\text{-}iFMRI}$ <0.001 and $q[FDR]_{LIT\text{-}fVASC}$ <0.01). It also reached significantly lower CNR values compared to the iFMRI layout for the MR task ($q[FDR]_{LIT\text{-}iFMRI}$ <0.01).

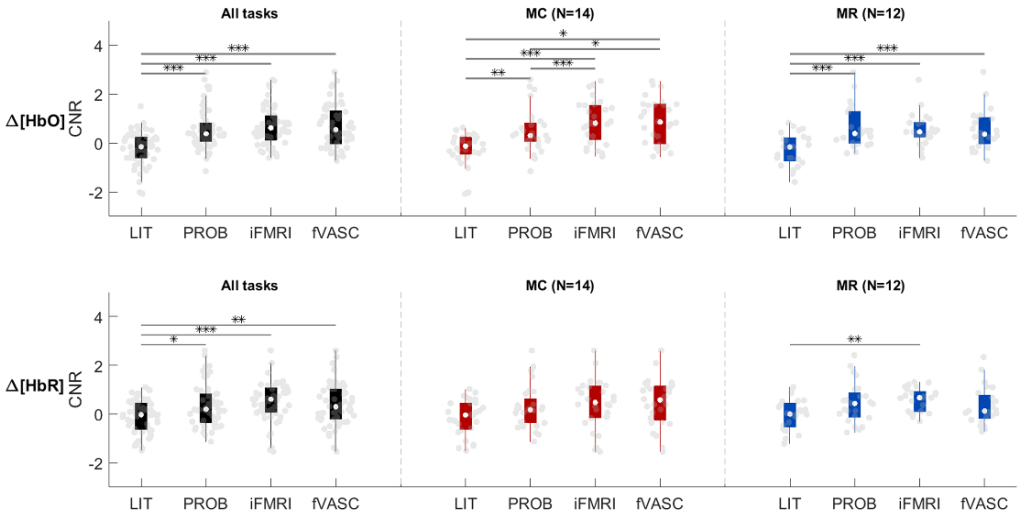

Figure 3.7. CNR-based group comparison across layouts. Results were evaluated separately for Δ[HbO] (a) and Δ[HbR] (b), when all three mental-imagery tasks were considered together as well as separately for MC and MR tasks (left, middle and right column, respectively). LIT performed significantly worse than the PROB, iFMRI and fVASC approaches for both chromophores when all tasks were considered together. A similar pattern was observed for MC and MR tasks for Δ[HbO]. Gray dots represent single-subject CNR values for a given mental-imagery task. Whiskers represent the 1.5 times the inter-quartile range. Significant parwise differences (calculated using Wilcoxon signed-rank test, one-sided and corrected for multiple comparisons) are indicated with asterisks: *** = q[FDR] < 0.001; ** q[FDR] < 0.01;* q[FDR] < 0.05. Abbreviations: MC = mental calculation; MR= mental rotation.

3.3 Significant differences in fNIRS-sensitivity across the four optode-placement approaches

3.3.1 *t*-statistics

For Δ[HbO], ROI *t*-statistics significantly differed across layouts (Fr = 31.66, df 3,14, $p < 0.0001$) when all mental-imagery tasks were considered together (see Figure 3.8). It also differed significantly across layouts for MC (Fr = 23.18, df 3,14 $p<0.0001$) and MR (Fr = 14.06, df 3,12 $p<0.005$). *Post-hoc* pairwise comparisons (signed-rank tests, one-sided) revealed that optodes placed using LIT approach measured significantly lower *t*-statistics compared to the other three approaches (1) when all mental-imagery tasks were considered together ($q[FDR]<0.001$), (2) for MC only ($q[FDR]_{LIT\text{-}PROB} <0.01$ and $q[FDR]_{LIT\text{-}iFMRI;\ LIT\text{-}fVASC} <0.001$) and (3) for MR only ($q[FDR] <0.01$).

Δ[HbR] ROI *t*-statistics significantly differed across layouts (Fr = 27.48, df 3,14, $p < 0.0001$) when all mental imagery tasks were considered together. It also differed significantly across layouts for MC (Fr = 15.46, df 3,14, $p<0.01$) and MR (Fr = 10.56, df 3,12, $p<0.05$). *Post-hoc* pairwise comparisons showed a similar trend as HbO: LIT approach measured significantly lower *t*-values compared to the other three approaches for almost all comparisons. In addition, the optodes placed according to the PROB approach measured significantly lower *t*-values than iFMRI ($q[FDR]_{PROB\text{-}iFMRI} <0.01$) and fVASC ($q[FDR]_{PROB\text{-}fVASC} <0.05$).

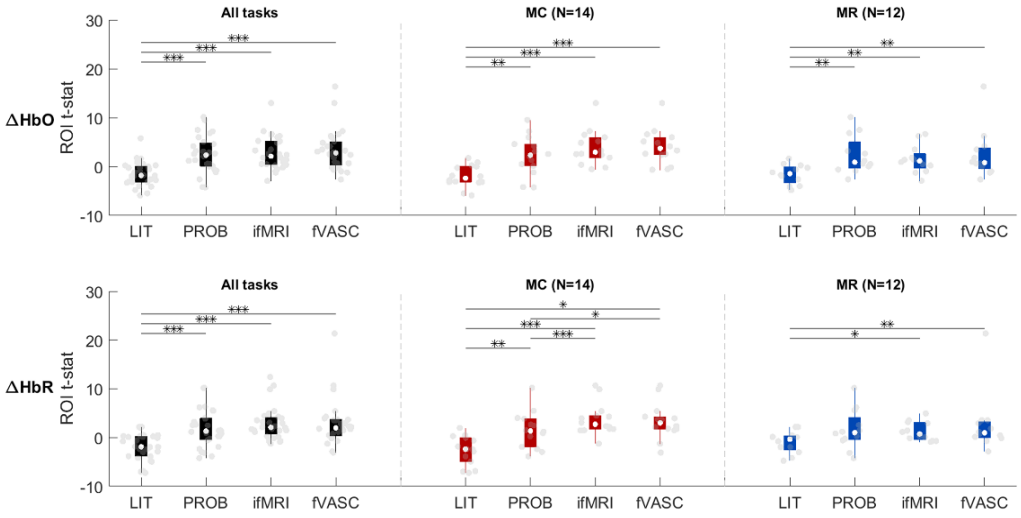

Figure 3.8. *t*-statistic based group comparison across layouts. Results were evaluated separately for Δ[HbO] (a) and Δ[HbR] (b), when all three mental-imagery tasks were considered together as well as separately for MC and MR tasks (left, middle and right column, respectively). LIT performed significantly worse than the PROB, iFMRI and fVASC approaches for both chromophores when all tasks were considered together. A similar pattern was observed for MC and MR tasks for both chromophores. Gray dots represent single-subject *t*-values for a given mental-imagery task. Whiskers represent the 1.5 times the inter-quartile range. Significant parwise differences (calculated using Wilcoxon signed-rank test, one-sided and corrected for multiple comparisons) are indicated with asterisks: *** = q[FDR] < 0.001; ** q[FDR] < 0.01; *q[FDR] < 0.05. Abbreviations: MC = mental-calculation; MR= mental-rotation.

3.3.2 Percent of participants with significantly active ROIs

Figure 3.9 shows the percent of participants that resulted in significant activation for each mental-imagery task. For both chromophores, the percent of participants with significant ROI activation increased with increasing the amount of individualized information, and plateaued after including individualized functional maps (for MC task) or was slightly reduced after including vascular information (MR task). For the IS task, PROB and fVASC approaches and PROB and iFMRI approaches contained significant ROI activation for both participants (100%) regarding Δ[HbO] and Δ[HbR], respectively. As for MC and MR tasks, the number of participants with significant activation was higher for more individualized approaches than the LIT approach. Specifically, for the MC task, the LIT approach contained significant ROI activation in 7% (one) participant for both chromophores, while the PROB approach reached significant ROI activation in 57% (eight) and 43% (six) participants for Δ[HbO] and Δ[HbR], respectively. IFMRI and fVASC approaches

contained significant ROI activation in 79% (eleven) participants for both chromophores. For the MR task, the LIT approach reached significant activation in 0% and 17% (two) participants, while the PROB approach reached significant activation in 42% (five) and 33% (four) of the participants, while iFMRI and fVASC approaches contained significant ROI activation in 33% (four) and 42% (five) participants for both chromophores, respectively. Figure S3.10 (a) shows examples of participants with typical hemodynamic responses (a positive deflection in Δ[HbO] and a negative deflection in Δ[HbR]) for the four approach-specific optode layouts, while Figure S3.10 (b) shows examples of participants with weak/inverted hemodynamic responses for the four approach-specific layouts.

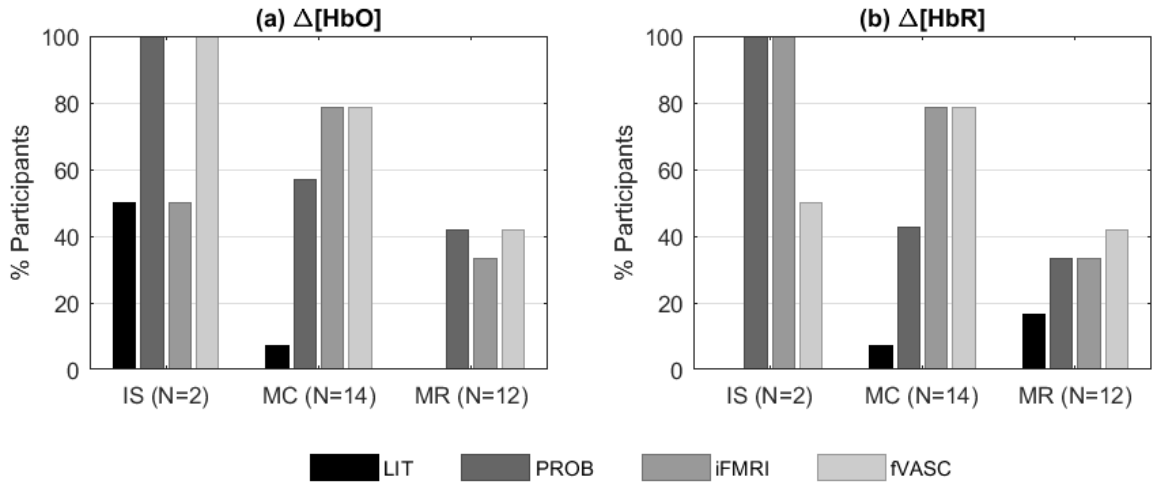

Figure 3.9. Percent of participants that resulted in significant activation for each mental-imagery task, optode layout and chromophore. For both chromophores, the percent of participants with significant ROI activation increased with increasing the amount of individualized information used to create optode layouts until a certain point: it plateaued after including individualized functional maps (for MC task) or was slightly reduced after including vascular information (MR task). Abbreviations: IS= inner-speech; MC = mental-calculation; MR= mental-rotation.

3.4 Spatial specificity of fNIRS-ROIs

To assess how well the fNIRS ROIs targeted individual fMRI activation maps, we computed weighted average and peak fMRI responses within the regions of the cortex interrogated by fNIRS channels. The two plots in Figure 3.10 (a) show results for sphere with r=20mm that both the average and peak responses for LIT are significantly lower than the other approaches (significance assessed by signed rank test, one-sided FDR corrected). Using different sphere sizes did not affect the results (data not shown). The temporal correlation

between fNIRS and fMRI time courses (bottom plots in Figure 3.10 (b)) showed a similar tendency but with smaller differences for Δ[HbO] (and examples of both fNIRS and fMRI time courses are shown in Figure S3.11).

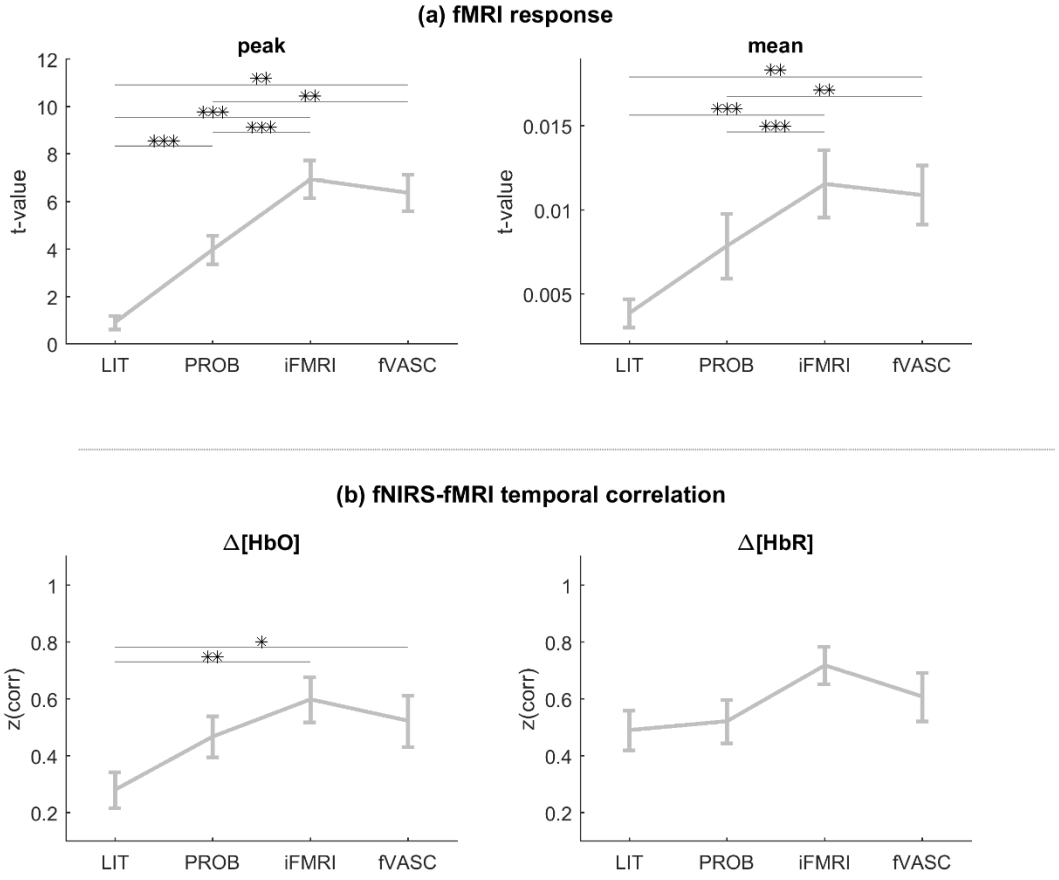

Figure 3.10. Assessment of layout specificity to fMRI activation maps (a) and of the temporal correlation between fNIRS and fMRI time courses (b). Peak and average values extracted from fMRI activation maps were highest for channels placed according to iFMRI and fVASC approaches and lowest for the LIT approach, independent of the size of projection spheres used to extract the values (data not shown). Times courses of channels placed according to the LIT approach showed significantly lower temporal correlations with fMRI-signal time courses than following the iFMRI and fVASC approaches. Significance was assessed with Wilcoxon paired signed tests (one-tailed) and was corrected for multiple comparisons. *** q[FDR] <0.001; ** q[FDR]<0.01; *q[FDR]<0.05.

4 Discussion

Designing optode layouts is an essential but challenging step in the preparation of an fNIRS experiment as the quality of the measured signal and the sensitivity to underlying cortex depends on how sources and detectors are arranged on the scalp. This becomes particularly relevant for fNIRS-based BCI and neurofeedback applications, where developing robust systems that use limited number of optodes is crucial to remain practical and comfortable for clinical applications. From the many approaches and tools currently available to optimize optode-layout design, we selected and compared four approaches that incrementally incorporated individual information of participants (LIT, PROB, iFMRI and fVASC) while participants performed mental-imagery tasks typically used in fNIRS-BCI experiments. Our results show that the four approaches resulted in different optode layouts and that the degree of overlap varied across approaches, with the highest overlap and smallest distance between iFMRI and fVASC layouts. Further, time course data of channels placed according to the LIT approach showed significantly lower CNR and *t*-values than those of the channels placed according to the remaining approaches. In addition, we observed no significant difference between PROB, iFMRI and fVASC approaches when all three mental tasks were considered together.

Understanding the difference in performance across layouts

Lower performance of the LIT approach

Concurrent fNIRS-fMRI studies show agreement in the hemodynamic signal measured by both modalities (at least in the motor cortex), both temporally (Cui et al., 2011) and spatially (Huppert et al., 2017), but inferior in spatial resolution when assessed with fNIRS. To assess how well the fNIRS ROIs targeted individual fMRI activation maps, we computed weighted average and peak fMRI responses within the regions of the cortex interrogated by fNIRS channels. As shown in Figure 3.10, the average and peak responses for LIT were significantly lower than the remaining approaches. The temporal correlation between fNIRS and fMRI time courses showed a similar tendency. These observations were expected since PROB, iFMRI and fVASC approaches were based on fMRI information. However, if the individual fMRI map is used as the ground-truth measure of cerebral activity due to its superior resolution and higher SNR, Figure 3.10 shows that the LIT approach could not capture the underlying signal as good as the other approaches.

Several factors may have contributed to that. First, the head model used for Monte Carlo simulations for LIT differed from the other three approaches (Colin27 head atlas *vs.* subject-specific anatomical model, respectively). Although head atlases are good approximations, the tissue geometries may significantly differ from other adult individuals (Strangman et al., 2013). Second, the ROI selection procedure for LIT differed from the PROB, iFMRI and fVASC approaches in that the ROI selection for LIT was based on a literature review, while the other three approaches relied on functional contrast maps. Due to the small number of participants for the IS task (N=2), the following lines will focus only on MC and MR tasks. The mental-imagery instructions used in this study differed from the reviewed studies, which may have contributed to a suboptimal selection of the ROIs for the LIT approach. Indeed, the majority of reviewed papers that reported using mental arithmetic used strategies that aimed at increasing the working memory demand and thus mainly measured brain activation in the frontal lobe. Examples of tasks used in these studies are subtraction to visually presented 3-digit or 2-digit numbers, or addition or multiplication of visually presented single or double digits to/with single or double digits (Rickard et al., 2000; Kawashima et al., 2004; Yoo et al., 2004; Naito et al., 2007; Ogata et al., 2007; Utsugi et al., 2007; Bauernfeind et al., 2008; Pfurtscheller et al., 2010; Ang et al., 2012; Power et al., 2012; Herff et al., 2013; Schudlo and Chau, 2013; Schudlo et al., 2013; Verner et al., 2013; Weyand and Chau, 2015; Shin et al., 2016). Here, we asked participants to recite common multiplication tables, which is considered an easy task and thus may have elicited lower responses in frontal and parietal areas when compared to more complex multiplication problems (Ischebeck et al., 2009). Regarding mental rotation, most of the reviewed work used visually presented cues that had to be mentally rotated, such as geometric object, alphanumeric character or hand rotations (Alivisatos and Petrides, 1997; Tagaris et al., 1998; Harris and Miniussi, 2003; Roberts and Bell, 2003; Kawamichi et al., 2007; Shimoda et al., 2008; Friedrich et al., 2013; Herff et al., 2013; Hwang et al., 2014; Khan and Hong, 2017; Hamada et al., 2018; Khalaf et al., 2018). In this study, we did not visually present the object to be mentally rotated, as participants were asked to imagine a diver spinning in the air while keeping their eyes closed. In addition, unlike the reported studies, there was no reference object to compare to the rotated object. The lack of visual support and a reference object could cause the recruitment of the areas involved in the task to be slightly different or to be recruited to a lesser extent. However, we would like to note that since we did not test the performance of approaches that use anatomical ROIs defined on individual head models,

we cannot disentangle if the lower performance of the LIT approach is due to the head model used or whether it is due to the nature of the ROI.

No significant difference between fVASC and iFMRI layouts

The fVASC and the iFMRI approaches only differed in the number of tissues used during Monte Carlo simulations: the fVASC condition included an additional participant-specific vascular information. Including an additional vascular information did not result in a significant difference compared to the iFMRI layout at the group level. This is mainly because the generated layouts were very similar between them, as indicated by the channel overlap across layouts and the Euclidian distance (Figure 3.6). This high similarity seems to be driven by the functional ROIs, which was the same for both approaches. Our decision to use a small number of optodes for each layout, the constraints to select them, and segmentation-related factors (see the limitations section below) may have also limited the improvements expected from the fVASC approach.

PROB performs similar to iFMRI and fVASC

Here we defined probabilistic functional activation maps for each participant and task from an independent dataset using a leave-one-subject-out scheme. This approach resulted in an improved sensitivity that is comparable with the improvement observed when using individual data of a given participant. Specifically, we observed that CNR and *t*-statistics performed similarly for the PROB approach compared to the iFMRI and fVASC approaches. Further, Figure 3.10 also shows that, descriptively speaking, the peak and average values captured by channels defined based on the PROB approach are closer to those of iFMRI and fVASC approaches than the LIT approach is. This is because PROB approach-based activation maps show high spatial correspondence when compared to the reference fMRI maps for each participant and mental task. Indeed, the average spatial correlation (assessed by Spearman correlation) between probabilistic maps and individual activation was 0.63 when all tasks are considered together and of 0.63 for MC and 0.64 for MR tasks. For IS the values ranged between 0.52 and 0.66. These values, together with the results presented in this study, suggest that using probabilistic maps based on a reasonable number of participants and defined on individual anatomical space can be used for any new participant (as long as the functional maps used to create the probabilistic maps are based on the same task or are closely related to it).

Optode-layout design and its limitations

Cost function, constraints and optimization problem

The optode layout for each of the four approaches consisted of two channels that shared one optode and that maximized the total sensitivity to the preselected ROI. The cost function to be maximized was the same as in Machado et al. (2014), but the algorithmic approach to solve the optimization problem was tailored to account for the constraints imposed by our particular research question(s) and experimental design. This entails that our algorithmic approach may not be (and was not designed to be) generalizable to other experimental designs. Importantly, although the approach by Machado et al. (2014) is very effective in covering focal ROIs, it fails to provide an appropriate solution when the ROI is extended or consists of multiple noncontiguous regions (Machado et al., 2014; Brigadoi et al., 2018), as was the case in this study.

Mental-imagery task selection

From the three mental-imagery tasks participants had to perform inside the MRI scanner, each participant performed two tasks during the fNIRS session. The selection of these two tasks was subject-specific and followed several pre-defined criteria. Combining approach-specific layouts for both mental-imagery tasks caused incompatible source and detector placements in some participants. The decisions taken to overcome these problems, together with the subject-specific task selection led to an unequal number of participants for each task (N_{IS} = 2, N_{MC} = 14, N_{MR} =12), which made the group analysis for IS task unfeasible. To overcome the incompatibility problem, future studies could test the performance of different layouts in different runs/sessions (by using a given layout at a time), whose order could be counter-balanced to account for run/session effects. In addition, a single mental-imagery task could be studied at a time (instead of multiple tasks as in this study).

Monte Carlo simulations

Our light sensitivity profiles may contain estimation errors due to a number of simplifications. First, the head models used in this study did not consider that the skull can contain cancellous and cortical bone, and the soft tissue may contain fat and muscle that have different optical properties (Herrera-Vega et al., 2017). Second, both sources and detectors were modeled as pencil sources instead of separately being modelled according to

their function (they emit or detect light) and technical characteristics. Third, we did not distinguish between arteries and veins when defining the head model. Even if our decision can be justified by the relatively small difference in optical properties between veins and arteries compared to the remaining tissues, we cannot discard potential divergence in the results if arteries and veins had been distinguished. Optical properties also differ depending on the diameter of blood vessels (Rajaram et al., 2010), which we did not take into account in the current study. Finally, our vascular maps depended on manual segmentation procedures, which may have introduced variability. Future studies may overcome these limitations by mapping superficial (scalp/skull) vasculature with more optimized MRI sequences (Rhéaume et al., 2017), and by distinguishing between arteries and veins and their diameters (Bizeau et al., 2017; Bernier et al., 2018).

Implications for BCI applications

In fNIRS-BCI applications for motor-independent communication and control, brain responses from a set of tasks are discriminated by exploiting information in distributed patterns of brain activity using multi-channel pattern analysis (the equivalent to multi-voxel pattern analysis in fMRI studies). Alternatively, univariate analysis in combination with temporal encoding paradigms can be used, where participants perform a (number of) task(s) in a specific time window and evoke brain activation in a single (distinct) brain location(s) (Sorger et al., 2009; Bardin et al., 2011; Sorger et al., 2012; Nagels-Coune et al., 2017; Benitez-Andonegui et al., 2020; Nagels-Coune et al., 2020). For either approach, it is important to ensure there is a set of channels that contains sufficient task-related information to discriminate responses.

The present study constitutes a relevant pre-step for these BCI applications as it compared approaches that used different amount of individualized information to design task-specific, optimized optode layouts that should result in informative channels. Neurofeedback applications can also benefit from layouts that ensure sufficient task-related information and improved spatial specificity. Our results show that the percent of participants with significant ROI activation increased when expanding the amount of individualized information to create the optode setup, but only until a certain point. Indeed, adding vasculature information did not increase the percent of participants for MC and reduced this number for MR. Although all participants showed significant activation levels for every

mental task during the fMRI run, none of the approaches using fMRI information managed to get all participants to have significant ROIs for MC and MR tasks. It is unclear whether a given level of fMRI activation is enough to guarantee the detection of task-related fNIRS signal. Even if both neuroimaging methods measure the hemodynamic response to neural activity, fNIRS is highly dependent on the individual anatomical features, such as the scalp-brain distance (which differs across the head)), the presence of hair, etc. (Coyle et al., 2005). In addition, our fNIRS results might have been affected by the discrete spatial locations used in this study (130 EEG positions). Spatially unrestricted optode placement would likely improve the results substantially (Machado et al., 2018).

Recommendations for optode placement and the way forward

Effective optode-layout design balances a number of potential tradeoffs. The extended layouts based on the international 10-20 system or its extensions can be used to study functional network dynamics and are adequate when target ROIs are not easy to define (Machado et al., 2018). In addition, although the target ROI may not be optimally sampled (due to unavoidable "blind spots", i.e., regions not covered by a source-detector pair, when creating optode layouts and the lower spatial resolution associated to fNIRS compared to fMRI), the chance of completely missing it is relatively low. That said, smaller setups are preferred in fNIRS-BCI applications due to their superior practicability and patient comfort. However, they run a much higher risk of missing signal from the target ROI due to anatomical or functional differences between individuals. As a result, small BCI setups are likely to benefit from supplementary f/MRI data investigated in the present work. The recommendations and conclusions presented here therefore focus on this particular fNIRS application.

Considering that any additional individualized information has an associated acquisition/analysis cost, it is worth asking, especially when temporal/monetary/material resources are limited: how much individual information is worth to include for designing optode layouts? Figure 3.11 shows the predicted percent improvement in performance (in terms of *t*-statistics [top] and CNR [bottom]) *vs.* the additional time required to acquire/analyze the data relative to the LIT layout, here considered the "baseline" approach. Points above the line indicate that the percent improvement of a given performance measure is higher than the temporal resources spent to achieve that gain. The figure suggests that

including individual anatomical data (PROB layout) or including both, individual anatomical and functional data (iFMRI layout), improves the performance while efficiently using temporal resources. It also suggests that the fVASC approach in its current form is not as cost-effective.

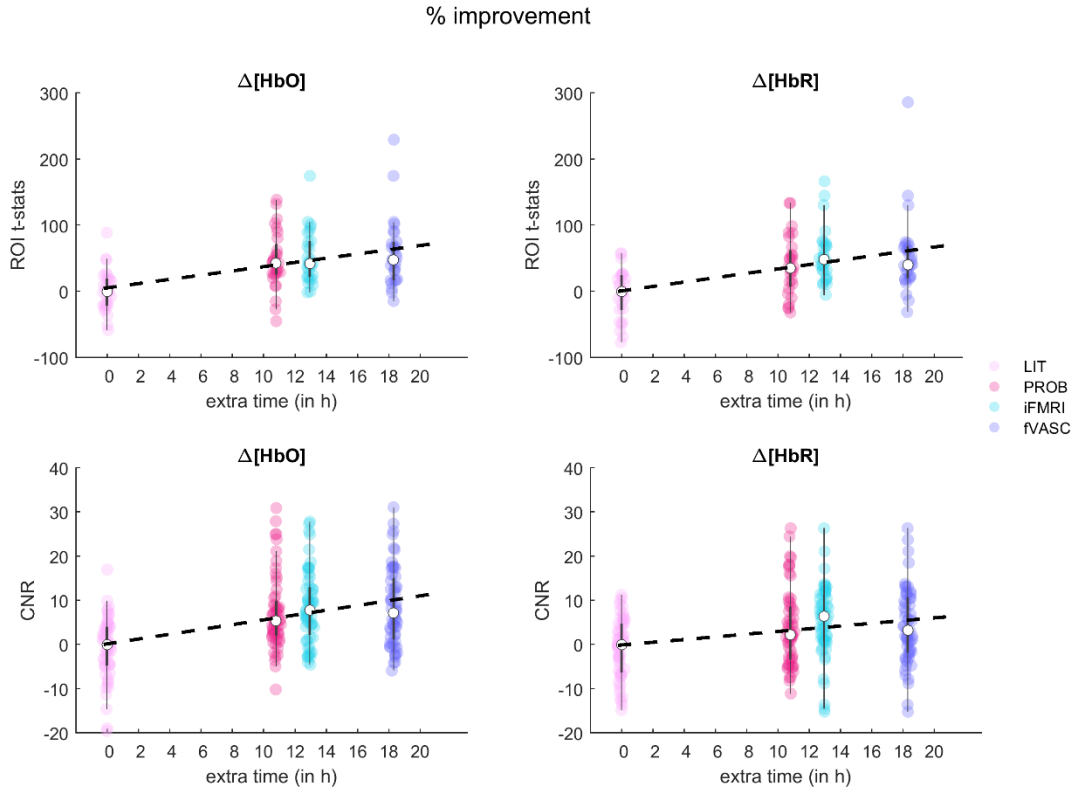

Figure 3.11. Percent improvement in performance (in terms of *t*-statistics (a) and CNR (b)) *vs.* the additional time required to acquire/analyze the data (in hours). All values are relative to the LIT approach (in light pink), here considered the "baseline". The bigger white circles represent the median of the percent improvement in *t*-statistics/CNR values for each layout when all three tasks are considered together. The dashed line represents the predicted percent improvement in performance for a given processing time. Points above/below the line indicate that the percent improvement of a given performance measure is higher/lower than the temporal resources spent to achieve that gain.

The analysis described above focused only on a small part of the multi-dimensional problem related to cost-effectiveness. Naturally, costs and benefits of including more individualized information for creating clinically practical layouts should be assessed in that very context. For example, in certain (rare) cases such as long-term BCIs in 'locked-in' patients, using individual (f)MRI data may result in increased ability to communicate, i.e., provide

considerable benefit. In that case, even though using individual (f)MRI is more resource-demanding, the benefits could outweigh the costs.

In view of these observations, we encourage researchers to use individual functional and anatomical data for designing optode layouts when possible, but when anatomical data is available and functional data is not, probabilistic functional maps constitute a promising and economic alternative. FMRI-based probabilistic functional maps of the human ventral occipital cortex (Rosenke et al., 2020), human motion complex (Huang et al., 2019), face selective areas (Tahmasebi et al., 2012; Zhen et al., 2015), finger dominance in the primary somatosensory cortex (O'Neill et al., 2020) or across the whole cortex (Frost and Goebel, 2012) are freely available or available on demand. However, we could not find any published work on probabilistic mental-imagery maps, which could be beneficial for optode placement in BCI research. To improve this situation, the probabilistic functional maps of the three mental-imagery tasks used in this study (in MNI space) are available upon request. Finally, in the absence of functional and anatomical information, ROI selection should be guided by relevant body of work or meta-analyses that describe tasks closely related to the ones to be used during the fNIRS session. In parallel, a larger setup could be initially employed in a "localizer" run to determine the most informative channels which could be subsequently scaled down to consider only the most informative channels. In the present study, once the target ROIs were selected, we used FOLD (Zimeo Morais et al., 2018) for designing our optode layout due to its user-friendly features. However, other toolboxes such as Array Designer (Brigadoi et al., 2018) and software, such as NIRStorm (a *BrainStorm* plugin for fNIRS analysis (Tadel et al., 2011)), also offer promising and flexible tools that were not explored in the present study.

5 Conclusions

In this paper, we compared four approaches to design small fNIRS optode layouts that represent various scenarios research groups may encounter when planning fNIRS-BCI experiments. By providing the insights of such comparisons, we hope to have offered an informative framework so that researchers can efficiently use resources for developing robust and convenient fNIRS-BCI systems for clinical use.

6 Supplementary Material

6.1 Materials and Methods

6.1.1 Preprocessing and analysis of functional MRI data

fNIRS coverage mask definition

A whole-head mask was created for each participant from the bias-corrected structural image. Each mask was iteratively eroded 50 times and all voxels that did not belong to this eroded mask were selected and intersected with the original head mask. The 'surviving' voxels were used to mask out active voxels from deeper regions, as we did not expect the fNIRS signal to be sensitive to these regions (Strangman et al., 2013).

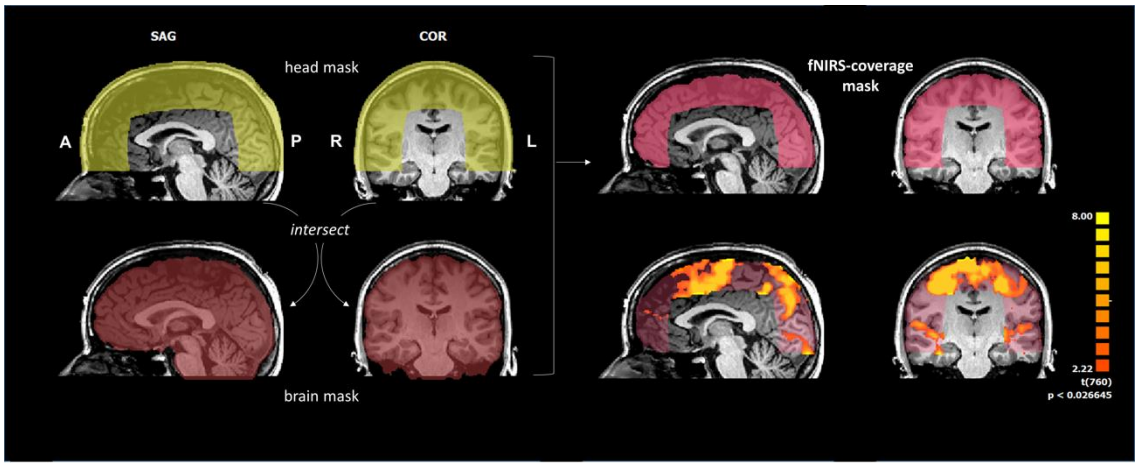

Figure S3.1. fNIRS-coverage mask definition and application. An fNIRS-coverage mask was created by the intersection of the eroded head mask and the brain mask, and it was used to mask out the active voxels from deeper regions. The activation map depicted in this figure resulted from the MR vs. Rest contrast for a representative participant. The activation map was corrected using a cluster-extent threshold at 5%.

Probabilistic functional maps

We defined subject-specific probabilistic functional maps based on an independent sample, i.e., the functional data from the remaining individuals. Figure S3.2 depicts an example of probabilistic functional maps for each of the mental-imagery task, from a left, top and right view. Colors represent the percent overlap of significant activation across participants for a task vs. rest contrast (corrected with a cluster threshold that allowed for a 5% loss of active voxels).

Vascular segmentations and reconstructions

Figure S3.3 summarizes the steps carried out for segmenting cerebral, pial and scalp vessels and Figure S3.4 depicts the resulting vascular reconstruction for a sample participant. Cerebral/pial vessels are shown in blue, while scalp vessels are shown in red. Scalp vasculature segmentation required more manual corrections than the cerebral/pial vasculature segmentation.

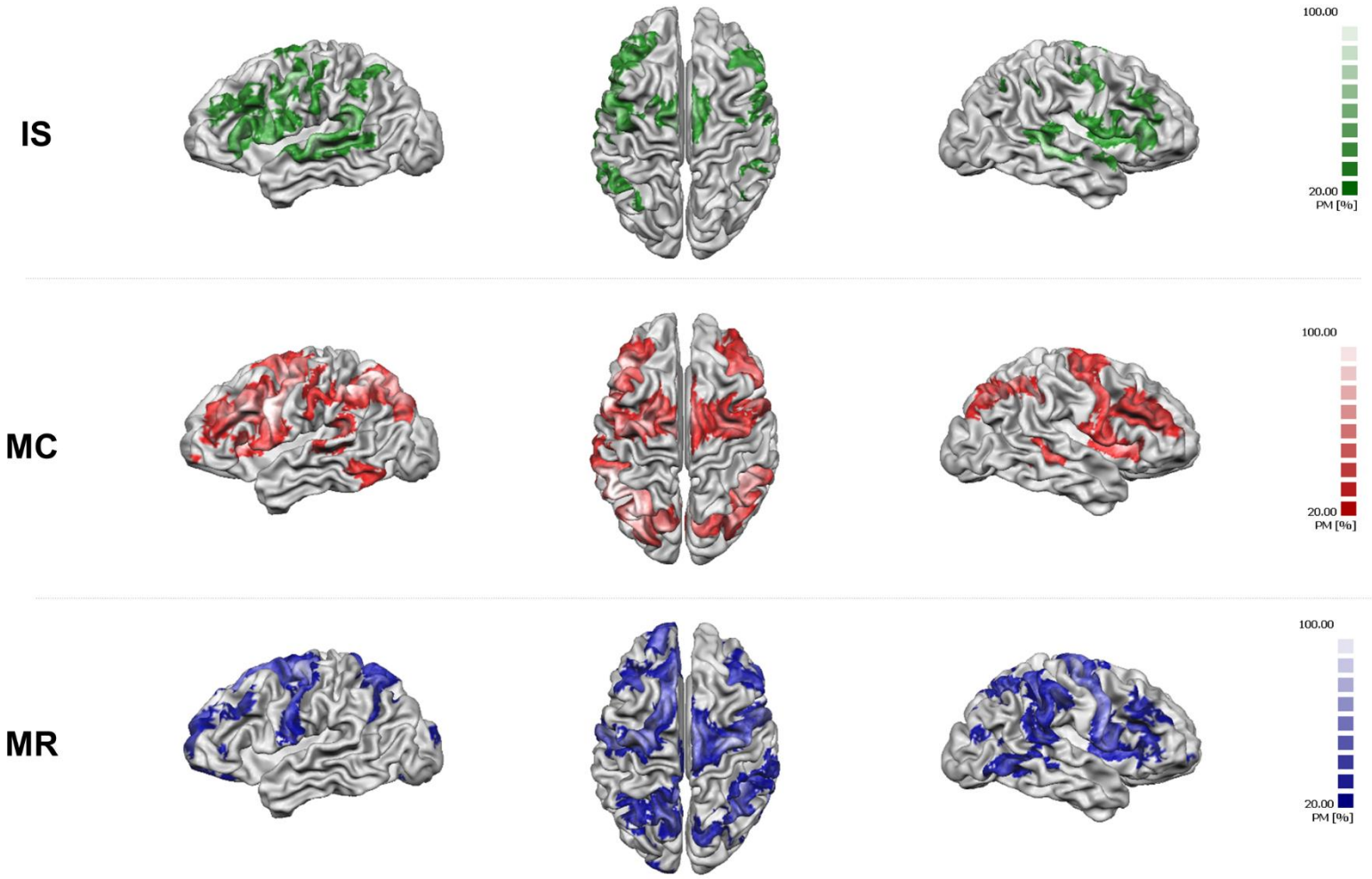

Figure S3.2. Example of functional probabilistic maps (left, top and right view) for each mental-imagery task (IS= inner speech; MC = mental calculation; MR = mental rotation).

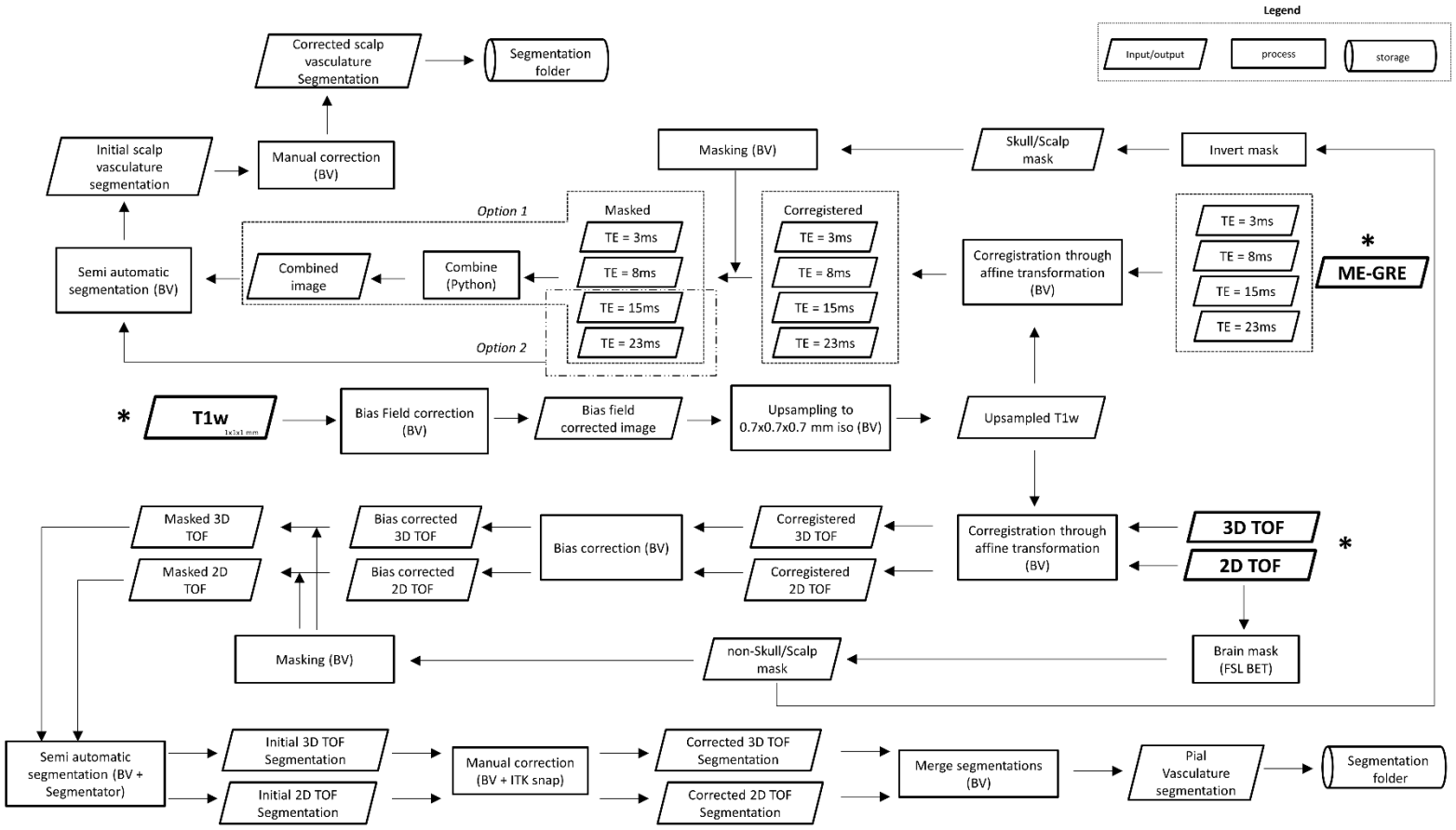

Figure S3.3. Steps involved in vascular data segmentation for each participant. Asterisks indicate starting points in the pipeline. BV = Brainvoyager QX; TOF = time-of-flight; T1w = structural (MPRAGE) image; ME-GRE: multi-echo gradient echo images.

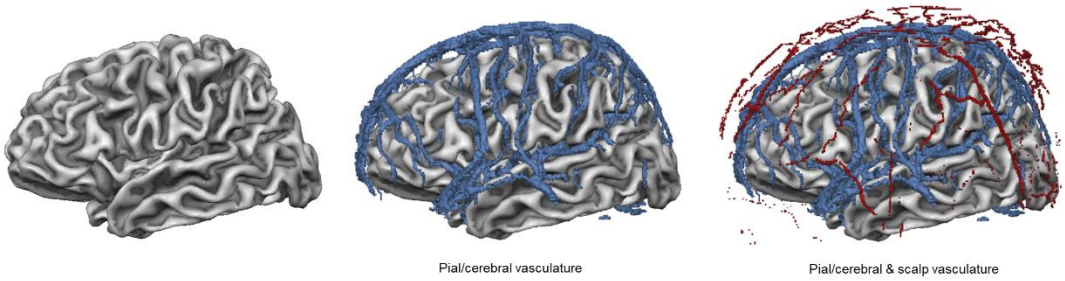

Figure S3.4. Example of vascular reconstructions (P16). Left. Cortical reconstruction (left hemisphere). Middle. Pial/cerebral vasculature reconstruction (in blue) overlaid onto the cortical mesh. Right. Scalp vasculature reconstruction (in red) overlaid onto the cortical mesh and the pial/cerebral vasculature reconstruction.

6.1.2 Optode layout creation

Monte Carlo simulations

Head models

Figure S3.5 shows the head models used for PROB (left figure), iFMRI (left figure) and fVASC (right figure) during Monte Carlo simulations. Both figures differ in the amount of tissues included: while the left figure represents a five-tissue model, the right figure includes a sixth tissue (vascular structures). Importantly, we did not distinguish between arteries and veins.

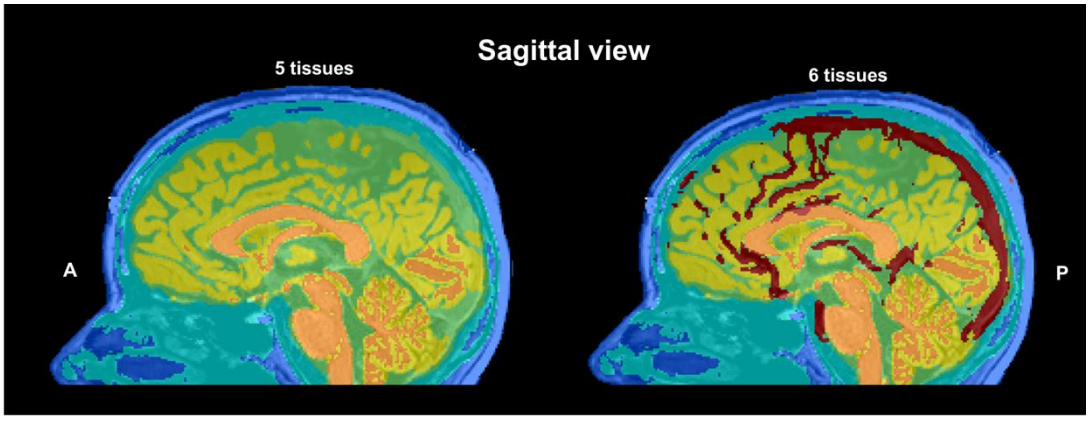

Figure S3.5. Example head model (P01) used for Monte Carlo simulations. (Left) Five-tissue model used for PROB and iFMRI. (Right) Six-tissue model used for fVASC.

Optical properties for vascular structures

The oxygen saturation of blood (SO_2) is defined as the ratio of the HbO_2 concentration to the total hemoglobin concentration, where SO_2[Arteries] ~ 97.5% and SO_2[Veins] ~ 75%. Bosschaart et al. (2014) reported optical coefficients for a range of wavelengths and SO_2 of 98% and SO_2 of 0%. SO_2=98% can be considered an approximation of the arterial blood and a combination of both (SO_2=98% and SO_2=0%) can be used to approximate the venous blood:

$$SO_2[\text{Veins}] = 0.75 \times SO_2[98\%] + 0.25 \times SO_2[0\%] \quad (3.6)$$

Table S3.1. Optical values reported in Bosschaart et al. (2014) for the four wavelengths used in the present study.

	proposed model						empirical data		
λ (nm)	**μs SO2 (98%)**	**μs SO2 (0%)**	**μs SO2 (75%)**	**g SO2 (98%)**	**g SO2 (0%)**	**g SO2 (75%)**	**μa SO2 (98%)**	**μa SO2 (0%)**	**μa SO2 (75%)**
690	85,84	75,63	83,2875	0,9843	0,9852	0,9845	0,13	1,17	0,39
750	77,04	67,62	74,685	0,9827	0,9836	0,9829	0,24	0,81	0,3825
780	72,59	63,73	70,375	0,9819	0,9827	0,9821	0,33	0,59	0,395
830	66,96	58,72	64,9	0,9804	0,9812	0,9806	0,46	0,43	0,4525

Note: The scattering (μs) and anisotropy (g) parameters were based on a mathematical model (proposed model, column 1 in the present table), while the absorption parameters (μa) based on empirical data (column 2). The columns in grey correspond to optical values for venous blood which was calculated based on a weighted sum of SO2 98% and 0% values (equation 1).

Table S3.2. Optical properties of arterial and venous blood based on the optical values reported in Bosschaart et al. (2014).

	μa	**μs**	**g**
Arterial blood (SO2 98%)	0,29	75,6075	0,982325
Venous blood (SO2 75%)	0,405	73,311875	0,982525

Note: Values were computed as the average of four wavelengths used in the present study.

LIT approach: ROI definition

Studies included in the literature review

We used the PubMed database and keywords for the search included: 'inner speech', 'covert speech', 'mental talking' and 'overt speech' for inner speech (overt speech was also included as both covert and overt speech share common networks, see, *e.g.*, Martin et al. (2014)); 'mental calculation' and 'mental arithmetic' for mental calculation; and 'mental rotation' for mental rotation. We included every work that reported using such mental-imagery tasks, independent of the neuroimaging modality and the population under study (see Table S3.3). Note that in the table, WG and WA stand for word generation and word association, respectively.

Selected ROIs

ROIs for each mental-imagery task were selected based on the most-frequent regions reported across studies. This number different across the three tasks (see Table S3.4).

Table S3.3. Selected regions of interest for the LIT-based approach.

Inner Speech (IS)	**Mental Calculation (MC)**	**Mental Rotation (MR)**
L | Inferior Frontal Gyrus (p. Opercularis)	L-R | Middle Frontal Gyrus	L-R | Superior Parietal Lobule
L | Inferior Frontal Gyrus (p. Triangularis)	R | Angular Gyrus	L-R | Inferior Parietal Lobule
L | Superior Temporal Gyrus	L | Superior Frontal Gyrus	L | Precentral Gyrus
L | Supramarginal Gyrus		L-R | Middle Frontal Gyrus
L | Rolandic Operculum		L-R | Middle Occipital Gyrus
L | Precentral Gyrus		

Note: L = left hemisphere; R = right hemisphere

Table S3.4. Literature review used to select ROIs for the LIT approach.

Author	Title paper	Task		Method
Shergill et al. (2001)	A functional study of auditory verbal imagery	IS		fMRI
Baciu et al. (1999)	fMRI assessment of hemispheric language dominance using a simple inner speech paradigm	IS		fMRI
Fujimaki et al. (2004)	Right-lateralized neural activity during inner speech repeated by cues	IS		fMRI + MEG
Hurlburt et al. (2016)	Exploring the Ecological Validity of Thinking on Demand: Neural Correlates of Elicited vs. Spontaneously Occurring Inner Speech	IS		fMRI
Girbau (2014)	A Neurocognitive Approach to the Study of Private Speech	IS		fMRI, PET, ERP, MEG
Cannestra et al. (2003)	Functional assessment of Broca's area using near infrared spectroscopy in humans	IS		fNIRS
Wan et al. (2018)	A functional near-infrared spectroscopic investigation of speech production during reading	IS		fNIRS
Zhang et al. (2017)	Signal processing of functional NIRS data acquired during overt speaking	IS		fNIRS
Aziz-Zadeh et al. (2005)	Covert Speech Arrest Induced by rTMS over both Motor and Nonmotor Left Hemisphere Frontal Sites	IS		rTMS
Martin et al. (2016)	Word pair classification during imagined speech using direct brain recordings	IS		ECOG
Yoo et al. (2004)	Brain computer interface using fMRI: spatial navigation by thoughts	IS	MC	fMRI
Sereshkeh et al. (2018)	Online classification of imagined speech using functional near-infrared spectroscopy signals	IS		fNIRS + EEG
Herff et al. (2012)	Cross-Subject Classification of Speaking Modes Using fNIRS	IS		fNIRS
Morin and Michaud (2007)	Self-awareness and the left inferior frontal gyrus: Inner speech use during self-related processing	IS		fMRI [review]
Verner et al. (2013)	Cortical oxygen consumption in mental arithmetic as a function of task difficulty: a near-infrarred spectroscopy approach		MC	fNIRS
Pfurtscheller et al. (2010)	Focal frontal (de)oxygemoglobin responses during simple arithmetic		MC	fNIRS
Kawashima et al. (2004)	A functional MRI study of simple arithmetic - a comparison between children and adults		MC	fMRI
Rickard et al. (2000)	The calculating brain: an fMRI study		MC	fMRI
Power et al. (2012)	Automatic single-trial discrimination of mental arithmetic, mental singing and the no-control state from prefrontal activity: toward a three-state NIRS-BCI		MC	fNIRS
Shin et al. (2016)	Near-infrared spectroscopy (NIRS)-based eyes-closed brain-computer interface (BCI) using prefrontal cortex activation due to mental arithmetic		MC	fNIRS
Naito et al. (2007)	A Communication Means for Totally Locked-in ALS Patients Based on Changes in Cerebral Blood Volume Measured with Near-Infrared Light		MC	fNIRS

Weyand and Chau (2015)	Correlates of Near-Infrared Spectroscopy Brain–Computer Interface Accuracy in a Multi-Class Personalization Framework	WG	MC		fNIRS
Bauernfeind et al. (2008)	Development, set-up and first results for a one-channel near-infrared spectroscopy system		MC		fNIRS
Ogata et al. (2007)	A Study on the Frontal Cortex in Cognitive Tasks using Near-Infrared Spectroscopy	WG	MC		fNIRS
Utsugi et al. (2007)	Development of an Optical Brain-machine Interface	WG	MC		fNIRS
Ang et al. (2012)	Extracting and selecting discriminative features from high density NIRS-based BCI for numerical cognition		MC		fNIRS
Schudlo et al. (2013)	Dynamic topographical pattern classification of multichannel prefrontal NIRS signals		MC		fNIRS
Schudlo and Chau (2013)	Dynamic topographical pattern classification of multichannel prefrontal NIRS signals: II. Online differentiation of mental arithmetic and rest		MC		fNIRS
Arsalidou and Taylor (2011)	Is 2+2=4? Meta-analyses of brain areas needed for numbers and calculations		MC		FMRI [meta analysis]
Hamada et al. (2018)	Comparison of brain activity between motor imagery and mental rotation of the hand tasks: a functional magnetic resonance imaging study			MR	fMRI
Kawamichi et al. (2007)	Distinct neural correlates underlying two- and three-dimensional mental rotations using three-dimensional objects			MR	fMRI
Shimoda et al. (2008)	Cerebral laterality difference in handedness: A mental rotation study with NIRS			MR	fNIRS
Harris and Miniussi (2003)	Parietal lobe contribution to mental rotation demonstrated with rTMS			MR	TMS
Khan and Hong (2017)	Hybrid EEG-fNIRS-Based Eight-Command Decoding for BCI: Application to Quadrucopter Control	WG	MC	MR	fNIRS and EEG
Tomasino and Gremese (2016)	Effects of Stimulus Type and Strategy on Mental Rotation Network: An Activation Likelihood Estimation Meta-Analysis			MR	PET + FMRI [meta analysis]
Herff et al. (2013)	Classification of mental tasks in the prefrontal cortex using fNIRS	WG	MC	MR	fNIRS
Khalaf et al. (2018)	Towards optimal visual presentation design for hybrid EEG—fTCD brain–computer interfaces	WG		MR	EEG + fTCD
Qureshi et al. (2017)	Enhancing Classification Performance of Functional Near-Infrared Spectroscopy- Brain–Computer Interface Using Adaptive Estimation of General Linear Model Coefficients			MR	fNIRS
Hwang et al. (2014)	Evaluation of various mental task combinations for near-infrared spectroscopy-based brain-computer interfaces		MC	MR	fNIRS
Roberts and Bell (2003)	Two- and three-dimensional mental rotation tasks lead to different parietal laterality for men and women			MR	EEG
Tagaris et al. (1998)	Functional magnetic resonance imaging of mental rotation and memory scanning: a multidimensional scaling analysis of brain activation patterns			MR	fMRI
Alivisatos and Petrides (1997)	Functional activation of the human brain during mental rotation			MR	PET
Friedrich et al. (2013)	Whatever Works: A Systematic User-Centered Training Protocol to Optimize Brain-Computer Interfacing Individually	WA	MC	MR	EEG

Mental-imagery task-pair selection process for fNIRS session

We carried out the task-pair selection at the individual subject level. For that, we first calculated the number of overlapping channels across all four layouts for each mental-imagery task, and selected the two tasks with the least number of overlapping channels. We computed the center of gravity (COG) for all four layouts per mental-imagery task in case this approach was not sufficient to select the two tasks (indicated with ? in Table S3.5). The mental tasks with the least number of overlapping channels and highest distance between them were the selected tasks.

Table S3.5. Summary of the steps involved in selected the task-pair for each participant.

	1st criterion: min # of overlapping channels between tasks			Result →		*2nd criterion: max distance between tasks*			Result →		*Change selected task pair if original combination proofs incompatible*		
	Overlapping channels			Selected task pair		**Distance between COGs (mm)**			Selected task pair		Conflict?	Selected task pair	
	IS	MC	MR			**IS**	**MC**	**MR**					
P01	2	2	0	?	MR	27,50	45,50	137,35	MC	MR	No	MC	MR
P02	0	0	2	IS	MC	136,18	173,11	106,48	IS	MC	No	IS	MC
P03	1	2	1	IS	MR	68,60	157,62	193,71	IS	MR	No	IS	MR
P04	2	1	0	MC	MR	107,60	187,46	195,29	MC	MR	No	MC	MR
P05	1	2	0	IS	MR	132,13	59,89	87,30	IS	MR	**YES**	IS	MC
P06	2	2	0	?	MR	71,25	120,98	206,58	MC	MR	No	MC	MR
P09	2	2	0	?	MR	143,84	152,83	212,09	MC	MR	No	MC	MR
P10	2	2	2	?	?	81,36	192,21	175,89	MC	MR	No	MC	MR
P11	3	2	2	MC	MR	75,69	74,12	123,46	MC	MR	No	MC	MR
P14	2	2	0	?	MR	65,48	145,50	226,89	MC	MR	No	MC	MR
P15	2	2	2	?	?	72,95	155,34	154,82	MC	MR	No	MC	MR
P16	1	1	2	IS	MC	107,86	220,43	164,65	IS	MC	**YES**	MC	MR
P17	0	2	0	IS	MR	112,77	163,57	237,51	IS	MR	**YES**	MC	MR
P19	1	2	2	IS	?	213,88	147,34	150,48	IS	MR	**YES**	MC	MR
P20	3	2	0	MC	MR	48,38	138,12	189,18	MC	MR	No	MC	MR
P21	2	2	1	?	MR	201,47	139,88	207,34	IS	MR	No	IS	MR

Subject-specific optode layout for the selected mental-imagery task pair

Figure S3.6 illustrates schematically the selected optode layout for each participant (top view). The optode layouts for each mental-imagery task have been separated in these plots for clarity.

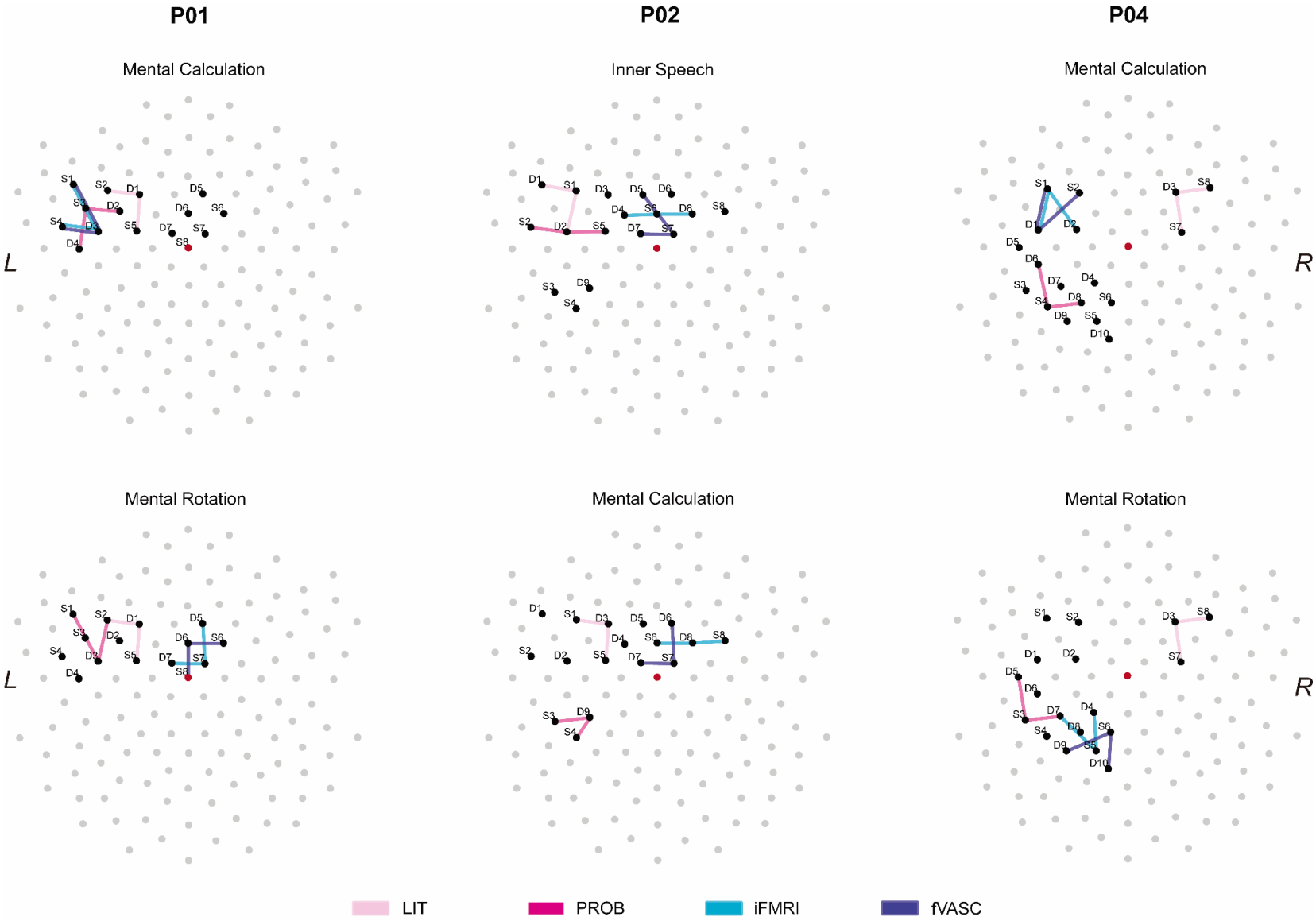
P01
P02
P04
Mental Calculation
Inner Speech
Mental Calculation
Mental Rotation
Mental Calculation
Mental Rotation
L
R
LIT
PROB
iFMRI
fVASC

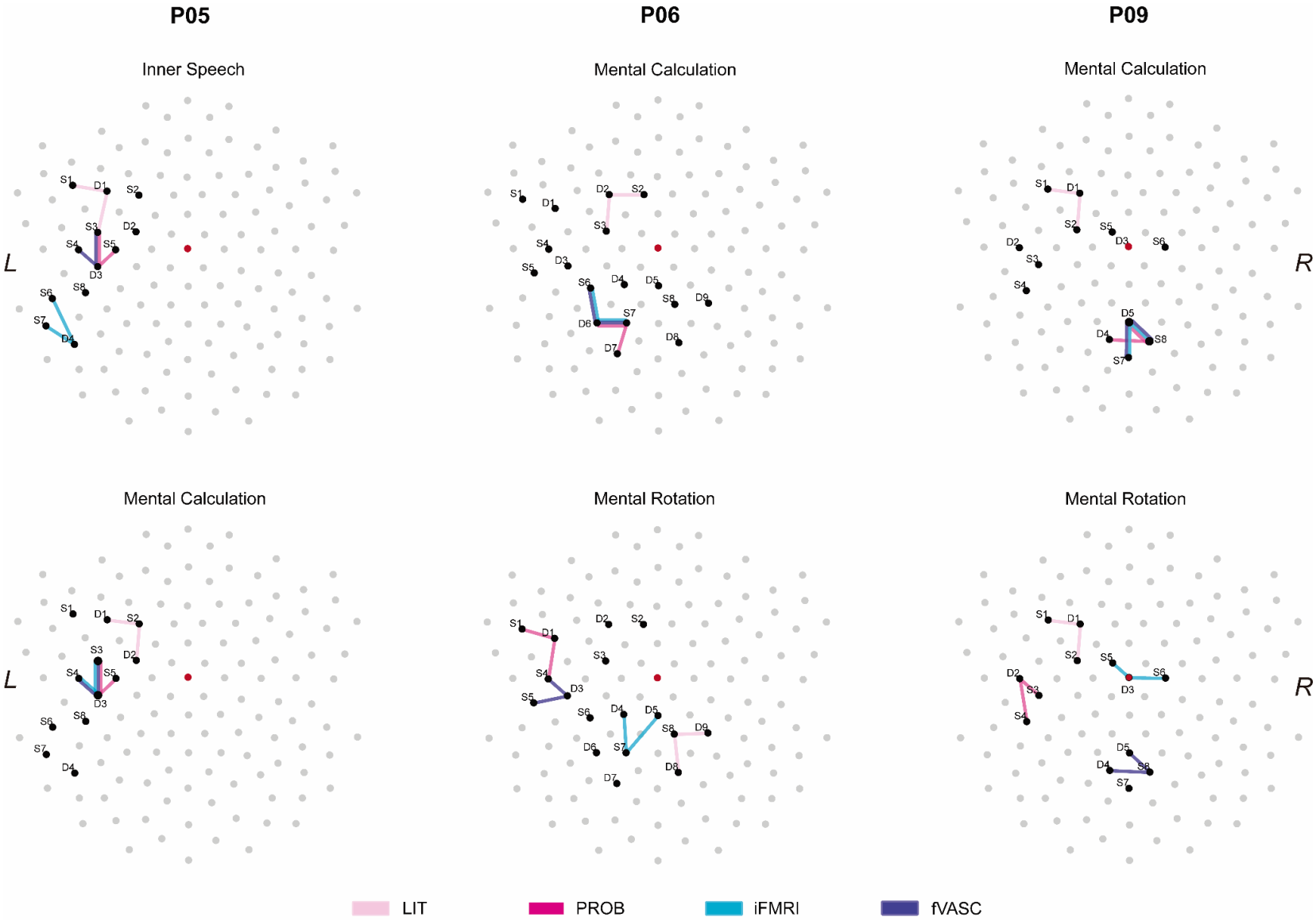
P05
P06
P09
Inner Speech
Mental Calculation
Mental Calculation
Mental Calculation
Mental Rotation
Mental Rotation
L
R
LIT
PROB
iFMRI
fVASC

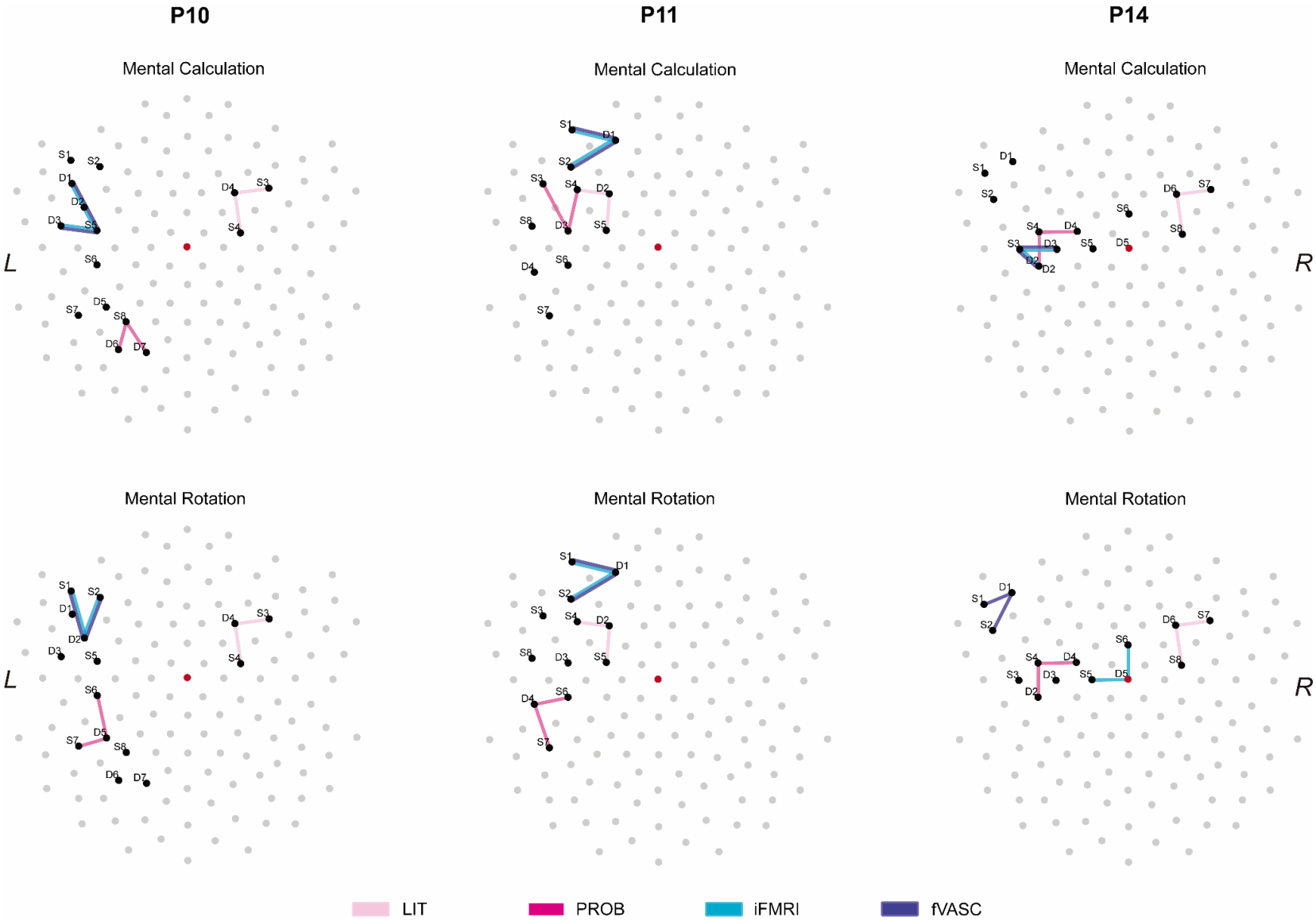
P10
P11
P14
Mental Calculation
Mental Calculation
Mental Calculation
Mental Rotation
Mental Rotation
Mental Rotation
L
R
LIT
PROB
iFMRI
fVASC

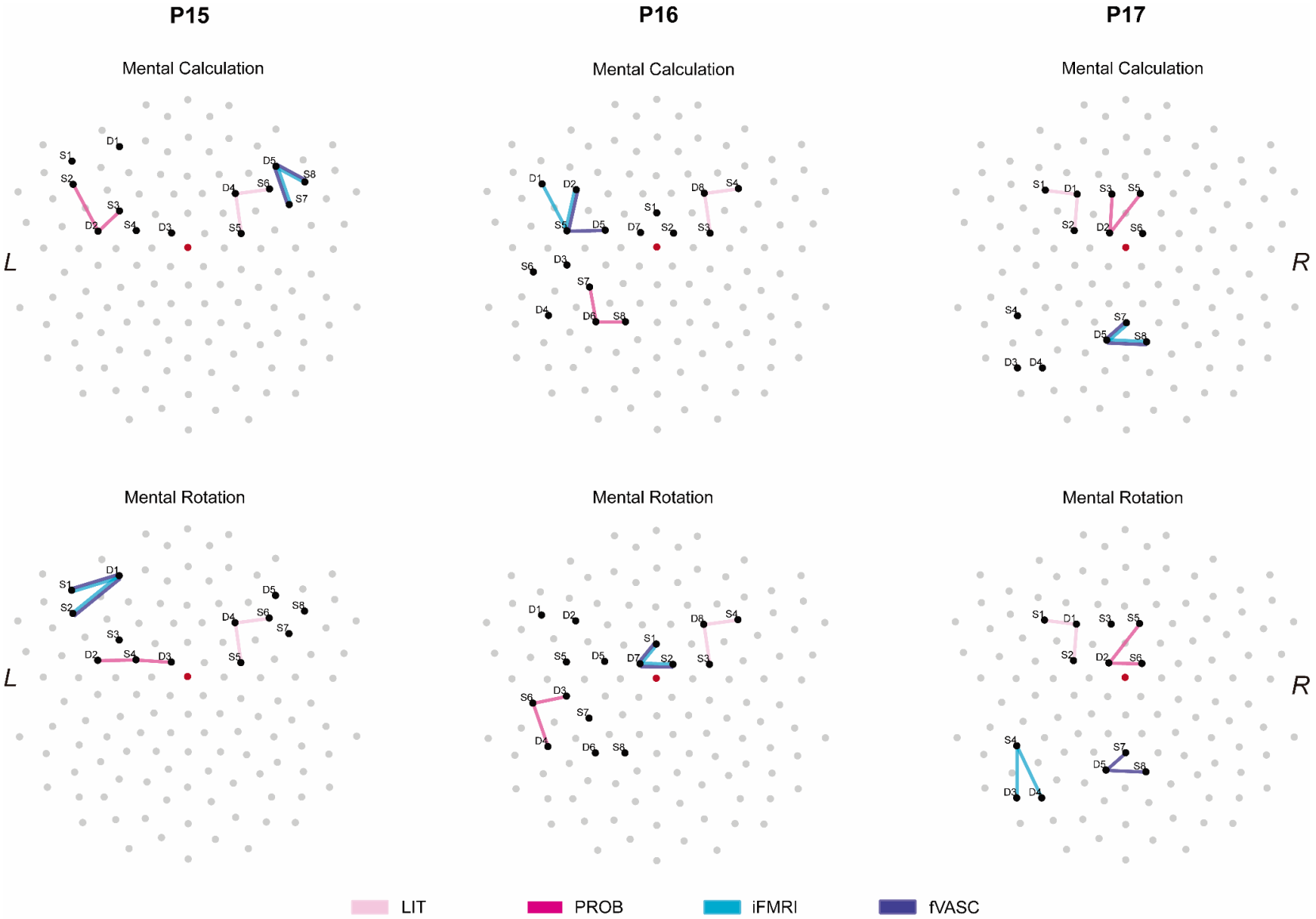
P15
P16
P17
Mental Calculation
Mental Calculation
Mental Calculation
Mental Rotation
Mental Rotation
Mental Rotation
L
R
LIT
PROB
iFMRI
fVASC

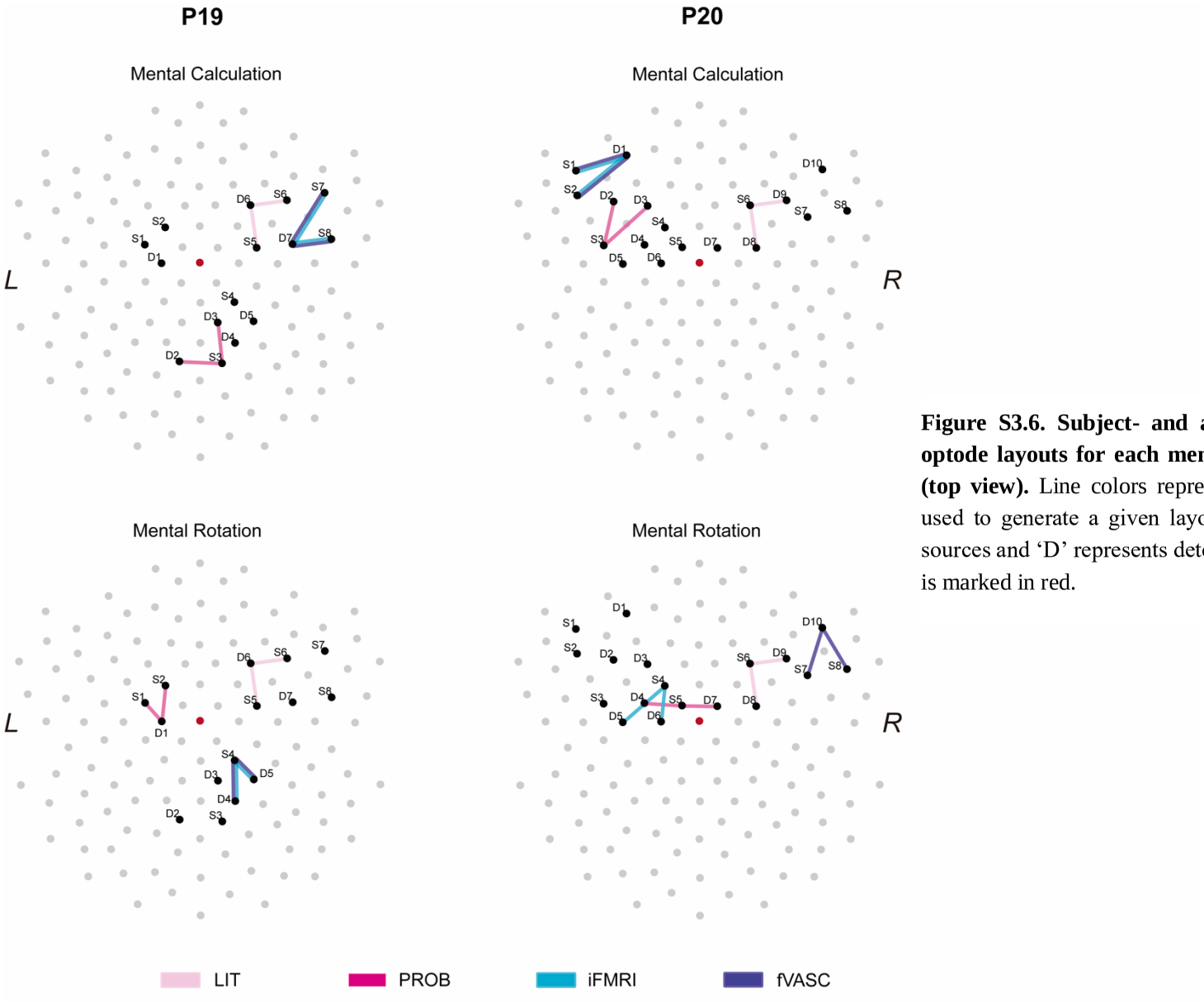

Figure S3.6. Subject- and approach-specific optode layouts for each mental-imagery task (top view). Line colors represent the approach used to generate a given layout. 'S' represents sources and 'D' represents detectors. Cz location is marked in red.

6.1.3 Data analysis

Data quality and presence of motion artifacts assessment

We computed the coefficient of variation (CV) to quantify the signal quality in each channel. Channels with CV >=7.5% were discarded from subsequent analyses. Figure S3.7 shows the percent of channels that fulfilled the CV criterion for each participant.

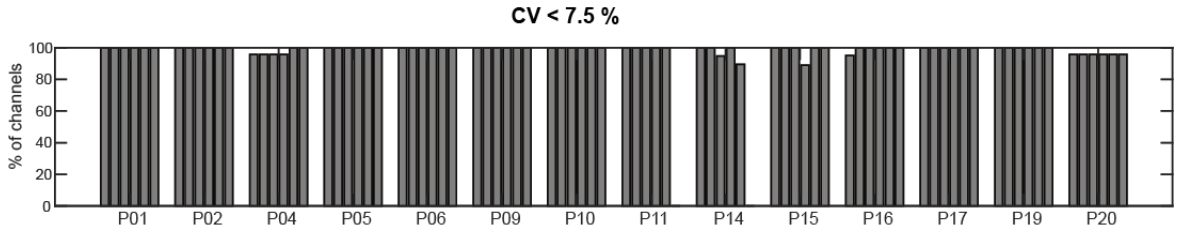

Figure S3.7. This figure shows the percent of channels (y-axis) across runs and participants (x-axis) that survived the CV threshold of 7.5%. Almost all channels met the CV criterion across participants.

The top panel of Figure S3.8 summarizes the detected motion events per channel and run for each participant. The bottom panel provides cumulative motion events across channels and runs for participant P14.

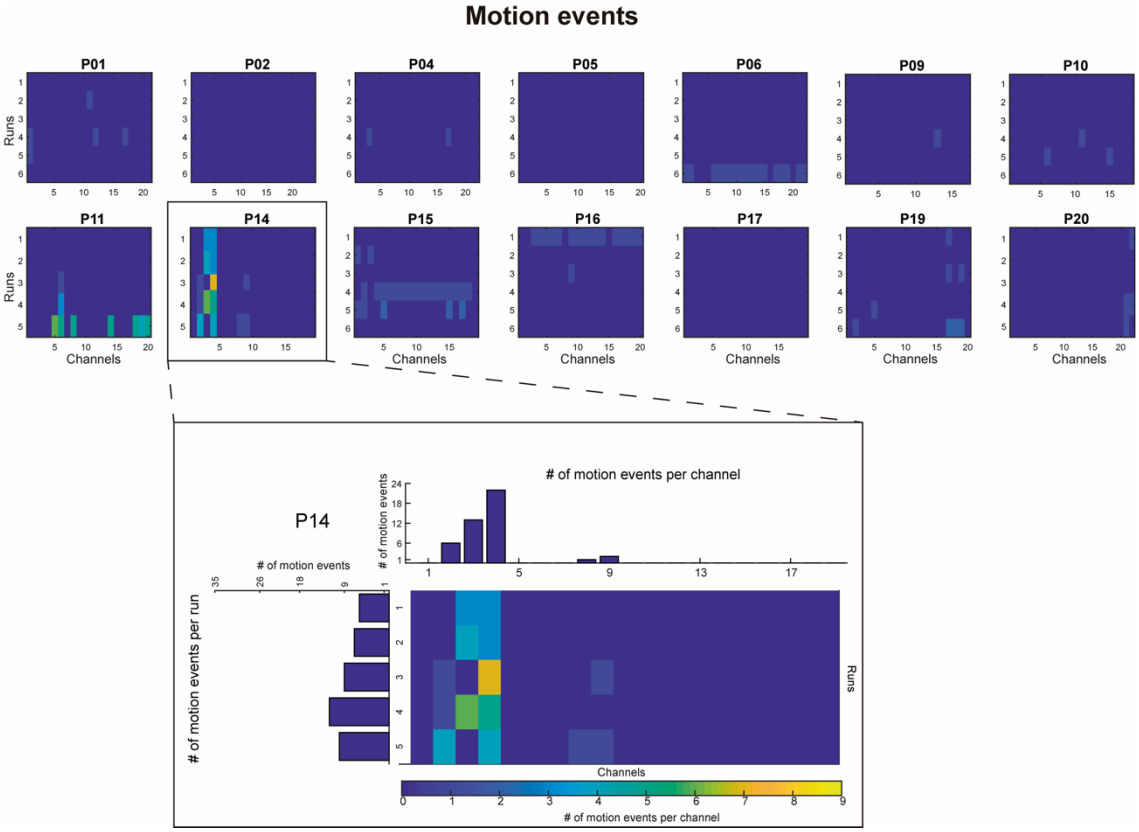

Figure S3.8. Motion artifacts. Top. Presence of motion artifacts across channels (x-axis in subplot), runs (y-axis in subplot) across participants. The color in each cell indicates the frequency of detected motion artifacts within a run for a given channel. Note that the number of channels and runs were different across participants. Bottom. Closer look into the motion artifacts in participant P14. The top histogram shows the cumulative number of motion events across runs for a given channel, while the histogram on the left shows the cumulative motion events over channels for a given run.

6.2 Results

6.2.1 Frequency maps

We computed frequency maps for each mental-imagery task and approach to assess the spatial agreement of the selected channels across participants. The frequency maps shown in Figure S3.9 indicate that the selected channels varied considerably across subjects for PROB, iFMRI and fVASC approaches. In addition, iFMRI and fVASC approaches (the two most individualized ones) show the highest and most similar spatial extension for MC and MR. It is important to note that the (low) variability observed in the LIT approach is due to

the use of the minimal individual anatomical information during the channel selection step (see Section 2.3.2.2).

6.2.2 Examples of typical and weak/inverted hemodynamic responses

Figure S3.10 (a) shows examples of four participants with typical hemodynamic responses (a positive deflection in Δ[HbO] and a negative deflection in Δ[HbR]) for a given approach, together with the projected activation on individual cortex reconstructions. Figure S3.10 (b) shows examples of four participants with weak/inverted hemodynamic responses.

6.3 Discussion

6.3.1 Correspondence between fMRI and fNIRS block averages

Figure S3.11 shows the correspondence between fMRI and fNIRS block averages calculated from channels placed according to the four approaches, for participants P01 and P16 during MR and MC tasks, respectively. We used channel-specific projection weights and projection spheres to compute spatially weighted fMRI block averages of the regions where the fNIRS signal most likely originated (see section 2.3.5.8 for details). The figure shows that channels placed based on approaches that use more individualized information show a better agreement with fMRI block averages. In addition, channels in close proximity can capture considerably different responses (see P01).

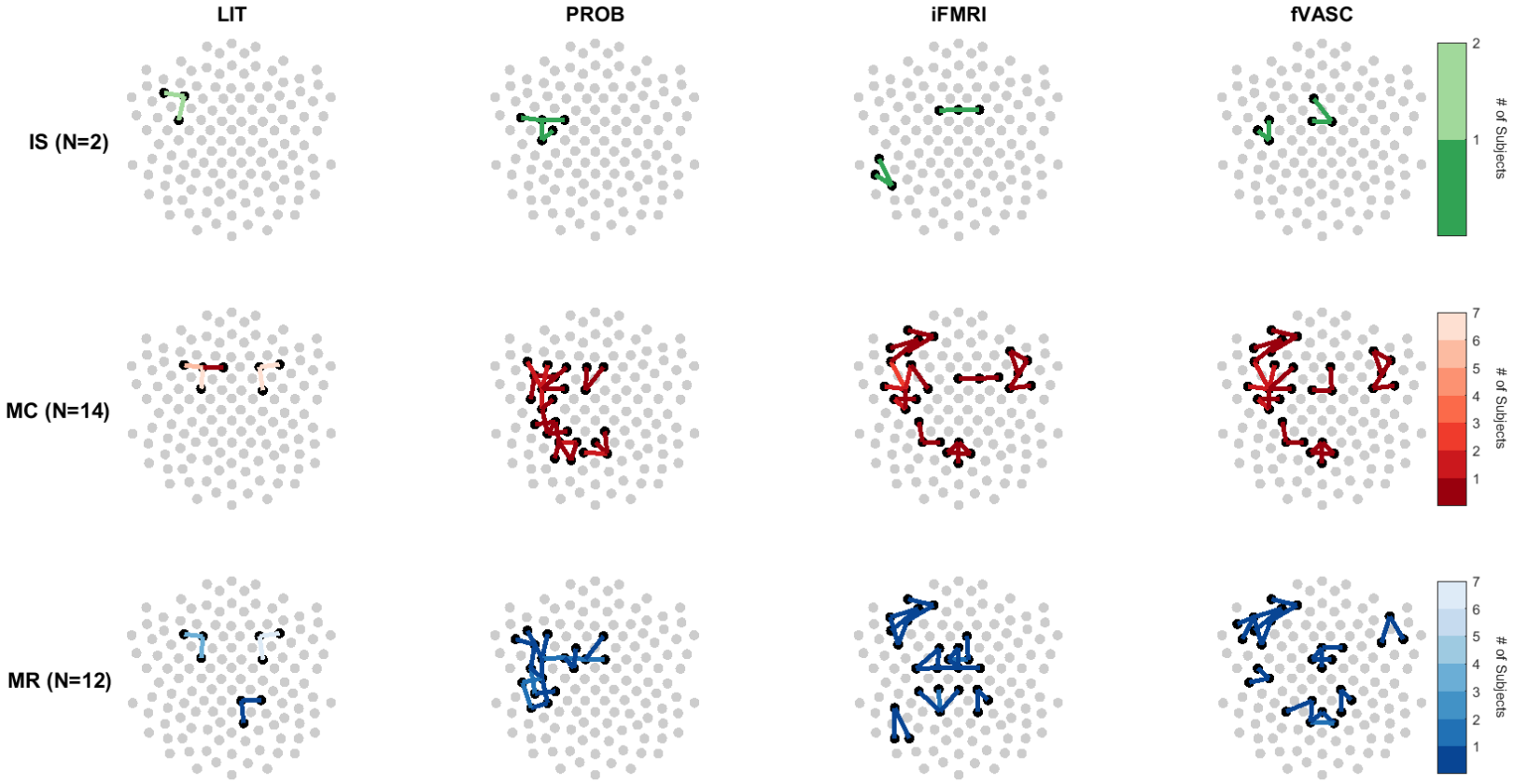

Figure S3.9. Top view of the channel frequency maps for each mental-imagery task (rows) and approach (columns). Black dots indicate the locations where optodes were placed, while grey dots represent all 130 locations optodes could be located. Channels are indicated with lines and their colors indicate the number of participants who used a given channel. The selected channels vary considerably across subjects for PROB, iFMRI and fVASC approaches. iFMRI and fVASC approaches show highest similarity and spatial extent.

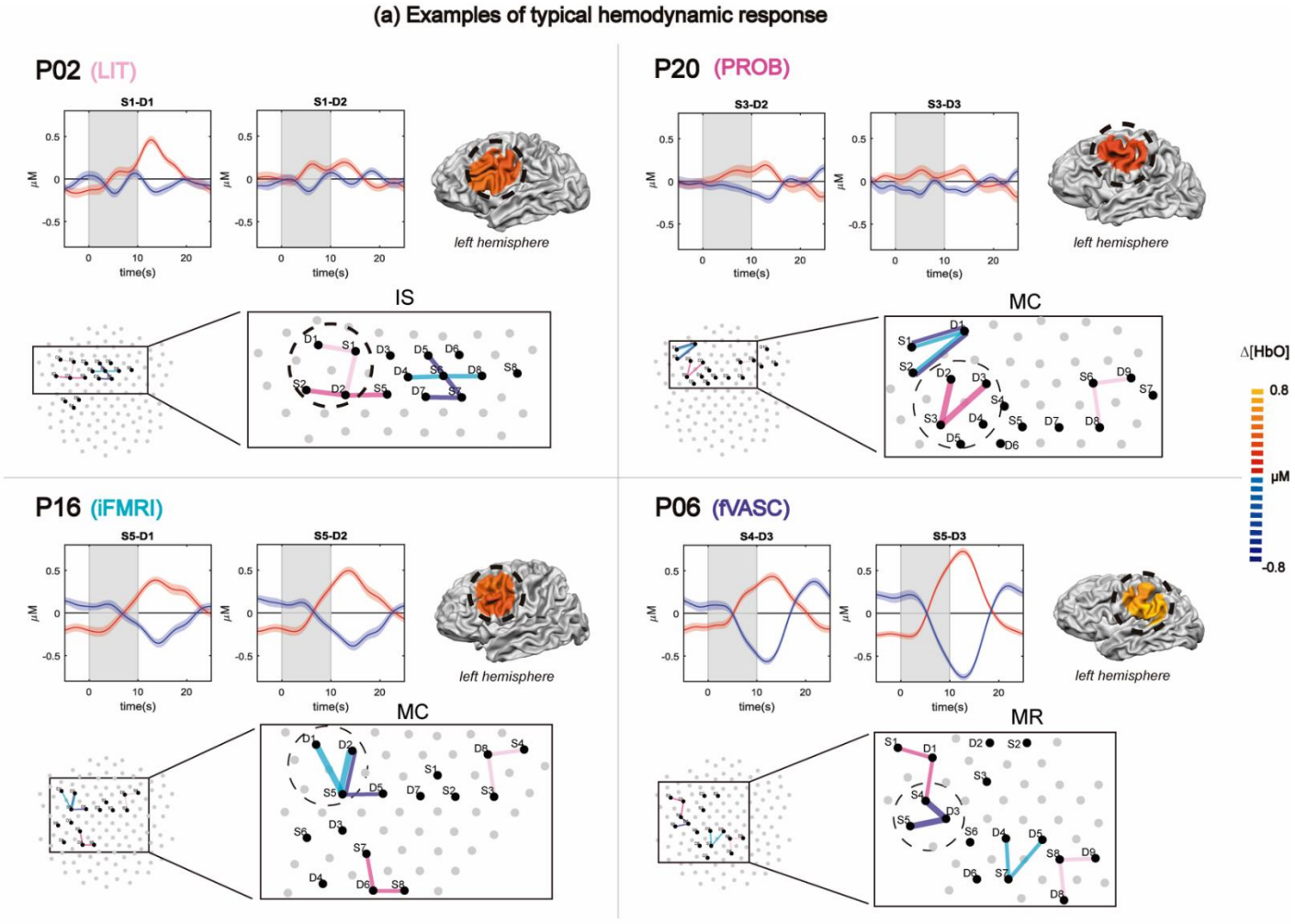

Figure S3.10. Examples of typical (a) and weak/inverted (b) hemodynamic responses, for every approach-specific layout and mental-imagery tasks. Every plot depicts a different participant. On the top part, fNIRS block averages of the two channels comprising a given layout are shown, with Δ[HbO]signal in red and Δ[HbR]signal in blue. (Continues on the next page)

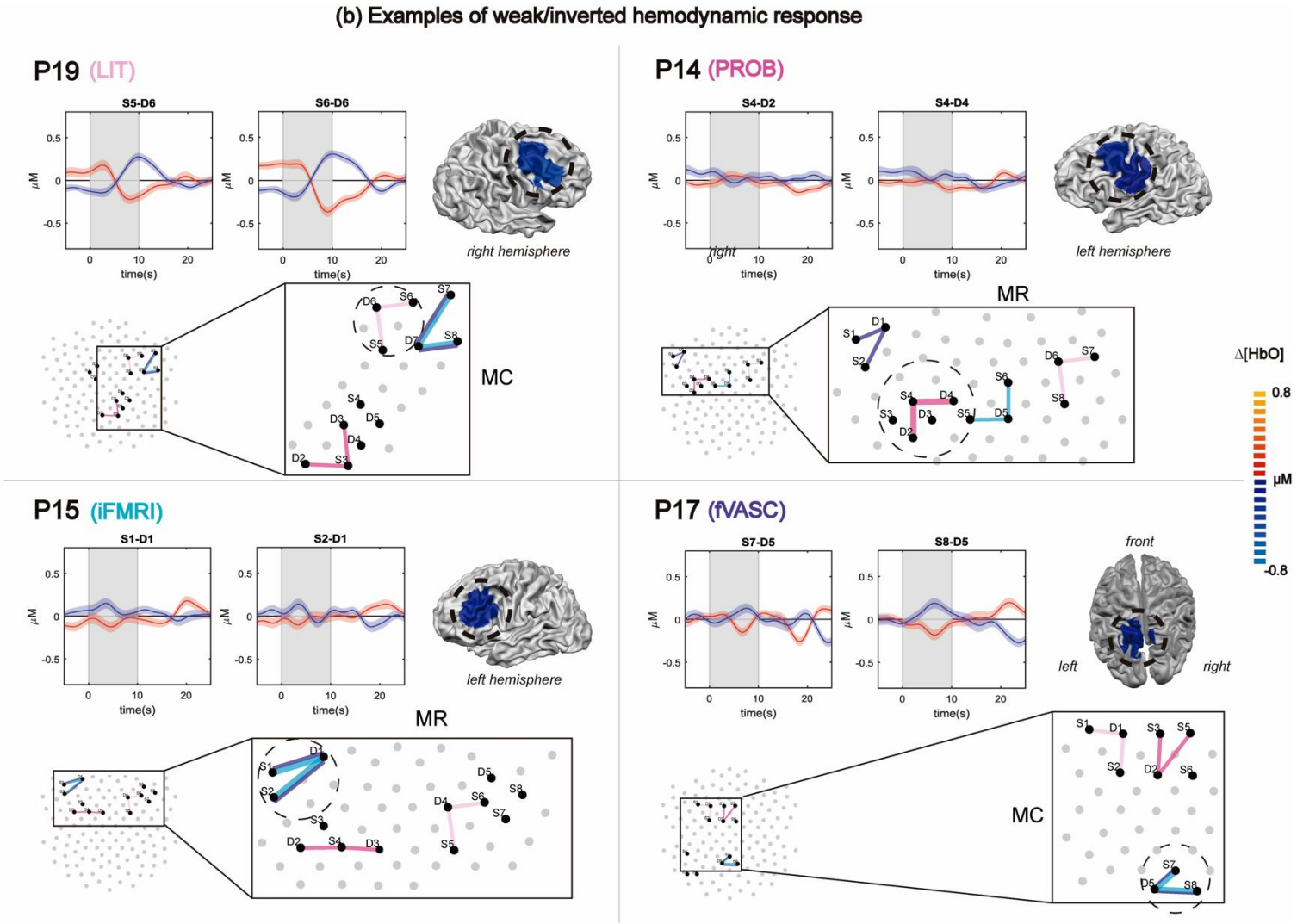

The grey area indicates the onset and duration of the mental-imagery task (MC = Mental Calculation; MR= Mental Rotation). The bottom left plot shows the approach-specific optode layout for the same mental-imagery task as the block averages. The bottom right plot illustrates the projection of the two fNIRS channels in the individual anatomical data (3D surface reconstructions) for Δ[HbO].

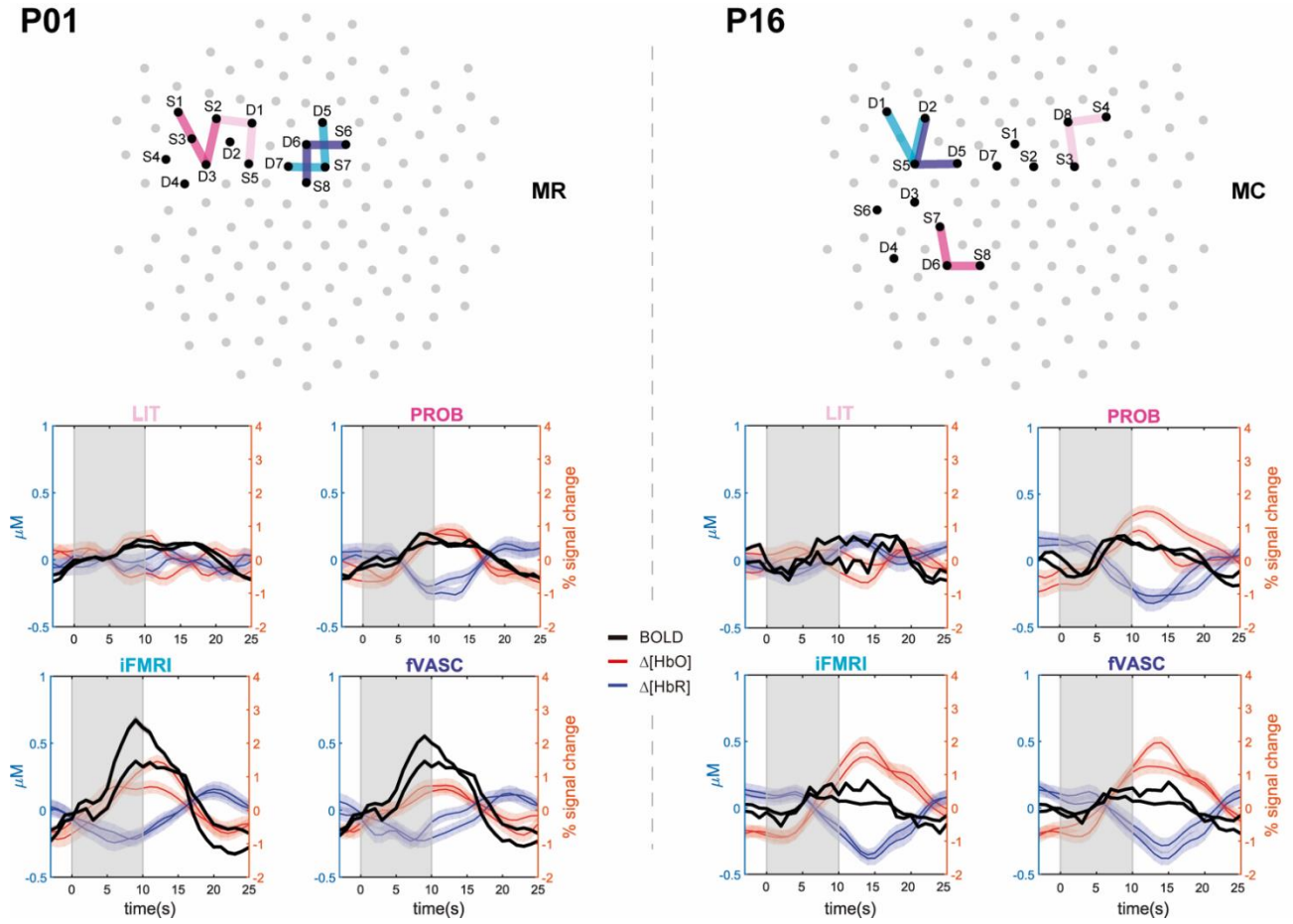

Figure S3.11. Correspondence between fMRI and fNIRS block averages across different approaches in participants P01 (left) and P16 (right) for one of the mental-imagery task they performed (mental rotation [MR] and mental calculation [MC], respectively). The y-axis on the left represents concentration changes in μM for Δ[HbO] (red) and Δ[HbR] (blue) data, while the y-axis on the right represents the percent signal change for the fMRI time course (BOLD response, black line). The 0 value in the x-axis represents the task onset time (in s) and the gray area depicts the task duration. fNIRS time courses were normalized by the peak value before computing the block averages. The fNIRS block averages derived from the more individualized approaches show better agreement with fMRI data.

7 References

Aasted, C.M., Yücel, M.A., Cooper, R.J., Dubb, J., Tsuzuki, D., Becerra, L., et al. (2015). Anatomical guidance for functional near-infrared spectroscopy: AtlasViewer tutorial. *Neurophotonics* 2(2)**,** 020801-020801. doi: 10.1117/1.NPh.2.2.020801.

Aihara, T., Takeda, Y., Takeda, K., Yasuda, W., Sato, T., Otaka, Y., et al. (2012). Cortical current source estimation from electroencephalography in combination with near-infrared spectroscopy as a hierarchical prior. *NeuroImage* 59(4)**,** 4006-4021. doi: https://doi.org/10.1016/j.neuroimage.2011.09.087.

Alivisatos, B., and Petrides, M. (1997). Functional activation of the human brain during mental rotation. *Neuropsychologia* 35(2)**,** 111-118. doi: https://doi.org/10.1016/S0028-3932(96)00083-8.

Allison, B., and Neuper, C. (2010). "Could anyone use a BCI?."), 35-54.

Ang, K.K., Juanhong, Y., and Guan, C. (Year). "Extracting and selecting discriminative features from high density NIRS-based BCI for numerical cognition", in: *The 2012 International Joint Conference on Neural Networks (IJCNN)*), 1-6.

Arsalidou, M., and Taylor, M.J. (2011). Is 2+2=4? Meta-analyses of brain areas needed for numbers and calculations. *NeuroImage* 54(3)**,** 2382-2393. doi: https://doi.org/10.1016/j.neuroimage.2010.10.009.

Aziz-Zadeh, L., Cattaneo, L., Rochat, M., and Rizzolatti, G. (2005). Covert Speech Arrest Induced by rTMS over Both Motor and Nonmotor Left Hemisphere Frontal Sites. *Journal of Cognitive Neuroscience* 17(6)**,** 928-938. doi: 10.1162/0898929054021157.

Baciu, M.V., Rubin, C., Décorps, M.A., and Segebarth, C.M. (1999). fMRI assessment of hemispheric language dominance using a simple inner speech paradigm. *NMR in Biomedicine* 12(5)**,** 293-298. doi: 10.1002/(SICI)1099-1492(199908)12:5<293::AID-NBM573>3.0.CO;2-6.

Bardin, J.C., Fins, J.J., Katz, D.I., Hersh, J., Heier, L.A., Tabelow, K., et al. (2011). Dissociations between behavioural and functional magnetic resonance imaging-based evaluations of cognitive function after brain injury. *Brain : a journal of neurology* 134(Pt 3)**,** 769-782. doi: 10.1093/brain/awr005.

Bauernfeind, G., Leeb, R., Wriessnegger Selina, C., and Pfurtscheller, G. (2008). Development, set-up and first results for a one-channel near-infrared spectroscopy system *Biomedizinische Technik. Biomedical engineering* 53(1)**,** 36-43. doi: 10.1515/BMT.2008.005.

Benitez-Andonegui, A., Burden, R., Benning, R., Möckel, R., Lührs, M., and Sorger, B. (2020). An Augmented-Reality fNIRS-Based Brain-Computer Interface: A Proof-of-Concept Study. *Frontiers in Neuroscience* 14**,** 346.

Bernier, M., Cunnane, S.C., and Whittingstall, K. (2018). The morphology of the human cerebrovascular system. *Human Brain Mapping* 39(12)**,** 4962-4975. doi: 10.1002/hbm.24337.

Bizeau, A., Gilbert, G., Bernier, M., Huynh, M.T., Bocti, C., Descoteaux, M., et al. (2017). Stimulus-evoked changes in cerebral vessel diameter: A study in healthy humans. *Journal of Cerebral Blood Flow & Metabolism* 38(3)**,** 528-539. doi: 10.1177/0271678X17701948.

Boas, D.A., Culver, J.P., Stott, J.J., and Dunn, A.K. (2002). Three dimensional Monte Carlo code for photon migration through complex heterogeneous media including the adult human head. *Optics Express* 10(3)**,** 159-170. doi: 10.1364/OE.10.000159.

Bosschaart, N., Edelman, G.J., Aalders, M.C.G., van Leeuwen, T.G., and Faber, D.J. (2014). A literature review and novel theoretical approach on the optical properties of whole blood. *Lasers in medical science* 29(2)**,** 453-479. doi: 10.1007/s10103-013-1446-7.

Brigadoi, S., Salvagnin, D., Fischetti, M., and Cooper, R.J. (2018). Array Designer: automated optimized array design for functional near-infrared spectroscopy. *Neurophotonics* 5(3)**,** 1-19, 19.

Cannestra, A.F., Wartenburger, I., Obrig, H., Villringer, A., and Toga, A.W. (2003). Functional assessment of Broca's area using near infrared spectroscopy in humans. *NeuroReport* 14(15)**,** 1961-1965.

Coyle, S., Markham, C., and Ward, T. (2005). A Mechanical Mounting System for Functional Near-Infrared Spectroscopy Brain Imaging Studies. *Proceedings of SPIE - The International Society for Optical Engineering* 5826. doi: 10.1117/12.604823.

Cui, X., Bray, S., Bryant, D.M., Glover, G.H., and Reiss, A.L. (2011). A quantitative comparison of NIRS and fMRI across multiple cognitive tasks. *NeuroImage* 54(4)**,** 2808-2821. doi: 10.1016/j.neuroimage.2010.10.069.

Culver, J.P., Ntziachristos, V., Holboke, M.J., and Yodh, A.G. (2001). Optimization of optode arrangements for diffuse optical tomography: A singular-value analysis. *Optics Letters* 26(10)**,** 701-703. doi: 10.1364/OL.26.000701.

Duecker, F., Frost, M.A., de Graaf, T.A., Graewe, B., Jacobs, C., Goebel, R., et al. (2014). The Cortex-based Alignment Approach to TMS Coil Positioning. *Journal of Cognitive Neuroscience* 26(10)**,** 2321-2329. doi: 10.1162/jocn_a_00635.

Fang, Q., and Boas, D.A. (2009). Monte Carlo simulation of photon migration in 3D turbid media accelerated by graphics processing units. *Optics express* 17(22)**,** 20178-20190. doi: 10.1364/OE.17.020178.

Fischl, B. (2012). FreeSurfer. *NeuroImage* 62(2)**,** 774-781. doi: 10.1016/j.neuroimage.2012.01.021.

Fischl, B., Rajendran, N., Busa, E., Augustinack, J., Hinds, O., Yeo, B.T.T., et al. (2007). Cortical Folding Patterns and Predicting Cytoarchitecture. *Cerebral Cortex* 18(8)**,** 1973-1980. doi: 10.1093/cercor/bhm225.

Fischl, B., Sereno, M.I., and Dale, A.M. (1999). Cortical Surface-Based Analysis: II: Inflation, Flattening, and a Surface-Based Coordinate System. *NeuroImage* 9(2)**,** 195-207. doi: https://doi.org/10.1006/nimg.1998.0396.

Friedrich, E.V.C., Neuper, C., and Scherer, R. (2013). Whatever Works: A Systematic User-Centered Training Protocol to Optimize Brain-Computer Interfacing Individually. *PLOS ONE* 8(9)**,** e76214. doi: 10.1371/journal.pone.0076214.

Frost, M.A., and Goebel, R. (2012). Measuring structural–functional correspondence: Spatial variability of specialised brain regions after macro-anatomical alignment. *NeuroImage* 59(2)**,** 1369-1381. doi: https://doi.org/10.1016/j.neuroimage.2011.08.035.

Fujimaki, N., Hayakawa, T., Matani, A., and Okabe, Y. (2004). Right-lateralized neural activity during inner speech repeated by cues. *NeuroReport* 15(15)**,** 2341-2345.

Giacometti, P., Perdue, K.L., and Diamond, S.G. (2014). Algorithm to find high density EEG scalp coordinates and analysis of their correspondence to structural and functional regions of the brain. *Journal of neuroscience methods* 229**,** 84-96. doi: 10.1016/j.jneumeth.2014.04.020.

Girbau, D. (2014). A Neurocognitive Approach to the Study of Private Speech. *The Spanish Journal of Psychology* 10(1)**,** 41-51. doi: 10.1017/S1138741600006302.

Goebel, R., Esposito, F., and Formisano, E. (2006). Analysis of functional image analysis contest (FIAC) data with brainvoyager QX: From single-subject to cortically aligned group general linear model analysis and self-organizing group independent component analysis. *Human Brain Mapping* 27(5)**,** 392-401. doi: 10.1002/hbm.20249.

Goodwin, J.R., Gaudet, C.R., and Berger, A.J. (2014). Short-channel functional near-infrared spectroscopy regressions improve when source-detector separation is reduced. *Neurophotonics* 1(1)**,** 015002-015002. doi: 10.1117/1.NPh.1.1.015002.

Gulban, O.F., Schneider, M., Marquardt, I., Haast, R.A.M., and De Martino, F. (2018). A scalable method to improve gray matter segmentation at ultra high field MRI. *PLOS ONE* 13(6)**,** e0198335. doi: 10.1371/journal.pone.0198335.

Hamada, H., Matsuzawa, D., Sutoh, C., Hirano, Y., Chakraborty, S., Ito, H., et al. (2018). Comparison of brain activity between motor imagery and mental rotation of the hand tasks: a functional magnetic resonance imaging study. *Brain imaging and behavior* 12(6)**,** 1596-1606. doi: 10.1007/s11682-017-9821-9.

Harris, I.M., and Miniussi, C. (2003). Parietal Lobe Contribution to Mental Rotation Demonstrated with rTMS. *Journal of Cognitive Neuroscience* 15(3)**,** 315-323. doi: 10.1162/089892903321593054.

Herff, C., Heger, D., Putze, F., Guan, C., and Schultz, T. (2012). Cross-Subject Classification of Speaking Modes Using fNIRS. *Proceedings of the 19th international conference on Neural Information Processing* 7664**,** 417-424. doi: 10.1007/978-3-642-34481-7_51.

Herff, C., Heger, D., Putze, F., Hennrich, J., Fortmann, O., and Schultz, T. (2013). Classification of mental tasks in the prefrontal cortex using fNIRS. *Conference proceedings : IEEE Engineering in Medicine and Biology Society* 2013**,** 2160-2163. doi: 10.1109/EMBC.2013.6609962.

Herrera-Vega, J., Montero-Hernández, S., Tachtsidis, I., Treviño-Palacios, C., and Orihuela-Espina, F. (2017). Modelling and validation of diffuse reflectance of the adult human head for fNIRS: scalp sub-layers definition. *13th International Symposium on Medical Information Processing and Analysis* 10572.

Hocke, M.L., Oni, K.I., Duszynski, C.C., Corrigan, V.A., Frederick, D.B., and Dunn, F.J. (2018). Automated Processing of fNIRS Data—A Visual Guide to the Pitfalls and Consequences. *Algorithms* 11(5). doi: 10.3390/a11050067.

Huang, T., Chen, X., Jiang, J., Zhen, Z., and Liu, J. (2019). A probabilistic atlas of the human motion complex built from large-scale functional localizer data. *Human Brain Mapping* 40(12)**,** 3475-3487. doi: 10.1002/hbm.24610.

Huppert, T., Barker, J., Schmidt, B., Walls, S., and Ghuman, A. (2017). Comparison of group-level, source localized activity for simultaneous functional near-infrared spectroscopy-magnetoencephalography and simultaneous fNIRS-fMRI during parametric median nerve stimulation. *Neurophotonics* 4(1)**,** 015001-015001. doi: 10.1117/1.NPh.4.1.015001.

Huppert, T.J., Diamond, S.G., Franceschini, M.A., and Boas, D.A. (2009). HomER: a review of time-series analysis methods for near-infrared spectroscopy of the brain. *Applied optics* 48(10)**,** D280-D298. doi: 10.1364/ao.48.00d280.

Hurlburt, R.T., Alderson-Day, B., Kühn, S., and Fernyhough, C. (2016). Exploring the Ecological Validity of Thinking on Demand: Neural Correlates of Elicited vs. Spontaneously Occurring Inner Speech. *PLOS ONE* 11(2)**,** e0147932. doi: 10.1371/journal.pone.0147932.

Hwang, H.-J., Lim, J.-H., Kim, D.-W., and Im, C.-H. (2014). Evaluation of various mental task combinations for near-infrared spectroscopy-based brain-computer interfaces. *Journal of Biomedical Optics* 19(7)**,** 077005.

Ischebeck, A., Zamarian, L., Schocke, M., and Delazer, M. (2009). Flexible transfer of knowledge in mental arithmetic — An fMRI study. *NeuroImage* 44(3)**,** 1103-1112. doi: https://doi.org/10.1016/j.neuroimage.2008.10.025.

Jenkinson, M., Beckmann, C.F., Behrens, T.E.J., Woolrich, M.W., and Smith, S.M. (2012). FSL. *NeuroImage* 62(2)**,** 782-790. doi: https://doi.org/10.1016/j.neuroimage.2011.09.015.

Jurcak, V., Tsuzuki, D., and Dan, I. (2007). 10/20, 10/10, and 10/5 systems revisited: Their validity as relative head-surface-based positioning systems. *NeuroImage* 34(4)**,** 1600-1611. doi: https://doi.org/10.1016/j.neuroimage.2006.09.024.

Kawamichi, H., Kikuchi, Y., Noriuchi, M., Senoo, A., and Ueno, S. (2007). Distinct neural correlates underlying two- and three-dimensional mental rotations using three-dimensional objects. *Brain research* 1144**,** 117-126. doi: 10.1016/j.brainres.2007.01.082.

Kawashima, R., Taira, M., Okita, K., Inoue, K., Tajima, N., Yoshida, H., et al. (2004). A functional MRI study of simple arithmetic – A comparison between children and adults. *Brain research. Cognitive brain research* 18**,** 227-233. doi: 10.1016/j.cogbrainres.2003.10.009.

Khalaf, A., Sejdic, E., and Akcakaya, M. (2018). Towards optimal visual presentation design for hybrid EEG—fTCD brain–computer interfaces. *Journal of Neural Engineering* 15(5)**,** 056019. doi: 10.1088/1741-2552/aad46f.

Khan, M.J., and Hong, K.-S. (2017). Hybrid EEG–fNIRS-Based Eight-Command Decoding for BCI: Application to Quadcopter Control. *Frontiers in Neurorobotics* 11**,** 6.

Koessler, L., Maillard, L., Benhadid, A., Vignal, J.P., Felblinger, J., Vespignani, H., et al. (2009). Automated cortical projection of EEG sensors: Anatomical correlation via the international 10–10 system. *NeuroImage* 46(1)**,** 64-72. doi: https://doi.org/10.1016/j.neuroimage.2009.02.006.

Kübler, A., Neumann, N., Kaiser, J., Kotchoubey, B., Hinterberger, T., and Birbaumer, N.P. (2001). Brain-computer communication: Self-regulation of slow cortical potentials for verbal communication. *Archives of Physical Medicine and Rehabilitation* 82(11)**,** 1533-1539. doi: https://doi.org/10.1053/apmr.2001.26621.

Machado, A., Cai, Z., Pellegrino, G., Marcotte, O., Vincent, T., Lina, J.M., et al. (2018). Optimal positioning of optodes on the scalp for personalized functional near-infrared spectroscopy investigations. *J Neurosci Methods* 309**,** 91-108. doi: 10.1016/j.jneumeth.2018.08.006.

Machado, A., Marcotte, O., Lina, J.M., Kobayashi, E., and Grova, C. (2014). Optimal optode montage on electroencephalography/functional near-infrared spectroscopy caps dedicated to study epileptic discharges. *Journal of Biomedical Optics* 19(2)**,** 1-17, 17.

Mansouri, C., L'Huillier, J.-P., Kashou, N.H., and Humeau, A. (2010). Depth sensitivity analysis of functional near-infrared spectroscopy measurement using three-dimensional Monte Carlo modelling-based magnetic resonance imaging. *Lasers in Medical Science* 25(3)**,** 431-438. doi: 10.1007/s10103-010-0754-4.

Martin, S., Brunner, P., Holdgraf, C., Heinze, H.-J., Crone, N.E., Rieger, J., et al. (2014). Decoding spectrotemporal features of overt and covert speech from the human cortex. *Frontiers in neuroengineering* 7**,** 14-14. doi: 10.3389/fneng.2014.00014.

Martin, S., Brunner, P., Iturrate, I., Millán, J.d.R., Schalk, G., Knight, R.T., et al. (2016). Word pair classification during imagined speech using direct brain recordings. *Scientific Reports* 6(1)**,** 25803. doi: 10.1038/srep25803.

Morin, A., and Michaud, J. (2007). Self-awareness and the left inferior frontal gyrus: Inner speech use during self-related processing. *Brain Research Bulletin* 74(6)**,** 387-396. doi: https://doi.org/10.1016/j.brainresbull.2007.06.013.

Nagels-Coune, L., Benitez-Andonegui, A., Reuter, N., Lührs, M., Goebel, R., De Weerd, P., et al. (2020). Brain-Based Binary Communication Using Spatiotemporal Features of fNIRS Responses. *Frontiers in Human Neuroscience* 14(113). doi: 10.3389/fnhum.2020.00113.

Nagels-Coune, L., Kurban, D., Reuter, N., Benitez, A., Gossé, L., Riecke, L., et al. (2017). Yes or no? binary brain-based communication utilizing motor imagery and fNIRS. *Proceedings of the 7th Graz Brain-Computer Interface*. doi: 10.3217/978-3-85125-533-1-65.

Naito, M., Michioka, Y., Ozawa, K., Ito, Y., Kiguchi, M., and Kanazawa, T. (2007). A Communication Means for Totally Locked-in ALS Patients Based on Changes in Cerebral Blood Volume Measured with Near-Infrared Light. *IEICE Transactions on Information and Systems* E90D. doi: 10.1093/ietisy/e90-d.7.1028.

Naseer, N., and Hong, K.-S. (2015a). fNIRS-based brain-computer interfaces: a review. *Frontiers in human neuroscience* 9**,** 3-3. doi: 10.3389/fnhum.2015.00003.

O'Neill, G.C., Sengupta, A., Asghar, M., Barratt, E.L., Besle, J., Schluppeck, D., et al. (2020). A probabilistic atlas of finger dominance in the primary somatosensory cortex. *NeuroImage***,** 116880. doi: https://doi.org/10.1016/j.neuroimage.2020.116880.

Ogata, H., Mukai, T., and Yagi, T. (Year). "A Study on the Frontal Cortex in Cognitive Tasks using Near-Infrared Spectroscopy", in: *2007 29th Annual International Conference of the IEEE Engineering in Medicine and Biology Society*), 4731-4734.

Okamoto, M., Dan, H., Sakamoto, K., Takeo, K., Shimizu, K., Kohno, S., et al. (2004). Three-dimensional probabilistic anatomical cranio-cerebral correlation via the international 10–20 system oriented for transcranial functional brain mapping. *NeuroImage* 21(1)**,** 99-111. doi: https://doi.org/10.1016/j.neuroimage.2003.08.026.

Oostenveld, R., and Praamstra, P. (2001). The five percent electrode system for high-resolution EEG and ERP measurements. *Clinical Neurophysiology* 112(4)**,** 713-719. doi: https://doi.org/10.1016/S1388-2457(00)00527-7.

Perdue, K.L., and Diamond, S.G. (2014). T1 magnetic resonance imaging head segmentation for diffuse optical tomography and electroencephalography. *Journal of biomedical optics* 19(2)**,** 026011-026011. doi: 10.1117/1.JBO.19.2.026011.

Perdue, K.L., Fang, Q., and Diamond, S.G. (2012). Quantitative assessment of diffuse optical tomography sensitivity to the cerebral cortex using a whole-head probe. *Physics in medicine and biology* 57(10)**,** 2857-2872. doi: 10.1088/0031-9155/57/10/2857.

Pfurtscheller, G., Bauernfeind, G., Wriessnegger, S.C., and Neuper, C. (2010). Focal frontal (de)oxyhemoglobin responses during simple arithmetic. *International Journal of Psychophysiology* 76(3)**,** 186-192. doi: https://doi.org/10.1016/j.ijpsycho.2010.03.013.

Piper, S.K., Krueger, A., Koch, S.P., Mehnert, J., Habermehl, C., Steinbrink, J., et al. (2014). A wearable multi-channel fNIRS system for brain imaging in freely moving subjects. *NeuroImage* 85**,** 64-71. doi: https://doi.org/10.1016/j.neuroimage.2013.06.062.

Power, S.D., Kushki, A., and Chau, T. (2012). Automatic single-trial discrimination of mental arithmetic, mental singing and the no-control state from prefrontal activity: toward a three-state NIRS-BCI. *BMC research notes* 5**,** 141-141. doi: 10.1186/1756-0500-5-141.

Quaresima, V., and Ferrari, M. (2016). Functional Near-Infrared Spectroscopy (fNIRS) for Assessing Cerebral Cortex Function During Human Behavior in Natural/Social Situations: A Concise Review. *Organizational Research Methods* 22(1)**,** 46-68. doi: 10.1177/1094428116658959.

Qureshi, N.K., Naseer, N., Noori, F.M., Nazeer, H., Khan, R.A., and Saleem, S. (2017). Enhancing Classification Performance of Functional Near-Infrared Spectroscopy- Brain-Computer Interface Using Adaptive Estimation of General Linear Model Coefficients. *Frontiers in neurorobotics* 11**,** 33-33. doi: 10.3389/fnbot.2017.00033.

Rajaram, N., Gopal, A., Zhang, X., and Tunnell, J.W. (2010). Experimental validation of the effects of microvasculature pigment packaging on in vivo diffuse reflectance spectroscopy. *Lasers in Surgery and Medicine* 42(7)**,** 680-688. doi: 10.1002/lsm.20933.

Rhéaume, M., Rebello, R., Pagnoux, C., Carette, S., Clements-Baker, M., Cohen-Hallaleh, V., et al. (2017). High-Resolution Magnetic Resonance Imaging of Scalp Arteries for the Diagnosis of Giant Cell Arteritis: Results of a Prospective Cohort Study. *Arthritis & Rheumatology* 69(1)**,** 161-168. doi: 10.1002/art.39824.

Rickard, T.C., Romero, S.G., Basso, G., Wharton, C., Flitman, S., and Grafman, J. (2000). The calculating brain: an fMRI study. *Neuropsychologia* 38(3)**,** 325-335. doi: https://doi.org/10.1016/S0028-3932(99)00068-8.

Roberts, J., and Bell, M.A. (2003). Two- and three-dimensional mental rotation tasks lead to different parietal laterality for men and women. *International journal of psychophysiology : official journal of the International Organization of Psychophysiology* 50**,** 235-246. doi: 10.1016/S0167-8760(03)00195-8.

Rosenke, M., van Hoof, R., van den Hurk, J., and Goebel, R. (2020). A probabilistic functional parcellation of human occipito-temporal cortex. *bioRxiv***,** 2020.2001.2022.916239. doi: 10.1101/2020.01.22.916239.

Rosenke, M., Weiner, K.S., Barnett, M.A., Zilles, K., Amunts, K., Goebel, R., et al. (2018). A cross-validated cytoarchitectonic atlas of the human ventral visual stream. *NeuroImage* 170**,** 257-270. doi: 10.1016/j.neuroimage.2017.02.040.

Santosa, H., Zhai, X., Fishburn, F., and Huppert, T. (2018). The NIRS Brain AnalyzIR Toolbox. *Algorithms* 11**,** 73. doi: 10.3390/a11050073.

Scarapicchia, V., Brown, C., Mayo, C., and Gawryluk, J.R. (2017). Functional Magnetic Resonance Imaging and Functional Near-Infrared Spectroscopy: Insights from Combined Recording Studies. *Frontiers in human neuroscience* 11**,** 419-419. doi: 10.3389/fnhum.2017.00419.

Scholkmann, F., Kleiser, S., Metz, A.J., Zimmermann, R., Mata Pavia, J., Wolf, U., et al. (2014). A review on continuous wave functional near-infrared spectroscopy and imaging instrumentation and methodology. *NeuroImage* 85**,** 6-27. doi: https://doi.org/10.1016/j.neuroimage.2013.05.004.

Scholkmann, F., and Wolf, M. (2013). General equation for the differential pathlength factor of the frontal human head depending on wavelength and age. *Journal of Biomedical Optics* 18(10)**,** 105004.

Schudlo, L.C., and Chau, T. (2013). Dynamic topographical pattern classification of multichannel prefrontal NIRS signals: II. Online differentiation of mental arithmetic and rest. *Journal of Neural Engineering* 11(1)**,** 016003. doi: 10.1088/1741-2560/11/1/016003.

Schudlo, L.C., Power, S.D., and Chau, T. (2013). Dynamic topographical pattern classification of multichannel prefrontal NIRS signals. *Journal of Neural Engineering* 10(4)**,** 046018. doi: 10.1088/1741-2560/10/4/046018.

Sereshkeh, A.R., Yousefi, R., Wong, A.T., and Chau, T. (2018). Online classification of imagined speech using functional near-infrared spectroscopy signals. *Journal of Neural Engineering* 16(1)**,** 016005. doi: 10.1088/1741-2552/aae4b9.

Shergill, S.S., Bullmore, E.T., Brammer, M.J., Williams, S.C.R., Murray, R.M., and McGuire, P.K. (2001). A functional study of auditory verbal imagery. *Psychological Medicine* 31(2)**,** 241-253. doi: 10.1017/S003329170100335X.

Shimoda, N., Takeda, K., Imai, I., Kaneko, J., and Kato, H. (2008). Cerebral laterality differences in handedness: A mental rotation study with NIRS. *Neuroscience Letters* 430(1)**,** 43-47. doi: https://doi.org/10.1016/j.neulet.2007.10.016.

Shin, J., Kwon, J., Choi, J., and Im, C.-H. (2017). Performance enhancement of a brain-computer interface using high-density multi-distance NIRS. *Scientific Reports* 7(1)**,** 16545. doi: 10.1038/s41598-017-16639-0.

Shin, J., Müller, K.-R., and Hwang, H.-J. (2016). Near-infrared spectroscopy (NIRS)-based eyes-closed brain-computer interface (BCI) using prefrontal cortex activation due to mental arithmetic. *Scientific Reports* 6(1)**,** 36203. doi: 10.1038/srep36203.

Sorger, B., Dahmen, B., Reithler, J., Gosseries, O., Maudoux, A., Laureys, S., et al. (2009). Another kind of 'BOLD Response': answering multiple-choice questions via online decoded single-trial brain signals. *Progress in brain research* 177**,** 275-292. doi: 10.1016/S0079-6123(09)17719-1.

Sorger, B., Reithler, J., Dahmen, B., and Goebel, R. (2012). A Real-Time fMRI-Based Spelling Device Immediately Enabling Robust Motor-Independent Communication. *Current Biology* 22(14)**,** 1333-1338. doi: https://doi.org/10.1016/j.cub.2012.05.022.

Strangman, G.E., Li, Z., and Zhang, Q. (2013). Depth Sensitivity and Source-Detector Separations for Near Infrared Spectroscopy Based on the Colin27 Brain Template. *PLOS ONE* 8(8)**,** e66319. doi: 10.1371/journal.pone.0066319.

Suzuki, S., Harashima, F., and Katsuhisa, F. (2010). Human Control Law and Brain Activity of Voluntary Motion by Utilizing a Balancing Task with an Inverted Pendulum. *Advances in Human-Computer Interaction* 2010. doi: 10.1155/2010/215825.

Tadel, F., Baillet, S., Mosher, J.C., Pantazis, D., and Leahy, R.M. (2011). Brainstorm: a user-friendly application for MEG/EEG analysis. *Computational intelligence and neuroscience* 2011**,** 879716-879716. doi: 10.1155/2011/879716.

Tagaris, G.A., Richter, W., Kim, S.-G., Pellizzer, G., Andersen, P., Uğurbil, K., et al. (1998). Functional magnetic resonance imaging of mental rotation and memory scanning: a multidimensional scaling analysis of brain activation patterns1Published on the World Wide Web on 24 February 1998.1. *Brain Research Reviews* 26(2)**,** 106-112. doi: https://doi.org/10.1016/S0165-0173(97)00060-X.

Tahmasebi, A.M., Artiges, E., Banaschewski, T., Barker, G.J., Bruehl, R., Büchel, C., et al. (2012). Creating probabilistic maps of the face network in the adolescent brain: A multicentre functional MRI study. *Human Brain Mapping* 33(4)**,** 938-957. doi: 10.1002/hbm.21261.

Tomasino, B., and Gremese, M. (2016). Effects of Stimulus Type and Strategy on Mental Rotation Network: An Activation Likelihood Estimation Meta-Analysis. *Frontiers in human neuroscience* 9**,** 693-693. doi: 10.3389/fnhum.2015.00693.

Tsuzuki, D., and Dan, I. (2014). Spatial registration for functional near-infrared spectroscopy: From channel position on the scalp to cortical location in individual and group analyses. *NeuroImage* 85**,** 92-103. doi: https://doi.org/10.1016/j.neuroimage.2013.07.025.

Tsuzuki, D., Jurcak, V., Singh, A.K., Okamoto, M., Watanabe, E., and Dan, I. (2007). Virtual spatial registration of stand-alone fNIRS data to MNI space. *NeuroImage* 34(4)**,** 1506-1518. doi: https://doi.org/10.1016/j.neuroimage.2006.10.043.

Utsugi, K., Obata, A., Sato, H., Katsura, T., Sagara, K., Maki, A., et al. (2007). Development of an Optical Brain-machine Interface. *29th Annual International Conference of the IEEE Engineering in Medicine and Biology Society***,** 5338-5341. doi: 10.1109/IEMBS.2007.4353547.

Verner, M., Herrmann, M.J., Troche, S.J., Roebers, C.M., and Rammsayer, T.H. (2013). Cortical oxygen consumption in mental arithmetic as a function of task difficulty: a near-infrared spectroscopy approach. *Frontiers in human neuroscience* 7**,** 217-217. doi: 10.3389/fnhum.2013.00217.

Wan, N., Hancock, A.S., Moon, T.K., and Gillam, R.B. (2018). A functional near-infrared spectroscopic investigation of speech production during reading. *Human Brain Mapping* 39(3)**,** 1428-1437. doi: 10.1002/hbm.23932.

Weyand, S., and Chau, T. (2015). Correlates of Near-Infrared Spectroscopy Brain–Computer Interface Accuracy in a Multi-Class Personalization Framework. *Frontiers in Human Neuroscience* 9(536). doi: 10.3389/fnhum.2015.00536.

Weyand, S., Schudlo, L., Takehara-Nishiuchi, K., and Chau, T. (2015). Usability and performance-informed selection of personalized mental tasks for an online near-infrared spectroscopy brain-computer interface. *Neurophotonics* 2(2)**,** 1-14, 14.

Wijeakumar, S., Spencer, J.P., Bohache, K., Boas, D.A., and Magnotta, V.A. (2015). Validating a new methodology for optical probe design and image registration in fNIRS studies. *NeuroImage* 106**,** 86-100. doi: https://doi.org/10.1016/j.neuroimage.2014.11.022.

Wolpaw, J.R., Birbaumer, N., McFarland, D.J., Pfurtscheller, G., and Vaughan, T.M. (2002). Brain–computer interfaces for communication and control. *Clinical Neurophysiology* 113(6)**,** 767-791. doi: https://doi.org/10.1016/S1388-2457(02)00057-3.

Yoo, S.-S., Fairneny, T., Chen, N.-K., Choo, S.-E., Panych, L.P., Park, H., et al. (2004). Brain–computer interface using fMRI: spatial navigation by thoughts. *NeuroReport* 15(10)**,** 1591-1595. doi: 10.1097/01.wnr.0000133296.39160.fe.

Yushkevich, P.A., Piven, J., Hazlett, H.C., Smith, R.G., Ho, S., Gee, J.C., et al. (2006). User-guided 3D active contour segmentation of anatomical structures: Significantly improved efficiency and reliability. *NeuroImage* 31(3)**,** 1116-1128. doi: https://doi.org/10.1016/j.neuroimage.2006.01.015.

Zhang, X., Noah, J.A., Dravida, S., and Hirsch, J. (2017). Signal processing of functional NIRS data acquired during overt speaking. *Neurophotonics* 4(4)**,** 041409-041409. doi: 10.1117/1.NPh.4.4.041409.

Zhen, Z., Yang, Z., Huang, L., Kong, X.-z., Wang, X., Dang, X., et al. (2015). Quantifying interindividual variability and asymmetry of face-selective regions: A probabilistic functional atlas. *NeuroImage* 113**,** 13-25. doi: https://doi.org/10.1016/j.neuroimage.2015.03.010.

Zimeo Morais, G.A., Balardin, J.B., and Sato, J.R. (2018). fNIRS Optodes' Location Decider (fOLD): a toolbox for probe arrangement guided by brain regions-of-interest. *Scientific Reports* 8(1)**,** 3341. doi: 10.1038/s41598-018-21716-z.

In the above reference list, 68.14% of first authors were male (vs. 31.86% that were female), while 84.50% of last authors were male (vs. 15.04% that were female).

8 Data Availability Statement

The raw data and code supporting the conclusions of this article will be made available by the authors, without undue reservation, to any qualified researcher.

9 Author Contributions

BS, LN-C, ML, RG and AB-A conceived the idea and designed the experiment. DI optimized the MRA acquisition protocols. AB-A prepared the stimuli. AB-A and BS collected (f)MRI data. AB-A carried out the fNIRS measurements. ML enabled the necessary infrastructure for data analysis. AB-A analyzed the data, and wrote the manuscript. BS, ML and LN-C assisted on the interpretation of results and data analysis. AB-A, BS, and ML structured the manuscript. LN-C, ML, DI, RG and BS revised the manuscript critically.

10 Funding

This work was supported by the European Commission (7th Framework Program 2007-2013, DECODER project, to BS and RG), by the Netherlands Organization for Scientific Research (Research talent grant 406-15-217 to LN-C) and by The Luik 3 grant for joint research between Cognitive Neuroscience and Knowledge Engineering Departments, Maastricht University, on advanced brain-robot interfaces, 2015-2019 (to RG and BS).

11 Conflict of Interest

The authors declare that the research was conducted in the absence of any commercial or financial relationships that could be construed as a potential conflict of interest.

12 Acknowledgments

We would like to thank Agustin Lage-Castellanos, Andrew Morgan, Faruk Gülban and Judith Eck for their advice on data analysis; and to all the participants for their time. The authors would also like to thank NIRx for providing the short-distance optode bundles and to the participants for their time.

4

The influence of extra-cerebral vasculature on the efficacy of the short-separation regression approach applied to fNIRS data

Abstract

Functional near-infrared spectroscopy (fNIRS) is a non-invasive, portable, and inexpensive optical neuroimaging technique with respectable spatial and temporal resolution. fNIRS is, however, susceptible to extra-cerebral physiological noise, potentially compromising its sensitivity to detect task-related brain activation. Previous studies have addressed this issue by correcting fNIRS signals with additional information recorded exclusively from extra-cerebral regions using short-distance channels (SDCs). This method, termed short-separation regression (SSR), can improve fNIRS-signal quality and the sensitivity to detect task-related brain activation. However, it is unclear whether the efficacy of SSR depends on factors such as the presence of blood vessels in the channel's vicinity. Here, we combined anatomical, functional and angiographic magnetic resonance imaging data with continuous-wave fNIRS data to quantify the impact of SSR on the fNIRS-signal quality and sensitivity and investigated how vascular proximity/density contributes to SSR efficacy. Our investigation verifies that SSR improves fNIRS-signal quality and the sensitivity to detect task-related brain activation considerably and shows that signals obtained via SDCs are affected by close vascular structures. The present study extends our understanding of the relationship between vasculature features, the fNIRS signal quality, and methods (e.g., SSR) designed to increase fNIRS applicability to accurately detect brain activity.

Based on: A. Benitez-Andonegui, A. Turšič, S. Dumitrescu, D. Ivanov, R. Goebel, M. Lührs, B. Sorger (Under review). The influence of extra-cerebral vasculature on the efficacy of the short-separation regression approach applied to fNIRS data analysis.

5

General Discussion

The principal rationale for the development of BCIs has been to ultimately restore communication and control in the absence of words/gestures/other motor actions to people with severe neuromuscular disabilities (Shih et al., 2012). Despite being the historically main target, the body of literature involving end-users with disease has lagged behind the nearly exponentially growth of general BCI-related literature (Kübler, 2020). fNIRS is a promising neuroimaging modality to measure brain signals for controlling BCIs. However, fNIRS-BCI systems suffer from a number of limitations that has hindered its translational potential. This dissertation aimed to address some of these limitations. In **Chapter 2**, we evaluated factors that could improve the feasibility of ecologically-friendly fNIRS-based BCIs, namely short task duration periods, the usage of single optode pairs and the use of augmented-reality (AR) technology for a more immersive experience. In **Chapter 3**, we investigated the effect of different strategies for optode placement on the fNIRS signal quality and sensitivity to detect brain activation. Finally, in **Chapter 4**, we assessed if the amount of unwanted physiological noise present in the fNIRS signal depends on the proximity and density of vascular structures around the optodes.

After summarizing the results from each study, we will discuss the implications of the work presented in this dissertation. Subsequently, we describe the limitations and challenges of the current work and suggest the directions research should take to assure the realization of the translational potential of fNIRS-based BCIs.

1 Summary

In **Chapter 2**, we aimed to improve the feasibility of ecologically-friendly fNIRS-based BCIs for communication and control purposes in healthy participants. We tested the feasibility of using AR technology to navigate a through a virtual control menu that consisted of four levels and six options in each level. Additionally, we evaluated the feasibility of using a single mental-imagery task and fNIRS channel to select an option in each level. This was possible by using a temporal en- and decoding approach, previously implemented in fMRI-BCIs but never tested in fNIRS. Participants could successfully navigate through the nested control menu and achieved a mean accuracy of 74%. With this work, we showed that fNIRS-based BCIs can be successfully combined with AR technology and flexible choice encoding in form of search trees, to increase the degrees of freedom of a BCI system using a single mental task and fNIRS channel.

In **Chapter 3**, we aimed to answer the following questions: does additional individual (f)MRI data help optimizing the proper placement of fNIRS sensors? If so, how much individual data is needed? To do so, we selected and compared four approaches that incrementally incorporated individual (f)MRI information. The first approach was the literature-based approach (LIT), which uses a literature review to guide the optode layout design. The second approach, the probabilistic approach (PROB), employed individual anatomical data and probabilistic maps of functional MRI (fMRI)-activation derived from an independent dataset. The third approach used individual anatomical and fMRI data (iFMRI approach) and, the fourth approach used individual anatomical, functional and vascular information of the same subject (fVASC). We observed that the four approaches produced different optode layouts and that the more informed approaches (PROB, iFMRI, and fVASC) outperformed the minimally informed LIT approach in terms of signal quality and sensitivity. Further, the three more informed approaches (PROB, iFMRI and fVASC) resulted in similar outcome. We thus conclude that acquiring additional individual MRI data leads to a better signal quality, but that not all the modalities tested are required to achieve a robust setup.

In **Chapter 4**, we investigated whether fNIRS channels capture physiological noise differently and whether potential differences depend on the density and proximity of vessels in the vicinity of channels. We looked into three physiological noise types: Mayer waves, respiration and heartbeat. Our analyses showed variability in the amount of noise captured by fNIRS channels, but no relation between the amplitude of physiological noise and vascular proximity/density in normal-distance channels (NDCs). One way for correcting physiological noise in NDCs is to use short-distance channels (SDCs) that record exclusively from extra-cerebral regions. This method assumes that the systemic physiological noise present in the NDCs is present in SDC signals as well (Gagnon et al., 2012) but that SDCs do not have the penetration power to access brain activity. Our analyses indicated that the Mayer-wave amplitude captured by SDCs was related to the presence and density of vascular structures in their vicinity, but only for Δ[HbO]. Since the Short-separation regression (SSR) approach reduces the presence of physiological noise in NDCs data, we investigated whether this reduction depended on the presence of vascular structures. If that were the case, it would help researchers to shape the physiological noise correction approaches. However, we did not find any evidence for this dependence.

Nevertheless, this chapter extends considerably our understanding of the relationship between the vasculature features and the presence of physiological noise in fNIRS channels.

Taken together, the empirical studies presented as part of this dissertation address a number of challenges affecting different stages of and fNIRS-BCI setup. The studies describe a temporal en-/decoding paradigm previously used in fMRI-BCIs and successfully transferred to fNIRS-BCI research, offer guidance to efficiently using resources for developing robust and convenient optode layouts and provide insights on a number of factors affecting the presence of physiological noise in the fNIRS signal. The knowledge gained in these studies can therefore improve data-acquisition and analysis strategies in fNIRS-BCI research.

2 Implications and challenges of the presented work, and the way forward

2.1 Optode-layout design

How many optodes should the optode layout contain? How should they be arranged? These are important questions impacting fNIRS signal quality and sensitivity to cortical regions of interest (Culver et al., 2001). Additionally, the coverage and number of optodes in a layout affect the comfort of the participant. The fNIRS community has developed several tools and pipelines that aim to optimize solutions to this problem. Using 3D visualization tools, researchers have proposed methods to design optode layouts "manually" and interactively that target specific cortical regions based on light sensitivity profiles (Aasted et al., 2015; Wijeakumar et al., 2015). Machado et al. (2014) proposed a mathematical optimization strategy to address the problem and combined it with light-sensitivity profiles from individual anatomical head models. In 2018 they improved their work by allowing optodes to take any position along the scalp surface (using water-resistant adhesive [e.g., collodion] to glue the optodes on the scalp), instead of using fixed discrete positions along an EEG cap (Machado et al., 2018). The same year, two toolboxes were published to automatically design optimized fNIRS arrays given a user-defined ROI, FOLD (Zimeo Morais et al., 2018) and Array Designer (Brigadoi et al., 2018). Each of the above-mentioned approaches allows for variable user-defined and system-tailored restrictions. These include the maximum channels/optodes comprising the layout and the coverage and solution space of the layout, to name just a few.

Optimal solutions to the optode-layout-design problem depend on the restrictions the problem is subject to. This in turn depends on a number of factors, including the research question or application, the available technical and financial resources, as well as the researcher's available time. Data availability are included in these resources and the tools presented above, with the exception of the FOLD method, have partially considered them. This is because they all enable creating layouts based on individual subject MRI data or using an MRI atlas. In **Chapter 3**, we defined four scenarios by varying the available resources a researcher could have and assessed the potential gain of incorporating not only individual anatomical data, but also functional and vascular MRI data when optimizing optode-layout designs. Based on our results, we suggested that researchers should use individual functional and anatomical data for designing optode layouts when possible. When anatomical data are available and functional data are not, probabilistic functional maps are a promising alternative.

So far, existing tools for optode-layout design do not provide an option for defining target regions of interest based on individual or probabilistic functional activation maps derived from fMRI. In **Chapter 3** we observed that using these information sources can benefit the optode layout design process. We hope that future iterations of these tools will consider incorporating this functionality. One obvious challenge is acquiring such data. Fortunately, freely available (or available upon request) fMRI probabilistic maps constitute a feasible solution. However, we could not find any published work on probabilistic mental-imagery maps, which could be particularly beneficial for fNIRS-BCI research. We have attempted to improve this situation by making inner-speech, mental-calculation and mental-rotation probabilistic functional maps available to the fNIRS community. We hope that more research groups follow these efforts.

2.2 Physiological noise in fNIRS

Accounting for and removing physiological noise from the fNIRS signal is important for developing effective and efficient BCI applications. Physiological noise can compromise sensitivity to brain activation measured by fNIRS channels and can feed back noise to a participant instead of brain activity. Among the many choices for physiological noise correction, we opted for the short-separation regression (SSR) approach. Short-separation regression requires additional channels that are easily integrated in a real-time experiment,

making them suitable for fNIRS-BCI applications. In **Chapter 2**, we created an in house-made single SDC, while in **Chapters 3** and **4** we used short-distance bundles from a certified fNIRS provider. We did not actively assess the effect of SDC correction in **Chapter 3**, so the following discussion will focus on **Chapters 2** and **4**.

In **Chapter 2**, we observed that applying the SSR approach increases the accuracy of the BCI system more for Δ[HbO]than for Δ[HbR]. In **Chapter 4**, SSR improved sensitivity to brain activation, and again this was more for Δ[HbO]than for Δ[HbR]. These improvements were independent of the task employed, as we used a motor-imagery task in **Chapter 2** and an overt and inner-speech task in **Chapter 4**. It was also independent of the number of SDCs in the setup, as a single SDC was used for the whole setup in **Chapter 2** and one was used for each source in **Chapter 4**. Further, the improvements did not depend on the inter-optode distance constituting the SDC, as ~13mm for **Chapter 2** and 8mm for all SDCs in **Chapter 4** was used. An important outcome was that when SDC bundles are not available, the improved accuracies after SDC correction for Δ[HbO] (and to a lower extent for Δ[HbR]) suggest that using a single in house-made SDC located relatively close to its respective NDC is already beneficial.

In **Chapter 4** we observed that physiological noise amplitude is higher in Δ[HbO]channels than in Δ[HbR] channels, as previously reported (Lina et al., 2008; Gagnon et al., 2011; Kirilina et al., 2013). In BCI studies it is more common to use Δ[HbO]-based features, as Δ[HbO]usually exhibits larger and more pronounced concentration changes than Δ[HbR]in response to mental tasks (Stangl et al., 2013; Sato et al., 2016). Therefore, strategies accounting for physiological noise are particularly advisable.

2.3 Vasculature mapping

In this dissertation, subject-specific vasculature maps were used to study the potential impact on physiological noise (**Chapter 4**) and on optode layout design (**Chapter 3**), because, similar to fMRI signals, fNIRS signals are influenced by the underlying vasculature. In **Chapter 4**, we observed a positive, non-linear relation between most superficial vessels and the presence in Mayer waves in short distance channels. This finding suggests that adding vasculature information can be useful to design strategies to mitigate the effect of physiological noise in fNIRS signals. In **Chapter 3**, we concluded that,

although including individual vascular information improved signal quality and sensitivity to the brain, the experimental resources spent to include such information was not efficient. This is mainly because whole brain vascular segmentations can be tedious and time consuming. Further, it is not common practice for fNIRS-based BCI studies or fNIRS studies in general to acquire vascular data at the MRI scanner.

Similar to functional activation maps, probabilistic vascular atlases of individual arteries (Forkert et al., 2012; Viviani, 2016; Dunås et al., 2017), veins (Ward et al., 2018) or both (Bernier et al., 2018) have been reported. It should be noted even though there is considerable inter-subject variability especially in smaller vessels (Nowinski et al., 2011; Bernier et al., 2018), effort to minimize this variability using nonlinear registration has been made (Viviani, 2016; Dunås et al., 2017; Bernier et al., 2018; Ward et al., 2018). Incorporating probabilistic maps at different thresholds into the anatomical models for Monte Carlo simulations would help to have (even) more accurate models without the need of costly and lengthy acquisition and preprocessing times. However, the maps mentioned above are "limited" to the brain. Unlike fMRI, vessels located between the skin and CSF influence the fNIRS signal, because light traveling from a source to a detector needs to travel twice through superficial tissues (Brigadoi and Cooper, 2015). To our knowledge, no openly available superficial vascular atlas exists[10]. This is because these vessels are not as relevant to the fMRI community as cerebral vessels are. After all, non-cerebral signals are not expected to be associated with fMRI activation (Uludag et al., 2005). Additionally, these types of vessels are generally smaller and in our own experience, highly variable across participants. We believe a large-scale effort to map both, scalp and cerebral vasculature would be highly beneficial for fNIRS studies.

2.4 Comfort-performance tradeoff

In this dissertation, we successfully transferred the temporal information encoding approach and a GLM-based decoding scheme previously reported in fMRI-based BCIs (Sorger et al., 2009; Bardin et al., 2011; Sorger et al., 2012) to an fNIRS-based BCI system. Further, we advanced previous applications by extending the four-choice paradigm (Sorger et al., 2009;

[10] Technically speaking, an atlas that includes scalp/skull vessels exists (Nowinski, et al. 2011). However, this atlas is based on a single participant and according to the authors data cannot be exported in a way that could be incorporated into, among other applications, Monte Carlo simulations.

Bardin et al., 2011) to six temporally unique (yet still differentiable) encoding phases. An advantage of using this procedure is that a single channel may be sufficient for decoding participants' intentions without hampering our decoding ability. In **Chapter 2**, a joint analysis of five trials from a single channel showed promising results, as eleven of the twelve participants reached above-chance level (37.5%) accuracies, with an average accuracy of 74%. Even seven of the twelve participants reached above-chance level accuracy when the number of trials was reduced to one (average accuracy was 42%).

While temporal encoding/decoding approach may work well when combining multiple trials, decoding on a single trial basis needs to be improved for real-world BCI applications. One way forward is to include more channels, since in general, having more (informative) channels increases SNR, as task information is coupled in channels but noise is often independent between channels (Shlens, 2014), at least after accounting for physiological noise. However, increasing the number of channels will most likely affect the comfort of participants. Whether there is an optimum number of channels to ensure participant comfort *and* maximize the performance of a BCI system remains an open question. Despite its relevance for fNIRS-BCIs, to our knowledge no study has systematically investigated the tradeoff between BCI performance and participant comfort by varying the number of channels comprising the layout, while recording comfort scores.

2.5 The potential of augmented reality

Comfort is closely linked to participant motivation and engagement: an uncomfortable setup will hinder the engagement and motivation of the participant, which can lead to lower performance. On the other hand, a highly engaged and motivated participant will probably have more tolerance to less comfortable setups or longer measurements. The BCI paradigm and interface can affect the engagement and motivation of the participant. In **Chapter 2**, we utilized AR technology, as it allowed participants to act on the environment using the BCI system while still being present in it. While still in a laboratory setting and using a in house-made, simple setup, participants indicated that AR was engaging and motivating. Still, augmented reality technology requires additional elements to be incorporated into a BCI system and thus asks for careful consideration to ensure the system remains ergonomic and feasible. One possible modification to increase usability would be to incorporate smart glasses into the BCI design. Proof-of-concept fNIRS-based BCIs have assessed the potential

of smart glasses. These include *Phylter* (Afergan et al., 2015) and *Zero Shutter Camera* (Shibata et al., 2014), which adaptively determine whether a user can receive notifications or trigger a photo based on the cognitive load. Importantly, these applications rely on users' visual abilities to control BCI systems. However, some individuals such as those with acute motor disabilities may suffer from severe visual impairments and/or disability to control eye movements (Käthner et al., 2015). Thus, BCIs based on other sensory modalities such as auditory and tactile stimulation have been proposed (Riccio et al., 2012; Kaufmann et al., 2013). Most of the AR applications have focused on visually integrating virtual objects into real environments, including those in this dissertation. Instead, researchers could explore auditory AR, in which virtual acoustic objects are integrated into the real world. This approach has been proposed (in a non-BCI context) for visually impaired users (Ribeiro et al., 2012). Future work could therefore explore its feasibility for BCI applications using fNIRS measurements. Overall, these promising studies suggest that AR-based fNIRS-BCIs are worth further investigation to develop practical real-world applications.

2.6 Beyond the technical improvements of fNIRS BCIs

The work presented in this thesis examined a number of factors affecting fNIRS-BCI performance. These include optode placement, physiological noise and BCI-paradigm parameters such as encoding time and the nature of the interface. Importantly, we examined each of these elements in isolation to best determine their potential effects on BCI systems. Future work focusing on improving technological aspects of fNIRS-BCI systems should aim to validate these factors jointly in real-world experiments. All empirical chapters of this dissertation were limited to a well-controlled laboratory setting, in healthy young participants with differing acquaintance of and experience with neuroscience and/or BCI technology. However, in practice, BCIs for communication and control are used in hospital rooms or at home and the profiles of end-users are likely to differ compared to healthy young adults. Focus groups with end-users and other stakeholders such as their family members, caregivers, doctors and other professionals will provide BCI developers a more practical perspective of the needs and expectations of BCI systems. Additionally, understanding the technical limitations of user environments, such as available measurement space, whether there is internet connection, level of noise, *etc.*, would help to shape the design of BCI systems.

One key advantage of fNIRS is that combining it with other modalities such as EEG is relatively easy. Combined EEG and fNIRS BCI systems, also known as hybrid systems (hBCIs), consist a promising way forward. They have demonstrated higher performances compared to unimodal BCIs in terms of classification accuracy and information transfer rate (Fazli et al., 2011; Khan et al., 2014; Khan and Hong, 2017; Shin et al., 2018a; Rezazadeh Sereshkeh et al., 2019). These advantages are intuitive given their increase in available information for BCI use since there is no significant interference between the EEG and fNIRS signals (Shin et al., 2018a; Shin et al., 2018b). That said, future work using hybrid systems should balance setup size and user comfort, similar to the work in this dissertation.

3 Conclusion

The work presented in this dissertation focused on addressing some of the challenges faced by fNIRS-BCIs under well-controlled laboratory conditions. These examinations were able to advance our understanding of the fNIRS signal used in BCI applications. We hope that future communication and control fNIRS-BCI studies will be able to combine the novel BCI paradigm developed in **Chapter 2**, the improved optode-placement schemes introduced in **Chapter 3** and the better understanding of the role of physiological noise in fNIRS signal correction methods obtained in **Chapter 4**. We believe that the way forward not only involves technical advancements of BCIs but also requires active collaboration between BCI researchers and end-user groups. With this joint effort in place, we will be able to materialize the translational potential of fNIRS-BCI applications to improve the lives of patients that would benefit from computer assistance for communication or motor control.

4 References

Aasted, C.M., Yücel, M.A., Cooper, R.J., Dubb, J., Tsuzuki, D., Becerra, L., et al. (2015). Anatomical guidance for functional near-infrared spectroscopy: AtlasViewer tutorial. *Neurophotonics* 2(2)**,** 020801-020801. doi: 10.1117/1.NPh.2.2.020801.

Afergan, D., Hincks, S.W., Shibata, T., and Jacob, R.J.K. (2015). Phylter: A System for Modulating Notifications in Wearables Using Physiological Sensing. *Foundations of Augmented Cognition: 9th International Conference, AC* doi: 10.1007/978-3-319-20816-9_17.

Bardin, J.C., Fins, J.J., Katz, D.I., Hersh, J., Heier, L.A., Tabelow, K., et al. (2011). Dissociations between behavioural and functional magnetic resonance imaging-based evaluations of cognitive function after brain injury. *Brain : a journal of neurology* 134(Pt 3)**,** 769-782. doi: 10.1093/brain/awr005.

Bernier, M., Cunnane, S.C., and Whittingstall, K. (2018). The morphology of the human cerebrovascular system. *Human Brain Mapping* 39(12)**,** 4962-4975. doi: 10.1002/hbm.24337.

Brigadoi, S., and Cooper, R.J. (2015). How short is short? Optimum source-detector distance for short-separation channels in functional near-infrared spectroscopy. *Neurophotonics* 2(2)**,** 025005-025005. doi: 10.1117/1.NPh.2.2.025005.

Brigadoi, S., Salvagnin, D., Fischetti, M., and Cooper, R.J. (2018). Array Designer: automated optimized array design for functional near-infrared spectroscopy. *Neurophotonics* 5(3)**,** 1-19, 19.

Culver, J.P., Ntziachristos, V., Holboke, M.J., and Yodh, A.G. (2001). Optimization of optode arrangements for diffuse optical tomography: A singular-value analysis. *Optics Letters* 26(10)**,** 701-703. doi: 10.1364/OL.26.000701.

Dunås, T., Wåhlin, A., Ambarki, K., Zarrinkoob, L., Malm, J., and Eklund, A. (2017). A Stereotactic Probabilistic Atlas for the Major Cerebral Arteries. *Neuroinformatics* 15(1)**,** 101-110. doi: 10.1007/s12021-016-9320-y.

Fazli, S., Mehnert, J., Steinbrink, J., Curio, G., Villringer, A., Müller, K.-R., et al. (2011). Enhanced performance by a hybrid NIRS–EEG brain computer interface. *NeuroImage* 59**,** 519-529. doi: 10.1016/j.neuroimage.2011.07.084.

Forkert, N.D., Suniaga, S., Fiehler, J., Wersching, H., Knecht, S., and Kemmling, A. (2012). Generation of a probabilistic arterial cerebrovascular atlas derived from 700 time-of-flight MRA datasets. *Stud Health Technol Inform* 180**,** 148-152.

Gagnon, L., Cooper, R.J., Yücel, M.A., Perdue, K.L., Greve, D.N., and Boas, D.A. (2012). Short separation channel location impacts the performance of short channel regression in NIRS. *NeuroImage* 59(3)**,** 2518-2528. doi: 10.1016/j.neuroimage.2011.08.095.

Gagnon, L., Perdue, K., Greve, D.N., Goldenholz, D., Kaskhedikar, G., and Boas, D.A. (2011). Improved recovery of the hemodynamic response in diffuse optical imaging using short optode separations and state-space modeling. *NeuroImage* 56(3)**,** 1362-1371. doi: 10.1016/j.neuroimage.2011.03.001.

Käthner, I., Kübler, A., and Halder, S. (2015). Comparison of eye tracking, electrooculography and an auditory brain-computer interface for binary communication: a case study with a participant in

the locked-in state. *Journal of NeuroEngineering and Rehabilitation* 12(1)**,** 76. doi: 10.1186/s12984-015-0071-z.

Kaufmann, T., Holz, E., and Kübler, A. (2013). Comparison of tactile, auditory, and visual modality for brain-computer interface use: a case study with a patient in the locked-in state. *Frontiers in Neuroscience* 7**,** 129.

Khan, M.J., and Hong, K.-S. (2017). Hybrid EEG–fNIRS-Based Eight-Command Decoding for BCI: Application to Quadcopter Control. *Frontiers in Neurorobotics* 11**,** 6.

Khan, M.J., Hong, M.J., and Hong, K.-S. (2014). Decoding of four movement directions using hybrid NIRS-EEG brain-computer interface. *Frontiers in Human Neuroscience* 8**,** 244.

Kirilina, E., Yu, N., Jelzow, A., Wabnitz, H., Jacobs, A., and Tachtsidis, I. (2013). Identifying and quantifying main components of physiological noise in functional near infrared spectroscopy on the prefrontal cortex. *Frontiers in Human Neuroscience* 7(864). doi: 10.3389/fnhum.2013.00864.

Kübler, A. (2020). The history of BCI: From a vision for the future to real support for personhood in people with locked-in syndrome. *Neuroethics* 13(2)**,** 163-180. doi: 10.1007/s12152-019-09409-4.

Lina, J.M., Dehaes, M., Matteau-Pelletier, C., and Lesage, F. (2008). Complex wavelets applied to diffuse optical spectroscopy for brain activity detection. *Optics Express* 16(2)**,** 1029-1050. doi: 10.1364/OE.16.001029.

Machado, A., Cai, Z., Pellegrino, G., Marcotte, O., Vincent, T., Lina, J.M., et al. (2018). Optimal positioning of optodes on the scalp for personalized functional near-infrared spectroscopy investigations. *J Neurosci Methods* 309**,** 91-108. doi: 10.1016/j.jneumeth.2018.08.006.

Machado, A., Marcotte, O., Lina, J.M., Kobayashi, E., and Grova, C. (2014). Optimal optode montage on electroencephalography/functional near-infrared spectroscopy caps dedicated to study epileptic discharges. *Journal of Biomedical Optics* 19(2)**,** 1-17, 17.

Nowinski, W.L., Chua, B.C., Marchenko, Y., Puspitsari, F., Volkau, I., and Knopp, M.V. (2011). Three-dimensional reference and stereotactic atlas of human cerebrovasculature from 7Tesla. *NeuroImage* 55(3)**,** 986-998. doi: https://doi.org/10.1016/j.neuroimage.2010.12.079.

Rezazadeh Sereshkeh, A., Yousefi, R., Wong, A.T., Rudzicz, F., and Chau, T. (2019). Development of a ternary hybrid fNIRS-EEG brain–computer interface based on imagined speech. *Brain-Computer Interfaces* 6(4)**,** 128-140. doi: 10.1080/2326263X.2019.1698928.

Ribeiro, F., Florencio, D., Chou, P., and Zhang, Z. (2012). Auditory augmented reality: Object sonification for the visually impaired. *IEEE 14th International Workshop on Multimedia Signal Processing (MMSP)***,** 319-324. doi: 10.1109/MMSP.2012.6343462.

Riccio, A., Mattia, D., Simione, L., Olivetti, M., and Cincotti, F. (2012). Eye-gaze independent EEG-based brain–computer interfaces for communication. *Journal of Neural Engineering* 9(4)**,** 045001. doi: 10.1088/1741-2560/9/4/045001.

Sato, T., Nambu, I., Takeda, K., Aihara, T., Yamashita, O., Isogaya, Y., et al. (2016). Reduction of global interference of scalp-hemodynamics in functional near-infrared spectroscopy using short

distance probes. *NeuroImage* 141**,** 120-132. doi: https://doi.org/10.1016/j.neuroimage.2016.06.054.

Shibata, T., Peck, E.M., Afergan, D., Hincks, S.W., Yuksel, B.F., and Jacob, R.J.K. (2014). Building implicit interfaces for wearable computers with physiological inputs: zero shutter camera and phylter. *Proceedings of the adjunct publication of the 27th annual ACM symposium on User interface software and technology***,** 89–90. doi: 10.1145/2658779.2658790.

Shih, J.J., Krusienski, D.J., and Wolpaw, J.R. (2012). Brain-Computer Interfaces in Medicine. *Mayo Clinic Proceedings* 87(3)**,** 268-279. doi: https://doi.org/10.1016/j.mayocp.2011.12.008.

Shin, J., Kwon, J., and Im, C.-H. (2018a). A Ternary Hybrid EEG-NIRS Brain-Computer Interface for the Classification of Brain Activation Patterns during Mental Arithmetic, Motor Imagery, and Idle State. *Frontiers in Neuroinformatics* 12**,** 5.

Shin, J., von Lühmann, A., Kim, D.-W., Mehnert, J., Hwang, H.-J., and Müller, K.-R. (2018b). Simultaneous acquisition of EEG and NIRS during cognitive tasks for an open access dataset. *Scientific Data* 5(1)**,** 180003. doi: 10.1038/sdata.2018.3.

Shlens, J. 2014. A Tutorial on Principal Component Analysis. arXiv: 1404.1100.

Sorger, B., Dahmen, B., Reithler, J., Gosseries, O., Maudoux, A., Laureys, S., et al. (2009). Another kind of 'BOLD Response': answering multiple-choice questions via online decoded single-trial brain signals. *Progress in brain research* 177**,** 275-292. doi: 10.1016/S0079-6123(09)17719-1.

Sorger, B., Reithler, J., Dahmen, B., and Goebel, R. (2012). A Real-Time fMRI-Based Spelling Device Immediately Enabling Robust Motor-Independent Communication. *Current Biology* 22(14)**,** 1333-1338. doi: https://doi.org/10.1016/j.cub.2012.05.022.

Stangl, M., Bauernfeind, G., Kurzmann, J., Scherer, R., and Neuper, C. (2013). A Haemodynamic Brain–Computer Interface Based on Real-Time Classification of near Infrared Spectroscopy Signals during Motor Imagery and Mental Arithmetic. *Journal of Near Infrared Spectroscopy* 21(3)**,** 157-171. doi: 10.1255/jnirs.1048.

Uludag, K., Dubowitz, D.J., and Buxton, R.B. (2005). "Basic principles of functional MRI," in *Clinical magnetic resonance imaging*, eds. K. Uludag, D.J. Dubowitz & R.B. Buxton. (Philadelphia: Saunders Elsevier), 249-287.

Viviani, R. (2016). A Digital Atlas of Middle to Large Brain Vessels and Their Relation to Cortical and Subcortical Structures. *Frontiers in Neuroanatomy* 10**,** 12.

Ward, P.G.D., Ferris, N.J., Raniga, P., Dowe, D.L., Ng, A.C.L., Barnes, D.G., et al. (2018). Combining images and anatomical knowledge to improve automated vein segmentation in MRI. *NeuroImage* 165**,** 294-305. doi: https://doi.org/10.1016/j.neuroimage.2017.10.049.

Wijeakumar, S., Spencer, J.P., Bohache, K., Boas, D.A., and Magnotta, V.A. (2015). Validating a new methodology for optical probe design and image registration in fNIRS studies. *NeuroImage* 106**,** 86-100. doi: https://doi.org/10.1016/j.neuroimage.2014.11.022.

Zimeo Morais, G.A., Balardin, J.B., and Sato, J.R. (2018). fNIRS Optodes' Location Decider (fOLD): a toolbox for probe arrangement guided by brain regions-of-interest. *Scientific Reports* 8(1)**,** 3341. doi: 10.1038/s41598-018-21716-z.

In the above reference list, 74.36% of first authors were male (vs. 25.64% that were female), while 89.74% of last authors were male (vs. 10.26 % that were female).

Summary

A brain-computer interface (BCI) is a system that measures and converts brain activity into artificial output that replaces, restores or enhances natural central nervous system output. Thus, BCIs have the potential to ultimately restore communication and control in the absence of words/gestures and other motor actions to people with severe neuromuscular disabilities. Functional near-infrared spectroscopy (fNIRS) is a promising functional-neuroimaging modality for this objective that has been used for BCIs in healthy participants and in few occasions, in clinical settings. This is because there are substantial challenges associated with fNIRS-based BCIs in everyday situations, such as home-use or hospital settings. This dissertation outlined progress to overcome some of these obstacles. In **Chapter 2**, we evaluated factors that can improve the feasibility of ecologically-friendly fNIRS-based BCIs. We evaluated short task-duration periods alongside augmented-reality (AR) technology that enables a more immersive setup. Further, we evaluated the feasibility of using a single mental-imagery task and fNIRS channel to select an option in each level. For that, we used a temporal en- and decoding approach. This proof-of-concept study revealed that participants can successfully control the BCI system with a single fNIRS channel and motor-imagery task when using a relatively short task duration (6s) while achieving a promising mean classification accuracy of 74%. Positive reports from study participants suggest that AR is a promising and feasible technology to enhance user experience for fNIRS-BCI applications. This work conveys fundamental steps towards developing fNIRS-based AR-BCI systems to be used as communication and control devices in a clinical setting or for home-use. In **Chapter 3**, we investigated how different quantities of individualized MRI-based data influence the optode placement and in turn, fNIRS signal quality and sensitivity to detect brain activation. This work revealed that acquiring additional individual MRI data leads to better outcomes and that not all the modalities tested are necessary to achieve a robust setup. Finally, in **Chapter 4** we assessed whether the quantity of unwanted physiological noise present in the fNIRS signal depends on the proximity and density of vascular structures around optodes. Further, we tested if this relationship affects one particular physiological noise-correction approach: short-separation regression (SSR). This approach uses short-distance fNIRS channels (SDCs) to regress out physiological noise from normal-distance channels (NDCs). We examined three sources of

physiological noise: Mayer waves, respiration and heartbeat. Our analyses indicated that the Mayer-wave amplitude captured by SDCs was related to the presence and density of vascular structures in their vicinity for oxyhemoglobin data only. We did not find any evidence that the reduction of physiological noise in NDCs after SSR is related to the presence of vascular structures. This chapter therefore extends our knowledge of the relationship between the vasculature features and the presence of physiological noise in fNIRS channels. Taken together, the three empirical studies provide insights that can contribute to the advancement of data acquisition and analysis strategies to improve the applicability of fNIRS-BCIs to everyday situations.

Knowledge Valorization

The principal motivation for the development of BCIs is to restore communication and control in the absence of words, gestures and other motor actions to people with severe neuromuscular disabilities (Shih et al., 2012). FNIRS is a promising functional-neuroimaging modality for this objective that has been used for BCIs in healthy participants (Naseer and Hong, 2013; Weyand and Chau, 2015; Batula et al., 2017; Nagels-Coune et al., 2017; Weyand and Chau, 2017; Sereshkeh et al., 2018; Rezazadeh Sereshkeh et al., 2019; Abdalmalak et al., 2020; Nagels-Coune et al., 2020) and in patients (Gallegos-Ayala et al., 2014; Abdalmalak et al., 2017). However, clinical applications of fNIRS-BCI systems suffer from a number of limitations that have slowed its translational potential. This dissertation outlined progress to overcome some of these limitations. First, we evaluated factors that could improve the feasibility of real-life fNIRS-based BCIs (**Chapter 2**). There we saw that participants can successfully control the BCI system by imagining doing a short task (mental imagery) and using a single pair of measurement sensors. Further, positive reports from participants suggest that augmented reality is a promising technology to enhance user experience for fNIRS-BCI applications. In the next chapters, we evaluated factors that can compromise fNIRS signal quality and its sensitivity to detect task-related brain activation, which is crucial to ensure a correct functioning of BCI systems. The way fNIRS sensors are arranged on the participant's head is one of such factors, and in this context, we investigated how different sensor placement strategies affect the fNIRS signal in **Chapter 3**. This study revealed that using gradually more individualized information obtained from the MRI scanner led to a better outcome, but that not all the information acquired at the scanner was required to achieve a robust setup. Another factor strongly influencing the fNIRS signal is the physiological noise such as heartbeat and breathing, to name a few. This physiological noise is measured at the same time as task-related brain signal by the fNIRS sensors, and it is not straightforward to tear them apart, which compromises our sensitivity to detect task-related brain activation. It has been suggested that the presence of vessels around fNIRS sensors can influence the amount of unwanted physiological noise, and in **Chapter 4**, we investigated precisely that. In addition, we tested whether the effectiveness of a physiological noise correction method named short-separation regression (SSR), which uses additional sensors placed on the participant's head, also depends on the proximity and

density of vessels. The study verified that SSR improves fNIRS-signal quality and the sensitivity to detect task-related brain activation considerably and shows that signals obtained via these additional channels are affected by close vascular structures.

Short- and long-term impact

Although the presented work was framed in a communication and control BCI context, the knowledge gained here can be extended to other BCI applications. As indicated in Figure KV1, the most immediate beneficiaries of the work presented in this dissertation are other research groups working directly on fNIRS-based BCI for communication and control as well as neurofeedback. This is because all empirical chapters addressed challenges shared amongst these applications. Moreover, the findings from **Chapters 3** and **4** are applicable to research that focuses on the study of other (if not all) neural processes using fNIRS. These chapters provide insight to factors influencing signal quality and sensitivity to brain activation which is relevant to any fNIRS study. Specifically, the knowledge gained in **Chapter 3** will help researchers to efficiently utilize resources when designing fNIRS experiments. Meanwhile, basic methodological investigations like the one presented in **Chapter 4** will form the basis of fNIRS physiological noise-removal strategies in the future. These two chapters are further relevant for those developing tools to optimize optode layout design and fNIRS data analyses. In addition, we have purposely made the dataset from **Chapter 2** and probabilistic maps from **Chapter 3** available to support this progress.

Within the realm of BCIs, our work contributes to ongoing development of brain-robot interfaces and their extended range of potential applications in the many domains where robots are used. Examples include disaster management (e.g. remote control of robots that inspect dangerous or contaminated areas), industrial manufacturing (e.g. training robots to determine what is defective on a conveyor belt and remove it automatically based on a human inspector's brain signals), entertainment (e.g. games with robotic agents) and healthcare (e.g. support for people with severe motor impairments completing daily-life activities or regaining functionality through neuroprosthetic devices).

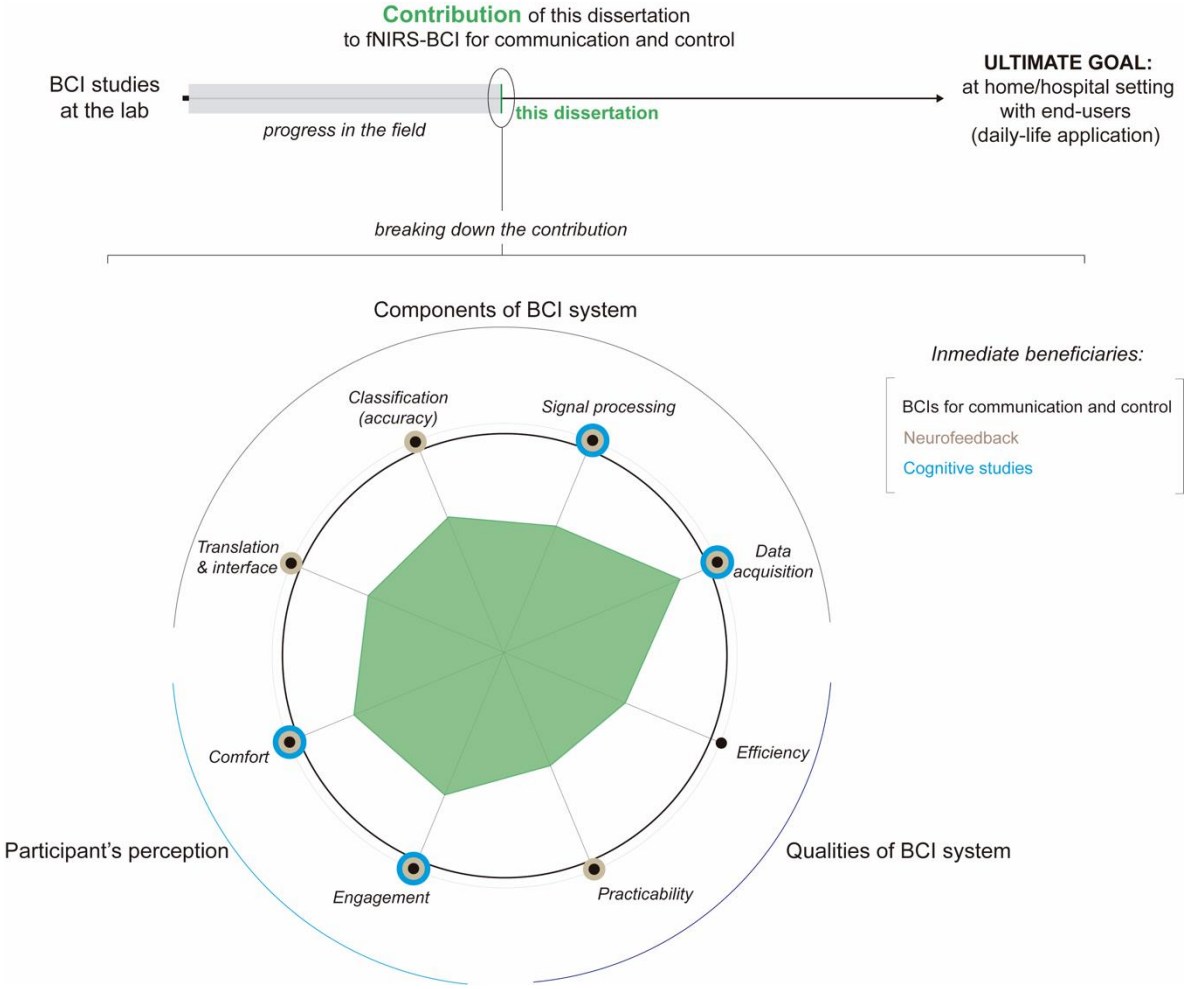

Figure KV1. Contribution of this dissertation and its immediate beneficiaries. The knowledge obtained in this thesis contributes to the advancement of data analysis and acquisition techniques to ultimately make fNIRS-BCIs applicable to everyday situations. The main contributions were divided into three categories, namely components constituting a BCI system, qualities of a BCI system and participant's perception. The polar diagram illustrates the contribution of this work regarding each subcategory. The concentric circles represent the immediate beneficiaries of this thesis: other fNIRS-based BCI researchers focusing on communication and control applications (in black), fNIRS-based neurofeedback applications (in beige) and other fNIRS-based cognitive studies (in blue).

The work presented in this dissertation can also benefit those with brain injuries and mental disorders. For example, patients with severe motor impairment (such as those with locked-in syndrome) have limited behavioral capabilities, yet it should be possible to express thoughts using preserved mental abilities (Sorger et al., 2012). Here, we worked to improve signal acquisition and analyses approaches while almost exclusively using mental tasks.

Together with the small optode setups featured in this thesis, we have set realistic foundations for applying our work in this and other patient groups sharing similar symptoms. Additionally, in **Chapter 2** we showed that AR technology can be successfully combined with fNIRS-BCI setups in the context of communication and control. Beyond these applications, AR technology can be used in neurofeedback therapy in patients suffering from anxiety disorders such as phobias to facilitate anxiety regulation. This is particularly interesting since AR provides a unique scenario where a realistic, anxiety-inducing stimulus can be presented in a controlled manner by imposing virtual stimuli, such as personalized threatening spider, over real objects and environments, such as the patient's arm (Gamito et al., 2011).

Future directions

A community effort

The ever-growing fNIRS community is well aware of the limitations of fNIRS technology and it has made collaborative effort to minimize and account for these. For example, several tools have been developed for designing informed and optimized optode setups that guarantee good signal quality and coverage (Machado et al., 2014; Aasted et al., 2015; Wijeakumar et al., 2015; Brigadoi et al., 2018; Machado et al., 2018; Zimeo Morais et al., 2018). A wide range of methods have been developed and implemented in analysis software to correct for the physiological and non-physiological noise sources, both offline (Homer 2 and Homer 3 (Huppert et al., 2009); Nirs toolbox (Santosa et al., 2018) and Nirstorm (Tadel et al., 2011)) and in real time (Lührs and Goebel, 2017). Further, validation and standardization efforts of these tools have promoted reproducibility. We hope that this collaborative effort will remain in the years to come.

Miniaturization of technology

Monitoring brain activity using fNIRS in real life situations has become increasingly accessible over recent years thanks to the development of miniaturized and wearable fNIRS devices. These systems do not use fiber optic bundles, making them more lightweight and more resistant to movement artifacts (Pinti et al., 2018). These are highly desirable features for real-life, fNIRS-based BCI applications, and we expect this progress to continue over the next years. Further, with the miniaturization of the technology and the improvement of

neuronavigation systems and auxiliary measurement devices, we expect to see a more streamlined integration of these tools and fNIRS systems. Of particular interest for the future of BCI applications is the development of hybrid BCIs that combine EEG and fNIRS measurements. Previous work has shown that they can achieve better performance than with unimodal BCIs (Fazli et al., 2011; Khan et al., 2014; Khan and Hong, 2017; Shin et al., 2018; Rezazadeh Sereshkeh et al., 2019). However, these systems are not frequently used in practical applications because the amount of hardware needed to capture two different types of signals simultaneously results in bulky and complex systems. We hope that the progress in miniaturization happening separately for fNIRS and EEG systems is extended to their integration.

Need for user-centered designs

It is important to emphasize that more work is required to realize these goals since the knowledge gained in this dissertation reflects basic scientific investigations that will consequently benefit these target patient groups. We addressed some of the limitations currently faced by fNIRS-BCI applications that hinder the translational potential of BCIs. We did so in ideal laboratory conditions, measuring healthy, young, motivated individuals and having minimal technical and temporal constraints. Naturally, BCI researchers will need to seek collaboration in the future with end-users and, when applicable, with their immediate caretakers, family members and medical staff. Interviews, surveys and focus groups will help researchers and developers understand and identify the needs and reality of the users. Further, direct contact with end-users will enable researchers to iteratively validate the methodological developments. This user-centered design approach has the potential to yield higher user satisfaction and better system adoption (Sujatha Ravindran et al., 2020).

Our contribution as researchers

Since their inception, BCIs have inspired countless science fiction novels and movies and have attracted substantial media coverage and attention. This can be a good thing, particularly when BCI applications are represented positively. Such coverage draws attention to struggles faced by individuals that would benefit from this technology, thereby creating a social awareness and interest in technological advancements. It can also serve as a platform for publicizing opportunities for participation in research studies. However, the image of BCI technology portrayed in these platforms can reflect dystopian views. These scenarios rarely contain technological limitations such as low information transfer rates or signal quality-related problems, and largely ignore end-user discomfort. Importantly though, dystopian scenarios stimulate open discussions about ethical concerns raised by BCI technology.

Simultaneously, unrealistic descriptions of BCI technology can inflate hopes of potential and future end-users. BCI researchers are therefore instrumental, having the expertise to educate end-users and their immediate social circle (when dealing with clinical populations), as well as the responsibility to help them manage their expectations about the technology. This can be done in a localized manner (e.g. in the aforementioned focus groups and interviews), or in bigger settings (e.g. science communication events or media platforms). Regardless of the chosen output channel, it is important to find a good balance between exhibiting enthusiasm about progress and potential of BCI applications and openly describing the current limitations and state of the technology. It is equally important to consider primary users (end-users) and a variety of secondary users when applicable, as their contribution is essential to move toward mature BCI technologies.

References

Aasted, C.M., Yücel, M.A., Cooper, R.J., Dubb, J., Tsuzuki, D., Becerra, L., et al. (2015). Anatomical guidance for functional near-infrared spectroscopy: AtlasViewer tutorial. *Neurophotonics* 2(2)**,** 020801-020801. doi: 10.1117/1.NPh.2.2.020801.

Abdalmalak, A., Milej, D., Norton, L., Debicki, D., Gofton, T., Diop, M., et al. (2017). Single-session communication with a locked-in patient by functional near-infrared spectroscopy. *Neurophotonics* 4(4)**,** 1-4. doi: 10.1117/1.NPh.4.4.040501.

Abdalmalak, A., Milej, D., Yip, L.C.M., Khan, A.R., Diop, M., Owen, A.M., et al. (2020). Assessing Time-Resolved fNIRS for Brain-Computer Interface Applications of Mental Communication. *Frontiers in Neuroscience* 14**,** 105.

Batula, A.M., Mark, J.A., Kim, Y.E., and Ayaz, H. (2017). Comparison of Brain Activation during Motor Imagery and Motor Movement Using fNIRS. *Computational intelligence and neuroscience* 2017**,** 5491296-5491296. doi: 10.1155/2017/5491296.

Brigadoi, S., Salvagnin, D., Fischetti, M., and Cooper, R.J. (2018). Array Designer: automated optimized array design for functional near-infrared spectroscopy. *Neurophotonics* 5(3)**,** 1-19, 19.

Fazli, S., Mehnert, J., Steinbrink, J., Curio, G., Villringer, A., Müller, K.-R., et al. (2011). Enhanced performance by a hybrid NIRS–EEG brain computer interface. *NeuroImage* 59**,** 519-529. doi: 10.1016/j.neuroimage.2011.07.084.

Gallegos-Ayala, G., Furdea, A., Takano, K., Ruf, C.A., Flor, H., and Birbaumer, N. (2014). Brain communication in a completely locked-in patient using bedside near-infrared spectroscopy. *Neurology* 82(21)**,** 1930-1932. doi: 10.1212/WNL.0000000000000449.

Gamito, P., Oliveira, J., Morais, D., Rosa, P., and Saraiva, T. (2011). "NeuAR@ A Review of the VR/AR Applications in the Neuroscience Domain," in *Augmented Reality - Some Emerging Application Areas,*, ed. A.Y.C. Nee. IntechOpen).

Huppert, T.J., Diamond, S.G., Franceschini, M.A., and Boas, D.A. (2009). HomER: a review of time-series analysis methods for near-infrared spectroscopy of the brain. *Applied optics* 48(10)**,** D280-D298. doi: 10.1364/ao.48.00d280.

Khan, M.J., and Hong, K.-S. (2017). Hybrid EEG–fNIRS-Based Eight-Command Decoding for BCI: Application to Quadcopter Control. *Frontiers in Neurorobotics* 11**,** 6.

Khan, M.J., Hong, M.J., and Hong, K.-S. (2014). Decoding of four movement directions using hybrid NIRS-EEG brain-computer interface. *Frontiers in Human Neuroscience* 8**,** 244.

Lührs, M., and Goebel, R. (2017). Turbo-Satori: a neurofeedback and brain-computer interface toolbox for real-time functional near-infrared spectroscopy. *Neurophotonics* 4(4)**,** 041504-041504. doi: 10.1117/1.NPh.4.4.041504.

Machado, A., Cai, Z., Pellegrino, G., Marcotte, O., Vincent, T., Lina, J.M., et al. (2018). Optimal positioning of optodes on the scalp for personalized functional near-infrared spectroscopy investigations. *J Neurosci Methods* 309**,** 91-108. doi: 10.1016/j.jneumeth.2018.08.006.

Machado, A., Marcotte, O., Lina, J.M., Kobayashi, E., and Grova, C. (2014). Optimal optode montage on electroencephalography/functional near-infrared spectroscopy caps dedicated to study epileptic discharges. *Journal of Biomedical Optics* 19(2)**,** 1-17, 17.

Nagels-Coune, L., Benitez-Andonegui, A., Reuter, N., Lührs, M., Goebel, R., De Weerd, P., et al. (2020). Brain-Based Binary Communication Using Spatiotemporal Features of fNIRS Responses. *Frontiers in Human Neuroscience* 14(113). doi: 10.3389/fnhum.2020.00113.

Nagels-Coune, L., Kurban, D., Reuter, N., Benitez, A., Gossé, L., Riecke, L., et al. (2017). Yes or no? binary brain-based communication utilizing motor imagery and fNIRS. *Proceedings of the 7th Graz Brain-Computer Interface*. doi: 10.3217/978-3-85125-533-1-65.

Naseer, N., and Hong, K.-S. (2013). Classification of functional near-infrared spectroscopy signals corresponding to the right- and left-wrist motor imagery for development of a brain–computer interface. *Neuroscience Letters* 553**,** 84-89. doi: https://doi.org/10.1016/j.neulet.2013.08.021.

Pinti, P., Aichelburg, C., Gilbert, S., Hamilton, A., Hirsch, J., Burgess, P., et al. (2018). A Review on the Use of Wearable Functional Near-Infrared Spectroscopy in Naturalistic Environments(). *The Japanese psychological research* 60(4)**,** 347-373. doi: 10.1111/jpr.12206.

Rezazadeh Sereshkeh, A., Yousefi, R., Wong, A.T., Rudzicz, F., and Chau, T. (2019). Development of a ternary hybrid fNIRS-EEG brain–computer interface based on imagined speech. *Brain-Computer Interfaces* 6(4)**,** 128-140. doi: 10.1080/2326263X.2019.1698928.

Santosa, H., Zhai, X., Fishburn, F., and Huppert, T. (2018). The NIRS Brain AnalyzIR Toolbox. *Algorithms* 11**,** 73. doi: 10.3390/a11050073.

Sereshkeh, A.R., Yousefi, R., Wong, A.T., and Chau, T. (2018). Online classification of imagined speech using functional near-infrared spectroscopy signals. *Journal of Neural Engineering* 16(1)**,** 016005. doi: 10.1088/1741-2552/aae4b9.

Shih, J.J., Krusienski, D.J., and Wolpaw, J.R. (2012). Brain-Computer Interfaces in Medicine. *Mayo Clinic Proceedings* 87(3)**,** 268-279. doi: https://doi.org/10.1016/j.mayocp.2011.12.008.

Shin, J., Kwon, J., and Im, C.-H. (2018). A Ternary Hybrid EEG-NIRS Brain-Computer Interface for the Classification of Brain Activation Patterns during Mental Arithmetic, Motor Imagery, and Idle State. *Frontiers in Neuroinformatics* 12**,** 5.

Sorger, B., Reithler, J., Dahmen, B., and Goebel, R. (2012). A Real-Time fMRI-Based Spelling Device Immediately Enabling Robust Motor-Independent Communication. *Current Biology* 22(14)**,** 1333-1338. doi: https://doi.org/10.1016/j.cub.2012.05.022.

Sujatha Ravindran, A., Tukiainen, A., Ramos-Murguialday, A., Biasiucci, A., Forsland, A., Paek, A., et al. (2020). Standards roadmap: Neurotechnologies for brain-machine interfacing. *IEEE NEUROTECH BMI*.

Tadel, F., Baillet, S., Mosher, J.C., Pantazis, D., and Leahy, R.M. (2011). Brainstorm: a user-friendly application for MEG/EEG analysis. *Computational intelligence and neuroscience* 2011**,** 879716-879716. doi: 10.1155/2011/879716.

Weyand, S., and Chau, T. (2015). Correlates of Near-Infrared Spectroscopy Brain–Computer Interface Accuracy in a Multi-Class Personalization Framework. *Frontiers in Human Neuroscience* 9(536). doi: 10.3389/fnhum.2015.00536.

Weyand, S., and Chau, T. (2017). Challenges of implementing a personalized mental task near-infrared spectroscopy brain–computer interface for a non-verbal young adult with motor impairments. *Developmental Neurorehabilitation* 20(2)**,** 99-107. doi: 10.3109/17518423.2015.1087436.

Wijeakumar, S., Spencer, J.P., Bohache, K., Boas, D.A., and Magnotta, V.A. (2015). Validating a new methodology for optical probe design and image registration in fNIRS studies. *NeuroImage* 106**,** 86-100. doi: https://doi.org/10.1016/j.neuroimage.2014.11.022.

Zimeo Morais, G.A., Balardin, J.B., and Sato, J.R. (2018). fNIRS Optodes' Location Decider (fOLD): a toolbox for probe arrangement guided by brain regions-of-interest. *Scientific Reports* 8(1)**,** 3341. doi: 10.1038/s41598-018-21716-z.

In the above reference list, 70.00% of first authors were male (vs. 30.00% that were female), while 93.33% of last authors were male (vs. 6.67% that were female).

Acknowledgements

First and foremost, I have to thank my supervisors. Bettina, thank you for giving me the opportunity to pursue a PhD under your guidance. I have learned a lot from and with you during these years. Thank you, too, for trusting that we could complete the various running projects whether I was in Maastricht or somewhere else. Rainer, thank you for your guidance and for the timely feedback that always proved useful. Rico, even though our interaction was not as frequent as I would have hoped for, I always enjoyed talking to you and appreciated your ideas.

Michael, my un-official supervisor, thank you for the many discussions and for sitting through countless long meetings with me. Your contribution was essential to complete this thesis. Dimo, your expertise was instrumental to carry out these projects. Thank you for always being ready to help. To the hemodynamic BCI group and occasional guests, thank you for the assistance and the interesting discussions. Special thanks to Simona and Rodion for assisting during the data collection, and to all of our participants, for their time and dedication.

Christl, José, Eva and Riny: thank you. You have helped me so much during these years. It was always a pleasure to walk by your offices and chat with you. Thank you, Jordi and Noël, and Johan and Erik for your support.

To the BrainInnovation team, thank you for your long-lasting assistance and for making me feel part of the group. Special thanks to Judith - I learned a lot with you. And to Faruk, the segmentation wizard, thank you for the excellent tips.

I would like to thank all my officemates, Michele, Tyler, Isma, Emily, Valentin, Sanae, Anita, Roef and Vaish, for making the office a cozy place to work. Valentin, I learned a lot from you. Vaish, thank you for being such a nice, calming and happy presence.

Anita, Shruti, Laurien and Michael, my powerhouse, thank you for the countless (non)scientific conversations and good memories. Tabea and Hannah, the same goes to you. I greatly missed not having you around. You are all awesome friends, colleagues and teammates. Iñigo, mi hermano no oficial, gracias por sacarme siempre una sonrisa and to Wieland (together with Laurien), for introducing me to the amazing world of gardening and

wine photography. To Maria and Panda, without whom my German family would not be complete: thank you for making me feel at home.

Agus, amigo, gracias por estar dispuesto a ayudarme con lo que fuera y por ser tan buena compañía. Siempre me he sentido comprendida y escuchada contigo. Patxi, agradezco tu amistad, y tus abrazos sanadores. Geral, gracias por tu (son)risa eterna. Echo de menos tu espíritu alegre. Marta, gracias por ser tan agradable y por ser una excelente compañera de viajes locos. Linda, Yawen, Stefano, Alix, Deni, Hannah [Marifé], Rick, Sri, Faruk, Marian, Ingo, Lars: hanging out with you - whether it was at the basketball court, at an occasional dinner or at the department - was always fun. To Sasja and Alexandra, thank you for the attentiveness. Seeing either of you at the front desk or the corridors was a mood lifter. Talking about mood lifters, I could not *not* mention my beloved Bandito brothers. Thank you for the fun times (and for the excellent coffee). To the rest of the members of the CN department: thank you for building such a nice working environment. It has been a pleasure to share these years with you.

To Peppe, Dennie, Anna, Martijn, Pieter, Monika, Nicola, Grace, Meche, thank you for the fun memories. Gara, Georgina, Almudena, Cristina y Mora, me siento muy afortunada de poder haber compartido parte de esta aventura con vosotras. Thank you, Sanae for being such a cheerful and inspiring company. Emma, my youngest friend, thank you for being a sunshine during these years. Thank you Anne, Rekha and Nici for your support and friendship. To the friends in Glasgow, thank you for making the trips even more fun. Uning, Medoza, and Nur, thank you for your friendship. Your strength is inspiring.

Sarri, zure hitz eta aholkuen falta handia sentitzen dut.

Zarauzko kuadrila eta gainontzeko lagunei, eskerrik asko doktoretzako gorabeherak erlatibizatzen laguntzeagatik eta distantzia oztopo ez dela berresteagatik.

Familiakoei, eskerrak bihotzetz zuen maitasun eta babesengatik. Zorionekoa ni, halako familia baten kide izateagatik! Ama eta aita, zuen esfortzu eta eskuzabaltasunek ez dute parekorik – eskerrik asko erraztu dizkidazueten aukera guztiengatik.

Tyler, my rock, thank you for being such a supportive partner. I love you. I cannot wait to start our next chapter *together*.

About the author

Amaia Benitez Andonegui was born on June 21st, 1991 in Zarautz, Spain. She attended school and high school in her hometown, at La Salle Ikastetxea and Lizardi Institutua, respectively. Between 2009 and 2013, she carried out her undergraduate studies in Biomedical Engineering at Tecnun College of Engineering in Donostia, Spain. In 2012 she spent a Erasmus semester at Chalmers University of Technology in Gothenburg, Sweden. In 2013 she was admitted to the Research Master program in Cognitive Neuroscience at Maastricht University. Her Master thesis focused on optimizing fNIRS optode placement to measure activity in the supplementary motor area. This research was supervised by Dr. Sorger and Prof. Goebel. Between 2015 and 2020, she conducted her doctoral research under the supervision of Dr. Sorger, Prof. Goebel and Dr. Möckel at the Department of Cognitive Neuroscience, Faculty of Psychology and Neuroscience, and the Department of Knowledge Engineering, Faculty of Science and Engineering, at Maastricht University. Currently she works as a research associate at the Department of Cognitive Neuroscience at Maastricht University on mapping axes of motion in the human motion complex using 7 Tesla magnetic resonance imaging with Prof. Goebel.

Publications

Peer-reviewed articles

Benitez-Andonegui, A., Burden, R., Benning, R., Möckel, R, Lührs, M., Sorger, B. (2020). *An augmented-reality fNIRS-based brain-computer interface: a proof- of-concept study*. Frontiers Neuroscience, Vol. 14(346). doi: 10.3389/fnins.2020.00346

Nagels-Coune, L., **Benitez-Andonegui, A.,** Reuter, N., Lührs, M., Goebel, R., De Weerd, P., et al. (2020). Brain-Based Binary Communication Using Spatiotemporal Features of fNIRS Responses. Frontiers in Human Neuroscience Vol. 14(113). doi: 10.3389/fnhum.2020.00113

Lührs M, Riemenschneider B, Eck J, **Benitez-Andonegui A**, Poser BA, Heinecke A, Krause F, Esposito F, Sorger B, Hennig J, Goebel R. (2019) *The potential of MR-Encephalography for BCI/Neurofeedback applications with high temporal resolution.* NeuroImage. Vol. 194, pp 228-243

Under review

Benitez-Andonegui, A., Lührs, M., Nagels-Couner, L., Ivanov, D., Goebel, R., Sorger, B. *The effect of considering individual functional and anatomical MRI on fNIRS optode-layout design*

Benitez-Andonegui, A., Dumitrescu, S., Tursic, A., Goebel, R., Ivanov, D., Lührs, M., Sorger, B. *Investigating the impact of vasculature on short distance channel correction in fNIRS*

Conference contributions

Benitez-Andonegui A, Burden R, Benning R, Möckel R, Lührs M, Sorger B (2019, December*). An augmented-reality fNIRS-based brain-computer interface: a proof-of-concept study*. Presented at rtFIN Maastricht The Netherlands

Tursic A, Muñoz-Moldes S, Lührs M, Eck J, **Benitez-Andonegui A**, Goebel R (2019, December). *The effect of session-specific region definition in multi-session fMRI neurofeedback*. Presented at rtFIN Maastricht The Netherlands

Tursic A, Muñoz-Moldes S, Lührs M, Eck J, **Benitez-Andonegui A**, Peters J, Cleeremans A, Goebel R (2019, December). *Level-specific modulation of supplementary motor area and self-monitoring of performance in multi-session fMRI neurofeedback.* Presented at rtFIN Maastricht The Netherlands

Rafeh R, Evenblij D, **Benitez-Andonegui A**, Kurban D, Valente G, Sorger B (2019, December). *A Comparison of Feature Selection Methods for fMRI-based Brain-Computer Interfaces*. Presented at rtFIN Maastricht The Netherlands

Koyun AH, **Benitez-Andonegui A**, Lührs M, Sorger B (2019, December). *Shining light on the influence of a task-relevant object on the fNIRS-response to mental imagery, active and passive movement stimulation*. Presented at rtFIN Maastricht The Netherlands

Van de Wauw C, Konstantakis A, **Benitez-Andonegui A**, Lührs M, Sorger B (2019, December). *fNIRS-based detection of SMA activity for neurofeedback applications*. Presented at rtFIN Maastricht The Netherlands

Evenblij D, Rafeh R, **Benitez-Andonegui A**, Kurban D, Valente G & Sorger B (2019, December). *An efficient fMRI-based brain-computer interface to encode yes/no answers*. Presented at rtFIN Maastricht The Netherlands

Tursic A, Muñoz-Moldes S, Lührs M, Eck J, **Benitez-Andonegui A**, Goebel R (2019, June). *The effect of session-specific region definition in multi-session fMRI neurofeedback*. Presented at OHBM Rome Italy

Benitez-Andonegui A, Lührs M, Dumitrescu S, Goebel R, Sorger B. (2018, October). *Investigating the effect of vascular structures on the fNIRS signal*. Presented in biennial meeting of the Society for FNIRS in Tokyo, Japan

Tursic A, Lührs M, **Benitez-Andonegui A**, Goebel R (2018, October). *Short distance channels: Do they contain task-related information?* Presented in biennial meeting of the Society for FNIRS in Tokyo, Japan

Nagels-Coune L, Kurban D, Reuter N, **Benitez-Andonegui A**, Gossé LK, Riecke L, Goebel R, Sorger B (2017, September) *Shedding Near-Infrared Light on Brain-based Communication using Motor Imagery*. Presented in Graz Brain-Computer Interface, Graz, Austria

Nagels-Coune L, Kurban D, Reuter N, **Benitez-Andonegui A,** Gossé L, Riecke L, Goebel R, Sorger B. (2017). *Yes or no? Binary brain-based communication utilizing motor imagery and fNIRS.* Proceedings of the 7th Graz Brain-Computer Interface, Graz (Austria)

Benitez-Andonegui A, Ivanov D, Goebel R, Sorger B (2017, June). *Towards optimization of fNIRS optode placement using functional and vascular MRI*. Presented in OHBM, Vancouver, Canada

Sorger B, Nagels-Coune L, **Benitez-Andonegui A**, Lührs M, Riecke L and Goebel R (2016, October). *Brain-based communication via online-decoded fNIRS signals*. Presented in biennial meeting of the Society for FNIRS in Paris, France

Vidorreta M, **Benitez-Andonegui, A**, Pastor M, Fernandez-Seara, M. (2014, May) *Reproducibility of resting state functional connectivity maps derived from ASL CBF data and concurrent BOLD.* Presented at ISMRM, Milan, Italy